UNIVERSITÀ DEGLI STUDI DI PALERMO
Dottorato di Ricerca in Ingegneria dell'Innovazione Tecnologica
Dipartimento dell'Innovazione Industriale e Digitale
Ingegneria Chimica Gestionale Informatica Meccanica
ING-IND/22

PLLA-BASED SCAFFOLDS FOR OSTEOCHONDRAL TISSUE REGENERATION VIA THERMALLY INDUCED PHASE SEPARATION TECHNIQUE

IL DOTTORE
ING. GIOACCHINO CONOSCENTI

IL COORDINATORE
PROF. SALVATORE GAGLIO

IL TUTOR
PROF. VINCENZO LA CARRUBBA

CICLO XXIX
ANNO CONSEGUIMENTO TITOLO 2017

Υπαρχουν μονο δυο πραγματα : η επιρτημη και η γνωημη.
Το πρωτο παραγει γνωση, την τελενταια αγνοια.

There are, indeed, two things, knowledge and opinion;
of which the one makes its possessor really to know, the other to be ignorant.

Hippocrates of Kos

Abstract

Tissue engineering (TE) is a multidisciplinary science aiming at designing and developing biological substitutes to improve, repair and/or replace tissues in human organisms. Based on the classical tissue engineering triad presented on the first chapter (Scaffold, Source and Signal), the scaffold acts as 3D template, the cells represent the source while the bioreactor provides the adequate physical/chemical signal. In this thesis work all three aspects were taken into account considering as a target the osteochondral regeneration

The osteochondral defects, regarding cartilage injuries extending deep into the subchondral bone, remains a challenging task in reconstructive surgery. They are difficult to treat because the two tissues present very different intrinsic healing capacities and completely different anatomic structures. Among the pletora of strategies in tissue engineering the use of a scaffold is one of the building blocks. It is a polymeric structure, biocompatible and biodegradable, able to replicate the extracellular matrix (ECM), whose major function is to provide a temporary support for tissue structures. The scaffold must mimic as closely as possible the structure of living tissue from a chemical and physical point of view. This implies specific characteristics such as high interconnected porosity, appropriate pore size and distribution (related to the tissue to be regenerated), sufficient initial mechanical strength, biodegradability and biocompatibility, ease of sterilisation and processability.

One of the most versatile methods for the fabrication of tissue engineering scaffolds is the so-called Thermally Induced Phase Separation (TIPS), presented in the second chapter, through which it is possible to obtain a porous structure with a high degree of interconnection. It has been widely reported in literature that via targeted temperature vs. time protocols it is easy to cover a wide range of pore dimensions (from ca. 10 μm to more than 200 μm) ensuring simultaneously remarkable levels of porosity, which makes those structures suitable for cell seeding, migration and colonisation.

TIPS technique is based on changes in Gibbs free energy to induce the demixing of a homogeneous polymer solution into a two-phase system. When phase separation occurs, the homogenous polymer solution separates into a polymer-rich and polymer-lean phase. For polymer-solvent systems, a miscibility gap can be identified in a T vs. composition diagram

and, as a function of the separation pathway, various mechanisms take place: nucleation and growth inside the metastable region, between the binodal and the spinodal curve; spinodal decomposition, inside the unstable region (i.e. below the spinodal line). Depending on the residence time inside the metastable region and/or the cooling rate, different morphologies can be obtained.

The most relevant operating parameters include: polymer type, solvent to non solvent ratio, polymer concentration and temperature vs. time history. These parameters are strongly important both in the early separation stages, when the onset of the first clusters takes place, and in the later stages, when the structure of the scaffold skeleton consolidates. It is evident from the aforementioned scenario that a crucial point in scaffold formation via TIPS is the thermal pathway, which allows one to obtain different morphologies by simply modifying the temperature vs. time protocol.

Among the all possible biocompatible polymers, the poly(α-hydroxy acids), approved by Food and Drug Administration (FDA) of USA for clinical applications, have been extensively studied as scaffolding materials for tissue regeneration. In the particular the poly-(L-lactic acid) (PLLA) has attracted most interest thanks to its suitable mechanical properties, low toxicity and predictable biodegradation kinetics. Furthermore the PLLA can be easily processed, and its mechanical and degradation properties can be tuned as a function of the target application.

As previous mentioned, the scaffold must present a high level of porosity and interconnectivity, but although the presence of pores is sufficient for cell growth inside the 3D structure, it is possible to significantly improve the quality of the regeneration by focusing on the appropriate pore size distribution. Each organ or tissue is characterized not only by a specific cell type but also by a specific spatial organization, for example: bone, from the compact to the sponge bone, blood vessel, three layers (tunica intima, media and adventitia), etc. This structure determines the overall characteristics and resulting behavior of the organ.

For this reasons, obtaining a porosity gradient becomes a crucial point in order to mimic in the best possible way the tissue to regenerate. In order to attain a gradient pore size in the 3D structure, an experimental apparatus able to impose the desired thermal history on two sides of a scaffold in an independent way was designed, set-up and tested. The peculiarity of the experimental apparatus, presented in the chapter 3, is the possibility to control simultaneously temperature(s) and cooling rate. The sample is located between two Peltier cells, controlled by a computer interface, able to apply and control a T vs. time protocol.

Polymers alone do not possess the adequate proprieties of bioactivity, osteoconductivity or tissue integration, and therefore to overcome these limits, composite polymer/ceramic scaffolds are necessary. The rational is to combine the processability of the polymer with

good chemical/mechanical properties of the ceramic filler. In the chapter 4 composite scaffold PLLA/hydroxyapatite(HA) and PLLA/bioglass(BG) were presented. The scaffolds were characterized in terms of porosity (pycnometry), molecular structure (XRD), morphology (SEM), filler content (TGA) and chemical structure (FT-IR).
To consider a specific scaffold suitable for tissue engineering purpose, the evaluation of cell proliferation and growth is necessary. Chapter 5 presents the cell culture of different cell strains in diverse substrates.
To evaluate the separate influence of scaffold morphology on chondrocyte growth and differentiation, PLLA scaffold with two different average pore dimensions were tested. Similarly, mesenchimal stem cell were cultured in gradient pore scaffold (from ~70 μm to ~200 μm) to assess their suitability. On the other hand chondrocytes and osteoblasts were cultured in PLLA/BG and PLLA/HA scaffolds, respectively, to check the influence of the filler in the 3D structure in relation to cell adhesion, proliferation and gene expression compared to the neat polymeric scaffold.
In this thesis work the three aspects of the typical tissue engineering pathway were considered. In particular, in chapter 6 a bioreactor able to replicate in vitro microphysiological conditions of the osteochondral junction was characterized and tested with the gradient pore size scaffold. The bioreactor consists of a dual chamber system to maintain separate chondrogenic/osteogenic specific differentiation media. A removable insert hosted the scaffold seeded with human bone marrow-derived mesenchymal stem cells (hBMSCs). The insert containing the gradient pore scaffold was positioned with the smaller pore side in the chondrogenic medium chamber (upper chamber) and the larger pore size in the osteogenic medium chamber (lower chamber). At the end of the cell culture period, cell viability, gene expression and histological staining were carried out.

Sommario

L'ingegneria tessutale (TE) è una scienza multidisciplinare che mira a progettare e sviluppare sostituti biologici per migliorare, riparare e/o sostituire i tessuti negli organismi umani. Sulla base della tipica triade dell'ingegneria tessutale è incentrato il primo capitolo *Scaffold, Source and Signal*; lo scaffold funge da struttura tridimensionale, le cellule rappresentano la *source* mentre il bioreattore fornisce gli adeguati segnali chimico/fisici. In questo lavoro di tesi sono stati presi in considerazione tutti e tre questi aspetti avendo come obiettivo la rigenerazione osteocondrale.

La guarigione dei difetti osteocondrali, riguardanti le lesioni della cartilagine che si estendono fino in profondità nell'osso subcondrale, rimangono tutt'oggi un difficile compito della chirurgia ricostruttiva. Tali difetti sono difficili da trattare perché i due tessuti hanno differenti capacità intrinseche di guarigione e diverse strutture anatomiche. Tra la pletora di strategie nella rigenerazione dei tessuti lo scaffold è sicuramente uno degli elementi costitutivi. Si tratta di una struttura polimerica, biocompatibile e biodegradabile, in grado di replicare la matrice extracellulare (ECM), la cui funzione principale è quella di fornire un supporto temporaneo per il tessuto vivente. Lo scaffold deve imitare nel miglior modo possibile il tessuto da rigenerare, il che implica adeguata resistenza meccanica, biodegradabilità, biocompatibilità, facilità di sterilizzazione e lavorabilità.

Uno dei metodi più versatili per la produzione di scaffold è probabilmente la Separazione di Fase Indotta Termicamente (TIPS), presentato nel secondo capitolo, mediante la quale è possibile ottenere una struttura porosa con un elevato grado di interconnessione. In letteratura è stato ampiamente dimostrato che mediante opportuni protocolli tempo/temperatura è possibile coprire un ampio range di dimensioni dei pori (da circa 10 μm a oltre 200 μm) assicurando contemporaneamente notevoli livelli di porosità, rendendo tali strutture idonee alla coltura cellulare.

La TIPS si basa sulla riduzione di energia libera di Gibbs per indurre la smiscelazione di una soluzione polimerica omogenea in un sistema bifasico. Nel momento in cui si verifica la separazione di fase, la soluzione polimerica omogenea si separa in una fase ricca in polimero e una povera in polimero. In funzione della storia termica avvengono meccanismi di sep-

arazione differenti: nucleazione e crescita all'interno della regione metastabile (tra curva binodale e curva spinodale) o decomposizione spinodale all'interno della regione instabile (al di sotto della linea spinodale). In funzione del tempo di permanenza all'interno delle varie regioni e/o della velocità di raffreddamento è possibile ottenere diverse morfologie finali dello scaffold.

I parametri operativi più importanti sono: tipologia di polimero, rapporto solvente/non solvente, concentrazione di polimero e storia termica. In particolare mantenendo constanti tutti gli altri parametri, variando semplicemente il protocollo tempo/temperatura è possibile ottenere morfologie dello scaffold molto diverse tra loro. Tra tutti i possibili polimeri biocompatibili, la famiglia dei poli(α-idrossiacidi), approvati dalla *Food and Drug Administration* (FDA) degli Stati Uniti per applicazioni cliniche, è stata ampiamente studiata come materiale per la reallizzazione di scaffold. In particolare all'interno di tale famiglia l'acido poli-L-lattico (PLLA) ha attirato notevole interesse grazie alle sue buone proprietà meccaniche, facilità di lavorazione e velocità di degradazione controllabile.

Come evidenziato precedentemente, lo scaffold deve possedere un'elevata porosità e interconnettività, ma sebbene la sola presenza dei pori sia sufficiente per la ricrescita delle cellule è tuttavia possibile incrementare significativamente la qualità della rigenerazione ponendo l'attenzione sulla distribuzione di dimensione dei pori. Ogni organo o tessuto non è solo contraddistinto dalle diverse tipologie di cellule che lo compongono, ma anche e soprattutto dal modo in cui queste cellule e la matrice che le circonda sono organizzate nello spazio, cosa che determina le caratteristiche globali e il funzionamento dell'organo. Esempi in tal senso sono: le ossa, dal tessuto osseo compatto al tessuto osseo spugnoso; i vasi sanguigni, tunica intima, media e avventizia, ecc.

Al fine di ottenere uno scaffold che presenti un gradiente di dimensione dei pori è stato realizzato e testata una strumentazione sperimentale in grado di imporre una data storia termica ai due lati del campione in modo indipendente. La peculiarità di tale strumentazione, presentata nel capitolo 3, è la possibilità di controllare contemporaneamente la temperatura e la velocità di raffreddamento.

I polimeri da soli non possiedono le proprietà adeguate di bioattività, osteoconduttività e capacità di integrazione nei tessuti, un modo per superare tali limitazioni è la produzione di scaffold compositi polimero/ceramico. L'idea è quella di combinare la processabilità del polimero con le buone proprietà chimico/fisiche del riempitivo ceramico. Scaffold compositi PLLA/idrossiapatite (HA) e PLLA/bioglass(BG) sono presentati nel capitolo 4 . Gli scaffold sono stati caratterizzati in termini di porosità (picnometro), struttura molecolare (XRD), morfologia (SEM), contenuto di riempitivo (TGA), e struttura chimica (FT-IR).

Affinché un determinato scaffold possa essere considerato idoneo per l'ingegneria tessutale è

necessario valutarne la sua capacità di favorire la coltura cellulare. Il capitolo 5 presenta i risultati delle colture di diversi tipi cellulari in varie tipologie di scaffold.
Per valutare la sola influenza della morfologia dello scaffold sulla crescita e la differenziazione dei condrociti, sono stati realizzati scaffold in puro PLLA con due diverse dimensioni dei pori. Allo stesso modo sono stati seminate cellule staminali mesenchimali per verificare l'idoneità degli scaffold con gradiente di dimensioni dei pori (da ~70 μm ~200 μm) alla crescita cellulare. D'altro canto sono stati seminati condrociti e osteoblasti in scaffold compositi PLLA/BG e PLLA/HA, rispettivamente, per verificare l'influenza del riempitivo nella struttura 3D in relazione all'adesione, la proliferazione e l'espressione genica cellulare rispetto al puro polimero.
In questo lavoro di tesi sono stati analizzati tutti e tre gli aspetti del tipico protocollo dell'ingegneria dei tessuti. In particolare nel capitolo 6 è stato caratterizzato e testato un bioreattore in grado di replicare *in vitro* le condizioni microfisiologiche *in vivo* della giunzione osteocondrale. Il bioreattore è costituito da una sistema a doppia camera per mantenere separati i mezzi di differenziazione condrogenico e osteogenico. Lo scaffold con gradiente di dimensioni di pori è stato posto all'interno di un inserto estraibile e seminato con cellule staminali mesenchimali umane estratte dal midollo osseo (hBMSCs). Lo scaffold è stato posto i pori di dimensioni inferiori nella camera con il mezzo condrogenico (camera superiore), mentre l'estremità con i pori maggiori è stata posta nella camera con il mezzo osteogenico (camera inferiore). Al termine del periodo di coltura sono stati effettuati test di vitalità cellulare, espressione genica e colorazioni istologiche.

Acknowledgements

The Ph.D. course is a three years long trip that includes experiments, data, meetings, travels and new partnerships. It allows you to grow from a professional and personal point of view, greatly enriching your own wealth of experience.
First of all I want to thank my supervisor prof. Vincenzo La Carrubba and prof. Valerio Brucato for their guide and support during these three years, passing on their experience to me.
Thanks to my co-workers Dr. Francesco Carfì Pavia, Dr. Gianluca Mannella and Dr. Salvatore Montesanto who helped me in the use of laboratory instruments, in the realization of the gradient pore experimental apparatus and to cheer the long working days.
I would like to express my gratitude to prof. Rocky S. Tuan from the University of Pittsburgh (Pennsylvania, United States of America), for accepting me in their research group for six months. Testing my scaffolds in the bioreactor opened new perspectives in my research project. I extend my thanks to all members of the research group and in particular to Dr. Riccardo Gottardi who assisted me during that period.
Another important step of my "trip" was at the University of Erlangen-Nuremberg and at the Paracelsus Medizinische Privatuniversitat (Erlangen and Nuremberg, Germany) where I spent five months. I deeply thank prof. Aldo R. Boccaccini and prof. Gundula Schulze-Tanzil to welcome me in their professional stimulating environment. In their lab I had the possibility to characterize the composite PLLA/BG scaffolds both material and cell culture viewpoints. I extend my thanks to all members of their lab.
Thanks to all students that shared with me a part of the Ph.D. course: Marina Micari, Matteo Bellina, Davide Marino, Giulia Gandolfo, Valentina Dulcetta, Giulia di Matteo, Alessandra Loria and Alfredo Ongaro.
I deeply acknowledge my family for their support and spur, especially during all the time of my stay abroad. Last but not least my deepest gratitude to Alessandra, she was next to me before and during this trip, but I am sure she will be with me for the rest of the journey.

Publications

During the Ph.D. course the following publications were produced:

ISI Publications

1. G. Conoscenti, T. Schneider, K. Stoelzel, F. Carfì Pavia, V. Brucato, C. Gogele, V. La Carrubba, G. Schulze-Tanzil. PLLA scaffolds produced by thermally induced phase separation allow human chondrocyte growth and extracellular matrix formation dependent on pore size. *Materials Science and Engineering C*. Submitted.

2. G. Conoscenti, F. Carfì Pavia, F. E. Ciraldo, L. Liverani, V. Brucato, V. La Carrubba, A. R. Boccaccini. In vitro degradation and bioactivity of composite PLLA/bioactive glass (BG) scaffolds: comparison of 45S5 and 1393 BG compositions. *Polymer Composites*. Submitted.

3. L. Iannetti, G. D'Urso, G. Conoscenti, E. Cutrì, M. T. Raimondi, R. Gottardi and P. Zunino. Distributed and lumped parameter models for the characterization of high throughput bioreactors. *Plos One*, 11(9): e0162774, 2016.

4. G. Ghersi, F. Carfì Pavia, G. Conoscenti, G. A. Mannella, S. Greco, S. Rigogliuso, V. La Carrubba, V. Brucato. PLLA scaffold via TIPS for bone tissue engineering. *Chemical Engineering Transactions*, 49:301-306, 2016

5. G. A. Mannella, G. Conoscenti, F. Carfì Pavia, V. La Carrubba, V. Brucato. Preparation of polymeric foams with a pore size gradient via Thermally Induced Phase Separation (TIPS). *Materials Letters*, 160:31-33, 2015.

6. G.A. Mannella, F. Carfì Pavia, G. Conoscenti, V. La Carrubba, V. Brucato. Evidence of Mechanisms Occurring in Thermally Induced Phase Separation of Polymeric Systems. *Journal of Polymer Science: Polymer Physics*, 52(14):979-983, 2014.

International conference

1. R. Gottardi, G. Conoscenti, P. G. Alexander, P. A. Manner, V. La Carrubba, V. Brucato, R. S. Tuan. A Continuous Pore Size Gradient PLLA Scaffold For Osteochondral Regeneration. TERMIS-AM 2016, San Diego (USA), December 2016.

2. R. Gottardi, L. Iannetti, G. D'Urso, G. Conoscenti, P. G. Alexander, P. Zunino, R. S. Tuan. A High Throughput Osteochondral Bioreactor. TERMIS-AM 2016, San Diego (USA), December 2016.

3. R. Gottardi, G. Conoscenti, P. G. Alexander, P.A. Manner, V. La Carrubba, V. Brucato, R. S. Tuan. A Continuous Pore Size Gradient PLLA Scaffold For Osteochondral Regeneration. The Biomedical Engineering Society. Minneapolis (USA). October 2016.

4. F. Carfì Pavia, V. La Carrubba, G. Ghersi, G. Conoscenti, V. Brucato. Double flow bioreactor for in vitro test of drug delivery. Latin Meeting on Vascular Research 2016, Ustica (It), September 2016.

5. G. Ghersi, F. Carfì Pavia, G. Conoscenti, G. A. Mannella, S. Greco, S. Rigogliuso, V. La Carrubba, V. Brucato. PLLA scaffold for Bone Tissue Engineering. International conference on Industrial biotechnology 2016. Bologna (It), April 2016

6. R. Gottardi, G. Conoscenti, P. G. Alexander, P. A. Manner, V. La Carrubba, V. Brucato, R. S. Tuan. A Poly-L-Lactide scaffold with continuous gradient pore size for osteochondral regeneration validated in a microphysiological tissue system bioreactor. Orthopaedic Research Society 2016, Orlando (USA), March 2016.

7. G. D'Urso, L. Iannetti, G. Conoscenti, E. Cutrì, R. Gottardi, F. Migliavacca, P. Zunino. Computational model of flow and biochemical transport in a multichamber bioreactor. International CAE conference 2015, Pacengo del Garda (It), October 2015.

8. G. Conoscenti, G. A. Mannella, F. Carfì Pavia, V. La Carrubba, V. Brucato. An Innovative Method to Produce Scaffolds with a Pore Size Gradient for Tissue Engineering. 5th International Conference on Biofoams, Sorrento (It), October 2015.

9. G. A. Mannella, F. Carfì Pavia, S. Montesanto, G.Conoscenti, V. La Carrubba, V. Brucato. Poly-L-lactide (PLLA) membranes and foams for biomedical applications. Euromembrane 2015, Aachen (De), September 2015.

10. G. Conoscenti, R. Gottardi, G. A. Mannella, P. G. Alexander, H. Lin, V. La Carrubba, V. Brucato, R. S.Tuan. PLLA Scaffold with Gradient pore size in microphysiological tissue system bioreactor for Osteochondral regeneration. International Material Research Congress 2015, Cancun (Mx), August 2015.

11. G. Conoscenti, G. A. Mannella, F. Carfì Pavia, V. La Carrubba, V. Brucato. An Innovative Method to Produce Scaffolds with a Pore Size Gradient for Tissue Engineering Applications. Latin Meeting on Vascular Research 2014, Valladolid (Sp), October 2014.

National conference

1. V. La Carrubba, G. Conoscenti, V. Brucato, Biodegradable PLLA based scaffolds with pore gradients for bone tissue engineering. Biomaterial Italian Society 2015, Ancona (It) June 2015.

2. G. Conoscenti, G.A. Mannella, F. Carfì Pavia, V. La Carrubba, V. Brucato. PLLA Biodegradable Scaffold with Gradient Pore Size for Bone Tissue Regeneration, Italian Association of Material Engineering 2014, Lecce (It), September 2014.

3. G. Conoscenti, G. A.Mannella, F. Carfì Pavia, V. La Carrubba, V. Brucato. Anisotropic scaffold for Bone Tissue Engineering. Biomaterial Italian Society 2014, Palermo (It) July 2014.

Table of contents

List of figures

List of tables

Chapter 1

Introduction

1.1 Tissue engineering (TE)

According to the definition provided by R. Langer and C. Vacanti in 1993 "Tissue engineering is an interdisciplinary field that applies the principles of engineering and the life sciences toward the development of biological substitutes that restore, maintain, or improve tissue function". Tissue engineering has evolved from the integration of knowledge of diverse fields; cell and developmental biology, basic medical and veterinary sciences, transplantation science, biomaterials, biophysics, biomechanics and biomedical engineering (O'Brien, 2011). On 1992 Eugen Bell defined tissue engineering as a list of a specific aims:

- Providing cellular prostheses or replacement parts for the human body
- Providing formed non-cellular replacement parts capable of inducing regeneration
- Providing tissue or organ-like model systems populated with cells for basic research and for many applied uses such as the study of diseased states using aberrant cells
- Providing vehicles for delivering engineered cells to the organism
- Surfacing non-biological devices to create hybrid devices and systems

Three different strategies can be individuated to pursue such goals:

1. Individual or small clusters of viable cells reintroduced into the body. This strategy is applicable in particular tissue in which the cells can directly interact with the living tissue such as hepatocytes, myocytes, etc. It eliminates the need for a surgery.
2. Injection of an appropriate tissue-inducing agent able to stimulate the injured tissue for self-recovery; example of tissue-inducing agents are cytokines and growth factors.

3. Cells accomodated within matrices. This strategy can be used in two ways: Closed system - cells or growth factors are contained in closed membranes that allow flow of nutrients and waste; Open system - cells are seeded or attached in scaffold and finally implanted in vivo.

To reach these targets a synergic cooperation between several knowledge fields is necessary. TE covers a broader range of applications and it is closely connected with other fields, i.e. transplantation of cells that perform a specific biochemical function (e.g., an artificial pancreas, or an artificial liver). The term regenerative medicine is often adopted as synonym of TE, althouth the first one focuses more on stem cells to produce tissue.
Among the different strategies the most adopted is probably the use of porous biodegradable 3-dimensional (3D) scaffold able to simulate the extracellular matrix (ECM) of the tissue to regenerate. Considering that each tissue is characterized by different functions and features, the scaffold should replicate as closely as possible the body structure to regenerate from a physical and chemical point of view. The scaffold characteristics strongly depend on the material and the production technique. The crucial point is the ability to shape the scaffold in the suitable cell environment for the specific tissue.
The typical tissue engineering triad is composed by a triple S: Signal, Source and Scaffold (fig. 1.1).

The signals can be chemical (growth factor) or physical (bioreactor), the source is the cell culture, while the scaffold acts as 3D template. Depending on the final purpose, membranes, tubes, gels or matrices can be developed.
Membranes are adopted when a barrier between two environments are necessary. Membrane technology is of major importance in medical applications, in particular in a number of life saving treatment methods. In literature is possible to find several applications involving membrane engineering (Stamatialis et al., 2008): transdermal drug delivery (Pérez et al., 2013), dialysis (Barzin et al., 2004), blood oxygenation (Messai et al., 2015), artificial liver (Bikhchandani et al., 2011), artificial pancreas (Munkhjargal et al., 2015), etc.
Tubular biomaterial are primarily adopted for vascular tissue engineering (Nemeno-Guanzon et al., 2012). Several tissue engineering strategies have emerged to address biological flaws at the blood-material interface of the synthetic scaffolds. The biomaterial design have been directed towards the generation of materials that does not only mimic the native vascular tissue's mechanical properties but also promote cell growth, inhibit thrombogenicity, and facilitate extracellular matrix production (Ravi and Chaikof, 2010). The principal ECM proteins of blood vessel are: collagen, elastin, fibronectin, vitronectin, and laminins (Pařzek et al., 2011). Materials for vascular replacements should be biomimetic and resistant not

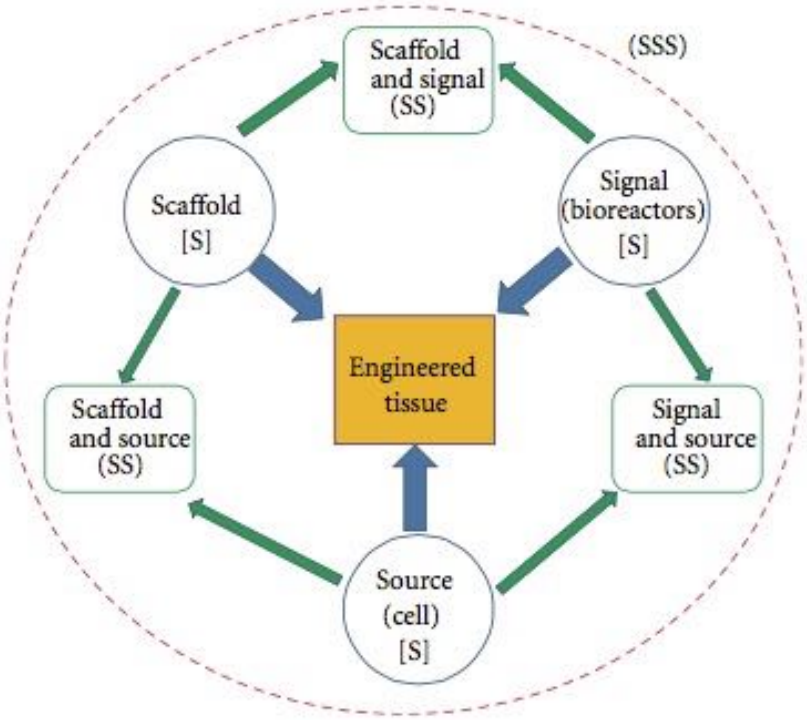

Fig. 1.1 *Typical tissue engineering triad: Signal (growth factor-chemical or bioreactor-physical), Source (cells) and Scaffold (3D network)*

only to thrombosis, but also to inflammation and neointimal proliferation. Several materials and technique has been adopted for vascular replacement, such as: polyglycolic acid (PGA) (Xu et al., 2008), chitosan via TIPS technique (Zhang et al., 2006), poly(glycerol sebacate) (PGS) (Gao et al., 2006), materials derived from amniotic membrane (Lee et al., 2012), etc. Hydrogel biomaterials can encapsulate and represent a specialised environment for isolated cells (Wolf et al., 2012). Collagen gels, as an example, can be used for the preservation and immunoprotection of xenograft and homograft cells, such as hepatocytes or chodrocytes, used for transplantation. Gels are particularly suitable in applications such as bone and cartilage tissue regeneration where polymerization in situ can a be an useful route (Bhattacharjee et al., 2015; Haleem-Smith et al., 2012; Ni et al., 2014). Semipermeable gels can be a support for cells in systems where cell-cell communication and interaction with surrounding tissue has to be minimised as well as the movement of peptide factors and nutrients through the implant (Nichol et al., 2010).

1.2 Bone

Bone tissue is a particular type of connective tissue specialised in support function. The tissue is constituted by an extracellular matrix, mineralised, and by four cell components: osteoblasts, bone lining cells, osteocytes, and osteoclasts.
Bone is composed by inorganic and organic matrix. The organic matrix is basically composed by collagenous proteins (90%), in particular type I collagen, and non collagenous proteins including osteocalcin, osteopontin, bone morphogenetic proteins (BMPs) and growth factors (Aszódi and Bateman, 2000).
The inorganic material of bone consists on calcium phosphate in the form of hydroxyapatite crystals, $Ca_{10}(PO_4)_6Ca(OH)_2$ (about 85%), calcium carbonate (~10%) and traces of the salts and elements (magnesium phosphate $Mg_3(PO_4)_2$, calcium fluoride CaF_2, sodium, potassium, etc.)
Bone matrix provides not only mechanical support on the body but also an essential role on homeostasis (constant concentration) of calcium.
Depending on the shape of the bones it is possible to classify them on: long bones, short bones, flat bones is possible to distinguish (fig. 1.2).
Leg and arm bones (femur, radius, phalanges and others) are examples of long bones. Long bone consists in a central part (diaphysis) and two terminal parts (epiphyses). Long bones are composed of a hard outer surface of compact bone and a spongy inner. At the epiphyses is located the red bone marrow, while the yellow bone marrow is located in a cavity within the diaphysis.
Short bones are wider than long and have a primary function of providing support and stability with little movement. Examples of short bones are the carpals and tarsals.
Flat bones have different shapes and dimensions. They are strong, flat plates of bone with the main function of providing protection to the bodies vital organs and being a base for muscular attachment. Flat bones consists in two layers of compact bone tissue. Classic examples of a flat bones are: scapula (shoulder blade), sternum (breast bone) and cranium (skull).
Two additional types of bone are: sesamoid bones, usually short or irregular bones imbedded in a tendon, and irregular bones, with a non-uniform shape.

Two types of bone tissues can be individuated: compact bones and spongy bone. The first one has higher density than the second one, due to higher packed structure. Externally, the bone is covered by a fibrous connective twisted bundles tissue, the periosteum, while the diarthrodial joints are covered with articular cartilage. In the case of the shaft of long bones, the spinal canal is covered by the endosteum, thin vascular membrane of connective tissue that lines the surface of the bony tissue.

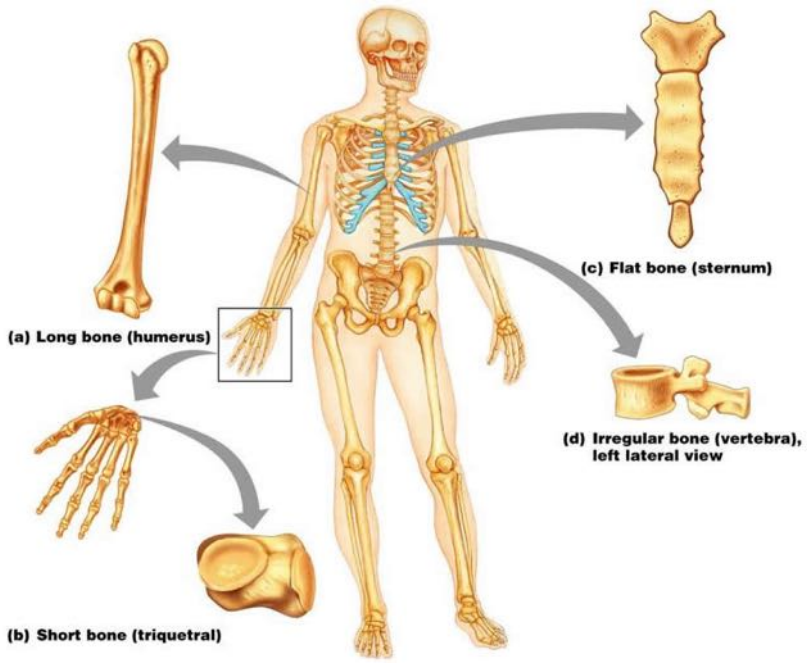

Fig. 1.2 *Different types of bones in the human body: long bones, short bones, flat bones and irregular bones*

The organic components of the bone are: collagen, proteoglycans, some non-collagenous proteins, cytokines and growth factors. The most abundant element is the type I collagen, which is organized into fibers, supporting the sedimentation of salts during the mineralization process.

Four types of cells contribuite to homeostasis: osteoblasts, osteoclasts, osteocytes and osteogenic cells. Osteoblasts are bone forming cells, supporting to the bone formation. Osteoblasts make and pack the matrix molecules, collagen protein fibres, and ions, Ca^{2+} and PO^{4-}, for release into the extracellular environment. Once released, the molecules in the matrix react with each other to form a rigid yet flexible bone tissue called osteoid that eventually hardens to form bone.

Osteoclasts cells are responsible for the dissolution and absorption of bone. Osteoclasts are formed by the fusion of many cells derived from circulating monocytes in the blood. In contacts with bone, osteoclasts produce enzymes, among which the acid phosphatase. Osteoclasts dissolve both the collagen and the inorganic calcium and phosphorus of the bone in two steps. In the first step, the mineralized bone is broken into fragments, in the second step the osteoclasts consume the fragments and digests them within cytoplasmic vacuoles.

The osteocyte is an osteoblast embedded within the bone matrix, occupying a small chamber called lacuna, which is contained in the calcified matrix of bone. Osteocytes are the most abundant cell type in mature bone tissue, surviving as long as the bone lifespan (up to

decades). The osteocyte is capable of bone deposition and resorption. It is also involved in bone remodeling by transmitting signals to other osteocytes in response to even slight deformations of bone caused by muscular activity.
The osteogenic cells are the only ones able to divide via mitosis mechanism. They are undifferentiated cells with high mitotic activity, able to differentiate in osteoblast cell and involved in the bone formation process.
The equilibrium among these cells maintains a health bone tissue.

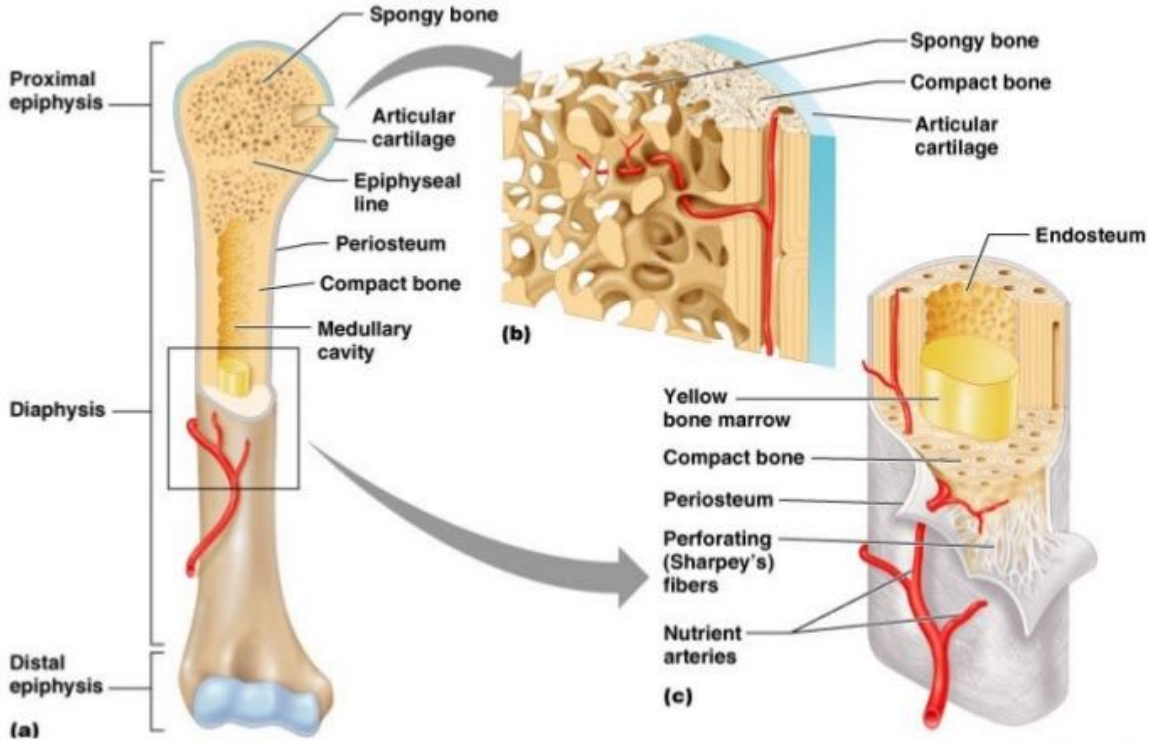

Fig. 1.3 *Internal structure of a bone: compact bone, outside, to provide the adequate mechanical properties; sponge bone, inside, with large pores to host the bone marrow*

In figure 1.3 the internal structure of a long bone is reported. The compact bone forms a shell around cancellous bone. Mature compact bone is lamellar, or layered. The structure is organized around vascular cavities to ensure the properly supply of nutrients to the osteocytes arranged in concentric lamellae; these channels can be parallel to the bone axis, Haversian canals, or transversally to the axis, Volkmann channels.
The bone is arranged in concentric layers around those canals, forming structural units called osteons, with a thickness from 4.5 to 11 µm. Immature compact bone does not contain osteons and exhibits a woven structure. It forms around a framework of collagen fibres and is eventually replaced by mature bone in a remodeling process of bone resorption and new bone formation that creates the osteons.

The spongy bone is a inner part of bone enclosing numerous large spaces that give a honeycombed or spongy appearance. The bone matrix, or framework, is organized into a three-dimensional latticework of bony processes, called trabeculae, arranged along lines of stress. The spaces inside the trabeculae is filled with marrow and blood vessels.

Bone diseases are disorders and conditions that cause abnormal development and/or impairment in normal bone development. The main bone diseases are:

- Osteoporosis, characterized by an abnormal loss of bone mass and disintegration of bone structure;
- Imperfect osteogenesis, genetic disorder characterized by brittlness bones;
- Osteomalacia, abnormal bone formation caused by a defect of vitamin D, the name is Rickets if the disease affects young people;
- Paget's disease, error in balancing between osteoblasts and osteoclasts populations that causes imperfect rebuilding and remoulding of bone tissue.

1.3 Cartilage

Cartilage is an important structural component of the body. It is a firm tissue but softer and much more flexible than bone. The cartilage is a metabolically active tissue, but the chondrocytes (corresponding to about 1% of the volume of hyaline cartilage) have a relatively slow turnover. Irrespective of cartilage species (joint, tracheal, laryngeal, nasoseptal, auricular cartilage etc.) it possesses low repair capacity due to the lack of vascular system that could support repair and remodeling. Furthermore, chondrocytes have not direct access to progenitor cells, as for many other tissue, then the limited capacity of self-renewal implies that even minor injuries may lead to progressive damage and degeneration.
Chrondrocytes are chondroblasts (cells that produce the collagen extracellular matrix) that are caught in the matrix. They lie in spaces called lacuna with up to eight chondrocytes located in each.
The base substance of cartilage is chondroitin sulfate and the microarchitecture is subtantially less organized than in bone. It is possible to distinguish three major types of cartilage that differ in biochemical composition and structure of extracellular matrix (ECM) (which implies a variety of mechanical properties).

- Elastic cartilage

- Hyaline cartilage
- Fibrocartilage

The elastic or yellow cartilage is characterized by chondrons with few cells and small concentration of proteoglycans (PGs), but much elastin. Elastin is the protein giving flexibility to the tissue, it is interwoven in the collagen mesh. This tissue is less vulnerable to degenerative process. It is found in the epiglottis (part of the larynx) and the pinnae (the external ear flaps of many mammals including humans). Elastin fibers turn dark purple/black with Verhoeff stain.

Hyaline cartilage is the most widespread cartilage type and, in adults, it forms the articular surfaces of long bones, the rib tips, the rings of the trachea, and parts of the skull. The name is due to the glassy appearance and it is predominately collagen with few collagen fibers. Hyaline cartilage is the first step of ossification before the formation of bone. The hyaline cartilage is externally covered by a fibrous membrane, called perichondrium except at the end of long bone. It consists of a rounded or bluntly angular cells, linked in groups of two or more forming a homogeneous matrix. Hyaline cartilage presents high resistance to compression and high tensile force for the relevant presence of collagen type II combined with high concentration of PGs. Articular cartilage is a particular type of hyaline cartilage, presents on the articular surfaces of bones. Figure 1.4 reports the schematic structure of the articular cartilage.

Fibrocartilage has different types of collagen fibers (Type I and Type II), and it tends to grade into dense tendon and ligament tissue. The fibrocartilage consists of a mixture of white fibrous and cartilaginous tissue. Flexibility and toughness are the results of this combination, the elasticity is basically due to cartilaginous tissue. Like the elastic type, the fibrocartilage contains small amount of PGs, but on the contrary small concentration of elastin. An example of fibrocartilaginous is the meniscus, but also the pubic symphysis and annulus fibrousus.
Among the possibles disease of the cartilage the costochondritis is probably the most common. It is an inflammation of the cartilage that connects a rib to the breastbone (sternum), causing severe pain. Other typical cartilage diseases are: herniation, achondroplasia, polychondritis, etc.

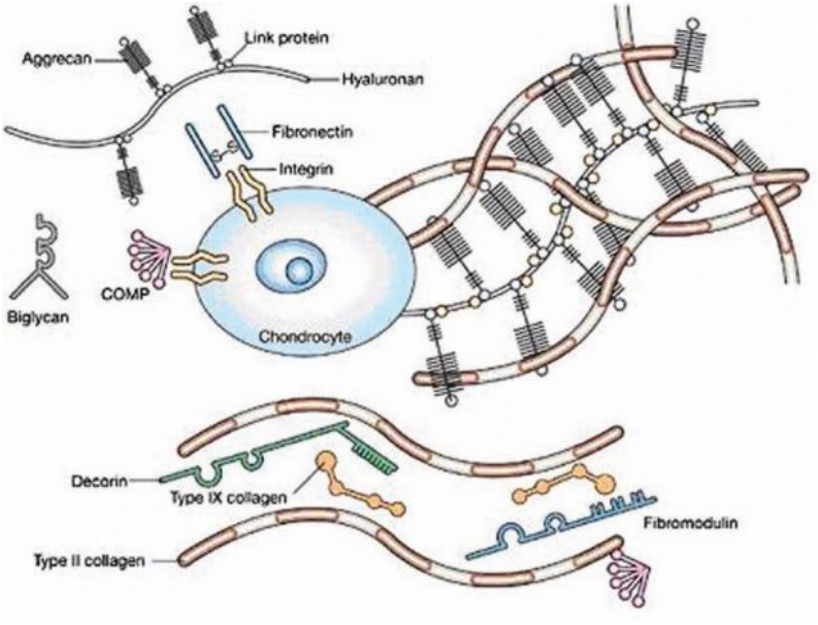

Fig. 1.4 *Extracellular matrix of articular cartilage. The interaction between collagen and proteoglycans provides the compressive and tensile strength of the tissue, from Sophia Fox et al. (2009)*

1.4 Osteochondral junction

The osteochondral junction is composed of the articular cartilage and the subchondral bone. This region has a multilayered structure, connecting the articular cartilage through the calcified cartilage with the subchondral bone.

This body structure is present in many joints in the human body, where cartilage connects to the subchondral bone, as the diarthrodial joints, knee or hip, or the fibrocartilaginous joints such as the intervertebral discs.

The osteochondral junction has a complex structure because several different tissue exist in a very small space. The upper part is the uncalcified cartilage, characterised by three layer: on the top, the superficial zone with collagen fibrils aligning parallel to the articular surface; a deep zone where chondrocytes and fibrils are organised perpendicular to the articular surface and a transition middle zone with less organization compared to the other two layers.

The deepest zone is the subchondral bone, consisting in a almost impermeable cortical bone. The thickness of the subchondral bone is around 2mm but it varies as a function of location, age and joint degeneration.

Between the uncalcified cartilage and the subchondral bone a wavy tidemark of basophilic matrix is present, the calcified cartilage. This latter provides mechanical stability and resistance against shear stress. It is composed by a large amount of HA (~65%), metabolically

active, including the ability to remodel with loading and aging. The thickness is maximum, ~200 µm, at 20 years old, and gradually decreases with age until 100 µm. (Lopa and Madry, 2014; Yousefi et al., 2014)
Figure 1.5 reports the osteochondral junction structure from articular cartilage to subchondral bone.

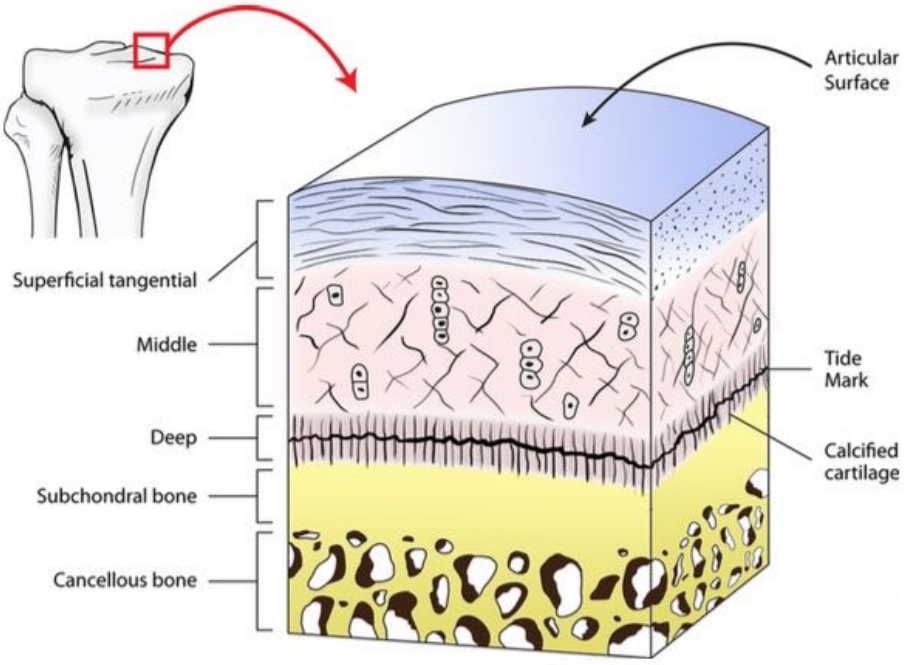

Fig. 1.5 *Osteochondral junction divided into five different zones. From the top to the bottom. 1 - Superficial zone has chondrocytes and collagen fibres parallel to the joint surface; 2 - Middle zone in which collagen fibres interlacing each other without a specific spatial organisation; 3 - Deep zone has fibres perpendicular to the joint surface; 4 - Tidemark of basophilic matrix; 5 - Subchondral bone, a thin cortical lamella, lying immediately beneath the calcified cartilage*

The most common disease of the osteochondral junction is the osteoarthritis. It is a chronic, degenerative disease of the articular joint that involves cartilage, bone, tendon, and peri-articular muscle. Healthy cartilage allows bones to move over one another and it absorbs energy from the shock of physical movement. In osteoarthritis, the cartilage breaks down, causing pain, swelling and problems when moving the joint. At further steps bits of bone or cartilage may chip off and float around in the joint. Osteoarthritis affects above all patients older than 40 of all races and sexes. Until now there are not specific medical treatments for the osteoarthritis, the only possibility being to reduce pain and improve function of the affected joints (Lozito et al., 2013).

1.5 Scaffold for tissue engineering purpose

Scaffold is one of the other major component of the tissue engineering approach; the choice of scaffold includes its constitutive material, its design and often the surface or bulk treatment. The scaffold is a three-dimensional support suitable for the growth of a tissue or an organ. The aim of the scaffold is the temporary replace of extracellular matrix to support the proliferation and growth of cell. Several studies showed that, without a guide, the cells tend to organise in a two-dimensional (2D) layer forming a flat structure with poor mechanical properties (Tian et al., 2008). In particular, by using scaffolds, transplanted cells can be delivered to a specific place in a tissue driving the growth of cells inside a desired site. Thus scaffolds represent the space available for the tissue to develop and a physical support for cells growth.
To achieve these objectives, the scaffold must possess some basic requirements:

- Biocompatibility. A materials causing minimal biological responses is considered biocompatible. In tissue engineering a biocompatible materials is defined as able to generate the most appropriate cellular or tissue response in the specific tissue to regenerate. Chemistry, structure, morphology or specific surface treatment are important parameters that can determine the scaffold's biocompatibility.
  Adhesion and proliferation of cells on materials primarily depends on the surface characteristics such as wettability, bulk chemistry, surface roughness, hydrophilicity/hydrophobicity ratio, etc.

- Biodegradability. One of the peculiarity of the scaffold is the degradation in a natural environments. This includes changes in chemical structure, loss of mechanical and structural proprieties and, at the end, the complete conversion in other small molecules such as water, carbon dioxide and various minerals. The biodegradation of the materials is due to chemical, biological and physical forces depending on temperature, pH, humidity, etc.

- Architecture. The morphology of the scaffold depends on the specific application (large or small pore size, interconnection, shape). A porous structure is usually needed for two critical functions. First, pore channels provide ports of entry for migrating cells or for capillary suction of blood. Secondly, a large area is available for specific and numerous cell interactions. In particular microporosity is fundamental for capillary ingrowth and cell-matrix interactions while macroporosity for nutrients supply and waste removal of cells grown on the scaffold.

- Mechanical properties. Scaffolds provide mechanical and shape stability to the tissue defect. The intrinsic mechanical properties those of biomaterials used for scaffolding

or their post-processing properties should match the host tissue. Recent studies demonstrated the connection between the mechanical characteristics and the cell seeding efficiency (mechanobiology, Jansen et al. (2015)).

- Sterilizability. Typical sterilisation process for biomaterials are: autoclave, UV, gamma or ethylene oxide treatment. These treatments are often poorly adapted to polymeric scaffolds due to their low melting points and degradation mechanisms. Furthermore, some methods can provoke undesirable polymer chain scission or crosslinking with an alteration of the final properties. Thus, the effect of the sterilisation procedure must be accounted for in the scaffold design process.

Several different types of biomaterials has been used for tissue engineering purposes, but the most important are natural and synthetic polymers. Ceramic materials are also used, particularly in combination with polymers, forming composite materials with improved mechanical and biological properties. In the next two paragraphs a small overview about synthetic and natural polymers is reported.

1.5.1 Natural polymers

The natural polymers are typically biocompatible and biodegradable via enzymatic process. The main advantage in using natural polymers is that they contain functional biomolecules helping the proliferation, attachment and differentiation of cells. However, there are some disadvantages, depending on the application. First of all the rate of degradation cannot be easily controlled, that implies a difficult to determine its duration when implanted. Furthermore, natural polymers often possess quite low breaking load, although this aspect improves considerably if the polymer is cross-linked. In figure 1.6 a panel of the principal adopted natural polymers is reported.

- Alginate. Alginate is a naturally derived polysaccharide abundant in cell walls of brown algae. It is a polyanion composed of two repeating monomer units: β-D-mannuronate (M) and α-L-guluronate (G). Chain length and relative proportions determine its physical and mechanical properties. The chemical structure of alginate allows a complete solubility in water.
  The conventional role of alginate in pharmaceutics includes its use is as thickening, gel forming, and as stabilizing agents, alginate can also play a significant role in controlled-release drug products. Alginate was used in bone tissue applications delivery of osteoinductive factors or bone-forming cells, but also in combination with HA to enhance the adhesion of osteosarcoma cells (Andersen et al., 2015; Gould et al., 2013; Haleem-Smith et al., 2012; Huang et al., 2015; Lee et al., 2007; Wen et al., 2014).

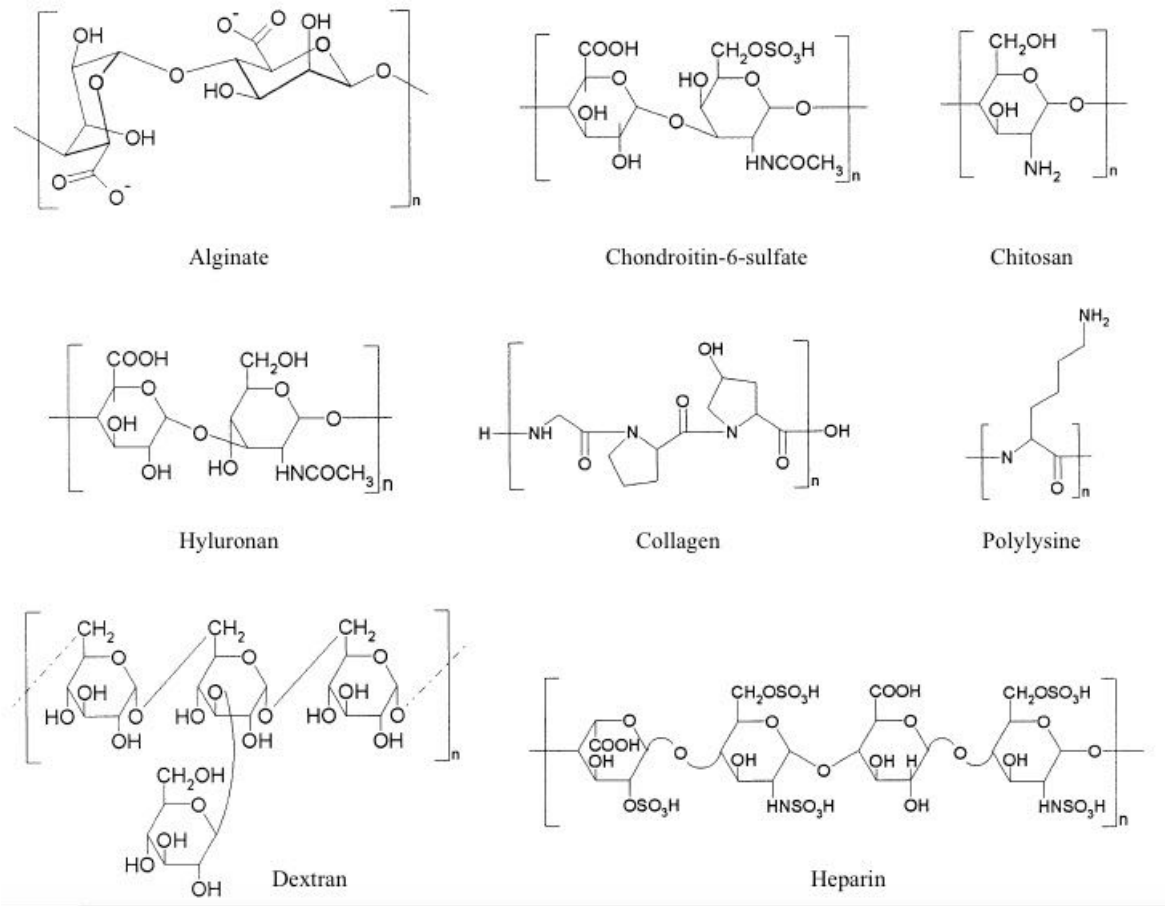

Fig. 1.6 *Chemical structure of principal natural polymer adopted in tissue engineering, adapted from Seal (2001)*

- Collagen. Collagen is the most abundant naturally occurring protein in connective tissue and thus constitutes a major component of the extracellular matrix, providing mechanical support. It is a fibrous protein with a long, stiff, triple-stranded helical structure. Due to high sequence homology between species, collagen exhibits low cytotoxicity and immunogenicity and high biocompatibility, making it one of the most promising biomaterials for tissue engineering. Type I (in skin and bone), type II (cartilage) and type III (blood vessels) are the three main collagen types. Collagen-based scaffolds have been used in a variety of tissue engineering applications: cartilage, ligament, heart valve, haemostatic agents in form of powder, sponge, plugs, etc. (Chen et al., 2010a; D'Anchise et al., 2005; Davidenko et al., 2012; Han et al., 2010; Juncosa-melvin et al., 2006; Knapp, 1997; Mullen et al., 2015; Nehrer et al., 1997; Zhang et al., 2014b)

- Chitosan. Chitosan is a linear, semi-crystalline polysaccharide composed β (1-4) linked D-glucosamine with randomly dispersed N-acetyl-D-glycosamine groups. Chitosan can be derived by partial deacetylation of the chitin via enzymatic hydrolysis of chitosanase and lysozyme. Molecular weight and deacetylation degree (DD) influence the behaviour of the polymer. Chitosan DD varies between 60 and 100% while the molecular weight from 300 to 1000 kDA, depending on source and preparation.
  Chitosan is poorly soluble in water. It is a very good candidate for biomaterial, possessing several remarkable properties like: haemostatic activity, antimicrobial activity and tunable crystallinity (maximum for DD 0% and 100% and decrease for intermediate DD) (Chicatun et al., 2013; Croisier and Jérome, 2013; Han et al., 2010; Hsieh et al., 2007; Wu et al., 2008).

- Hyaluronic acid. Hyaluronic acid or hyaluronan is an unbranched non-sulfated glycosaminoglycan (GAG) composed of repeating disaccharides (β-1,4-D-glucuronic acid (known as uronic acid) and β-1,3-N-acetyl-D-glucosamide). This material is an anionic polysaccharide, with extremely high water-binding capacity and very high molecular weight ($10^5 - 10^7$ Da); this implies that also dilute solutions show high viscosity values.
  Hyaluronic acid is one of the major elements in the ECM of vertebrate tissues. It is present in a large part of body fluids and tissue, i.e. skin, cartilage, synovial fluid, etc. The acid is produced and secreted by cells including fibroblasts, keratinocytes, or chondrocytes and degraded via a step-wise process in enzymatic or non-enzymatic reactions.
  Tissue engineering applications of hyaluronic acid regard dermal filler, osteoarthritis treatment, scaffold material to support chondrocyte growth, etc. (Jakobsen et al., 2010; Kim et al., 2008; Pietrucha, 2005; Sawatjui et al., 2014; Zhao et al., 2014; Zhu et al., 2014)

1.5.2 Synthetic polymers

Synthetic polymers offer considerable advantages compared to the natural ones. The main benefit is that their properties (e.g., porosity, degradation time, and mechanical characteristics) can be tailored for specific applications. Synthetic polymers are often cheaper than natural polymer; they can be produced in large uniform quantities under controlled conditions assuring reproducible behaviour. Furthermore, most of the synthetic polymers exhibits a hydrolytic degradation almost independent of the host tissue. The most common synthetic polymers are the polyesters that include polyanhydrides, polycarbonates, and polyphos-

phazenes (fig. 1.7). A significant disadvantage in the use of synthetic polymers is the degradation into undesirable products such as acids that at high concentrations can cause inflammation (Barton and McHugh, 2000; Dhandayuthapani et al., 2011; Gunatillake and Adhikari, 2003; Guo and Ma, 2014; Ma et al., 2010; Ma and Choi, 2001; Muñoz-Bonilla and Fernández-Garcia, 2012; Singh and Singh, 2007).

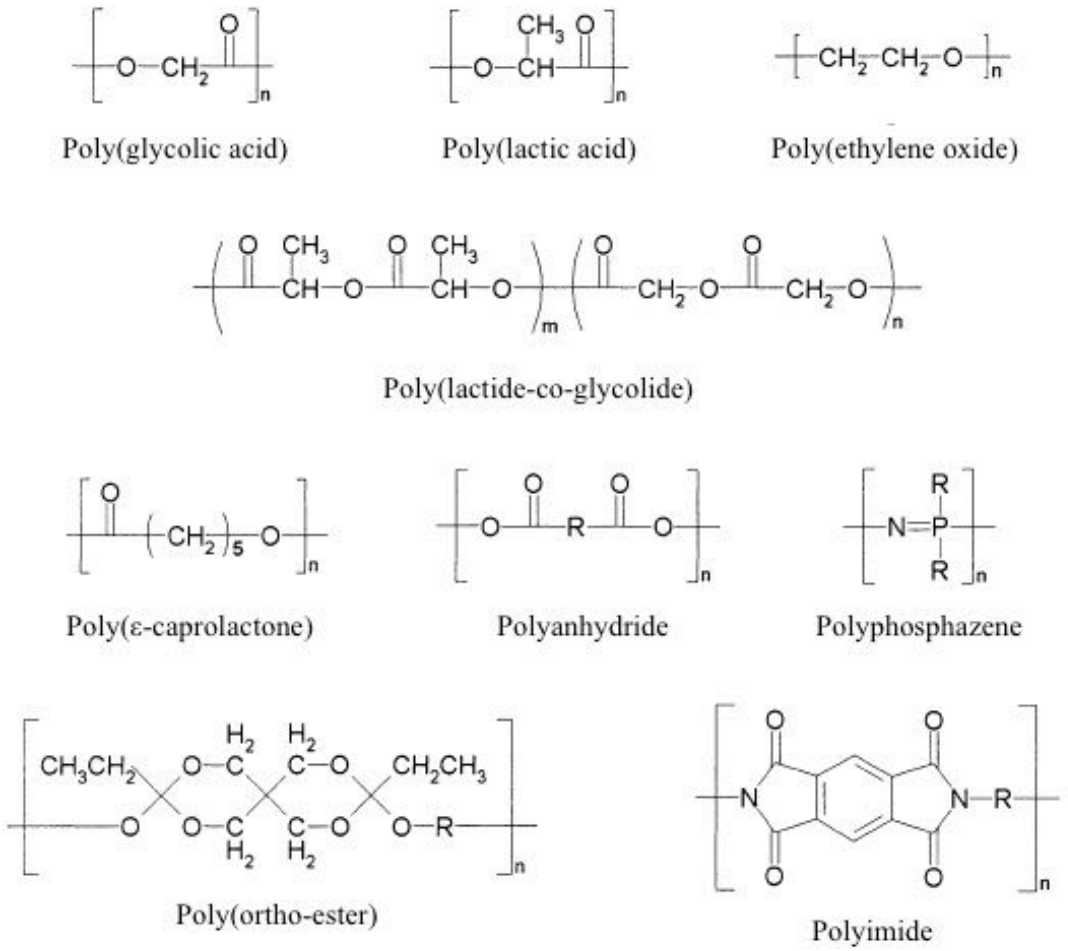

Fig. 1.7 *Chemical structure of principal synthetic polymer adopted in tissue engineering, adapted from Seal (2001)*

- Poly (α-hydroxyacids). Aliphatic polyesters are, probably, the most used synthetic polymers in tissue engineering. The Poly (α-hydroxyacids) includes: Polylactide (PLA), polyglycolide (PGA), and their copolymer poly(lactide-co-glycolide) (PLGA). Besides their biodegradability and biocompatibility, these polymers are approved by the U.S. Food and Drug Administration (FDA) for human clinical applications such

as surgical sutures and some implantable devices (Curran et al., 2013; Gentile et al., 2014; Park et al., 2005; Stölzel et al., 2014).
Degradation rates and degradation products of these linear aliphatic polyesters depend on composition, molecular weight, exposed surface area, crystallinity, stresses, site of implantation and, in the case of copolymers, the ratio of the hydroxy acid monomers. Usually these polymers are synthesised by ring-opening polymerisation and shaped in film, tubes, matrices, etc. (Burns et al., 2010; Maquet et al., 2003; Parent et al., 2013)

- Poly(ε-caprolactone). Poly(ε-caprolactone) (PCL) is a semi-crystalline polymer with a very low glass-transition temperature of around -60°C and low melting point, about 60°C. Thus, it is always in the rubbery state, with high material permeability under physiological conditions and a quite high thermal stability (the decomposition temperature is 350°C). PCL degrades by hydrolytic mechanism at slower rate than PGA or PLA. Usually PCL is adopted as blend with other polymers to increase the degradation time and for drug-delivery systems (Dell'Erba et al., 2001; Du et al., 2014; Dziadek et al., 2015; Hsu et al., 2013; Kouya et al., 2013; Ma et al., 2010; Nottrodt et al., 2014; Oh et al., 2007; Salerno et al., 2011b; Vaquette and Cooper-White, 2013; Vert et al., 1992).

- Poly(ortho-esters). Poly(ortho-esters) are hydrophobic, surface eroding polymers that have three geminal ether bonds. During the biodegradation, the material becomes thinner and thinner without a breaking of the material: for this reason, it has been exploited for drug delivery applications. Degradation of poly (ortho-esters) occurs via hydrolysis with a self-catalyst process due to the acidic products. The capacity to be used as typical tissue engineering scaffolds are limited by their weak mechanical properties and the tendency to induce an inflammatory response in the body (Andriano et al., 1999).

- Polyphosphazenes. Polyphosphazenes are inorganic/organic hybrid polymers of high molecular weight. The polymer backbone consists of alternating phosphorus and nitrogen atoms and organic substituents are linked to the phosphorus atoms as side groups. The properties of the resulting material are highly dependent on the side-substituents and their ratios, then various synthetic methods have been used to achieve different properties (Babensee et al., 1998; Nichol et al., 2014; Peach et al., 2012). Furthermore, the organic groups do not have to be identical; this offers the possibility to add mixed substituents to control the functionality and the properties of the polymer, such

as amphiphilic properties, combination of recognition and release sites, bioerodible properties, etc. (Babensee et al., 1998; Morozowich et al., 2011; Rothemund et al., 2015; Teasdale and Brüggemann, 2013)

1.6 Scaffold fabrication technique

The choice of the biomaterial is also related to the production technique. Many fabrication methods have been developed in order to attain the optimum porosity, pore interconnectivity and mechanical properties to best match those of the tissue to regenerate. Among all the possible techniques the widely adopted are: solvent-casting and particulate leaching, phase separation techniques, gas-foaming, CAD based technique and electrospinning.

Solvent-casting and particulate leaching

The solvent casting technique consists of dissolving a polymer in a solvent and then adding particles of a porogen: paraffin spheres, salt particles, wax, etc. The mixture is poured in a mold and left to dry in air or under vacuum until the complete evaporation of the solvent. At the end of the process the porogen is leached out and the polymer creates a network of interconnected polymer. The dimension of the pores is a function of the porogen dimension. In the case of composites, the filler is added with the porogen and it remains after the porogen is leached out (Yanpeng et al., 2007).
It is possible to tune the crystallinity of the polymer via thermal treatment by controlling the cooling rate. Polylactic and polyglycolic acid are the most adopted polymer for this technique. The main advantage is the simplicity of the method without the necessity of sophisticated apparatus. The disadvantages is directly related to use of porogen, inhomogeneity and lack in interconnection of pores, as well as the presence of residual porogen and solvent (Huang et al., 2014; Kothapalli et al., 2005). In fig. 1.8 the protocol of solvent-casting particulate-leaching technique is reported.

Gas-foaming

Gas foaming technique uses high pressure CO_2 gas as porogen agent. The porosity and porous structure of the scaffolds depend upon the amount of gas dissolved and the rate and type of gas nucleation. Under high pressure (50 bar) the dissolved carbon dioxide becomes unstable and it separates from the polymer. To minimise the free energy of the system the CO_2 molecules become spherical (cluster) and the results is the formation of pores (Goswami et al., 2013; Salerno et al., 2011b; Spadaccio et al., 2009).

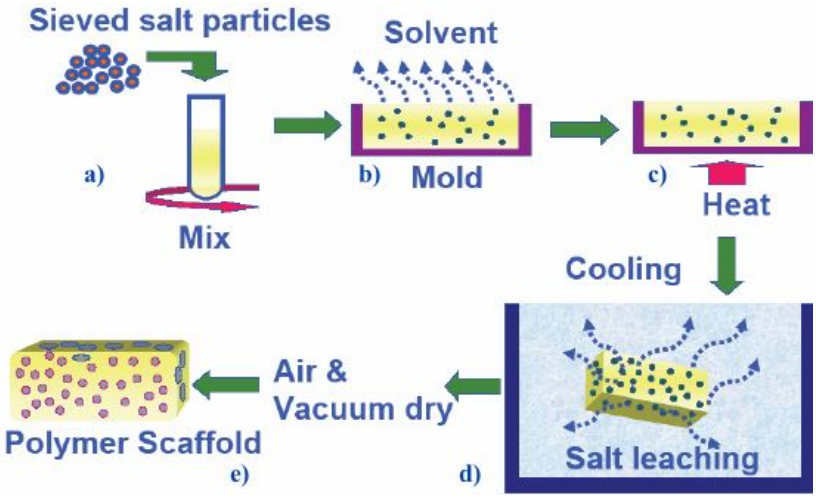

Fig. 1.8 *Schematic protocol of solvent-casting particulate-leaching technique. a) Mixing of the sieved particles in a polymeric solution, b-c) Evaporation of the solvent leaving the polymeric structure with salt particles, d) Removal of the salt, e) Drying in a vacuum oven, from Liu and Webster (2007)*

Despite this process cause a significant expansion of polymer volume often the structure is still to compact for the cells, then a combination between gas-foaming and particulate leaching is adopted. Figure 1.9 reports an example of combination of gas foaming and particulate leaching in which effervescent salt particles are used. The mix polymer and porogen are exposed to high pressure until the complete saturation with carbon dioxide, followed by foaming process porogen is removed. The advantage is that gas foaming does not require the utilization of organic solvent and high temperatures that can denature the biologically active molecules incorporated into the scaffold (Salerno et al., 2008, 2011a; Sunny et al., 2011).

Phase separation technique

Phase separation technique is based in the induction of a demixing of a solution in two phases, one with low polymer concentration (polymer lean phase) and the other one with high polymer concentration (polymer rich phase). Phase separation of polymer solutions (solvent/polymer or nonsolvent/solvent/polymer) can be induced in four different ways.

- Thermally Induced Phase Separation (TIPS). This method is based on the change of free energy of the system by varying the temperature. After the demixing of the solution, the solvent is removed by extraction, evaporation or freeze drying.

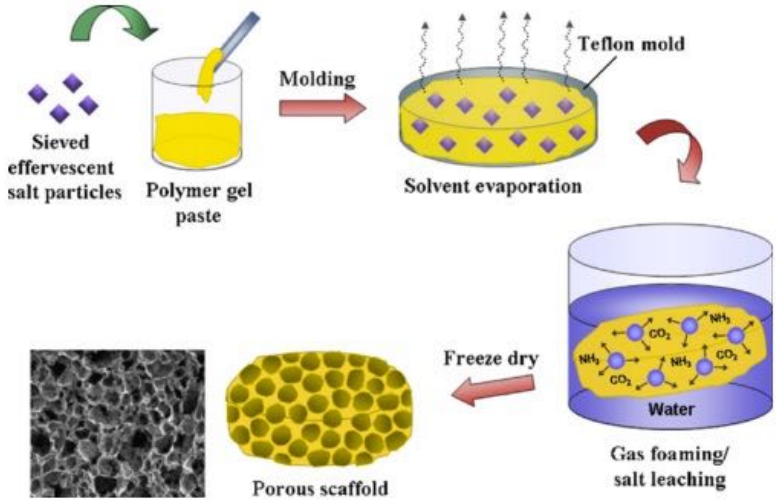

Fig. 1.9 *Fabrication of porous scaffolds by gas foaming/particulate leaching. The process is divided in four steps: 1) The effervescent salt particles are dispersed in the polymer, 2) The solution is poured in a teflon mold for solvent evaporation, 3) The solution is immersed in water for gas foaming/salt leaching, 4) The solution is freeze dried, adapted from Chung and Park (2007)*

- Air-casting of a polymer solution. In this case the polymer is dissolved in a mixture of a volatile solvent and a non-volatile non solvent. The phase separation takes place when the solubility of the polymer decreases caused by evaporation of the solvent.

- Precipitation from the vapour phase. The demixing is induced by penetration of non solvent vapour in the solution.

- Diffused Induced Phase Separation (DIPS). A polymer solution is cast as a film on a support (tube, membrane), then it is immersed in a non solvent bath. The phase separation occur as a consequence of the change between the solvent and the non solvent (fig. 1.10).

The technique can be easily combined with other fabrication technology to obtain 3D structures with controlled pore morphology, while to take advantage of this scaffold production technology it is necessary to know the phase diagram of the solution, which is very different to determine experimentally and to predict theoretically. (Akbarzadeh and Yousefi, 2014; Chen et al., 2010b; Gong et al., 2006; Hsu et al., 2013; Hu et al., 2009, 2008; Keshaw et al., 2010; Ma et al., 2010; Zhang et al., 2002; Zhang and Ma, 1999).

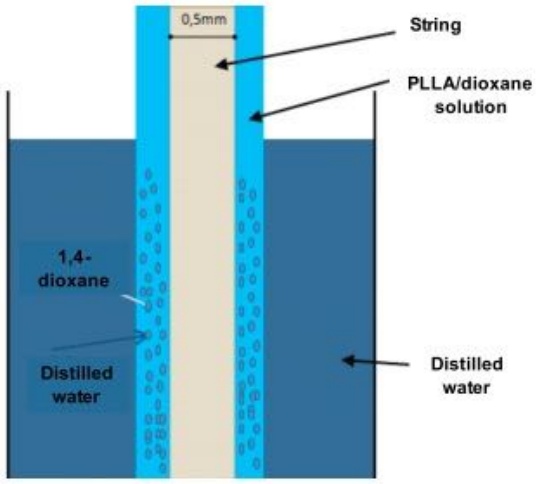

Fig. 1.10 *Example of DIPS process. A fibre cover of a binary polymeric solution PLLA/Dioxane is immersed in a non-solvent bath, water, where the phase separation takes place, from Carfì Pavia et al. (2010)*

Electrospinning

Via electrospinning technique is possible to produce scaffolds composed of fibers from the nanoscale to microscale. A polymer solution is pumped at a constant rate through a needle with a small-diameter in a space exposed to a very high electric field. The field is created by two electrodes with opposite polarity. One electrode is placed in the polymer solution and the other is placed in the collector. The polymer solution generally consists in a polymer dissolved in a volatile organic solvent. When the polymer solution comes out of the needle a droplet forms on the tip of the needle and deforms into a conical shape as the applied voltage increases and causes electrostatic repulsion on the polymer droplet.
This process implies solvent evaporation and polymer deposition (in form of fibers) on collector's surface. The process is very versatile in terms of use of polymers, non-invasive and does not require the use of coagulation chemistry or high temperature for fiber generation. The morphology of electrospun structures is greatly affected by four main adjustable parameters: a) flow rate of the polymer solution through the syringe, b) voltage applied to the needle, c) concentration of the polymer solution and d) the distance between the needle and the collecting plate. It can produce fibers with specific orientation, high aspect ratio, high surface area, and ensure control over pore geometry (fig. 1.11).
The final product is a mat composed of a continuous nanofibers that can be used in many different applications, including drug delivery (Vakilian et al., 2015) and tissue engineering. Moreover, the nanofiber scaffolds typically result in pore sizes on the sub-micron to few

micron scale scaffold thickness and usually the electrospun scaffolds tend to be thin, typically less than one millimeter with a difficulty to precisely control where the fibers are deposited (Huang et al., 2003; Kasuga et al., 2012; Kim et al., 2006; Leach et al., 2011; Li et al., 2006, 2002a,b; Liao et al., 2012; Rowe et al., 2015; Song et al., 2015; Vaquette and Cooper-White, 2013; Wang et al., 2009).

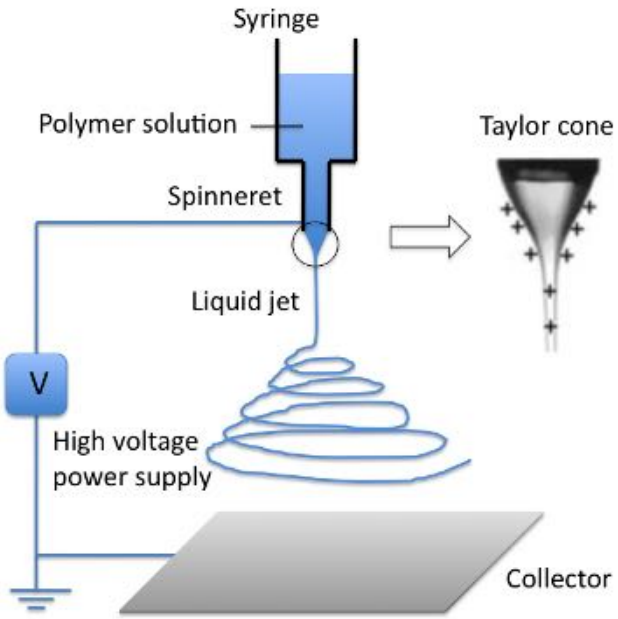

Fig. 1.11 *Setup and principle of elettrospinning*

CAD based technique

Computer Aided Design (CAD)-based manufacturing technologies are being developed for the fabrication of tissues to overcome problems due to use of "cell unfriendly" chemicals, UV or gamma rays, lasers, and high temperatures of the traditional methods. The advantages of this fabrication are: the direct control of the structure from microscope to macroscale yielding biomimetic feature, the ability to easy tune design and material composition. Solid free-form fabrication (SFF) (Lee et al., 2010) or rapid prototyping (RP) are typical examples of CAD technique. The computer transforms the model to slices or layers and the 3D objects are constructed layer by layer. This process can take place by using RP techniques such as fused deposition modeling (FDM), selective laser sintering (SLS), 3D printing (3D-P) (Chumnanklang et al., 2007) or stereolithography. Furthermore, CAD technique can easily integrated with the imaging technique to recreate the anatomical defect for particular applications or for an individual patient. One of the main disadvantage the process, due to

curing and shrinkage after post-processing is the fact that it presents a low resolution and, especially for complicated objects, deformation phenomena can occur (Giannitelli et al., 2014). To adopt these technique, the polymer must be photopolymerisable and only a few of biocompatible polymer can be adopted, such as: Polyethylene glycol (PEG) acrylate, PEG methacrylate, polyvinyl alcohol (PVA), hyaluronic acid and dextran methacrylate (Sachlos and Czernuszka, 2003; Serra et al., 2014; Wu et al., 2014; Yang et al., 2014; Zhang et al., 2014a). In figure 1.12 a typical pathway to fabricate a scaffold via CAD techniques is reported.

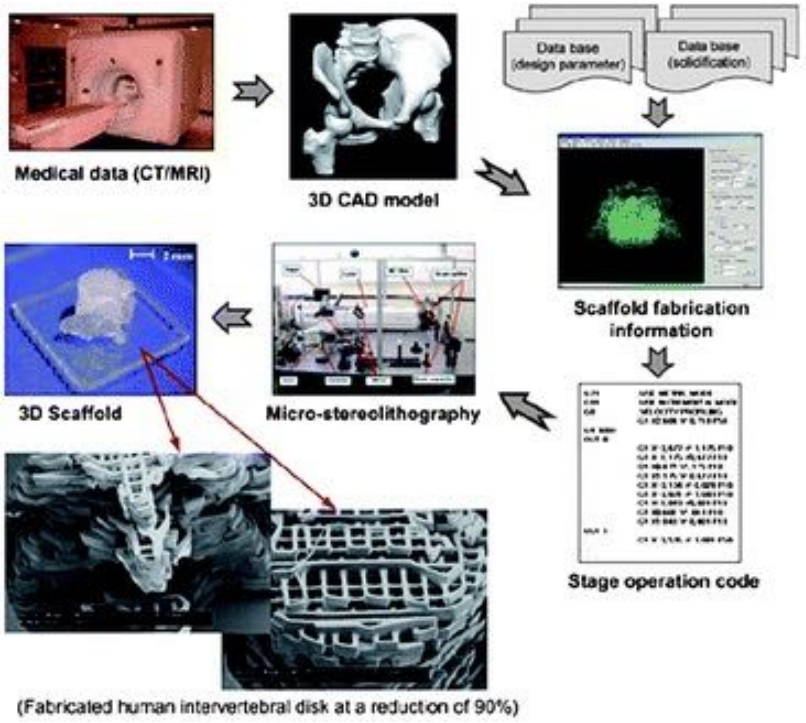

Fig. 1.12 *The image represents a scaffold fabricated via RP starting from a computational modelling. Starting from the CT scan of the defect, this latter is adopted to generate a computer-based 3D model. Thus the scaffold is generated via RP technique layer by layer, adapted from Seol et al. (2012)*

References

R. Akbarzadeh and A.-M. Yousefi. Effects of processing parameters in thermally induced phase separation technique on porous architecture of scaffolds for bone tissue engineering. *Journal of biomedical materials research. Part B, Applied biomaterials*, pages 1–12, 2014.

T. Andersen, P. Auk-Emblem, and M. Dornish. 3D Cell Culture in Alginate Hydrogels. *Microarrays*, 4(2):133–161, 2015.

K. P. Andriano, Y. Tabata, Y. Ikada, and J. Heller. In vitro and In vivo comparison of bulk and surface hydrolysis in absorbable polymer scaffolds for tissue engineering. *Journal of Biomedical Materials Research*, 48(5):602–612, 1999.

A. Aszódi and J. F. Bateman. Mammalian Skeletogenesis and Extracellular Matrix. What can We Learn from Knockout Mice? *Cell structure and . . .* , 84:73–84, 2000.

J. E. Babensee, J. M. Anderson, L. V. McIntire, and A. G. Mikos. Host response to tissue engineered devices. *Advanced Drug Delivery Reviews*, 33:111–139, 1998.

B. F. Barton and A. J. McHugh. Modeling the dynamics of membrane structure formation in quenched polymer solutions. *Journal of Membrane Science*, 166(1):119–125, 2000.

J. Barzin, C. Feng, K. C. Khulbe, T. Matsuura, S. S. Madaeni, and H. Mirzadeh. Characterization of polyethersulfone hemodialysis membrane by ultrafiltration and atomic force microscopy. *Journal of Membrane Science*, 237(1-2):77–85, 2004.

M. Bhattacharjee, J. Coburn, M. Centola, S. Murab, A. Barbero, D. L. Kaplan, I. Martin, and S. Ghosh. Tissue engineering strategies to study cartilage development, degeneration and regeneration. *Advanced Drug Delivery Reviews*, 84:107–122, 2015.

J. Bikhchandani, M. Metcalfe, S. Illouz, F. Puls, and A. Dennison. Extracorporeal liver perfusion system for artificial liver support across a membrane. *Journal of Surgical Research*, 171(1):e139–e147, 2011.

S. A. Burns, R. Hard, W. L. Hicks, F. V. Bright, D. Cohan, L. Sigurdson, and J. A. Gardella. Determining the protein drug release characteristics and cell adhesion to a PLLA or PLGA biodegradable polymer membrane. *Journal of Biomedical Materials Research - Part A*, 94 (1):27–37, 2010.

F. Carfì Pavia, V. La Carrubba, G. Ghersi, and V. Brucato. A composite PLLA scaffold for regeneration of complex tissues. *International Journal of Material Forming*, 3(SUPPL. 1): 571–574, 2010.

References

J. L. Chen, Z. Yin, W. L. Shen, X. Chen, B. C. Heng, X. H. Zou, and H. W. Ouyang. Efficacy of hESC-MSCs in knitted silk-collagen scaffold for tendon tissue engineering and their roles. *Biomaterials*, 31(36):9438–9451, 2010a.

J. S. Chen, S. L. Tu, and R. Y. Tsay. A morphological study of porous polylactide scaffolds prepared by thermally induced phase separation. *Journal of the Taiwan Institute of Chemical Engineers*, 41(2):229–238, 2010b.

F. Chicatun, N. Muja, V. Serpooshan, M. Quinn, and S. N. Nazhat. Effect of chitosan incorporation on the consolidation process of highly hydrated collagen hydrogel scaffold. *Soft matter*, 9:10811–10821, 2013.

R. Chumnanklang, T. Panyathanmaporn, K. Sitthiseripratip, and J. Suwanprateeb. 3D printing of hydroxyapatite: Effect of binder concentration in pre-coated particle on part strength. *Materials Science and Engineering: C*, 27(4):914–921, 2007.

H. J. Chung and T. G. Park. Surface engineered and drug releasing pre-fabricated scaffolds for tissue engineering. *Advanced Drug Delivery Reviews*, 59(4-5):249–262, 2007.

F. Croisier and C. Jérome. Chitosan-based biomaterials for tissue engineering. *European Polymer Journal*, 49(4):780–792, 2013.

J. M. Curran, S. Fawcett, L. Hamilton, N. P. Rhodes, C. V. Rahman, M. Alexander, K. Shakesheff, and J. a. Hunt. The osteogenic response of mesenchymal stem cells to an injectable PLGA bone regeneration system. *Biomaterials*, 34(37):9352–64, 2013.

R. D'Anchise, N. Manta, E. Prospero, C. Bevilacqua, and A. Gigante. Autologous implantation of chondrocytes on a solid collagen scaffold: Clinical and histological outcomes after two years of follow-up. *Journal of Orthopaedics and Traumatology*, 6(1):36–43, 2005.

N. Davidenko, T. Gibb, C. Schuster, S. M. Best, J. J. Campbell, C. J. Watson, and R. E. Cameron. Biomimetic collagen scaffolds with anisotropic pore architecture. *Acta biomaterialia*, 8(2):667–76, 2012.

R. Dell'Erba, G. Groeninckx, G. Maglio, M. Malinconico, and A. Migliozzi. Immiscible polymer blends of semicrystalline biocompatible components: Thermal properties and phase morphology analysis of PLLA/PCL blends. *Polymer*, 42(18):7831–7840, 2001.

B. Dhandayuthapani, Y. Yoshida, T. Maekawa, and D. S. Kumar. Polymeric scaffolds in tissue engineering application: A review. *International Journal of Polymer Science*, 2011 (ii), 2011.

Y. Du, X. Chen, Y. Hag Koh, and B. Lei. Facilely fabricating PCL nanofibrous scaffolds with hierarchical pore structure for tissue engineering. *Materials Letters*, 122:62–65, 2014.

M. Dziadek, J. Pawlik, E. Menaszek, E. Stodolak-Zych, and K. Cholewa-Kowalska. Effect of the preparation methods on architecture, crystallinity, hydrolytic degradation, bioactivity, and biocompatibility of PCL/bioglass composite scaffolds. *Journal of biomedical materials research. Part B, Applied biomaterials*, 103(8):1580–93, 2015.

J. Gao, P. Crapo, and Y. Wang. Macroporous Elastomeric Scaffolds with Extensive Micropores for Soft Tissue Engineering. *Tissue Engineering*, 12(4):917–925, 2006.

P. Gentile, V. Chiono, I. Carmagnola, and P. V. Hatton. An overview of poly(lactic-co-glycolic) Acid (PLGA)-based biomaterials for bone tissue engineering. *International Journal of Molecular Sciences*, 15(3):3640–3659, 2014.

S. M. Giannitelli, D. Accoto, M. Trombetta, and A. Rainer. Current trends in the design of scaffolds for computer-aided tissue engineering. *Acta Biomaterialia*, 10(2):580–594, 2014.

Y. Gong, Z. Ma, C. Gao, W. Wang, and J. Shen. Specially elaborated thermally induced phase separation to fabricate poly(L-lactic acid) scaffolds with ultra large pores and good interconnectivity. *Journal of Applied Polymer Science*, 101(5):3336–3342, 2006.

J. Goswami, N. Bhatnagar, S. Mohanty, and A. K. Ghosh. Processing and characterization of poly(lactic acid) based bioactive composites for biomedical scaffold application. *Express Polymer Letters*, 7(9):767–777, 2013.

T. W. a. Gould, J. P. Birchall, A. S. Mallick, T. Alliston, L. R. Lustig, K. M. Shakesheff, and C. V. Rahman. Development of a porous poly(DL-lactic acid-co-glycolic acid)-based scaffold for mastoid air-cell regeneration. *Laryngoscope*, 123(12):3156–3161, 2013.

P. a. Gunatillake and R. Adhikari. Biodegradable synthetic polymers for tissue engineering. *European cells & materials*, 5:1–16; discussion 16, 2003.

B. Guo and P. X. Ma. Synthetic biodegradable functional polymers for tissue engineering: A brief review. *Science China Chemistry*, 57(4):490–500, 2014.

H. Haleem-Smith, R. Calderon, Y. Song, R. S. Tuan, and F. H. Chen. Cartilage oligomeric matrix protein enhances matrix assembly during chondrogenesis of human mesenchymal stem cells. *Journal of Cellular Biochemistry*, 113(4):1245–1252, 2012.

References

C.-m. Han, L.-p. Zhang, J.-z. Sun, H.-f. Shi, J. Zhou, and C.-y. Gao. Application of collagen-chitosan/fibrin glue asymmetric scaffolds in skin tissue engineering. *Journal of Zhejiang University. Science. B*, 11(7):524–30, 2010.

W.-C. Hsieh, C.-P. Chang, and S.-M. Lin. Morphology and characterization of 3D micro-porous structured chitosan scaffolds for tissue engineering. *Colloids and surfaces. B, Biointerfaces*, 57(2):250–5, 2007.

S.-H. Hsu, S. Huang, Y.-C. Wang, and Y.-C. Kuo. Novel nanostructured biodegradable polymer matrices fabricated by phase separation techniques for tissue regeneration. *Acta biomaterialia*, 9(6):6915–27, 2013.

J. Hu, K. Feng, X. Liu, and P. X. Ma. Chondrogenic and osteogenic differentiations of human bone marrow-derived mesenchymal stem cells on a nanofibrous scaffold with designed pore network. *Biomaterials*, 30(28):5061–7, 2009.

X. Hu, H. Shen, F. Yang, J. Bei, and S. Wang. Preparation and cell affinity of microtubular orientation-structured PLGA(70/30) blood vessel scaffold. *Biomaterials*, 29(21):3128–3136, 2008.

R. Huang, X. Zhu, T. Zhao, and A. Wan. Preparation of tissue engineering porous scaffold with poly(lactic acid) and polyethylene glycol solution blend by solvent-casting/particulate-leaching. *Materials Research Express*, 1(4):045403, 2014.

Z. Huang, P. Nooeaid, B. Kohl, J. A. Roether, D. W. Schubert, C. Meier, A. R. Boccaccini, O. Godkin, W. Ertel, S. Arens, and G. Schulze-Tanzil. Chondrogenesis of human bone marrow mesenchymal stromal cells in highly porous alginate-foams supplemented with chondroitin sulfate. *Materials Science and Engineering C*, 50:160–172, 2015.

Z. M. Huang, Y. Z. Zhang, M. Kotaki, and S. Ramakrishna. A review on polymer nanofibers by electrospinning and their applications in nanocomposites. *Composites Science and Technology*, 63:2223–2253, 2003.

R. B. Jakobsen, A. Shahdadfar, F. P. Reinholt, and J. E. Brinchmann. Chondrogenesis in a hyaluronic acid scaffold: Comparison between chondrocytes and MSC from bone marrow and adipose tissue. *Knee Surgery, Sports Traumatology, Arthroscopy*, 18(10):1407–1416, 2010.

K. A. Jansen, D. M. Donato, H. E. Balcioglu, T. Schmidt, E. H. J. Danen, and G. H. Koenderink. A guide to mechanobiology: Where biology and physics meet, 2015.

N. Juncosa-melvin, J. T. Shearn, G. P. Boivin, C. Gooch, M. T. Galloway, J. R. West, S. Victor, G. Bradica, and D. L. Butler. Effects of Mechanical Stimulation on the Biomechanics and Histology of Stem Cell–Collagen Sponge Constructs for Rabbit Patellar Tendon Repair. *Tissue Engineering*, 12(8), 2006.

T. Kasuga, A. Obata, H. Maeda, Y. Ota, X. Yao, and K. Oribe. Siloxane-poly(lactic acid)-vaterite composites with 3D cotton-like structure. *Journal of Materials Science: Materials in Medicine*, 23(10):2349–2357, 2012.

H. Keshaw, N. Thapar, A. J. Burns, N. Mordan, J. C. Knowles, A. Forbes, and R. M. Day. Microporous collagen spheres produced via thermally induced phase separation for tissue regeneration. *Acta biomaterialia*, 6(3):1158–66, 2010.

H.-w. Kim, H.-h. Lee, and J. C. Knowles. Electrospinning biomedical nanocomposite fibers of hydroxyapatite/poly (lactic acid) for bone regeneration. *Journal of Biomedical Materials Research Part A*, pages 643—-649, 2006.

T. G. Kim, H. J. Chung, and T. G. Park. Macroporous and nanofibrous hyaluronic acid/collagen hybrid scaffold fabricated by concurrent electrospinning and deposition/leaching of salt particles. *Acta Biomaterialia*, 4(6):1611–1619, 2008.

D. M. Knapp. Rheology of reconstituted type I collagen gel in confined compression. *Journal of Rheology*, 41(5):971, 1997.

C. R. Kothapalli, M. T. Shaw, and M. Wei. Biodegradable HA-PLA 3-D porous scaffolds: effect of nano-sized filler content on scaffold properties. *Acta biomaterialia*, 1(6):653–62, 2005.

T. Kouya, S.-i. Tada, H. Minbu, Y. Nakajima, M. Horimizu, T. Kawase, D. R. Lloyd, and T. Tanaka. Microporous membranes of PLLA/PCL blends for periosteal tissue scaffold. *Materials Letters*, 95:103–106, 2013.

M. K. Leach, Z.-Q. Feng, S. J. Tuck, and J. M. Corey. Electrospinning fundamentals: optimizing solution and apparatus parameters. *Journal of visualized experiments : JoVE*, (47):1–5, 2011.

C. S. D. Lee, J. P. Gleghorn, N. Won Choi, M. Cabodi, A. D. Stroock, and L. J. Bonassar. Integration of layered chondrocyte-seeded alginate hydrogel scaffolds. *Biomaterials*, 28 (19):2987–2993, 2007.

References

J. W. Lee, J. Y. Kim, and D.-W. Cho. Solid Free-form Fabrication Technology and Its Application to Bone Tissue Engineering. *International journal of stem cells*, 3(2):85–95, 2010.

P. H. Lee, S. H. Tsai, L. Kuo, C. Y. Hwang, C. Y. Kuo, V. C. Yang, and J. K. Chen. A prototype tissue engineered blood vessel using amniotic membrane as scaffold. *Acta Biomaterialia*, 8(9):3342–3348, 2012.

C. Li, C. Vepari, H.-J. Jin, H. J. Kim, and D. L. Kaplan. Electrospun silk-BMP-2 scaffolds for bone tissue engineering. *Biomaterials*, 27(16):3115–24, 2006.

W. J. Li, C. T. Laurencin, E. J. Caterson, R. S. Tuan, and F. K. Ko. Electrospun nanofibrous structure: A novel scaffold for tissue engineering. *Journal of Biomedical Materials Research*, 60(4):613–621, 2002a.

W. J. Li, C. T. Laurencin, E. J. Caterson, R. S. Tuan, and F. K. Ko. Electrospun nanofibrous structure: A novel scaffold for tissue engineering. *Journal of Biomedical Materials Research*, 60(4):613–621, 2002b.

G. Liao, S. Jiang, X. Xu, and Y. Ke. Electrospun aligned PLLA/PCL/HA composite fibrous membranes and their in vitro degradation behaviors. *Materials Letters*, 82:159–162, 2012.

H. Liu and T. J. Webster. Bioinspired Nanocomposites for Orthopedic Applications Huinan. *Nanotechnology for the regeneration of hard and soft tissues*, (Capitolo 1):1–52, 2007.

S. Lopa and H. Madry. Bioinspired scaffolds for osteochondral regeneration. *Tissue engineering. Part A*, 20(15-16):2052–76, 2014.

T. P. Lozito, P. G. Alexander, H. Lin, R. Gottardi, A. W.-M. Cheng, and R. S. Tuan. Three-dimensional osteochondral microtissue to model pathogenesis of osteoarthritis. *Stem cell research & therapy*, 4 Suppl 1(Suppl 1):S6, 2013.

H. Ma, J. Hu, and P. X. Ma. Polymer scaffolds for small-diameter vascular tissue engineering. *Advanced Functional Materials*, 20(17):2833–2841, 2010.

P. X. Ma and J. W. Choi. Biodegradable polymer scaffolds with well-defined interconnected spherical pore network. *Tissue engineering*, 7(1):23–33, 2001.

V. Maquet, A. R. Boccaccini, L. Pravata, I. Notingher, and R. Jérôme. Preparation, characterization, and in vitro degradation of bioresorbable and bioactive composites based on Bioglass(R)-filled polylactide foams. *Biomed Mater Res A*, 66A:335–346, 2003.

E. Messai, A. Bouguerra, G. Harmelin, G. Di, M. Bonizzoli, and M. Bonacchi. A numerical model of blood oxygenation during veno-venous ECMO : analysis of the interplay between blood oxygenation and its delivery parameters. *Journal of Clinical Monitoring and Computing*, 30(3):327–332, 2015.

N. L. Morozowich, A. L. Weikel, J. L. Nichol, C. Chen, L. S. Nair, C. T. Laurencin, and H. R. Allcock. Polyphosphazenes Containing Vitamin Substituents: Synthesis, Characterization, and Hydrolytic Sensitivity. *Macromolecules*, 44(6):1355–1364, 2011.

L. M. Mullen, S. M. Best, S. Ghose, J. Wardale, N. Rushton, and R. E. Cameron. Bioactive IGF-1 release from collagen–GAG scaffold to enhance cartilage repair in vitro. *Journal of Materials Science: Materials in Medicine*, 26(1):1–8, 2015.

M. Munkhjargal, K. Hatayama, Y. Matsuura, K. Toma, T. Arakawa, and K. Mitsubayashi. Glucose-driven chemo-mechanical autonomous drug-release system with multi-enzymatic amplification toward feedback control of blood glucose in diabetes. *Biosensors & bioelectronics*, 67:315–320, 2015.

A. Muñoz-Bonilla and M. Fernández-Garcia. Polymeric materials with antimicrobial activity. *Progress in Polymer Science*, 37(2):281–339, 2012.

S. Nehrer, H. A. Breinan, A. Ramappa, G. Young, S. Shortkroff, L. K. Louie, C. B. Sledge, I. V. Yannas, and M. Spector. Matrix collagen type and pore size influence behaviour of seeded canine chondrocytes. *Biomaterials*, 18(11):769–776, 1997.

J. G. Nemeno-Guanzon, S. Lee, J. R. Berg, Y. H. Jo, J. E. Yeo, B. M. Nam, Y. G. Koh, and J. I. Lee. Trends in tissue engineering for blood vessels. *Journal of Biomedicine and Biotechnology*, 2012, 2012.

P. Ni, Q. Ding, M. Fan, J. Liao, Z. Qian, J. Luo, X. Li, F. Luo, Z. Yang, and Y. Wei. Injectable thermosensitive PEG-PCL-PEG hydrogel/acellular bone matrix composite for bone regeneration in cranial defects. *Biomaterials*, 35(1):236–48, 2014.

J. L. Nichol, N. L. Morozowich, T. E. Decker, and H. R. Allcock. Crosslinkable citronellol containing polyphosphazenes and their biomedical potential. *Journal of Polymer Science, Part A: Polymer Chemistry*, 52(16):2258–2265, 2014.

J. W. Nichol, S. T. Koshy, H. Bae, C. M. Hwang, S. Yamanlar, and A. Khademhosseini. Cell-laden microengineered gelatin methacrylate hydrogels. *Biomaterials*, 31(21):5536–5544, 2010.

References

N. Nottrodt, D. Leonhäuser, Y. Bongard, E. Bremus-Köbberling, and A. Gillner. Local ultraviolet laser irradiation for gradients on biocompatible polymer surfaces. *Journal of biomedical materials research. Part A*, 102(4):999–1007, 2014.

F. J. O'Brien. Biomaterials & scaffolds for tissue engineering. *Materials Today*, 14(3):88–95, 2011.

S. H. Oh, I. K. Park, J. M. Kim, and J. H. Lee. In vitro and in vivo characteristics of PCL scaffolds with pore size gradient fabricated by a centrifugation method. *Biomaterials*, 28 (9):1664–71, 2007.

M. Parent, C. Nouvel, M. Koerber, A. Sapin, P. Maincent, and A. Boudier. PLGA in situ implants formed by phase inversion: Critical physicochemical parameters to modulate drug release. *Journal of Controlled Release*, 172(1):292–304, 2013.

G. E. Park, M. A. Pattison, K. Park, and T. J. Webster. Accelerated chondrocyte functions on NaOH-treated PLGA scaffolds. *Biomaterials*, 26(16):3075–3082, 2005.

M. Pařzek, K. Novotná, and L. Bačáková. The role of smooth muscle cells in vessel wall pathophysiology and reconstruction using bioactive synthetic polymers. *Physiological Research*, 60(3):419–437, 2011.

M. S. Peach, S. G. Kumbar, R. James, U. S. Toti, D. Balasubramaniam, M. Deng, B. Ulery, A. D. Mazzocca, M. B. McCarthy, N. L. Morozowich, H. R. Allcock, and C. T. Laurencin. Design and optimization of polyphosphazene functionalized fiber matrices for soft tissue regeneration. *Journal of Biomedical Nanotechnology*, 8(1):107–124, 2012.

R. A. Pérez, J. E. Won, J. C. Knowles, and H. W. Kim. Naturally and synthetic smart composite biomaterials for tissue regeneration. *Advanced Drug Delivery Reviews*, 65(4): 471–496, 2013.

K. Pietrucha. Changes in denaturation and rheological properties of collagen-hyaluronic acid scaffolds as a result of temperature dependencies. *International Journal of Biological Macromolecules*, 36(5):299–304, 2005.

S. Ravi and E. Chaikof. Biomaterials for vascular tissue engineering. *Regenerative Medicine*, 5(1):1–21, 2010.

S. Rothemund, T. B. Aigner, A. Iturmendi, M. Rigau, B. Husár, F. Hildner, E. Oberbauer, M. Prambauer, G. Olawale, R. Forstner, R. Liska, K. R. Schröder, O. Brüggemann, and

I. Teasdale. Degradable glycine-based photo-polymerizable polyphosphazenes for use as scaffolds for tissue regeneration. *Macromolecular Bioscience*, 15(3):351–363, 2015.

M. J. Rowe, K. Kamocki, D. Pankajakshan, D. Li, A. Bruzzaniti, V. Thomas, S. B. Blanchard, and M. C. Bottino. Dimensionally stable and bioactive membrane for guided bone regeneration: An in vitro study. *Journal of Biomedical Materials Research - Part B Applied Biomaterials*, pages 594–605, 2015.

E. Sachlos and J. T. Czernuszka. Making tissue engineering scaffolds work. Review: the application of solid freeform fabrication technology to the production of tissue engineering scaffolds. *European cells & materials*, 5:29–40, 2003.

A. Salerno, S. Iannace, and P. A. Netti. Open-pore biodegradable foams prepared via gas foaming and microparticulate templating. *Macromolecular bioscience*, 8(7):655–64, 2008.

A. Salerno, S. Zeppetelli, E. Di Maio, S. Iannace, and P. A. Netti. Processing/structure/property relationship of multi-scaled PCL and PCL-HA composite scaffolds prepared via gas foaming and NaCl reverse templating. *Biotechnology and Bioengineering*, 108(4):963–976, 2011a.

A. Salerno, S. Zeppetelli, E. Di Maio, S. Iannace, and P. A. Netti. Design of bimodal PCL and PCL-HA nanocomposite scaffolds by two step depressurization during solid-state supercritical CO 2 foaming. *Macromolecular Rapid Communications*, 32(15):1150–1156, 2011b.

N. Sawatjui, T. Damrongrungruang, W. Leeanansaksiri, P. Jearanaikoon, and T. Limpaiboon. Fabrication and characterization of silk fibroin–gelatin/chondroitin sulfate/hyaluronic acid scaffold for biomedical applications. *Materials Letters*, 126:207–210, 2014.

B. Seal. Polymeric biomaterials for tissue and organ regeneration. *Materials Science and Engineering: R: Reports*, 34:147–230, 2001.

Y.-J. Seol, T.-Y. Kang, and D.-W. Cho. Solid freeform fabrication technology applied to tissue engineering with various biomaterials. *Soft Matter*, 8(6):1730–1735, 2012.

T. Serra, M. Ortiz-Hernandez, E. Engel, J. a. Planell, and M. Navarro. Relevance of PEG in PLA-based blends for tissue engineering 3D-printed scaffolds. *Materials science & engineering. C, Materials for biological applications*, 38:55–62, 2014.

S. Singh and J. Singh. Phase-sensitive polymer-based controlled delivery systems of leuprolide acetate: In vitro release, biocompatibility, and in vivo absorption in rabbits. *International Journal of Pharmaceutics*, 328(1 SPEC. ISS.):42–48, 2007.

References

X. Song, L. Wei, A. Chen, and Y. Shao. Poly(L-lactide) nanofibers containing trypsin for gelatin digestion. *Fibers and Polymers*, 16(4):867–874, 2015.

A. J. Sophia Fox, A. Bedi, and S. A. Rodeo. The Basic Science of Articular Cartilage: Structure, Composition, and Function. *Sports Health: A Multidisciplinary Approach*, 1(6): 461–468, 2009.

C. Spadaccio, A. Rainer, M. Trombetta, G. Vadalà, M. Chello, E. Covino, V. Denaro, Y. Toyoda, and J. A. Genovese. Poly-l-lactic acid/hydroxyapatite electrospun nanocomposites induce chondrogenic differentiation of human MSC. *Annals of Biomedical Engineering*, 37(7):1376–1389, 2009.

D. F. Stamatialis, B. J. Papenburg, M. Girones, S. Saiful, S. N. M. Bettahalli, S. Schmitmeier, and M. Wessling. Medical applications of membranes: Drug delivery, artificial organs and tissue engineering. *Journal of Membrane Science*, 308(1-2):1–34, 2008.

K. Stölzel, G. Schulze-Tanzil, H. Olze, S. Schwarz, E. M. Feldmann, and N. Rotter. Immortalised human mesenchymal stem cells undergo chondrogenic differentiation in alginate and PGA/PLLA scaffolds. *Cell and Tissue Banking*, pages 159–170, 2014.

M. C. Sunny, P. V. Vincy, P. R. Anil Kumar, and P. Ramesh. Porous composites of hydroxyapatite-filled poly[ethylene-co-(vinyl acetate)] for tissue engineering. *Polymer International*, 60(1):51–58, 2011.

I. Teasdale and O. Brüggemann. Polyphosphazenes: Multifunctional, biodegradable vehicles for drug and gene delivery. *Polymers*, 5(1):161–187, 2013.

X.-F. Tian, B.-C. Heng, Z. Ge, K. Lu, A. J. Rufaihah, V. T.-W. Fan, J.-F. Yeo, and T. Cao. Comparison of osteogenesis of human embryonic stem cells within 2D and 3D culture systems. *Scandinavian journal of clinical and laboratory investigation*, 68(1):58–67, 2008.

S. Vakilian, S. Mashayekhan, I. Shabani, M. Khorashadizadeh, A. Fallah, and M. Soleimani. Structural stability and sustained release of protein from a multilayer nanofiber/nanoparticle composite. *International Journal of Biological Macromolecules*, 75:248–257, 2015.

C. Vaquette and J. Cooper-White. A simple method for fabricating 3-D multilayered composite scaffolds. *Acta biomaterialia*, 9(1):4599–608, 2013.

M. Vert, S. M. Li, G. Spenlehauer, and P. Guerin. Bioresorbability and biocompatibility of aliphatic polyesters. *Journal of Materials Science: Materials in Medicine*, 3:432–446, 1992.

H. B. Wang, M. E. Mullins, J. M. Cregg, A. Hurtado, M. Oudega, M. T. Trombley, and R. J. Gilbert. Creation of highly aligned electrospun poly-L-lactic acid fibers for nerve regeneration applications. *Journal of neural engineering*, 6:016001, 2009.

C. Wen, L. Lu, and X. Li. Mechanically Robust Gelatin-Alginate IPN Hydrogels by a Combination of Enzymatic and Ionic Crosslinking Approaches. *Macromolecular Materials and Engineering*, 299(4):504–513, 2014.

M. T. Wolf, K. a. Daly, E. P. Brennan-Pierce, S. a. Johnson, C. a. Carruthers, A. D'Amore, S. P. Nagarkar, S. S. Velankar, and S. F. Badylak. A hydrogel derived from decellularized dermal extracellular matrix. *Biomaterials*, 33(29):7028–38, 2012.

G. Wu, W. Wu, Q. Zheng, J. Li, J. Zhou, and Z. Hu. Experimental study of PLLA/INH slow release implant fabricated by three dimensional printing technique and drug release characteristics in vitro. *Biomedical engineering online*, 13(1):97, 2014.

H. Wu, Y. Wan, X. Cao, S. Dalai, S. Wang, and S. Zhang. Fabrication of chitosan-g-polycaprolactone copolymer scaffolds with gradient porous microstructures. *Materials Letters*, 62(17-18):2733–2736, 2008.

Z. C. Xu, W. J. Zhang, H. Li, L. Cui, L. Cen, G. D. Zhou, W. Liu, and Y. Cao. Engineering of an elastic large muscular vessel wall with pulsatile stimulation in bioreactor. *Biomaterials*, 29(10):1464–1472, 2008.

S. Yang, J. Wang, L. Tang, H. Ao, H. Tan, T. Tang, and C. Liu. Mesoporous bioactive glass doped-poly (3-hydroxybutyrate-co-3-hydroxyhexanoate) composite scaffolds with 3-dimensionally hierarchical pore networks for bone regeneration. *Colloids and surfaces. B, Biointerfaces*, 116:72–80, 2014.

J. Yanpeng, L. Zonghua, and Z. Changren. Fabrication and characterization of PLLA–chitosan hybrid scaffolds with improved cell compatibility. *Journal of biomedical materials research. Part A*, 80(4):820–825, 2007.

A.-M. Yousefi, M. E. Hoque, R. G. S. V. Prasad, and N. Uth. Current strategies in multiphasic scaffold design for osteochondral tissue engineering: A review. *Journal of Biomedical Materials Research. Part A*, pages 1–22, 2014.

References

J. Zhang, S. Zhao, Y. Zhu, Y. Huang, M. Zhu, C. Tao, and C. Zhang. Three-dimensional printing of strontium-containing mesoporous bioactive glass scaffolds for bone regeneration. *Acta Biomaterialia*, 10(5):2269–2281, 2014a.

K. Zhang, Y. Ma, and L. F. Francis. Porous polymer/bioactive glass composites for soft-to-hard tissue interfaces. *Journal of Biomedical Materials Research*, 61(4):551–563, 2002.

L. Zhang, Q. Ao, A. Wang, G. Lu, L. Kong, Y. Gong, N. Zhao, and X. Zhang. A sandwich tubular scaffold derived from chitosan for blood vessel tissue engineering. *Journal of Biomedical Materials Research - Part A*, 77(2):277–284, 2006.

Q. Zhang, H. Lu, N. Kawazoe, and G. Chen. Pore size effect of collagen scaffolds on cartilage regeneration. *Acta Biomaterialia*, 10(5):2005–2013, 2014b.

R. Zhang and P. X. Ma. Poly(a-hydroxyl acids)/hydroxyapatite porous composites for bone-tissue engineering. I. Preparation and morphology. *Journal of Biomedical Materials Research*, 44(4):446–455, 1999.

M. Y. Zhao, L. H. Li, B. Li, and C. R. Zhou. LBL coating of type I collagen and hyaluronic acid on aminolyzed PLLA to enhance the cell-material interaction. *Express Polymer Letters*, 8(5):322–335, 2014.

C. Zhu, D. Fan, and Y. Wang. Human-like collagen/hyaluronic acid 3D scaffolds for vascular tissue engineering. *Materials Science and Engineering C*, 34(1):393–401, 2014.

Chapter 2

Scaffold fabrication

In this chapter materials and method adopted in this thesis work will be described. The scaffold technique adopted for the fabrication of the scaffold is based on the thermally induced phase separation (TIPS). The produced scaffolds are PLLA-based with diverse filler: bioglass and hydroxyapatite.

2.1 Thermally Induced Phase Separation (TIPS)

Thermally Induced Phase Separation (TIPS) is one of the most widely adopted techniques for scaffold production, useful to obtain a well-interconnected porous structure.
This technique is based on the change in temperature to induce the de-mixing of a homogeneous polymer solution, creating a multi-phase system. When the de-mixing of the solution occurs, the homogeneous solution separates into a polymer-rich and a polymer-less phase. The de-mixing can be solid-liquid, for binary polymer-solvent mixture, or liquid-liquid, for ternary polymer/solvent/non-solvent mixture. As a function of the separations conditions, it is possible to obtain different morphologies and various characteristics, such as: open or close pores, fibrous structure, membrane, etc. (He et al., 2009; Kim et al., 2009; Phaechamud and Chitrattha, 2016; Yang et al., 2004).
One of the biggest advantages of this technique is the possibility to obtain a well-interconnected polymer network with a simple, fast and adaptable process.
Many polymers have been used in this technique, among all: polylactic acid (Ruggiero et al., 2015), polyurethane (Jing et al., 2014), polycaprolactone (Salerno and Domingo, 2015), etc.

In fig. 2.1 the phase diagram of a typical ternary solution is reported. The thermodynamic equilibrium is represented by the binodal and the spinodal curve.

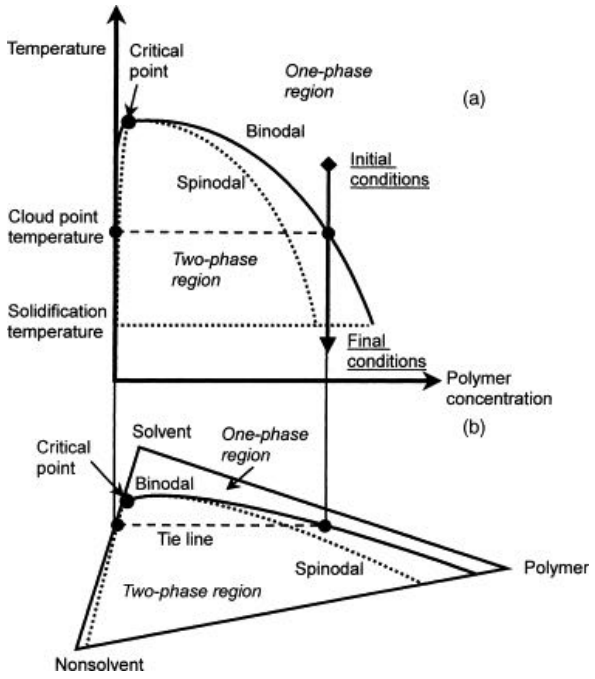

Fig. 2.1 *Ternary phase diagram. a) Phase diagram temperature vs polymer concentration, b) Isothermal phase diagram at the cloud point temperature, from Tanaka and Lloyd (2004)*

At high temperatures (above the binodal curve) the polymer solution is located in the one-phase region and the solution is homogeneous. Keeping constant the concentration and decreasing the temperature, the solution reaches the binodal curve and de-mixing in a polymer rich and a polymer less phase occurs. The region between binodal and spinodal curve is the metastable region, where a mechanism of nucleation and growth takes place. The spinodal curve takes places above the unstable region, the separation mechanism of the phase in this region is called spinodal decomposition.

The maximum of the temperature vs composition diagram, where binodal and spinodal curve are in contact, is called critical point. The nucleating phase depends upon the initial concentration, before or after the critical point. By changing the nucleating phase the final morphology will be completely different, the proportion between the two phases being determined by the lever rule. If the initial concentration is on the left of the critical point, the nucleation of the polymer-rich phase occurs, forming a dense phase. On the other hand, if the concentration is on the right of the critical point, the nucleation of the polymer-lean phase occurs. In this latter case, once removed the solvent, the polymer-rich phase will form a polymer network, suitable for tissue engineering purpose (fig. 2.2). Figure 2.2 reports a schematic representation of the obtainable morphologies as a function of the initial concentration of polymer. In black the polymer-rich phase, in white the polymer-lean phase.

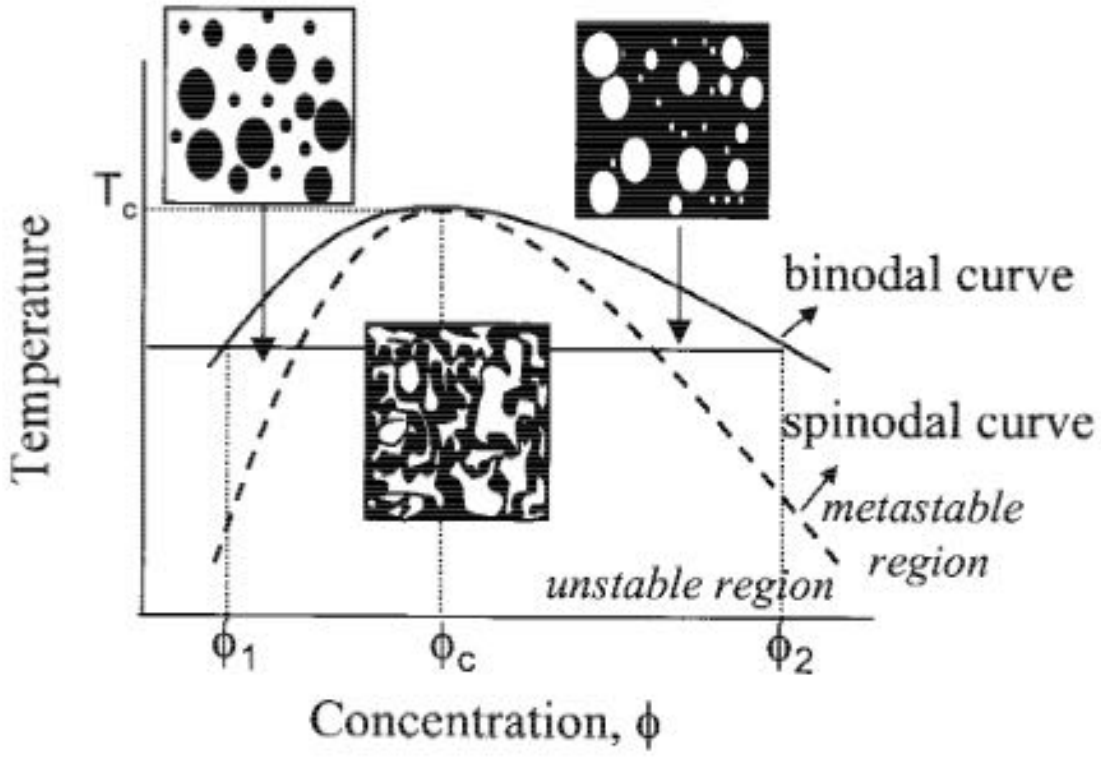

Fig. 2.2 *Schematic representation of the obtainable morphologies in a temperature-composition phase diagram of polymer solution, from Nam and Park (1999)*

The spinodal curve, as mentioned, divides the miscibility gap in two areas, the metastable and the unstable region. Along the spinodal curve the second derivative energy is null. Distribution, shape and size of the pores are the result of a delicate balance between different parameters, such as molecular weight of the polymers, concentration, cooling rate, etc... (Akbarzadeh and Yousefi, 2014) These criteria have a significant influence not only on the onset of the phase separation, in which the domains of the nucleating phase start to grow, but also in the next steps. Indeed, the coalescence of the separate phase, continues minimising the free energy due to the presence of the interfacial surfaces. This process, called coarsening, causes the increase of the pore dimension (Li et al., 2006b).

The principal operating parameters are:

1. Polymer type and concentration
2. Polymer molecular weight
3. Solvent/non-solvent ratio
4. Cooling path

Polymer type and concentration

As aforementioned different polymers were adopted in the TIPS technique to produce scaffolds with diverse properties, but there ids also the possibility to change the characteristics of the scaffolds simply by varying the polymer concentration.
Hua et al. (2002) report the different morphologies in a PLLA/Dioxane/water system, 87/13 solvent/non-solvent weight ratio, as a function of concentration and aging. In figure 2.3 the scaffold morphologies at different times (10, 30 minutes) and different concentration (4.5% and 6%) are shown.
It is evident that as the polymer concentration increases, keeping constant the cooling path, pore dimension and porosity decrease accordingly.

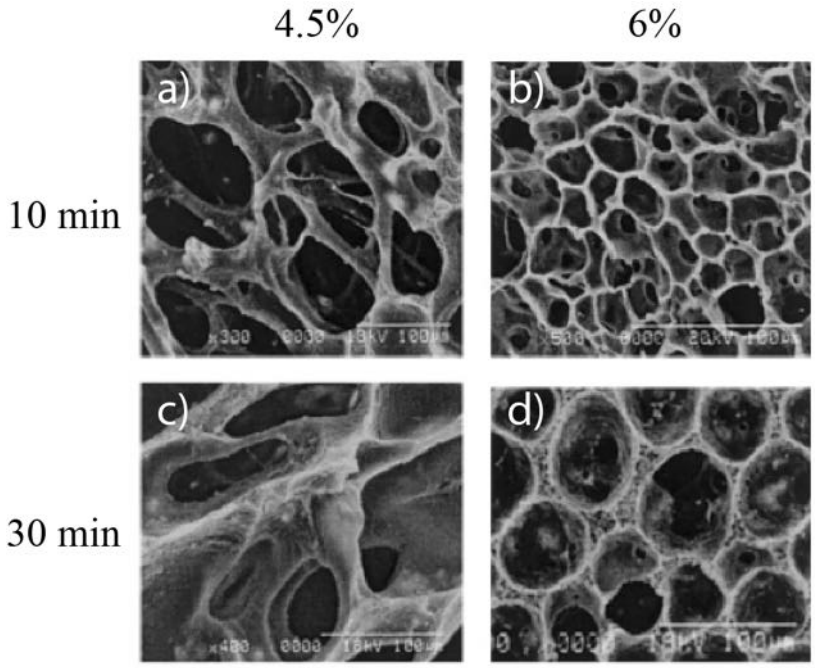

Fig. 2.3 *Effect of the polymer concentration on the morphology of the scaffold, a) 4.5% PLLA, 10 min, b) 6% PLLA, 10 min, c) 4.5% PLLA, 30 min, d) 6% PLLA, 30 min; adapted from Hua et al. (2002)*

Polymer molecular weight

The effect of the PLA molecular weight was investigated by Chen et al. (2010). In particular, the molecular weight for PDLLA and PLLA in fig. 2.4 are reported. Dioxane/water ratio was 87/13 and 7.5% polymer concentration; two different molecular weight for PDLLA and PLLA were used: $Mn = 12000$ and $Mn = 71000$ for PDLLA and $Mn = 42000$ and

$Mn = 170000$ for PLLA.
The foams at higher molecular weight result more homogeneous compared to the other ones. The polymer solution with PDLLA at $Mv = 12000$ was even unable to form a complete scaffold structure, but a powder structure was observed. This fact can be due to the first steps of the phase separation, during the coarsening of the separated phases. In this step, indeed, the viscosity plays a crucial role, an increase of the molecular weight implies an increase of the viscosity of the solution that helps the complete formation of the two phases.

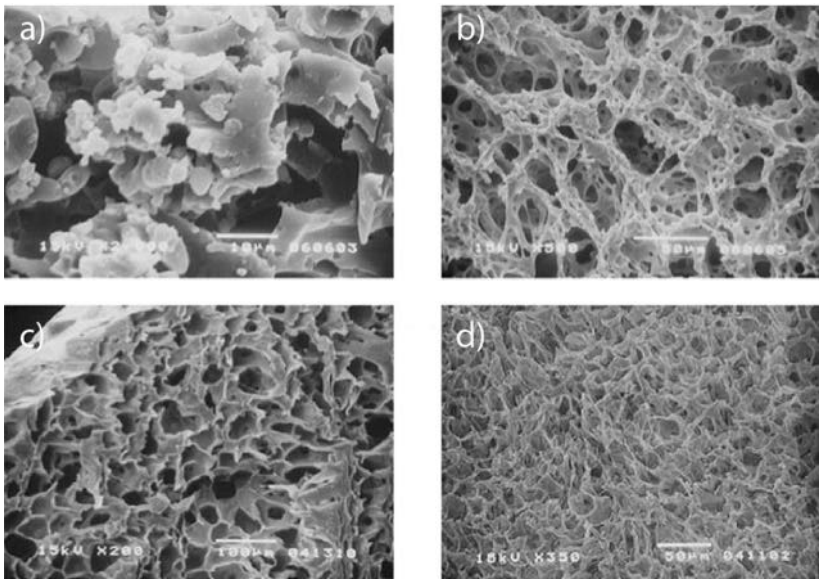

Fig. 2.4 *Effect of the molecular weight on the morphology of the scaffold: a) PDLLA: Mn* = 12000 *[2000X], b) Mn* = 71000 *[500X]; c) PLLA: Mn* = 42000 *[200X], d)* 170000 *[350X], from Chen et al. (2010)*

Solvent/non-solvent ratio

The solvent to non-solvent ratio is probably one of the most important parameters in the TIPS technique as non-solvent allows the liquid-liquid phase separation. In figure 2.5 the SEM micrographs of foam with different solvent/non-solvent ratio are reported.
The polymer adopted was PLLA with a concentration of 7.5% and the solution was directly quenched in liquid nitrogen (-196°C). The first image (fig. 2.5a) presents a typical ladder-like structure. This morphology is due to the presence of the solvent. In this case it is not a liquid-liquid phase separation but a solid-liquid phase separation. There is not a cloud point but only a freezing-point curve could be define. The ultimate scaffold structure was dominated by the progress of the crystallization of the dioxane solvent.

The structure completely change when adding the non-solvent. The liquid-liquid phase separation allows the tuning of the pore dimension according e.g. to the thermal history. The other two scaffolds (90/10 and 85/15) exhibited an isotropic lacy structure with interconnected pores. The 85/15 foam shows larger, around 50 μm and less interconnected pores compared to 90/10. The cloud point of the solution with higher concentration of dioxane is lower than the other one. This means that the 85/15 spends more time inside the metastable region compared to the 90/10 which determines at larger coarsening effect.

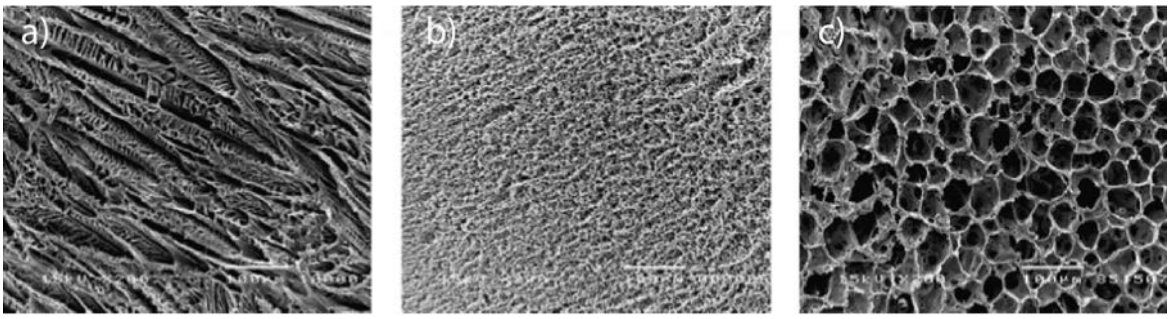

Fig. 2.5 *Effect of the solvent/non-solvent ratio on the morphology of the scaffold: a) 100% Dioxane, b) 90/10 Dioxane/Water, c) 85/15 Dioxane/Water; from Chen et al. (2010)*

Cooling path

One of the principal advantage of the TIPS technique is the possibility to tune the structure by changing the pathway. Starting from the same solution, the final morphology of the scaffold can change (in terms of pore dimension, distribution, interconnectivity, etc) by tuning the cooling path. The starting solution in the work of Carfì Pavia et al. (2008) is PLLA/Dioxane/Water; 4% PLLA, 87/13 Dioxane/Water. In figure 2.6a the morphology of the scaffold depending on the demixing time inside the metastable region is reported. At the temperature of 35°C, when increasing the demixing time the pores appear larger and with a major presence of micropores between the larger pores.
The graph in figure 2.6b reports the trend of the pore dimension as a function of the temperature and time. It is clear that at 25°C the pore size is basically independent of the demixing time. For the examined solution at 25°C the predominant process is spinodal decomposition, not related by the time. For the other two temperatures 30°C and 35°C, when increasing the demixing time from 15 to 45 minutes the pore dimensions are more then quintupled.

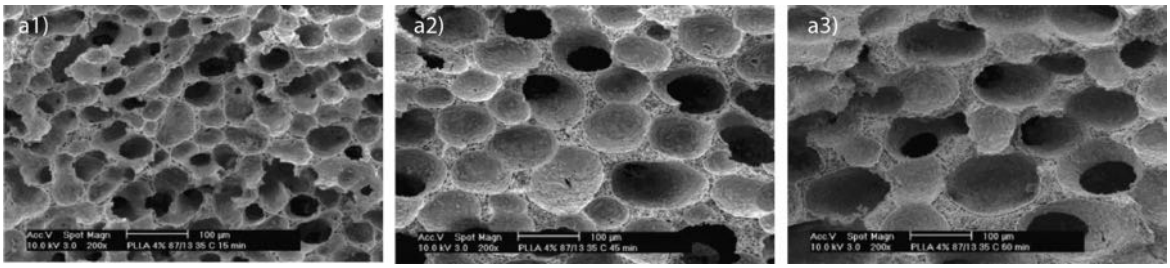

(a)

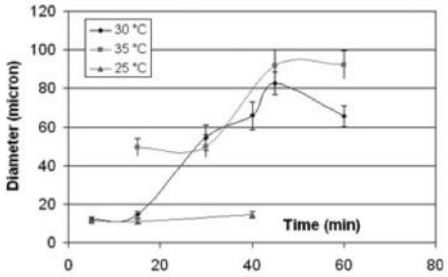

(b)

Fig. 2.6 *Effect of the cooling path on the morphology of the scaffold. a) SEM micrographs at 35°C and different demixing time: a1) 15 minutes, a2) 45 minutes, a3) 60 minutes; adapted from Carfì Pavia et al. (2008)*

2.1.1 Thermodynamic and kinetic aspect

Two components in a mixture, e.g. polymer/solvent, will be miscible if the Gibbs free energy of mixing is less then zero, $\Delta G_m < 0$, otherwise if $\Delta G_m > 0$ the system will be immiscible. A completely miscible system exists when the second derivative of the Gibbs free energy with respect to the composition is less then zero for every composition:

$$\frac{\partial^2 \Delta G_\xi}{\partial \xi^2} < 0 \tag{2.1.1}$$

where $\partial^2 \Delta G_\xi = \frac{\Delta G_m}{X}$, ΔG_ξ is the molar Gibbs free energy, X the total volume or number of moles and ξ the volumetric or molar fraction.
There is not difference between a total and a partial miscibility system in therms of Gibbs free energy of mixing, in both cases , $\Delta G_m < 0$, is lower than zero the difference is only in the second derivative.
In figure 2.7 the molar Gibbs free energy as a function of the composition is reported.

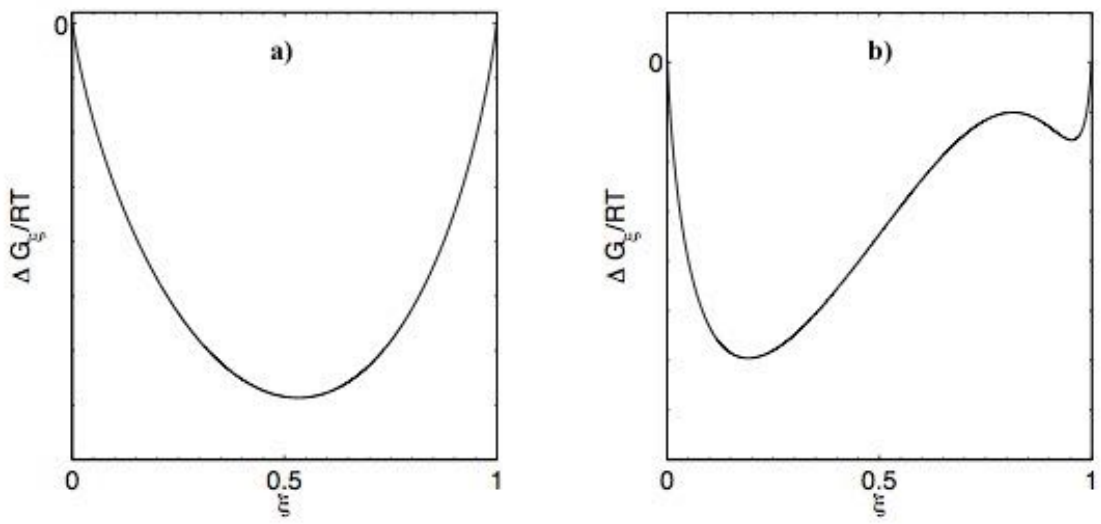

Fig. 2.7 *Gibbs free energy of mixing vs volumetric fraction for binary system. a) Complete miscible system, b) Partially miscible system*

Two phases in a system will be in thermodynamic equilibrium if:

$$\Delta\mu_i^{\alpha} = \Delta\mu_i^{\beta} \tag{2.1.2}$$

where $\Delta\mu$ is the chemical potential of the i species in α or β phase; defined as

$$\Delta\mu_i = \left.\frac{\partial \Delta G}{\partial n_i}\right|_{T,P,n_j} \tag{2.1.3}$$

n_i is the number of moles of the $i-$component and $j \neq i$.

If re-writing the definition of chemical potential 2.1.3 as a function of ΔG_ξ, the relation becomes:

$$\frac{\partial \Delta G}{\partial n_i}|_{T,P,n_j} = X_i\left[\Delta G_\xi + \frac{\partial \Delta G_\xi}{\partial \xi_i} - \sum_{i=1}^{c-1}\xi_i \Delta G_\xi + \frac{\partial \Delta G_\xi}{\partial \xi_i}\right] \tag{2.1.4}$$

$X_i = \frac{\partial X}{\partial n_i}$ and c is the number of species in the mixing. From 2.1.4 is possible to obtain the chemical potential for the two species

$$\Delta\mu_1 = X_1\left[\Delta G_\xi + (1-\xi_1)\frac{\partial \Delta G_\xi}{\partial \xi_1}\right] = X_1\left[\Delta G_\xi + \xi_2\frac{\partial \Delta G_\xi}{\partial \xi_2}\right] \tag{2.1.5}$$

$$\Delta\mu_2 = X_2\left[\Delta G_\xi + (1-\xi_2)\frac{\partial \Delta G_\xi}{\partial \xi_2}\right] = X_2\left[\Delta G_\xi + \xi_1\frac{\partial \Delta G_\xi}{\partial \xi_1}\right] \tag{2.1.6}$$

Combining the 2.1.5, 2.1.6 equations and indicating $\xi = \xi_1 = 1 - \xi_2$, the equilibrium condition can be written as

$$\left.\frac{\partial \Delta G}{\partial \xi}\right|_{\xi_\alpha} = \left.\frac{\partial \Delta G}{\partial \xi}\right|_{\xi_\beta} \tag{2.1.7}$$

then on the $\Delta G_\xi - \xi$ diagram a tangent represents the equilibrium among the two phases.

Taking into account figure 2.1 it is possible to identify the various regions from a thermodynamic point of view.
Above the binodal curve, so-called one phase region, the solution is completely homogeneous. The points where the equation 2.1.7 is satisfied are called binodal points and the curve connecting these point is called called binodal curve.
Below the binodal curve the second derivative of the Gibbs free energy with respect to the composition is positive

$$\frac{\partial^2 \Delta G_\xi}{\partial \xi^2} > 0 \tag{2.1.8}$$

in this metastable region, one phase is possible but it is not stable.
The inflection points, represented by

$$\frac{\partial^2 \Delta G_\xi}{\partial \xi^2} = 0 \tag{2.1.9}$$

are the spinodal points and the curve connecting them is the spinodal curve. Below the spinodal curve the system is unstable, in this case

$$\frac{\partial^2 \Delta G_\xi}{\partial \xi^2} < 0 \tag{2.1.10}$$

the system spontaneously demixes in two continuos phases.
The point of contact between the spinodal and binodal curve is called critical point and the thermodynamic condition is

$$\frac{\partial^2 \Delta G_\xi}{\partial \xi^2} = \frac{\partial^3 \Delta G_\xi}{\partial \xi^3} = 0 \tag{2.1.11}$$

above this point the solution is homogenous at all compositions.
Introducing a third component the phase diagram can considerably change compared to the binary case. The third component can increase or decrease the miscibility gap. In particular thermodynamic conditions it is possible that a mixture of two low molecular weight liquids can dissolve large amounts of a given polymer, whereas each of these liquids alone exhibits a miscibility gap with the polymer. This phenomenon is called co-solvency. (Hsu et al., 2013)
Depending in which region of the diagram the phase separation occurs, the mechanism is different. Inside the metastable region the demixing process takes place via nucleation and growth. Inside the spinodal curve, the phase separation process takes place spontaneously, because any fluctuation in concentration means a reduction in the Gibbs energy. In accord to the different demixing processes, the morphology of the two phase systems looks considerably different.
In figure 2.8 an example of the different mechanism occurred in the thermally induced phase separation. In both cases the ternary solution adopted is PLLA/Dioxane/water, 4% in polymer, 87/13 Dioxane/Water weight ratio is presented. In figure 2.8a the cooling path adopted for the two morphology is reported. The first steps are common. The solution was initially kept at 60°C to ensure the homogenisation, then the temperature was slowly decreased at 1°C/min until 35°C and maintained for 30 minutes. In the first case (blue line) the solution was immediately quenched at -20°C, in the second case (red line) the temperature was slowly decreased reaching -20°C at 1°C/min. Fig. 2.8b shows a closed-pore morphology typical of nucleation and growth mechanism, fig. 2.8c shows a micro-structure with very small pores and highly interconnected, basically related to spinodal decomposition.
In the case of nucleation and growth mechanism the droplets of the minor phase formed at the beginning of the process grow slowly. The droplets are dispersed in a matrix of the other phase and gradually increase their dimension.
For spinodal decomposition, the morphology is co-continuous. The driving force for this process is the minimisation of the interface in order to reduce the Gibbs free energy of the system.

The most common way to determinate the phase diagram of a ternary system is via experimental approach.

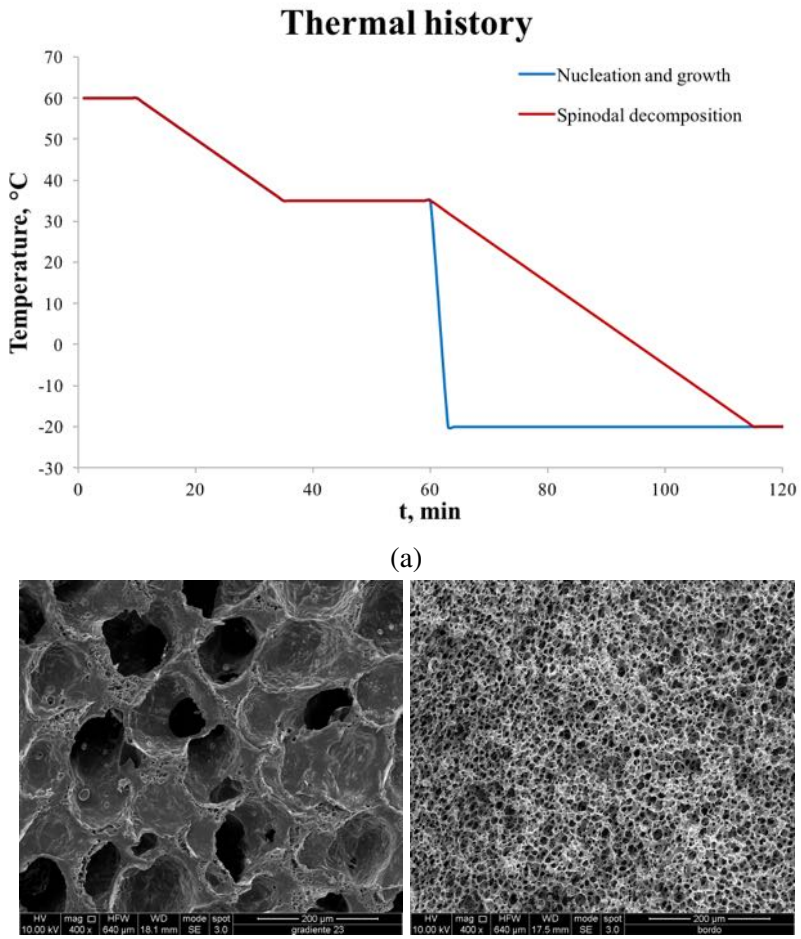

(a)

(b) (c)

Fig. 2.8 *Evidence of mechanism in ternary PLLA/Dioxane/Water solution, a)Thermal history, b) Nucleation and growth mechanism, c) Spinodal decomposition; adapted from Mannella et al. (2014)*

Starting from a homogeneous solution, this is brought to a specific temperature inside the miscibility gap. Thus the solution is maintained for 12-24h, to allow the phase separation and segregation. At the end the two formed phases are weighted and it is possible to determine the composition (Tanaka et al., 2006).

A useful way to determine the miscibility gap is based on the detection of the cloud point. This latter is determined by cooling or heating a given homogeneous solution until it becomes turbid. The temperature when this phenomena occurs is called cloud point temperature T_{cp} caused by the phase separation of a second phase. The reason for this milky appearance lies in the normally pronouncedly different refractive indices of the components. The dependence of T_{cp} on the composition of the mixture is called cloud point curve.

The lost of transparence can be identified via light attenuation or laser diffraction. The

sample is placed between the laser, on the top, and a photodiode, on the bottom, and kept at a controlled temperature. In the one phase region the solution will be transparent, when the temperature reaches the two-phase boundary for the specific composition, the amount of laser-light through the samples will decrease. The temperature at which occurs the variation of intensity is the cloud point.
Theoretically the cloud point corresponds to the binodal curve but this is not always true. The value of temperature, at certain compositions, changes as a function of the cooling modality and rate. Furthermore, at the beginning of the demixing the domains have very small dimension what makes them, basically impossible to determine.
Usually, the cloud point diagrams are diagrams temperature-polymer concentration. In figure 2.9 an example of the diagram is reported.

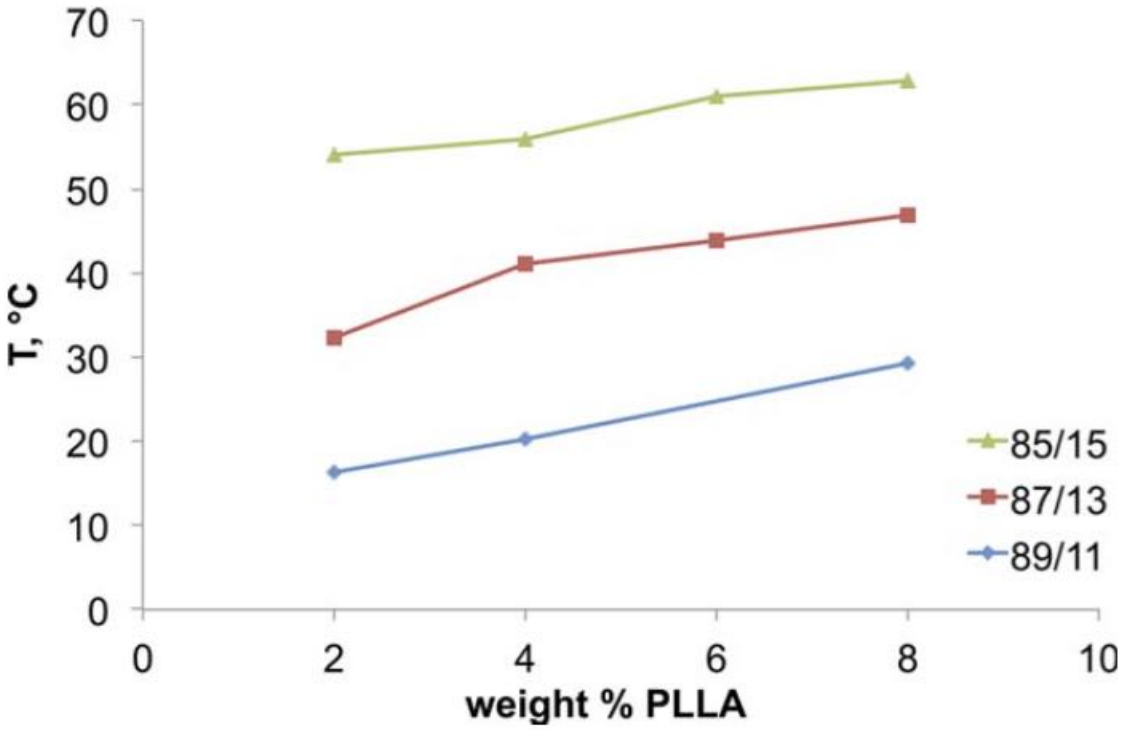

Fig. 2.9 *Cloud point curves at 4% of PLLA and different Dioxane/Water weight ratio, from Mannella et al. (2014)*

When comparing the cloud point diagram to a binary phase diagram there are three main differences:

1. There in not a maximum on the curve
2. It is not possible to determine the composition of the separate phases

3. It is not possible to individuate the spinodal curve

The kinetics of the process influences the different steps of the mechanism and then the final morphology of the foam.
In the traditional nucleation theory for the formation of spherical cluster the free energy change (ΔF) is given by

$$\Delta F = -\frac{4\pi}{3}R^3\Delta G + 4\pi R^2\sigma \tag{2.1.12}$$

where R is the radius of the cluster, σ is the interfacial energy between the polymer-rich cluster and the other phase and ΔG is the change in the Gibbs free energy related to the level of supersaturation.
In the eq. 2.1.12 the first therm is proportional to the cluster volumes, while the second term is proportional to the surface area.
Figure 2.10 represents the effect of the two contribution as a function of R.

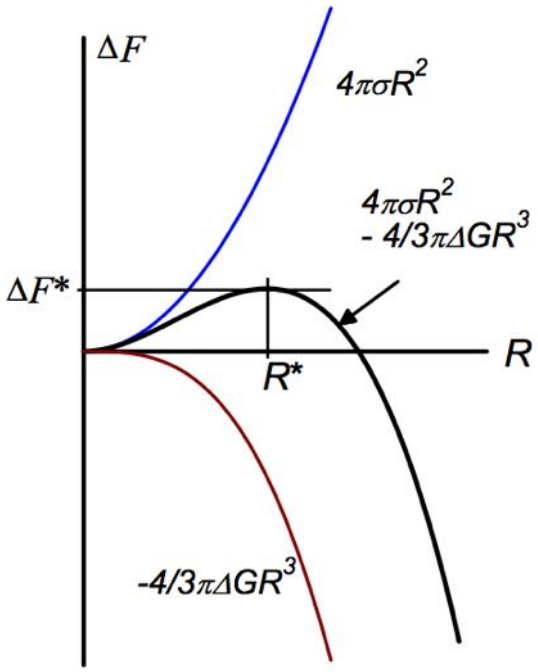

Fig. 2.10 *Energy barrier as a function of domain radius*

By deriving the 2.1.12 equation as a function of R it is possible to calculate the R^* value, maximum of the curve, and the corresponding ΔF^*.

$$R^* = -\frac{2\sigma}{\Delta G} \tag{2.1.13}$$

$$\Delta F^* = \frac{16\pi\sigma^3}{3\Delta G^2} \tag{2.1.14}$$

If $R > R^*$ the clusters grow spontaneously, otherwise, if $R < R^*$ the clusters redissolve in the continuous phase. Inside the spinodal region $R^* \to 0$, the clusters grow independently from the initial dimension.
Assuming a steady state condition and considering that the growth rate is slower than the cluster generation, the nucleation rate can be written as:

$$r = N_s Z j \, exp\left(-\frac{\Delta F^*}{k_b T}\right) = r_0 \, exp\left(-\frac{\Delta F^*}{k_b T}\right) \tag{2.1.15}$$

N_s represents the number of nucleation sites, j is connected to the mobility of the molecules, Z is the probability that a nucleus at ΔF^* will form the new phase. $k_b T$ is the thermal energy of the system with T the absolute temperature and k_b the Boltzmann constant. $N_s jZ$ can be summarised in an unique pre-exponential factor r_0.

2.2 Ternary system: PLLA-Dioxane-Water

The ternary system adopted in this thesis was PLLA-Dioxane-Water (polymer-solvent-nonsolvent). The dioxane to water ratio was 87/13 wt/wt in all cases, the polymer concentration was varied as a function of application. It is possible to find in literature different works adopting this ternary system for different applications: adipose tissue engineering (Frydrych et al., 2015), membranes (Kouya et al., 2013), bone tissue engineering (Eftekhari et al., 2014), vascular tissue engineering (Carfì Pavia et al., 2012), cartilage tissue engineering (Bian et al., 2013), etc.

2.2.1 PLLA

The polylactid acid (PLA) is s a biodegradable thermoplastic aliphatic polyester. It is one of the most promising environmental friendly material, showing high-strength and high-

modulus. It is mainly used in the biomedical fields in forms of fibers, films, microparticles or microspheres.
The lactid acid is the simplest 2-hydroxycarboxylic acid. This latter has a chiral carbon atom and exists in two stereoisomers, namely L and D enantiomers (S and R respectively). The racemic acid DL-lactic shows different optical characteristic from the singular enantiomers. In fig. 2.11 the stereoisomers are reported.

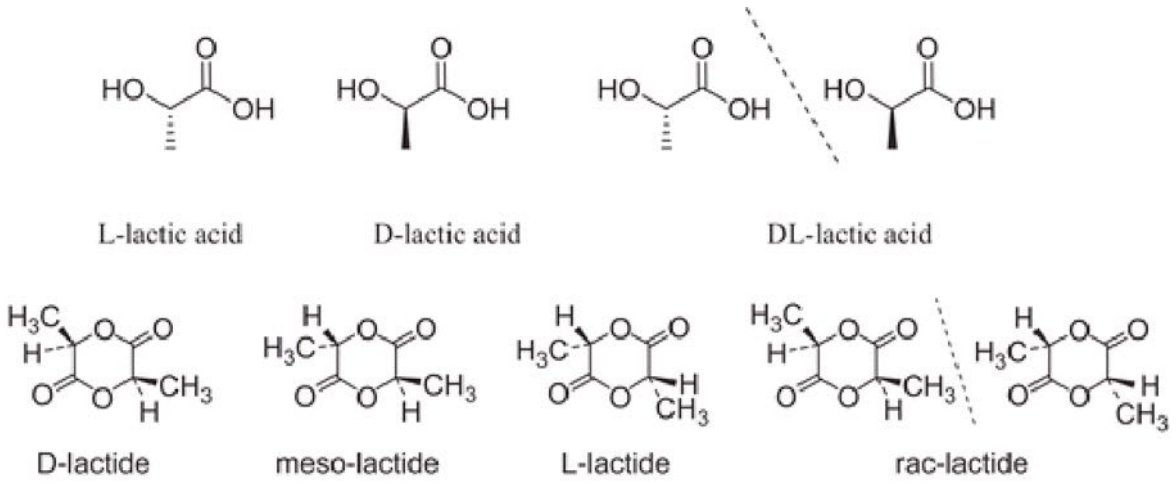

Fig. 2.11 *First row: chemical structures of L-, D- and DL-lactic acids. Second row: chemical structures of lactides*

As a function of the lactic unit, different lactide can be obtained. The typical way to produce the lacted is by depolymerization of the corresponding oligo(lactic acid) (OLLA) obtained by polycondensation of the lactic acid. This reaction is catalysed by metal compounds of Sn, Zn, Al, etc. The crude lactide is purified by melt crystallisation or recrystallisation from solution (fig. 2.12).

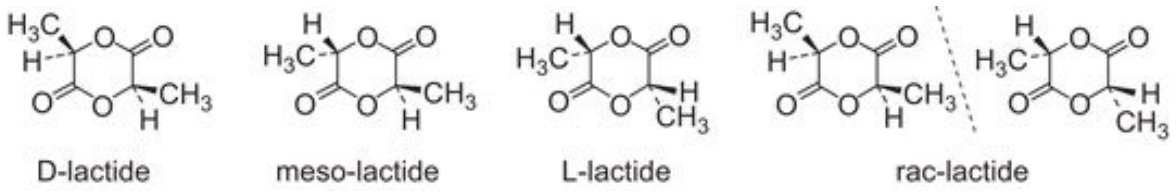

Fig. 2.12 *Chemical production from lactic acid to lactide via oligolactide*

Figure 2.13 the two main synthetic routes to produce PLA polymers are:

1. Direct polycondensation of lactic acid

2. Ring-opening polymerization (ROP) of lactide

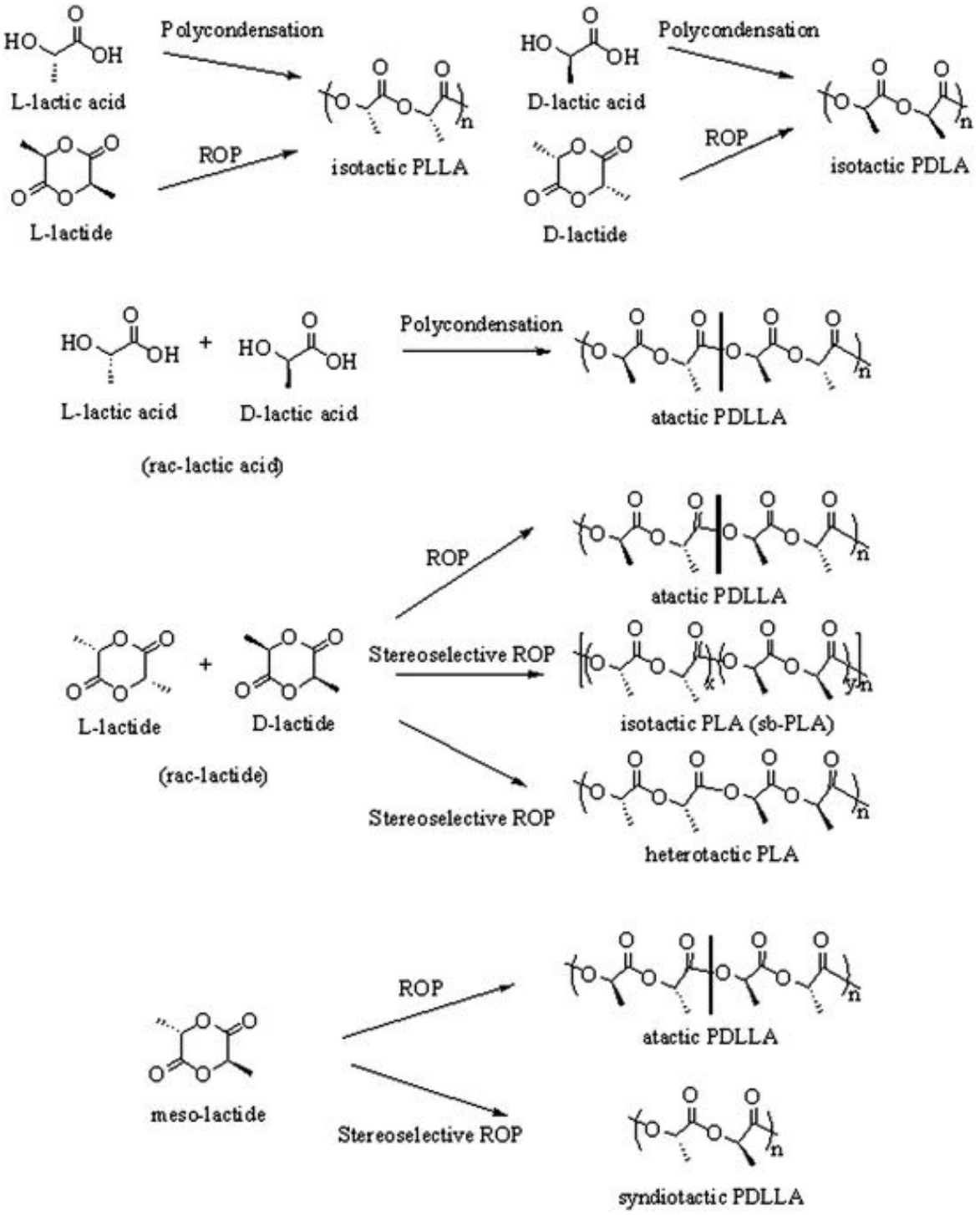

Fig. 2.13 *Polymerisation process for different PLAs, from Masutani and Kimura (2014)*

The first one was established by Mitsui Chemicals Co. (Japan), wherein lactic acid and catalyst are azeotropically dehydrated in a refluxing, high boiling point, aprotic solvent such as diphenyl ether, under reduced pressure to obtain PLA with very high weight-average molecular weight.
The second one is most used for industrial production. The polymerisation of the pure L- or D-lactides gives isotactic hoopolymers of, respectively, PLLA and PDLA. If the starting compound is pure, L or D stereoisomer, the final product is semicrystalline showing a melting temperature around 180°C. A decrease of the purity of L- and D- lactose means a reduction of crystallinity and T_m. If the reagents are rac- and meso-lactides the obtained polymer will be PDLLA. This latter is an amorphous polymer with an atactic sequence of D and L units. In any case crystalline polymer can be obtained also controlled stereo-regularity of the D- L- units (Masutani and Kimura, 2014). Table 2.1 shows the solubility of different poly-lactide in different solvents. Rissanen et al. (2008) tested co-polymer PLLA-PDLA at various ratio, 96/4 (two inherent viscosity 2.2 and 4.8 dL/g), 70/30 and 50/50. The solubility is dependent on the ratio of the two polymers, except for dicholomethane. This latter is able to dissolve every polymers ratio. Increasing the D segment, the amorphous regions increase accordingly. then to dissolve the polymer results gradually easier. P(D,L)LA can be dissolved in every tested solvents. The two polymers with different inherent viscosity show a slight different solubility. Low molecular weight (2.2 dL/g) promotes the ability of molecules of the solvents to penetrate into the polymer structure, thus increasing the solubility.

2.2.2 Dioxane

The solvent adopted to prepare the ternary solution is the dioxane at all proportions. The dioxane is a stable, clear liquid at ambient temperatures and miscible with water. Dioxane is produced by the acid-catalysed dehydration of diethylene glycol, derived the hydrolysis of ethylene oxide.
It is used primarily as a solvent for chemical processing. It has also been used as a laboratory reagent; in plastic, rubber, insecticides, and herbicides; as a chemical intermediate; as part of a polymerization catalyst; and as an extraction medium of animal and vegetable oils. Dioxane may also be found as a contaminant in ethoxylated surfactants, which are used in consumer cosmetics, detergents, and shampoos. The boiling point is 101°C and the melting point 12°C. Three different isomers of the dioxane exist (fig. 2.14), but the most common is 1,4-Dioxane.

	Polymer			
	P(L,D)LA 96/4, IV = 2.2 dL/g	P(L,D)LA 96/4, IV = 4.8 dL/g	P(L,DL)LA 70/30	P(L,D)LA 50/50
Solvent				
Dichloromethane	1	1	1	1
1,4-Dioxane	3	4	3	1
Propylene carbonate	6	5	4	1
Acetone	5	5	3	1
Methyl acetate	5	5	3	1
Tetrahydrofuran	4	5	3	1
Pyridine	3	5	3	1
Formic acid (98%)	5	5	2	1
Nonsolvent				
n-Hexane	6	6	6	6
Methanol	6	6	6	5
Ethanol	6	6	6	5
Isopropyl alcohol	6	6	6	6

Table 2.1 *Solubility test of co-polymer PLLA-PDLA at different ratio. The interaction between polymer and solvent were classified with the following legend: 1) a clear solution; 2) gel-like, thread-shaped structures; 3) a gelatinous solid; 4) very swollen; 5) slightly swollen; 6) insoluble, from Rissanen et al. (2008)*

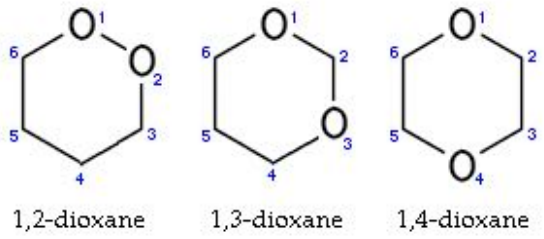

Fig. 2.14 *Dioxane isomers*

Binary-ternary solution

Dioxane and water are miscible in all composition forming a not-ideal mixture. The vapour-liquid equilibrium presents an azeotrope (Nayak et al., 2004) and the freezing point is lower of the pure compound (Goates and Sullivan, 1958), with a minimum of -15°C at 0.14 dioxane molar fraction (fig. 2.15).

Van de Witte et al. (1996) analyzed the thermodynamics characteristics of PLLA and PDLLA (semicrystalline and amorphous, respectively) as a function of the ternary system. In figure 2.16 the variation of the intrinsic viscosity is reported. In the case of chloroform/methanol the decrease of the intrinsic viscosity of the solution is almost linear for both

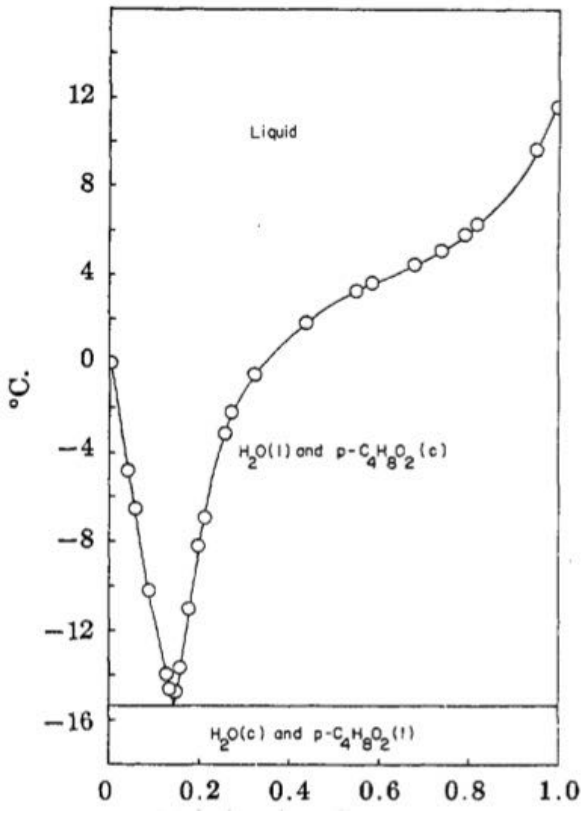

Fig. 2.15 *Freezing point at different dioxane/water molar ratio, from Goates and Sullivan (1958)*

PLLA and PDLLA. On the other hand adopting dioxane/water as system, the reduction of intrinsic viscosity is almost cubic. Passing from 4 dl/g and 3 dL/g, for PLLA and PDLLA respectively, to 1.5 dL/g for both polymers in less 1.5% of volumetric ratio of water.

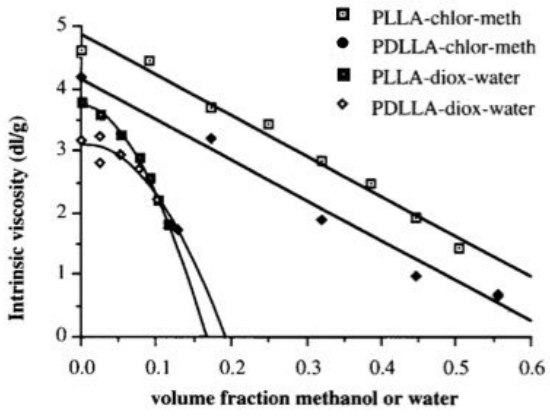

Fig. 2.16 *Intrinsic viscosity vs volume fraction of non-solvent for PLLA and PDLLA, from Van de Witte et al. (1996)*

Figure 2.17 shows the cloud point varying the dioxane/water ratio at fixed temperature, 25°C. It is clear that to induce the demixing of the solution at 25°Cit is necessary an amount of water at least of 12% for PLLA and 14% for PDLLA. The limit of solubility of PLLA in pure dioxane is 15% at 25°Cand increase to 26% at 50°C.

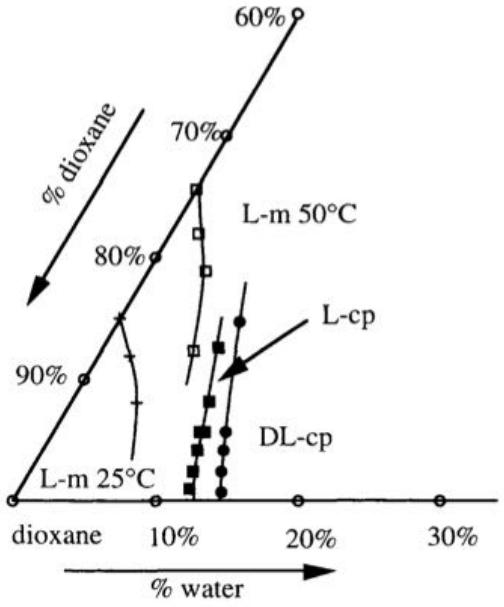

Fig. 2.17 *Isothermal ternary phase diagram of PLLA-PDLLA/Dioxane/water. L: PLLA, DL: PDLLA, m: solubility curve at 25°C and 50°C, cp: cloud point curve at 25°C, from Van de Witte et al. (1996)*

2.3 Composite scaffold

Ceramics are solid compounds formed by application of heat or heat and pressure. They are inorganic non-metallic solid made up of either metal or non-metal compounds, hard, corrosion-resistant and brittle. Ceramics comprised of calcium phosphates, silica, alumina, zirconia and titanium dioxide are used for various medical applications due to their positive interactions with human tissues (Carter and Norton, 2007).
Different examples in literature show the possibility to use the ceramic in various biomedical field: dentistry (Duraccio et al., 2015), othophedics (Taksali et al., 2004), platic surgery (Spetzger et al., 2013), etc.
The ceramics present interesting features such as osteoconductivity, good mechanical proprieties in compression, biocompatibility, but on the other hand they present very slow degradation rate and brittle behaviour.

Abbreviation	Name	Formula	Ca/P-ratio
ACP	Amorphous calcium phosphate	–	$1.25<x<1.55$
BCP	Biphasic calcium phosphate	$Ca_3(PO_4)_2+Ca_{10}(PO_4)_6(OH)_2$	$1.50<x<1.67$
CA	Carbonated apatite, dahlite	$Ca_5(PO_4,CO_3)_3$	1.67
CDHA	Calcium deficient hydroxyapatite	$Ca_{10-x}(HPO_4)_x(PO_4)_{6-x}(OH)_{2-x}$	$1.50<x<1.67$
DCPA	Dicalcium phosphate anhydrous, Monetite	$CaHPO_4$	1.00
DCPD	Dicalcium phosphate dihydrate, Brushite	$CaHPO_4{\cdot}H_2O$	1.00
HA	Hydroxyapatite	$Ca_{10}(PO_4)_6(OH)_2$	1.67
MCPM	Monocalcium phosphate monohydrate	$Ca(H_2PO_4)_2{\cdot}H_2O$	0.50
OCP	Octacalcium phosphate	$Ca_8H_2(PO_4)_6{\cdot}5H_2O$	1.33
pHA	Precipitated hydroxyapatite	$Ca_{10-x}(HPO_4)_x(PO_4)_{6-x}(OH)_{2-x}$	$1.50<x<1.67$
α-TCP	α-Tricalcium phosphate, Whitlockite	α-$Ca_3(PO_4)_2$	1.50
β-TCP	β-Tricalcium phosphate, Whitlockite	β-$Ca_3(PO_4)_2$	1.50
TTCP	Tetracalcium phosphate, Hilgenstockite	CaO-$Ca_3(PO_4)_2$	2.00

Table 2.2 *Ca-P compounds with their formula and Ca/P ratio, from Habraken et al. (2007)*

To increase the biodegradability of the ceramics, porosity at different scale can be introduced, from macroporosity to microporosity but, in any case, they are hard to tune according to the specific necessity.

For this reason, increasing attention has been posed in ceramic/polymer composite. A large variety of polymers has been used in combination with the biopolymers, e.g. chitosan, collagen, poly(lactic acid), poly(glycolic acid) and so on. These latter are approved from FDA for medical purpose but they are not intrinsically bioactive and will not bond directly to living tissue. Furthermore they are lack in mechanical strength required to meet the demands of orthopaedic surgery. The composite scaffolds can combine the tailored degradability of the polymer with the osteoconductivity and the ability to bond with the living tissue of the ceramic materials. The polymer can also counterbalance the brittleness of the ceramic material, given it main handling proprieties of the pure calcium phosphate cement.

Due to their similarity to human bone, calcium phosphate ceramics are probably the most used filler for diverse clinical applications since the last 30 years. Different types of CaP-ceramics are available, though they can be classified as either hydroxyapatite (HA), beta-tricalcium phosphate (β-TCP), biphasic calcium phosphate (BCP), amorphous calcium phosphate (ACP), carbonated apatite (CA) or calcium deficient HA (CDHA).

Table 2.2 shows the principal calcium phosphates with their composition. In the following two paragraphs a small overview of the composite scaffold with hydroxyapatite and bioglass are reported.

2.3.1 Hydroxyapatite

Scaffold for bone tissue, besides the typical characteristics, must supply the necessary mechanical strength and osteogenic environment. The hydroxyapatite (HA), chemical formula $Ca_{10}(PO_4)_6(OH)_2$, is the main mineral presents in the osseous tissue. Over then 70% of

the overall mass of the bone is hydroxyapatite (the other 30% is collagen type I). Natural bone is a complex inorganic-organic nanocomposite materials, in which hydroxyapatite nanocrystallites and collagen fibrils are organised in a hierarchical architecture.
The HA is a basic calcium phosphate of the apatite family. In its structure large Ca polyhedra share faces and thus form chains parallel to the crystallographic c-axis [0001]. These chains are linked into a hexagonal array via sharing edges and corners with PO_4 tetrahedra. The OH^- ions are located in wide hexagonal channels parallel [0001]. The unit cell of hydroxyapatite with orthohexagonal metric is reported in fig. 2.18a, while the phase diagram in fig. 2.18b.

The open channel structure of HA is able to incorporate other ions by substituting Ca^{2+} as

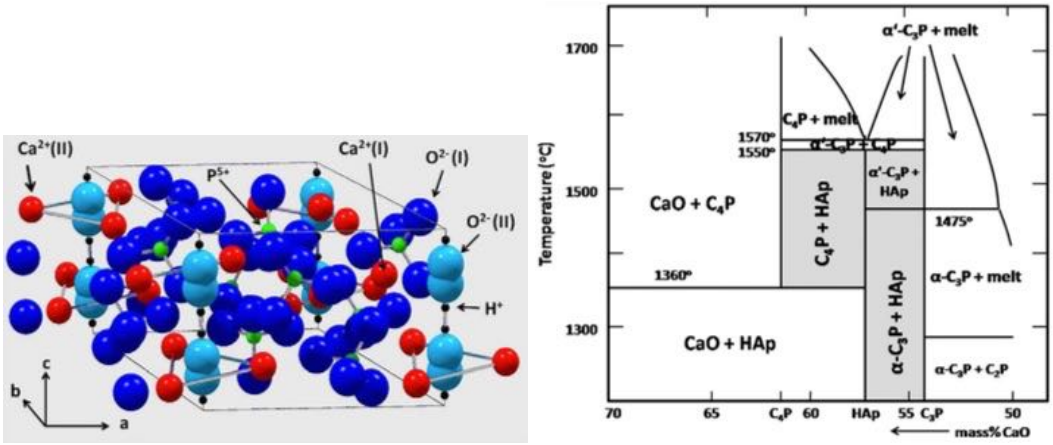

(a) (b)

Fig. 2.18 *a) Crystallographic structure of the hydroxyapatite, b) Phase diagram of the quasi-binary system* $CaO - P_2O_5 - H_2O$*, from Heimann (2013)*

well as OH^- and PO_4^{3-} anions without large distortion of the structure or other cations sch as Na^+,Mg^{2+}, Sr^{2+}, K^+, moreover it is possible to find trace of metabolically important elements such as Pb^{2+}, Ba^{2+}, Zn^{2+} and Fe^{2+} (Heimann, 2013). This compositional variability of HAp causes its high biocompatibility and osteoconductivity. The Hydroxyapatite can be synthesised in different ways, e.i. wet chemical process (Ethirajan et al., 2008), hydrothermal method (Liu et al., 1997), use of sol-gel procedures (Weng and Baptista, 1998), solid-state reaction (Ramachandra Rao and Kannan, 2002), emulsion or micro-emulsion routes (Lim et al., 1999). As regards the physical-chemical properties of this material, it is characterised by high melting temperature, good toughness and high resistance to compression, extremely important factor for scaffolds that need high mechanical properties; unfortunately, however, it has a certain fragility and difficult processability (Kothapalli et al., 2005; Swetha et al., 2010).

HA has been applied widely in medical field as a bone repair material because of its excellent biocompatibility and bioactive properties (Sun et al., 2011). Furthermore HA is known for its osteoconductive, non-toxic, non-inflammatory, non-immunogenic properties. Thus, HA is one of the ideal materials for bone substitution and composite scaffolds.
In order to achieve the requirements for bone regeneration, biomimetic matrices are usually adopted which may provide a suitable microenvironment to promote osteoblast proliferation and osteogenesis.
Different technique has been adopted to produce composite HA scaffold, such as: solvent casting (Albano et al., 2013; Tanaka et al., 2008), in situ mineralization of HA in polymers (Verma et al., 2006), electrospinning (Li et al., 2006a; Sui et al., 2007), fabrication methods of 3-D microstructures (Tanodekaew et al., 2013), electrodeposition (Yang et al., 2008) and TIPS (Akbarzadeh and Yousefi, 2014; Krishnan and Lakshmi, 2013).

2.3.2 Bioglass

Over the past year the use of the bioglass for tissue engineering purpose was widely studied and applied. Several studies show that the bioglass can stimulate a rapid expression of the genes that regulate the osteogenesis and the production of the growth factors.
The bioglass was discovered around the 60s and 70s by Professor L. Hench. The research was funded by the US army to solve the problem of the rejection by the human body of the insert in metal or plastic, the only material available for surgeons in that period. The idea was to find a new family of materials able to bind to living tissue, avoiding the necrosis of the tissue.
Thus the idea to fabricate a material able to produce a layer of hydroxyapatite.The first produced bioglass was the 45S5, with a nominal composition in weight of $45\%SiO_2 - 24.5\%Na_2O - 24.5\%CaO - 6\%P_2O_5$.
This composition was chosen for the high amount of CaO with some P_2O_5 in a $Na_2O - SiO_2$ matrix. Furthermore this composition is near the eutectic point, then easy to melt (Krishnan and Lakshmi, 2013).
Small samples of bioglass 45S5 were used in rat femoral implant model. After six weeks, the bioglass showed a strong bond with the bone, forming a layer of hydroxyapatite. This layer of hydroxyapatite crystals, perfectly compatible with the human bone, was firmly connected to the native tissue through collagen fibrils.
Wilson et al. (1981) showed the possibility of the bond between bioglass and soft connective tissue with an immobile interface.
In figure 2.19 the ternary phase diagram $SiO_2 - Na_2O - CaO$ is reported at a fixed composi-

tion, 6% of P_2O_5.

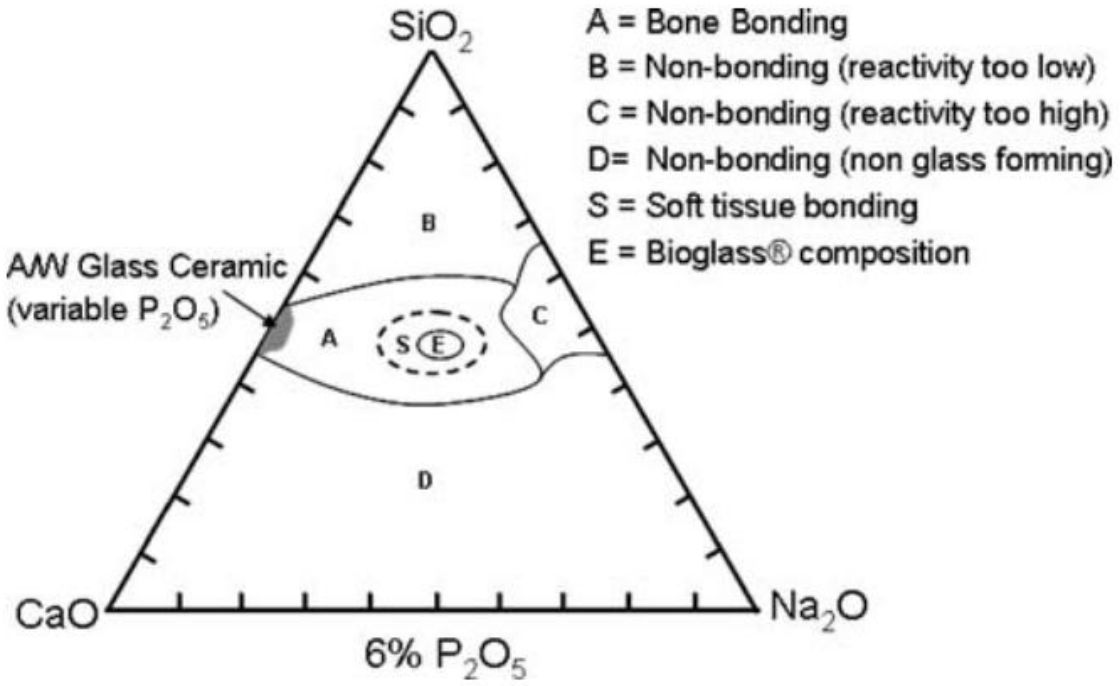

Fig. 2.19 *Ternary phase diagram $SiO_2 - Na_2O - CaO$ and bone bonding, from Hench (2006)*

- Region A: The compositional range for bonding of bone to bioactive glasses and glass-ceramics;
- Region B: The concentration of SiO_2 is too high (over 60%), the material is bioinert;
- Region C: The reaction is too fast and there is not the formation of bonding;
- Region D: The concentration of SiO_2 is too low, there is not the formation of the glass;
- Region E: Glasses with the highest degree of bioactivity (the 45S5 is this region);
- Region S: The glasses with rapid reaction can form soft tissue bond. If the glass composition exceeds 52% by weight of SiO2 the glass will bond to bone but not to soft tissues.

The 45S5 composition is not the only kind of bioactive glass, in table 2.3 other types of bioglass with related chemical composition are reported.

	45S5	1393	6P53B	58S	70S30C	1393B1	1393B3	$P_{50}C_{35}N_{15}$
Na_2O	24.5	6.0	10.3	0	0	5.8	5.5	9.3
K_2O	0	12.0	2.8	0	0	11.7	11.1	0
MgO	0	5.0		0	0	4.9	4.6	0
CaO	24.5	20.0	18.0	32.6	28.6	19.5	18.5	19.7
SiO_2	45.0	53.0	52.7	58.2	71.4	34.4	0	0
P_2O_5	6.0	4.0	6.0	9.2	0	3.8	3.7	71.0
B_2O_3	0	0	0	0	0	19.9	56.6	0

Table 2.3 *Small overview about the different type of bioglass and their composition*

As example 1393 and 6P53B start from the same composition of the 45S5 but adding K_2O and MgO, 58S presents a higher amount of CaO, 1393B1 and 1393B3 modified by boron.

Two important parameters concerning the bioglass are: the bioactivity index (IB) and the class of bioceramics.
The first one is defined as:

$$I_B = 100/t_{0.5} \tag{2.3.1}$$

where $t_{0.5}$ is the time necessary to bind that more the half of the material is linked to the tissue. Materials with $I_B > 8$, like bioglass, can bond to hard and soft tissue, material with $0 < I_B < 8$ can bond only to hard tissue.
The bonding between bioglass and tissue has been attributed to the formation of a carbonate-substitute hydroxyapatite-like (HCA) forming on the surface of the bioglass in contact with the body fluid. For the similarity of HCA with the hydroxyapatite this layer is able to firmly bond with the living tissue and bone (Huang et al., 2006; Kaur et al., 2014; Rahaman et al., 2011).
Hench (1998) proposed a mechanism for the formation of HCA starting from bioglass, as a sequence of reactions of ion exchange:

- 1^{st} Step: Exchange of ions between the H^+ from the solution and the glass network modifiers (Na^+ and Ca^{2+}) leads to formation of silanol $Si-O$ groups as a consequence of hydrolysis of the silica groups. During this process the pH of the solution increases due to the increasing of the OH^- ions. The reaction mechanism is the following:

$$Si-O-Na^+ + H^+ \rightarrow Si-OH^+ + Na^+ \tag{2.3.2}$$

- 2^{nd} Step: The increase in pH (or OH^- concentration) leads to attack of the SiO_2 glass network. The dissolution of silica occurs resulting in the formation of silicic acid leads that is Si(OH)4 on the surface of glass as follows:

$$Si-O-Si+H_2O \rightarrow 2Si-OH \tag{2.3.3}$$

  The silanol group act as nucleation site for the apatite formation. The dissolution process is controlled by interface reaction with a linear dependence on the time. The kinetic equation can be written as:

$$\frac{dC}{dt} = ks(C_e - C) \tag{2.3.4}$$

  where C_e is the equilibrium concentration of silicon, C is the concentration of silica in solution, S is the surface of the particles, k is the rate constant and t is time.

- 3^{rd} Step: Condensation and polymerization process allows the formation of a silica gel layer of 1-2 µm on the surface of the glass. Thus the precipitation and migration of calcium ions from the supersaturated solution to the particles occurs.

- 4^{th} Step: Migration and incorporation of Ca^{2+} and PO_4^{3-} anions from the solution to the SiO_2-rich layer leads the formation of an amorphous calcium phosphate layer (ACP). The concentration of Ca^{2+} and $Si(OH)_4$ are crucial parameters for HA formation.

- 5^{th} Step: The incorporation of OH^- and CO_3^{2-} ions from the solution to the layer continues, converting the ACP layer to an HA layer. The formation of HA is pseudomorphic as it starts at the surface of the glass and gradually spreads in all available surface

The different types of bioceramics can be divided in two classes:

- Class A: bioactive materials osteogenetic and osteoconductive;

- Class B: bioactive materials only osteoconductive.

The bioglass belongs to the class A.
The bioglass scaffold can be divided in two main families: bioglass scaffold and bioglass as

filler in a polymer matrix.
In the first case the production of the scaffold can occur via sol-gel technique, foam replica technique or gel casting. The sol-gel consists in the formation of an oxide network via polycondensation reactions of a molecular precursor in a liquid. The idea is to dissolve the compound in a liquid in order to obtain a solid in a desiderated shape (Dziadek et al., 2015). In the foam replica technique a polymer network (e.g. polyurethane) is immersed in a slurry of bioglass. At the end of the process, the system polymer-bioglass is placed in a furnace to reach around 1400°C. In this way at 300-400°C the polymer is degraded and at 1350°C, there is the sintering of the bioglass, to obtain the final morphology (Chen et al., 2006).
About the gel-casting, the starting point is the mixing of glass powder with deionized water, monomer (e.g. acrylamide) and the cross-linker to produce a slurry. The mixture, then, is vigorously agitated to produce a foam with the aid of surfactants. Initiator and catalyst are added to the mixture and poured in a mold where the pore structure is stabilised by the completion of gelation. Finally the structure is dried and sintered to eliminate all the organic matter, leaving the porous network. (Ghomi et al., 2011; Wu et al., 2010, 2011)
Concerning the bioglass as filler, different polymer processing technique has been developed to produce composite scaffold. As example solvent casting with and without particle leaching (Huang et al., 2014; Lu et al., 2014), TIPS (Barroca et al., 2010; Noh et al., 2016), etc.

References

R. Akbarzadeh and A.-M. Yousefi. Effects of processing parameters in thermally induced phase separation technique on porous architecture of scaffolds for bone tissue engineering. *Journal of biomedical materials research. Part B, Applied biomaterials*, pages 1–12, 2014.

C. Albano, G. Gonza, and J. Palacios. PLLA-HA vs. PLGA-HA Characterization and Comparative Analysis. *Polymer Composites*, 34(9):1433–1442, 2013.

N. Barroca, a. L. Daniel-da Silva, P. M. Vilarinho, and M. H. V. Fernandes. Tailoring the morphology of high molecular weight PLLA scaffolds through bioglass addition. *Acta biomaterialia*, 6(9):3611–20, 2010.

S. Bian, L. Wei, X. Cancan, Y. Fan, and Z. Xingdong. In Vitro Cartilage Tissue Engineering Using Porous Collagen / PLLA Nanoparticle Hybrid Scaffold. *Journal of Medical and Biological Engineering*, 34(1):36–43, 2013.

F. Carfì Pavia, V. La Carrubba, S. Piccarolo, and V. Brucato. Polymeric scaffolds prepared via thermally induced phase separation: Tuning of structure and morphology. *Journal of Biomedical Materials Research - Part A*, 86(2):459–466, 2008.

F. Carfì Pavia, S. Rigogliuso, V. La Carrubba, G. A. Mannella, G. Ghersi, and V. Brucato. Poly lactic acid based scaffolds for vascular tissue engineering. *Chemical Engineering Transactions*, 27:409–414, 2012.

C. B. Carter and M. G. Norton. *Ceramic Materials: Science and Engineering*. 2007.

J. S. Chen, S. L. Tu, and R. Y. Tsay. A morphological study of porous polylactide scaffolds prepared by thermally induced phase separation. *Journal of the Taiwan Institute of Chemical Engineers*, 41(2):229–238, 2010.

Q. Z. Chen, K. Rezwan, D. Armitage, S. N. Nazhat, and A. R. Boccaccini. The surface functionalization of 45S5 Bioglass-based glass-ceramic scaffolds and its impact on bioactivity. *Journal of Materials Science: Materials in Medicine*, 17(11):979–987, 2006.

D. Duraccio, F. Mussano, and M. G. Faga. Biomaterials for dental implants: current and future trends. *Journal of Materials Science*, 50(14):4779–4812, 2015.

M. Dziadek, E. Menaszek, B. Zagrajczuk, J. Pawlik, and K. Cholewa-Kowalska. New generation poly(ε-caprolactone)/gel-derived bioactive glass composites for bone tissue engineering: Part I. Material properties. *Materials science & engineering. C, Materials for biological applications*, 56:9–21, 2015.

S. Eftekhari, I. El Sawi, Z. S. Bagheri, G. Turcotte, and H. Bougherara. Fabrication and characterization of novel biomimetic PLLA/cellulose/hydroxyapatite nanocomposite for bone repair applications. *Materials Science and Engineering: C*, 39:120–125, 2014.

A. Ethirajan, U. Ziener, A. Chuvilin, U. Kaiser, H. Cölfen, and K. Landfester. Biomimetic Hydroxyapatite Crystallization in Gelatin Nanoparticles Synthesized Using a Miniemulsion Process. *Advanced Functional Materials*, 18(15):2221–2227, 2008.

M. Frydrych, S. Román, S. MacNeil, and B. Chen. Biomimetic poly(glycerol sebacate)/poly(l-lactic acid) blend scaffolds for adipose tissue engineering. *Acta biomaterialia*, 18:40–9, 2015.

H. Ghomi, M. H. Fathi, and H. Edris. Fabrication and characterization of bioactive glass/hydroxyapatite nanocomposite foam by gelcasting method. *Ceramics International*, 37(6):1819–1824, 2011.

J. R. Goates and R. J. Sullivan. Thermodynamic Properties of the System Water-p-Dioxane. *The Journal of Physical Chemistry*, 62(2):188–190, 1958.

W. J. E. M. Habraken, J. G. C. Wolke, and J. A. Jansen. Ceramic composites as matrices and scaffolds for drug delivery in tissue engineering. *Advanced Drug Delivery Reviews*, 59 (4-5):234–248, 2007.

L. He, Y. Zhang, X. Zeng, D. Quan, S. Liao, Y. Zeng, J. Lu, and S. Ramakrishna. Fabrication and characterization of poly(l-lactic acid) 3D nanofibrous scaffolds with controlled architecture by liquid–liquid phase separation from a ternary polymer–solvent system. *Polymer*, 50(16):4128–4138, 2009.

R. B. Heimann. Structure, properties, and biomedical performance of osteoconductive bioceramic coatings. *Surface and Coatings Technology*, 233:27–38, 2013.

L. L. Hench. Bioceramics. *Journal of the American Ceramic Society*, 8:1705–1728, 1998.

L. L. Hench. The story of Bioglass®. *Journal of Materials Science: Materials in Medicine*, 17(11):967–978, 2006.

S.-H. Hsu, S. Huang, Y.-C. Wang, and Y.-C. Kuo. Novel nanostructured biodegradable polymer matrices fabricated by phase separation techniques for tissue regeneration. *Acta biomaterialia*, 9(6):6915–27, 2013.

References

F. J. Hua, G. E. Kim, J. D. Lee, Y. K. Son, and D. S. Lee. Macroporous poly(L-lactide) scaffold 1. Preparation of a macroporous scaffold by liquid-liquid phase separation of a PLLA-dioxane-water system. *Journal of Biomedical Materials Research*, 63(2):161–167, 2002.

R. Huang, X. Zhu, T. Zhao, and A. Wan. Preparation of tissue engineering porous scaffold with poly(lactic acid) and polyethylene glycol solution blend by solvent-casting/particulate-leaching. *Materials Research Express*, 1(4):045403, 2014.

W. Huang, D. E. Day, K. Kittiratanapiboon, and M. N. Rahaman. Kinetics and mechanisms of the conversion of silicate (45S5), borate, and borosilicate glasses to hydroxyapatite in dilute phosphate solutions. *Journal of Materials Science: Materials in Medicine*, 17(7): 583–596, 2006.

X. Jing, H.-Y. Mi, M. R. Salick, T. Cordie, W. C. Crone, X.-F. Peng, and L.-S. Turng. Morphology, mechanical properties, and shape memory effects of poly(lactic acid)/thermoplastic polyurethane blend scaffolds prepared by thermally induced phase separation. *Journal of Cellular Plastics*, 50(4):361–379, 2014.

G. Kaur, O. P. Pandey, K. Singh, D. Homa, B. Scott, and G. Pickrell. A review of bioactive glasses: Their structure, properties, fabrication and apatite formation. *Journal of Biomedical Materials Research - Part A*, 102(1):254–274, 2014.

J.-W. Kim, K. Taki, S. Nagamine, and M. Ohshima. Preparation of porous poly(L-lactic acid) honeycomb monolith structure by phase separation and unidirectional freezing. *Langmuir : the ACS journal of surfaces and colloids*, 25(9):5304–12, 2009.

C. R. Kothapalli, M. Wei, R. Z. Legeros, and M. T. Shaw. Influence of temperature and aging time on HA synthesized by the hydrothermal method. *Journal of materials science. Materials in medicine*, 16(5):441–6, 2005.

T. Kouya, S.-i. Tada, H. Minbu, Y. Nakajima, M. Horimizu, T. Kawase, D. R. Lloyd, and T. Tanaka. Microporous membranes of PLLA/PCL blends for periosteal tissue scaffold. *Materials Letters*, 95:103–106, 2013.

V. Krishnan and T. Lakshmi. Bioglass: A novel biocompatible innovation. *Journal of advanced pharmaceutical technology & research*, 4(2):78–83, 2013.

C. Li, C. Vepari, H.-J. Jin, H. J. Kim, and D. L. Kaplan. Electrospun silk-BMP-2 scaffolds for bone tissue engineering. *Biomaterials*, 27(16):3115–24, 2006a.

D. Li, W. B. Krantz, A. R. Greenberg, and R. L. Sani. Membrane formation via thermally induced phase separation (TIPS): Model development and validation. *Journal of Membrane Science*, 279(1-2):50–60, 2006b.

G. K. Lim, J. Wang, S. C. Ng, and L. M. Gan. Formation of Nanocrystalline Hydroxyapatite in Nonionic Surfactant Emulsions. *Langmuir*, 15(22):7472–7477, 1999.

H. Liu, T. Chin, L. Lai, S. Chiu, K. Chung, C. Chang, and M. Lui. Hydroxyapatite synthesized by a simplified hydrothermal method. *Ceramics International*, 23(1):19–25, 1997.

W. Lu, K. Ji, J. Kirkham, Y. Yan, A. R. Boccaccini, M. Kellett, Y. Jin, and X. B. Yang. Bone tissue engineering by using a combination of polymer/Bioglass composites with human adipose-derived stem cells. *Cell and tissue research*, 2014.

G. A. Mannella, F. Carfì Pavia, G. Conoscenti, V. La Carrubba, and V. Brucato. Evidence of mechanisms occurring in thermally induced phase separation of polymeric systems. *Journal of Polymer Science, Part B: Polymer Physics*, 52(14):979–983, 2014.

K. Masutani and Y. Kimura. PLA Synthesis. From the Monomer to the Polymer. In *Poly(lactic acid) Science and Technology: Processing, Properties, Additives and Applications*, pages 1–36. 2014.

Y. S. Nam and T. G. Park. Porous biodegradable polymeric scaffolds prepared by thermally induced phase separation. *Journal of Biomedical Materials Research*, 47(1):8–17, 1999.

J. Nayak, M. Aralaguppi, B. V. Naidu, and T. Aminabhavi. Thermodynamic Properties of Water+Tetrahydrofuran and Water+1,4-Dioxane Mixtures at (303.15, 313.15, and 323.15) K. *J. Chem. Eng. Data*, 49:468–474, 2004.

D.-Y. Noh, Y.-H. An, I.-H. Jo, Y.-H. Koh, and H.-E. Kim. Synthesis of nanofibrous gelatin/silica bioglass composite microspheres using emulsion coupled with thermally induced phase separation. *Materials Science and Engineering: C*, 2016.

T. Phaechamud and S. Chitrattha. Pore formation mechanism of porous poly(dl-lactic acid) matrix membrane. *Materials Science and Engineering: C*, 61:744–752, 2016.

M. N. Rahaman, D. E. Day, B. Sonny Bal, Q. Fu, S. B. Jung, L. F. Bonewald, and A. P. Tomsia. Bioactive glass in tissue engineering. *Acta Biomaterialia*, 7(6):2355–2373, 2011.

R. Ramachandra Rao and T. Kannan. Synthesis and sintering of hydroxyapatite–zirconia composites. *Materials Science and Engineering: C*, 20(1-2):187–193, 2002.

References

M. Rissanen, A. Puolakka, P. Nousiainen, M. Kellomäki, and V. Ellä. Solubility and Phase Separation of Poly(L,D-Lactide) Copolymers. *Journal of applied polymer science*, 110: 2399–2404, 2008.

F. Ruggiero, P. A. Netti, and E. Torino. Experimental Investigation and Thermodynamic Assessment of Phase Equilibria in the PLLA/Dioxane/Water Ternary System for Applications in the Biomedical Field. *Langmuir*, 31(47):13003–13010, 2015.

A. Salerno and C. Domingo. Pore structure properties of scaffolds constituted by aggregated microparticles of PCL and PCL-HA processed by phase separation. *Journal of Porous Materials*, 22(2):425–435, 2015.

U. Spetzger, A. Von Schilling, G. Winkler, J. Wahrburg, and A. König. The past, present and future of minimally invasive spine surgery: a review and speculative outlook. *Minimally invasive therapy & allied technologies : MITAT : official journal of the Society for Minimally Invasive Therapy*, 22(4):227–41, 2013.

G. Sui, X. Yang, F. Mei, X. Hu, G. Chen, X. Deng, and S. Ryu. Poly-L-lactic acid/hydroxyapatite hybrid membrane for bone tissue regeneration. *Journal of Biomedical Materials Research Part A*, 82(2):445–454, 2007.

F. Sun, H. Zhou, and J. Lee. Various preparation methods of highly porous hydroxyapatite/polymer nanoscale biocomposites for bone regeneration, 2011.

M. Swetha, K. Sahithi, A. Moorthi, N. Srinivasan, K. Ramasamy, and N. Selvamurugan. Biocomposites containing natural polymers and hydroxyapatite for bone tissue engineering. *International Journal of Biological Macromolecules*, 47(1):1–4, 2010.

S. Taksali, J. N. Grauer, and A. R. Vaccaro. Material considerations for intervertebral disc replacement implants. *The spine journal : official journal of the North American Spine Society*, 4(6 Suppl):231S–238S, 2004.

M. Tanaka, K. Yoshizawa, A. Tsuruma, H. Sunami, S. Yamamoto, and M. Shimomura. Formation of hydroxyapatite on a self-organized 3D honeycomb-patterned biodegradable polymer film. *Colloids and Surfaces A: Physicochemical and Engineering Aspects*, 313-314:515–519, 2008.

T. Tanaka and D. R. Lloyd. Formation of poly(L-lactic acid) microfiltration membranes via thermally induced phase separation. *Journal of Membrane Science*, 238(1-2):65–73, 2004.

T. Tanaka, T. Tsuchiya, H. Takahashi, M. Taniguchi, H. Ohara, and D. R. Lloyd. Formation of biodegradable polyesters membranes via thermally induced phase separation. *Journal of Chemical Engineering of Japan*, 39(2):144–153, 2006.

S. Tanodekaew, S. Channasanon, P. Kaewkong, and P. Uppanan. PLA-HA scaffolds: Preparation and bioactivity. *Procedia Engineering*, 59:144–149, 2013.

P. Van de Witte, P. J. Dijkstra, J. W. A. Aan den Berg, and J. Feijen. Phase Behavior of Polylactides in Solvent-Nonsolvent Mixtures. *Journal of Polymer Science Part B: Polymer Physics*, 34(15):2553–2568, 1996.

D. Verma, K. S. Katti, and D. R. Katti. Bioactivity in Insitu Polycaprolactone-Hydroxyapatite composites. *Journal of Biomedical Materials Research*, 78A:772–780, 2006.

W. Weng and J. L. Baptista. Sol-gel derived porous hydroxyapatite coatings. *Journal of materials science. Materials in medicine*, 9(3):159–63, 1998.

J. Wilson, G. H. Pigott, F. J. Schoen, and L. L. Hench. Toxicology and biocompatibility of bioglasses. *Journal of biomedical materials research*, 15(6):805–17, 1981.

Z. Y. Wu, R. G. Hill, and J. R. Jones. Optimizing the Processing of Porous Melt-Derived Bioactive Glass Scaffolds. *Bioceramics Development and Applications*, 1:1–4, 2010.

Z. Y. Wu, R. G. Hill, S. Yue, D. Nightingale, P. D. Lee, and J. R. Jones. Melt-derived bioactive glass scaffolds produced by a gel-cast foaming technique. *Acta Biomaterialia*, 7 (4):1807–1816, 2011.

D. Yang, Y. Jin, G. Ma, X. Chen, F. Lu, and J. Nie. Fabrication and characterization of chitosan/PVA with hydroxyapatite biocomposite nanoscaffolds. *Journal of Applied Polymer Science*, 110(6):3328–3335, 2008.

F. Yang, R. Murugan, S. Ramakrishna, X. Wang, Y.-X. Ma, and S. Wang. Fabrication of nano-structured porous PLLA scaffold intended for nerve tissue engineering. *Biomaterials*, 25(10):1891–1900, 2004.

Chapter 3

Gradient pore scaffolds

A high level of porosity of the scaffold is a crucial parameter to allow the tissue regeneration in vivo. Although the only presence of pores is sufficient for cell growth inside the 3D structure, however, it is possible to significantly improve the quality of the regeneration by focusing on pore size distribution. Each organ or tissue is characterised not only by a specific cell type but also by well defined spatial organization, such as: bone, from the compact to the sponge bone, blood vessel, three layers (tunica intima, media and adventitia), etc. This structure determines the overall characteristics and behaviour of the organ. For this reason obtaining a porosity gradient becomes a crucial point in order to mimic in the best possible way the tissue to regenerate. Three different kinds of gradients as a function of the gradient direction is possible to distinguish:

1. Radial pore size
2. Axial pore size
3. Longitudinal pore size

In the case of a cylindrical shaped scaffold, a change of pore dimensions along the radius is called radial pore size gradient. A typical body tissue example of radial pore variation is the bone tissue, starting from the maximum pore size in the inner part that gradually decreases to minimum in correspondence of the outer radius.
Taking as a reference a cylindrical scaffold, we have axial gradient if the scaffold shows a pore size modification along the axis of the cylinder, with large pore size at the bottom of the cylinder and gradually decreasing along the direction of the cylinder axis.
The longitudinal porosity gradient refers to the scaffolds of different geometries in which the pore size varies along one of the characteristic dimensions of the structure. For example in a cubic scaffold, a longitudinal porosity gradient means that the pore size variation insists

along one of its sides. In literature it is possible to find different method to obtain scaffold with radial (Harley et al., 2006; Kalita et al., 2003; Ma et al., 2010; Tang et al., 2013), axial (Davidenko et al., 2012; Oh et al., 2007; Salerno et al., 2008; Wu et al., 2008; Zhu et al., 2014), or longitudinal (Matsuyama et al., 1998, 1999; Sherwood et al., 2002; Sobral et al., 2011; Zhang et al., 2013) pore size gradient. In the next paragraphs two examples for each gradient are reported.

3.0.1 Radial pore size

One of the adopted techniques to obtain a radial pore size was the spinning process. A collagen-glycosaminoglycan (CG) suspension in acetic acid was spun in a cylindrical mold able to rotate around its longitudinal axis at variable angular velocities and for different times (fig. 3.1). After the specified spinning time, the mold was placed into a bath of liquid nitrogen where the suspension was rapidly frozen in liquid nitrogen and then the frozen solvent was removed via sublimation. By varying the time or the speed of rotation a change in the structure of the obtained scaffolds was observed. In this work 5000 rpm was individuated as the minimum speed to produces the radial porosity gradient. Increasing velocity and spinning time an increasing amount of solid in the external region and ultimately a hollow tube with an homogeneous inner diameter was obtained (Harley et al., 2006).

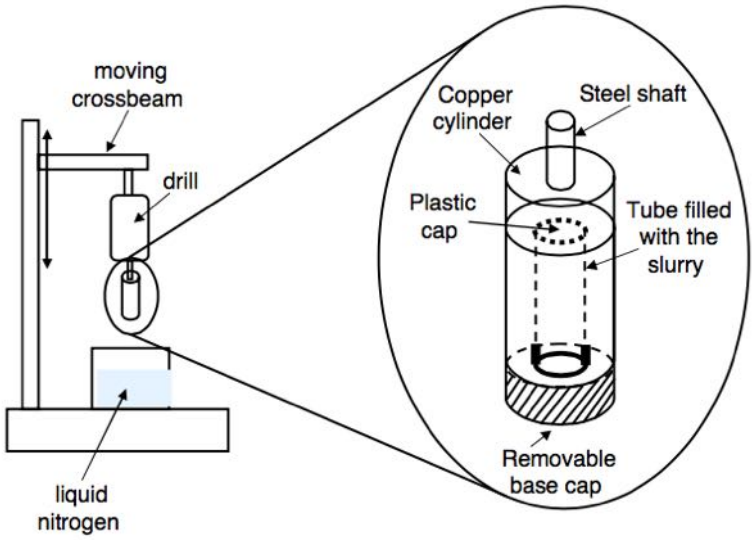

Fig. 3.1 *Spinning apparatus from Harley et al. (2006)*

Producing scaffolds with radial porosity gradient it is also possible via TIPS technique. To obtain this result a mould that allows to establish a radial temperature gradient between the center and edge was realised (Ma et al., 2010). The mold, figure 3.2 is composed by an outer steel cylindrical wall, while inner cylindrical wall, base and lid of teflon. The solution polymer/solvent (PLLA/benzene) is poured between the two cylindrical walls of the mold. The difference of thermal conductivity between the two materials (the steel layer cools faster than the walls of teflon) will create a radially distributed temperature gradient in the sample. The as-obtained sample shows lowest pore size in the outer part, in contact with the steel wall, which increases progressively to reach the maximum in the inner part in contact with the teflon wall. It is also noted that the pores are arranged along the temperature gradient (forming a radial structure in a herringbone pattern, fig. 3.2). A range of pore size is possible to obtain by varying the polymer/solvent ratio or the temperature at which the cooling process takes place. For example a decrease of porosity and pore size dimension was observed by increasing the polymer concentration from 2.5% to 10% or reducing the freezing temperature of from - 20°C to -196°C.

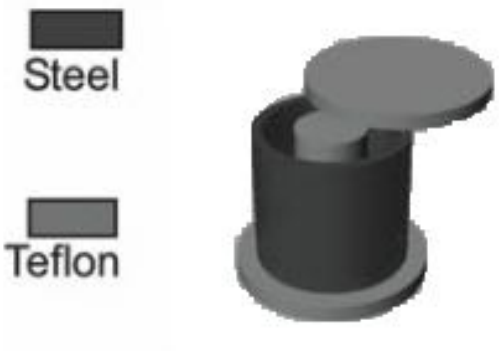

Fig. 3.2 *Schematic illustrations of the molds, from Ma et al. (2010)*

3.0.2 Axial pore size

Wu et al. (2008) adopted the particulate-leaching technique to fabricated scaffold with a well defined gradient pore size. The used salt in the study was the NaCl. The latter was ground to obtain different size particles. A copolymer chitosan/PCL (called CPC) was adopted. The powders of CPC and salt are then mixed with a predetermined weight ratio and arranged in a circular form with a movable base. A thin layer (around 1 mm) of mixed powders was first spread and pressed tightly, then a motor-controlled syringe reciprocally moved above the powder bed and deposited very small solvent (dimethyl sulfoxide, DMSO) droplets. In this way the powders were bound into many parallel filaments in one layer. After one layer was

completed, the bottom of the mould was lowered (around 1 mm), turned a given angle and a new layer of powders with an increasing weight ratio and particle size of salt was spread and pressed, followed by additional deposition of solvent droplets. The fabrication was repeated until the required structure were built, figure 3.3 The result is a scaffold with a varying pore size along its axis from 100µm to 400µm to the bottom on top. Although particulate-leaching technique is commonly used to fabricate porous scaffolds, this technique has, however, some disadvantages. In this case, for example, even with high percentages of porosity the salt particles remain trapped between the layers of the scaffold, this involves the impossibility to achieve a continuous variation of microstructure (Wu et al., 2008).

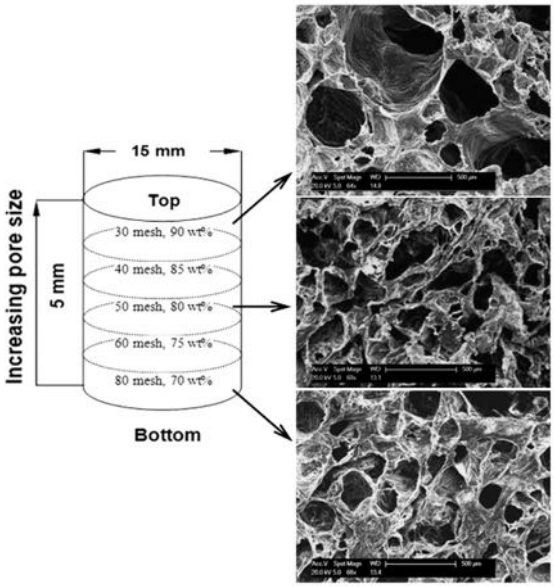

Fig. 3.3 *Micrographs of scaffold sections at different layers, from Wu et al. (2008)*

A combination of gas foaming and salt microparticles was adopted by Salerno et al. (2008). The employed polymers were PCL and NaCl as pore-forming agent. PCL and salt was initially mixed together and then compressed to 90°C and 30 bars to obtain a sample of 3 mm thick. After the mixing so obtained was saturated with CO_2 at 70°C and 65 bar for 3 hours (fig. 3.4). By changing the value of temperature, the rate of pressure drop and the ratio polymer/salt is possible to control porosity, interconnection and average pore size.

3.0.3 Longitudinal pore size

Longitudinal gradient pore size scaffold was fabricated via freeze-drying technique. Collagen was dissolved in a mixture of ethanol and acetic acid. Then the latter was immersed in liquid nitrogen to create the suspension of ice crystals. The ice particulates were prepared

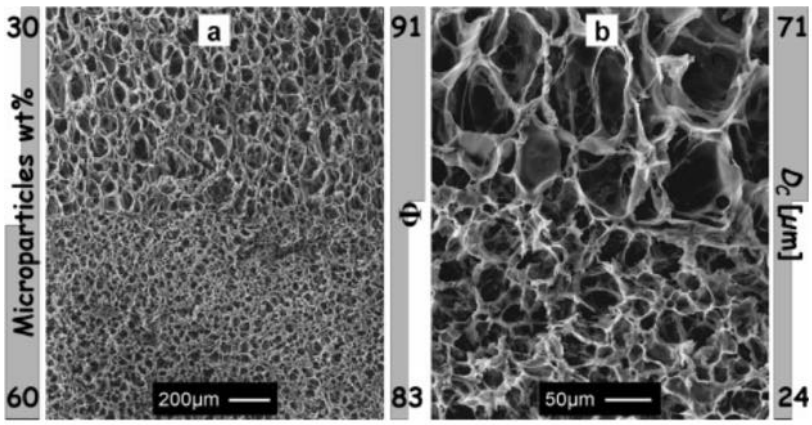

Fig. 3.4 *micrographs of PCL foams; a) 100X, b) 500X, from Salerno et al. (2008)*

by spraying deionized water into liquid nitrogen using a sprayer. In this way ice crystals of spherical form with diameters of 150-250, 250-355, 355-425, 425-500 μm were obtained. The four scaffolds are then stacked in a silicon structure, with particulates size growing from the bottom to the top (fig. 3.5). The whole set was frozen at the temperature of -80°C for 6 hours and then lyophilized to remove the ice. At the end of the process the scaffold shows a good pores interconnection, a porosity of 98.8% in all regions and a pore size gradient along the scaffold (Zhang et al., 2013).

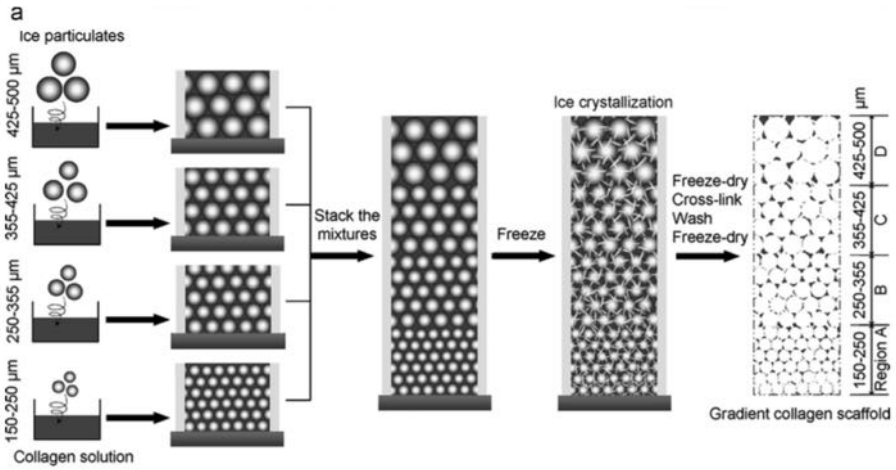

Fig. 3.5 *The preparation scheme for gradient collagen scaffolds, from Zhang et al. (2013)*

The 3D plotting technique allows to sketch the scaffold design. The material studied in this work was a blend of corn starch with PCL previously optimised for use in 3D scaffolds produced by 3D plotting and injection molding for tissue engineering applications. SPCL granules were milled in an ultra-centrifugal mill with liquid nitrogen. Alternating layers were

oriented at 90^o to each other fig. 3.6. The scaffolds were fabricated as 5 x 5 x 5mm cubes. Via this technique different kind of scaffolds were fabricated by varying the spacing between the layer (Sobral et al., 2011).

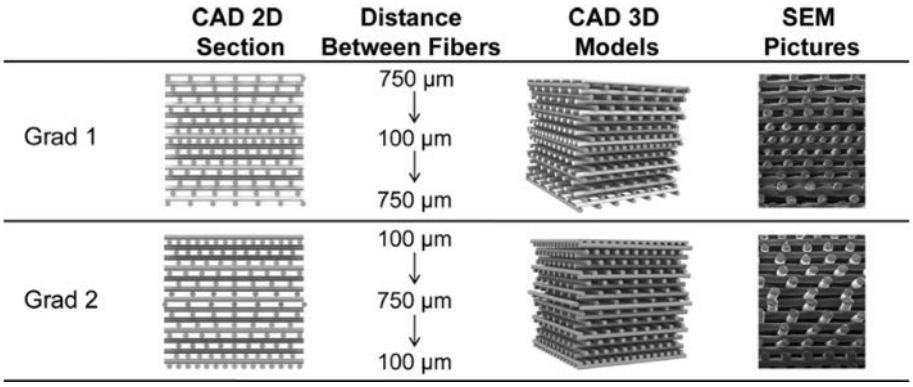

Fig. 3.6 *CAD 2D sections, pore size along the scaffolds and 3D models pore size gradient scaffolds, from Sobral et al. (2011)*

3.1 Experimental apparatus

In order to obtain a gradient of pore dimension along scaffold thickness, an experimental apparatus able to impose a different T vs time pathway on two sides of a sample was designed and set up. Previous studies about TIPS process have highlighted that, when a nucleation-and-growth mechanism occurs, the pore dimension is mainly dependent on the thermal history (Mannella et al., 2014). Thus, by varying the residence time in the metastable region, it is possible to control the pore sizes. The peculiarity of this instrumentation is the possibility to control simultaneously temperature and cooling rate. The experimental apparatus consists in: two heat sinks, two Peltier cells in which the sample is located and four thermocouples to control the temperature of heat sinks and Peltier cells. The sample holder is a bag (35x35 mm surface, 10 mm thickness), a multilayer package, polycarbonate in the inner surface and polyethylene in the outer surface. All components have been connected to input/output devices and remotely controlled via personal computer (PC). The software was been realised in LabVIEW, a system-design platform and development environment, by National Instruments. Below a schematic diagram of the experimental instrumentation is shown, figure 3.7.

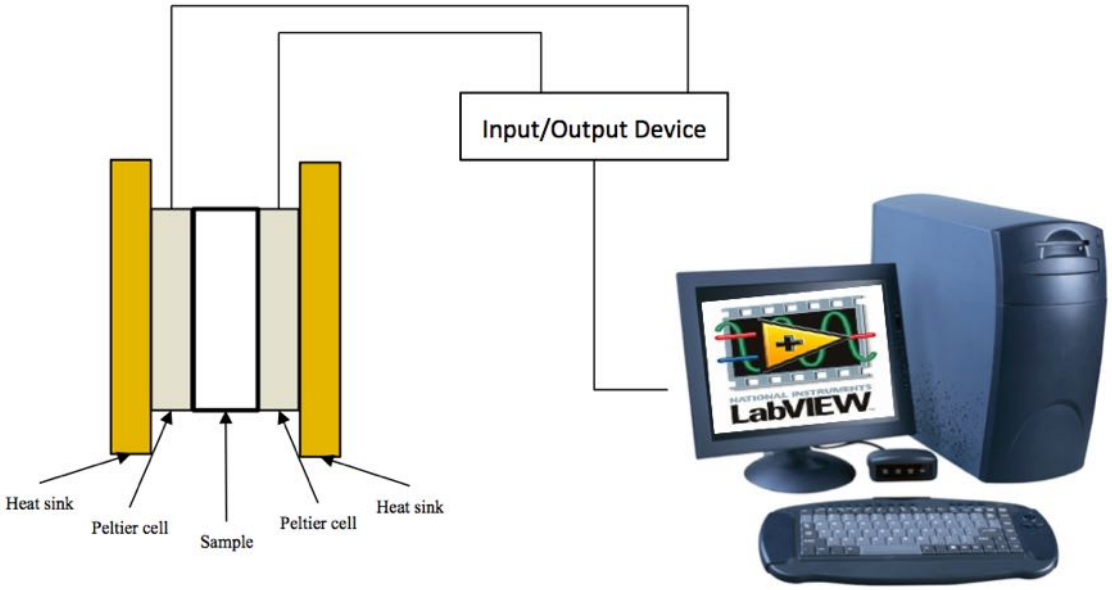

Fig. 3.7 *Experimental apparatus*

3.1.1 Circuit diagram

The experimental apparatus is connected to a PC via a NI-6210 (National Instruments) for the analog input/output and an Arduino-Uno for the digital input/output. In figure 3.8 the connection of analog input (AI) channels was reported. Four thermocouples (TC) were connected to a signal amplifier to reduce the background noise and then to four AI channels in nonreferenced single-ended (NRSE) mode. A thermistor, needful as reference, is connected to a +5V voltage source and the corresponding ground, DG; 100 Ω resistance and a zener diode were adopted to reduce the signal noise and for the sake of protection, respectively.
Four digital channels were employer to control the Peltier cells via Arduino UNO board. Two channels (P1-P2) were used for H bridge to control the direction of the current across the Peltier cells. These letters are controlled via pulse width modulation (PWM) controller (CTR1-CTR0) to tune the duty cycle. All channels were connected to a DG. Scheme 3.9 reports the digital input channels.

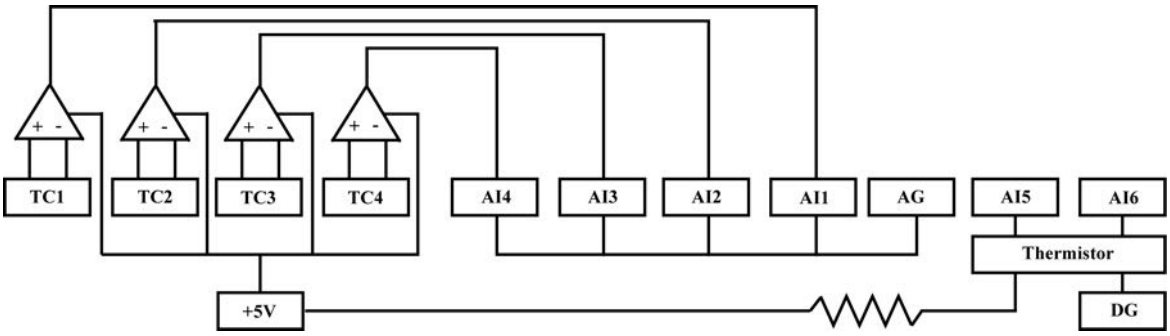

Fig. 3.8 *Circuit scheme of the analog input channels*

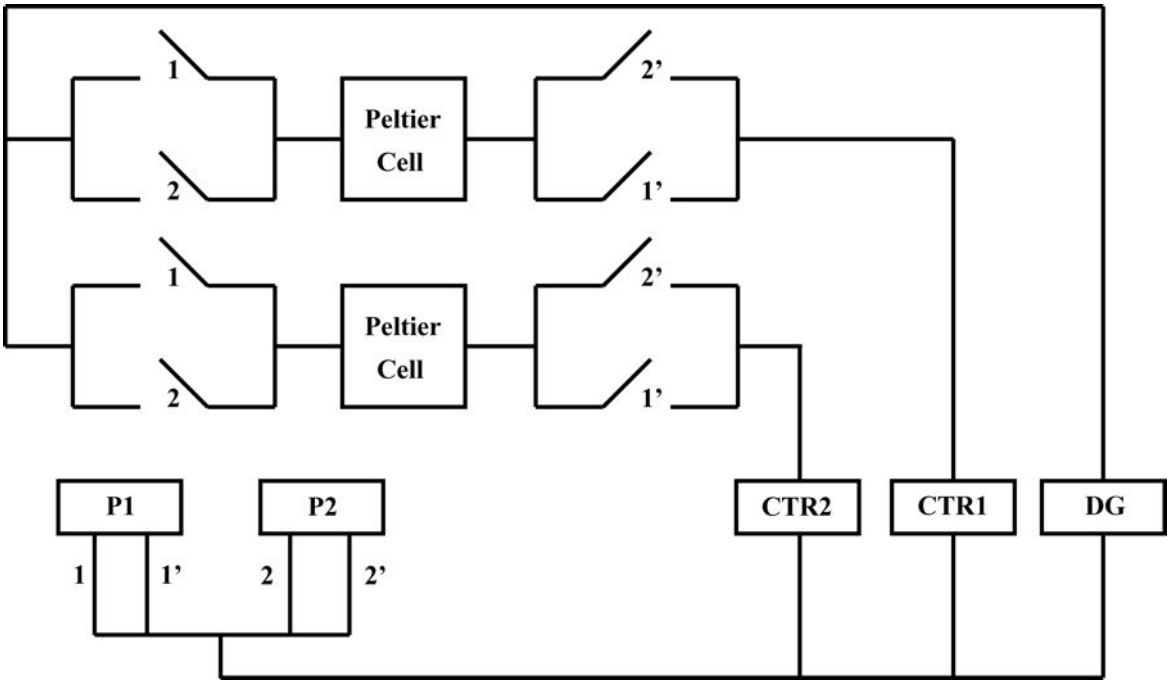

Fig. 3.9 *Circuit scheme of the analog input channels*

3.1.2 Peltier cell

Peltier cells (or Thermoelectric Module, TEM) are thermoelectric devices based on a principle known as Peltier-Seebeck effect, which describes the reversible conversion of thermal energy into electrical energy or viceversa (Drebushchak, 2008). When a voltage is supplied through the material a temperature difference between the faces of the Peltier is produced; a temperature difference between the two faces causes a voltage across the terminals (Hermes and Barbosa, 2012).

The Peltier-Seebeck effect is due to the charge carriers drift, electrons or holes depending on semiconductor, caused by a variation of electric potential inside the module. Electrons

are the charge carriers for n-type semiconductor, holes for p-type semiconductor (fig. 3.11) (Zhang et al., 2010).

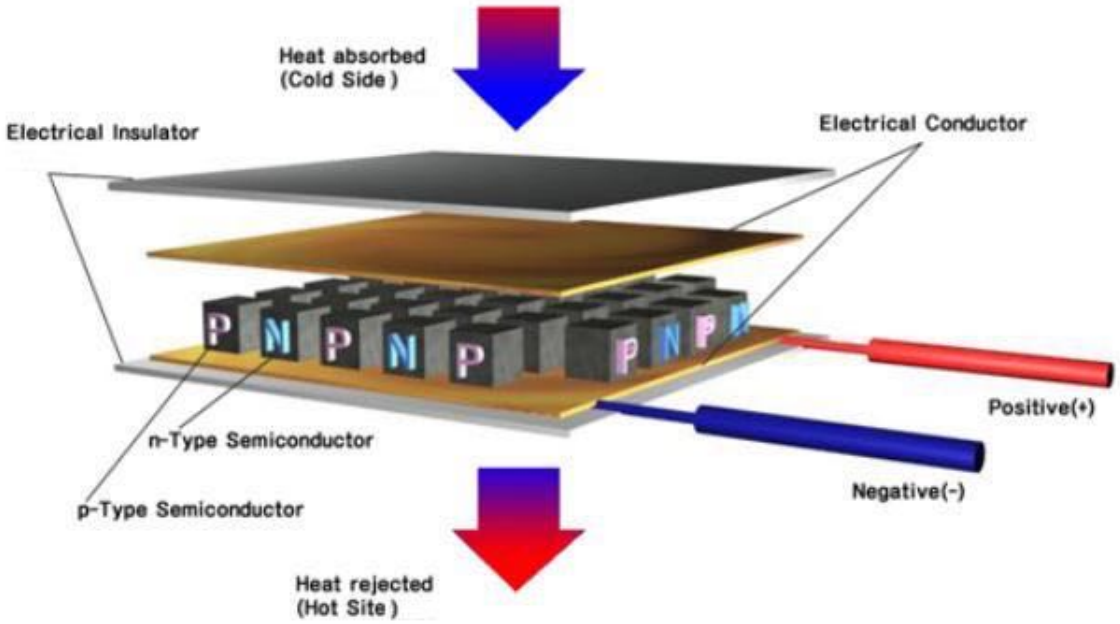

Fig. 3.10 *Schematic structure of Peltier Cell*

Heating a peltier cell face produces an increase of kinetic energy of the charge carriers, then these latter flow towards the lower temperature face, according to energy gradient (Chakraborty and Kim Choon, 2006). The migration will continue until the amount of charge will be sufficient to produce an electrical potential to oppose the Seebeck-Peltier effect. (Huang and Duang, 2000). The Seebeck voltage is the result of the application of a temperature difference, it is defined as

$$S = \frac{V}{\Delta T} \tag{3.1.1}$$

where S is the Seebeck coefficient, V is the voltage and ΔT the temperature difference. However the Seebeck coefficient is on the order of microvolts per kelvin degree, even for the best thermoelectric materials. For this reason, to increase the generated voltage, a large number of elements (even more than 100) are connected in series from an electrical point of view but in parallel from an thermal point of view. Figure 3.10 shows the internal structure of a Peltier cell.

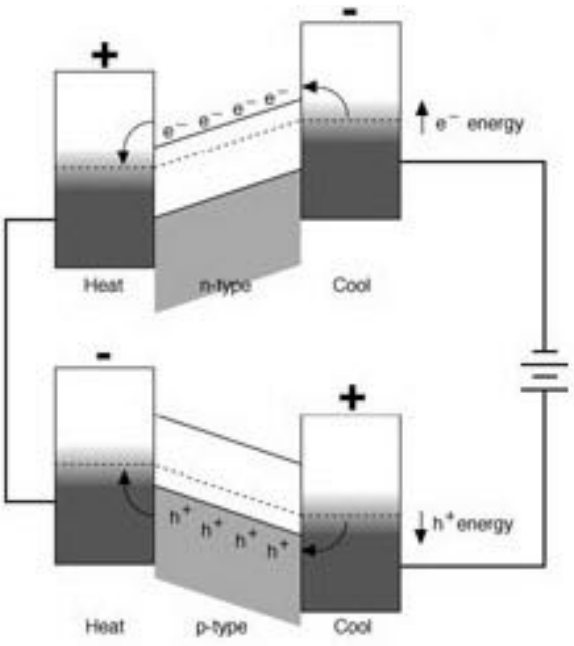

Fig. 3.11 *Band of Peltier effect*

The Seebeck coefficient is around 10-60 μV/K, for metals or alloys employed in the thermocouples, while this value is much higher for semiconductors (Casano and Piva, 2011). The Peltier effect is opposite of the Seebeck effect, applying a potential difference it is possible to provide or subtract heat between the two sides of the Peltier. Electrical current (I) and the heat flux (Q) are linked by the Peltier coefficient (Π)

$$Q = \Pi I \tag{3.1.2}$$

Peltier and Seebeck coefficient are in a direct relationship by the absolute temperature (Pérez-Aparicio et al., 2012), in fact

$$\Pi = S\Delta T \tag{3.1.3}$$

Peltier faces are in ceramic material with a high thermal conductivity but a low electrical conductivity. In this way they allow an easy heat transport avoiding energy losses. To achieve the maximum efficiency, the thermoelectric material must minimize the heat loss and maximize the current. The thermoelectric figure of merit, Z, measures the effective electrical transport capacity compared with the thermal transport capacity. Z is defined as:

$$Z = \frac{S^2\sigma}{k} \tag{3.1.4}$$

where σ is the electrical conductivity, S the Seebeck coefficient and k the thermal conductivity, indicates the thermodynamic efficiency. High Z values indicate great efficiency of the Peltier Cell. It can be observed that a low thermal conductivity is necessary for high efficiency.
The electrical conductivity defines the internal resistance of a TEM and consequently the heat generated by Joule effect, while the thermal conductivity represent the ability to conduct heat. For metallic systems k and σ are linked by the Wiedemann-Franz's law

$$\frac{k}{\sigma} = LT \tag{3.1.5}$$

where L is Lorenz's number $2.45x10^{-8}W\Omega/K^2$ and T the absolute temperature.
The Peltier cell efficiency is given by

$$\eta = \frac{Q_{el}}{Q_h} \tag{3.1.6}$$

Q_{el} is the released electrical power while Q_h is the input electrical power. The heat transferred through the module is given by the Fourier's first law

$$Z = \frac{kA}{t}\Delta T \tag{3.1.7}$$

with A and t, respectively, TEM surface and thickness.
$Q_{el} = \frac{V^2}{R}$ is the electrical power generated and R is the global electrical resistivity which includes external and internal resistance. The resistance can be measured directly, while the thermal conductivity should be measured indirectly by determining the heat transferred through the cell (Mitrani et al., 2003).
An ideal thermoelectric device should have infinite electrical conductivity and zero thermal conductivity. In absence of losses the total heat flux can be written as:

$$Q = IS\Delta T \tag{3.1.8}$$

because $Q = \Pi I$ and $\Pi = S\Delta T$. Thus, in an ideal case (Carnot's efficiency) the thermoelectric efficiency (η) can be rewritten as $\eta = \frac{S\Delta T}{\Pi}$ or $\eta = \frac{\Delta T}{T_h}$. This equation can be considered as a verification of second law of thermodynamics if Peltier and Seebeck coefficient were calculate independently each other.
The performance of a real thermoelectric device depends, however, on the figure of merit and the temperature at the two cell sides. Using crystalline mixtures, substitutional point defects and radiation damage, reduce the semiconductor thermal conductivity. Currently the most efficient materials for the construction of Peltier cells are Bismuth telluride (Bi_2Te_3) and lead

telluride (PbTe) p-type and n-type doped, respectively. The efficiency of a real thermoelectric generator can be lower than the Carnot's efficiency.
Considering the aforementioned contributions the heat flux globally removed from the cold side and transferred to the hot side of the TEM and viceversa are respectively:

$$Q_c = \Pi_c I - \frac{1}{2} I^2 R - K\Delta T \tag{3.1.9}$$

$$Q_h = \Pi_h I - \frac{1}{2} I^2 R - K\Delta T \tag{3.1.10}$$

The first terms, $\Pi_c I$ and $\Pi_h I$, are peltier cooling and heating term. The second term, $\frac{1}{2} I^2 R$, represents the Joule heating effect associated the passage of an electric current through a resistance. The Joule heat is distributed throughout the element, so 1/2 the heat goes towards the cold side, and 1/2 the heat goes towards the hot side. The last term, $K\Delta T$, represents the Fourier effect, transferring heat from regions of higher temperature to regions of lower temperature. So, the peltier cooling term is reduced by the losses associated with electrical resistance and thermal conductance. An example of electric current versus temperature difference is shown in figure 3.12.
From the energy conservation, the electrical power output of a thermoelectric module is expressed as:

$$P = Q_h - Q_c = SI(T_h - T_c) + I^2 R \tag{3.1.11}$$

The coefficient of performance (COP) is one of the main parameters to estimate a Peltier cell efficiency. COP is the ratio of heating or cooling provided to work required.

$$COP = \frac{Q_c}{P} = \frac{\Pi_h I - \frac{1}{2} I^2 R - K\Delta T}{SI\Delta T + I^2 R} \tag{3.1.12}$$

The coefficient depends both on current and temperature difference. Usually the Seebeck coefficient is negligible, this one will be relevant only for very low current (Huang et al., 2000). If $I^2 R << SI\Delta T$ and $\Delta T = 0$ the Carnot's efficiency will be reached.
By considering the maximum performance of a module it is possible to obtain the internal parameters of a TEM . ΔT_{max} is the largest temperature differential that can be obtained between the hot and cold plates for a specific T_h. I_{max} is the input current which will produce the maximum possible ΔT across the TEM. V_{max} is the voltage that will deliver the maximum possible ΔT at the supplied I_{max}. Q_{max} is the maximum heat absorbed when

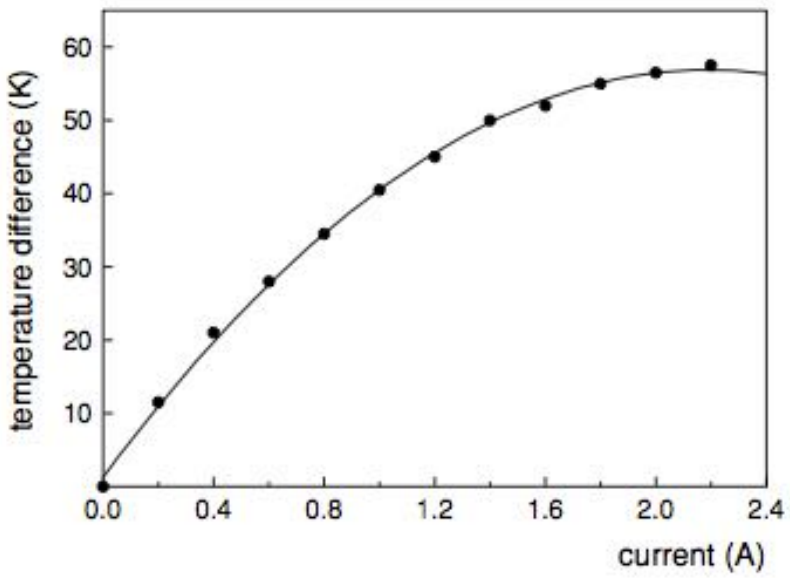

Fig. 3.12 *The temperature difference versus the electric current*

$\Delta T = 0$. Adopting the figure of merit Z is possible writing the relations as:

$$\Delta T_{max} = T_h + \frac{1 - \sqrt{1 + 2T_h Z}}{Z} \tag{3.1.13}$$

$$I_{max} = \frac{(\sqrt{1 + 2T_h Z} - 1)k}{S} \tag{3.1.14}$$

$$Q_{max} = \frac{(\sqrt{1 + 2T_h Z}(\sqrt{1 + 2T_h Z} - 1)^2)k}{2Z} \tag{3.1.15}$$

Then k (thermal conductivity), R (electrical conductivity) and S (Seebeck coefficient) are calculated from 3.1.4

$$k = \frac{I_{max} V_{max} (T_h - \Delta T_{max})}{\Delta T_{max} 2T_h} \tag{3.1.16}$$

$$\sigma = \frac{I_{max} T_h}{V_{max} (T_h - \Delta T_{max})} \tag{3.1.17}$$

$$S = \frac{V_{max}}{T_h} \tag{3.1.18}$$

The aforementioned values can be regarded as constant, though increasing T_h, Seebeck coefficient and electrical resistance increase while thermal conductivity decreases. Assuming constant the hot side temperature, the temperature difference can be written as:

$$\Delta T = T_h - T_c = \frac{SIT_h - \frac{1}{2}I^2R}{SI + k} \tag{3.1.19}$$

The difference of temperature can be expressed also as a function of the duty cycle (ψ). This latter is generally defined as percentage of one period during which a component, device, or system is active. In the adopted experimental apparatus the Peltier cells are controlled by means of the duty cycle. In this case the duty cycle is described as ratio between the supplied current (I) and the maximum deliverable current $I_m = 5A$. The duty cycle have a range from 0 and 1, $\psi = 0 \Rightarrow I = 0$, $\psi = 1 \Rightarrow I = I_m$.
The temperature difference can be written as a function of duty cycle as

$$\Delta T = \psi S T_h - \frac{\frac{1}{2}\psi^2 I_m R}{\psi S + \frac{k}{I_m}} \tag{3.1.20}$$

In figures 3.13 and 3.14 is shown the temperature difference versus duty cycle in cooling and heating.

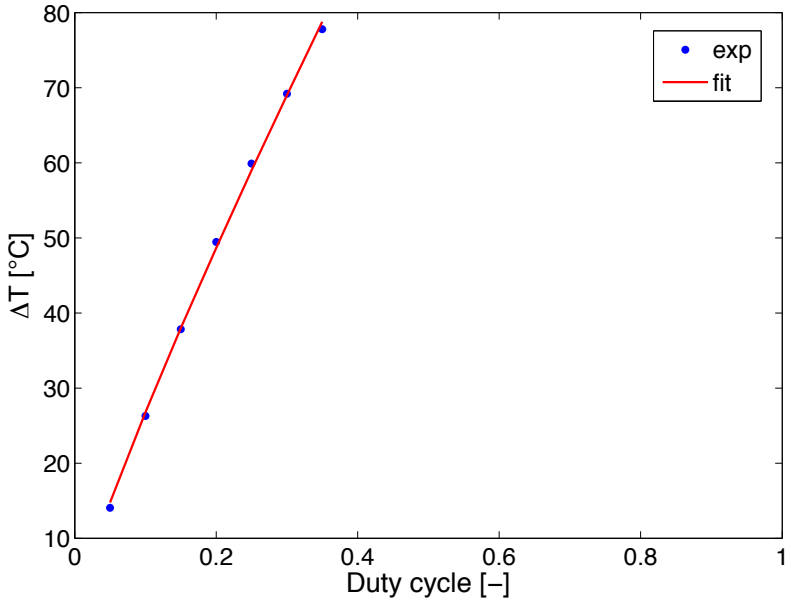

Fig. 3.13 *Heating process: temperature versus duty cycle*

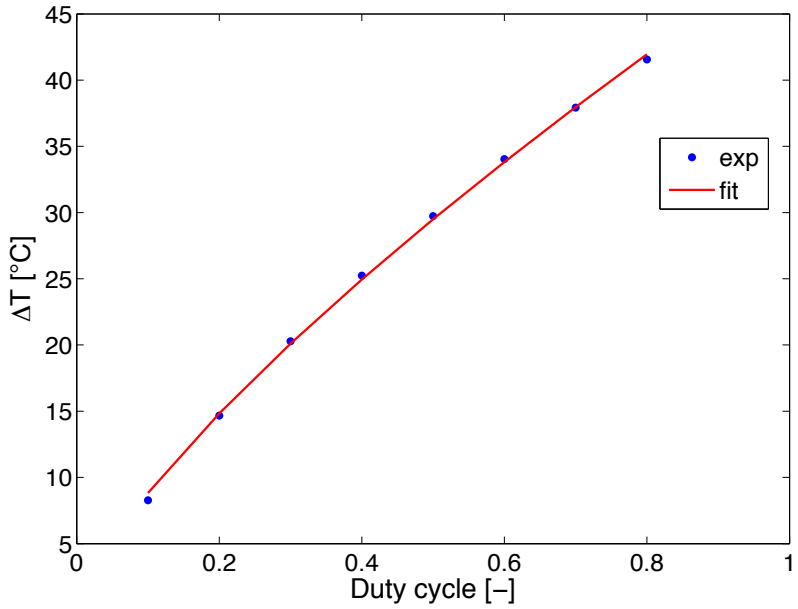

Fig. 3.14 *Cooling process: temperature versus duty cycle*

3.1.3 Dynamics and control

The Peltier Cells can be considered as first order transfer function

$$G_p(s) = \frac{Kp}{\tau_p s + 1} \tag{3.1.21}$$

where K_p and τ_p are process gain and constant time, respectively. Generally a transfer Function is the ratio of the output to the input of a system in the Laplace domain considering its initial conditions and equilibrium point to be zero. In this case the output is the difference temperature between the hot and cold side, while the input is the duty cycle. Thus the relation between output and input can be rewritten as

$$G_p = \frac{\Delta T}{\psi} \tag{3.1.22}$$

Identifying with an overline the steady state value, the gain and the constant time of the system are obtainable by

$$K_p = \frac{\overline{\Delta T}}{\overline{\psi}} \tag{3.1.23}$$

$$\Delta T(t) = \Delta T_0 \, e^{-\frac{t}{\tau_p}} \tag{3.1.24}$$

K_p and τ_p are values tentatively acquired, depending by the complete system (heat sink, Peltier Cell, sample holder, etc.). In fig. 3.15a, 3.16a and 3.15b, 3.16b are shown, respectively, the system response for a step input of duty cycle 0.1 and 0.3. The graphs show, at constant duty cycle, the temperature difference obtained in heating process is significantly higher that in cooling process. As example, at $\psi = 0.3 \Rightarrow \Delta T = 70°C$, while in cooling process $\psi = 0.3 \Rightarrow \Delta T = 22°C$. This behavior is caused by Joule effect, which creates a heat generation to the current passage, regardless of the direction. This one involves a summative term in heating, but a subtractive term in cooling.

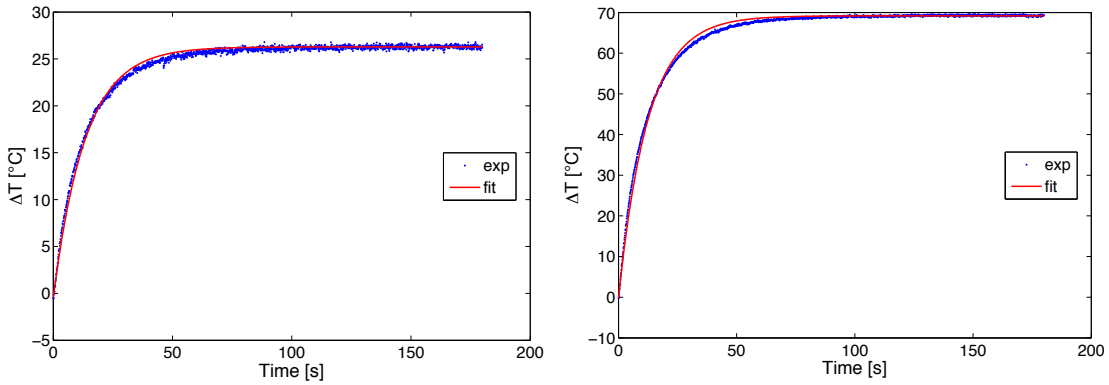

(a) *Step input duty cycle 0.1* (b) *Step input duty cycle 0.3*

Fig. 3.15 *System dynamic behaviour for a duty cycle step input in heating process*

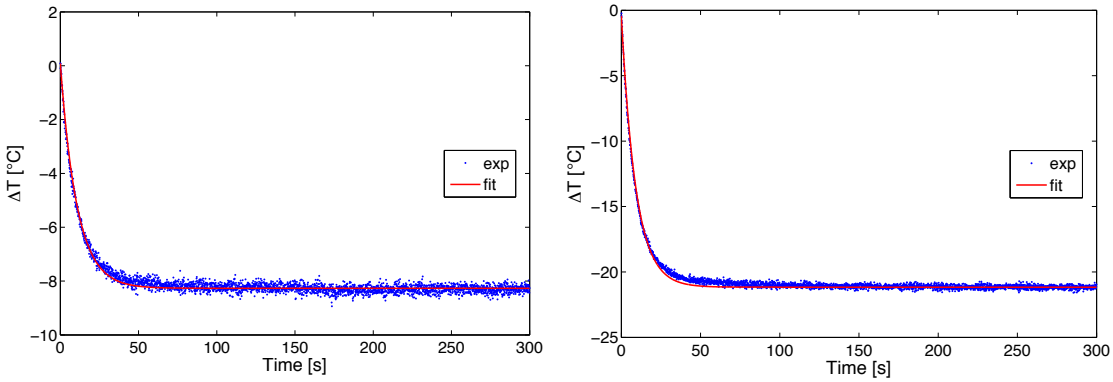

(a) *Step input duty cycle 0.1* (b) *Step input duty cycle 0.3*

Fig. 3.16 *System dynamic behaviour for a duty cycle step input in cooling process*

To realize the control system the characteristic values of Peltier cells in heating and cooling were calculated by means of a step input. Simulink software, a graphical environment

for multidomain simulation, fully integrated in Matlab, was adopted to simulate the system response of the system. In fig. 3.17 is shown the closed-loop block diagram.

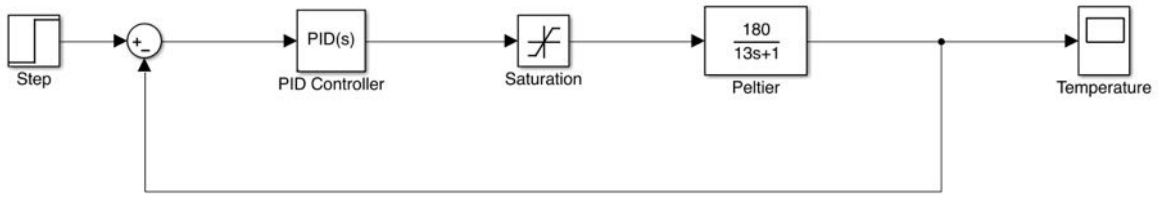

Fig. 3.17 *Closed-loop block diagram in negative feedback*

A negative feedback control loop was used, figure 3.17. Negative feedback is the most common form of used feedback control in process, micro-computer and amplifier systems. Negative feedback opposes or subtracts from the input signals providing it many advantages in the design and stabilization of control systems. For example, if the systems output changes for any reason, then negative feedback affects the input in such a way as to counteract the change. Feedback reduces the overall gain of a system with the degree of reduction being related to the systems open-loop gain. Negative feedback has effects of reducing distortion, noise, sensitivity to external changes as well as improving system bandwidth and input and output impedances. Primarily the configuration control has been simulated on Simulink, inserted in the real system and adapted to obtain the best results. The used control algorithm was the following:

$$\psi(i) = \overline{\psi} + P\varepsilon(i) + I\Delta t \sum_{j=1}^{i} \varepsilon(j) + D\frac{N\frac{\varepsilon(i)-\varepsilon(i-1)}{\Delta t}}{\frac{\varepsilon(i)-\varepsilon(i-1)}{\Delta t} + N} \tag{3.1.25}$$

Where P, I, D and N are respectively: proportional, integral, derivative action and filter. For a first estimation of the parameters Ziegler-Nichols method was adopted (Seborg et al., 2010). The Ziegler-Nichols rule is a heuristic PID tuning rule that attempts to produce good values for the three PID gain parameters. Initially turning PID controller into a P controller by setting $I = 0$ and $D = \text{inf}$. Starting from $P = 0$ the proportional gain is manually increased up to reach a sustained oscillations in the signals in the control system. Then via specific table it is possibile obtaining the other parameters.
After the first estimation with the Ziegler-Nichols rule, the autotuning command presents in the latest versions of Simulink was adopted. Finally these parameters were applied in the real system and slightly modify to better matching with system applications. Figure 3.18 represents the experimental and the simulated response of the system for a step input from 15°C to 60°C.

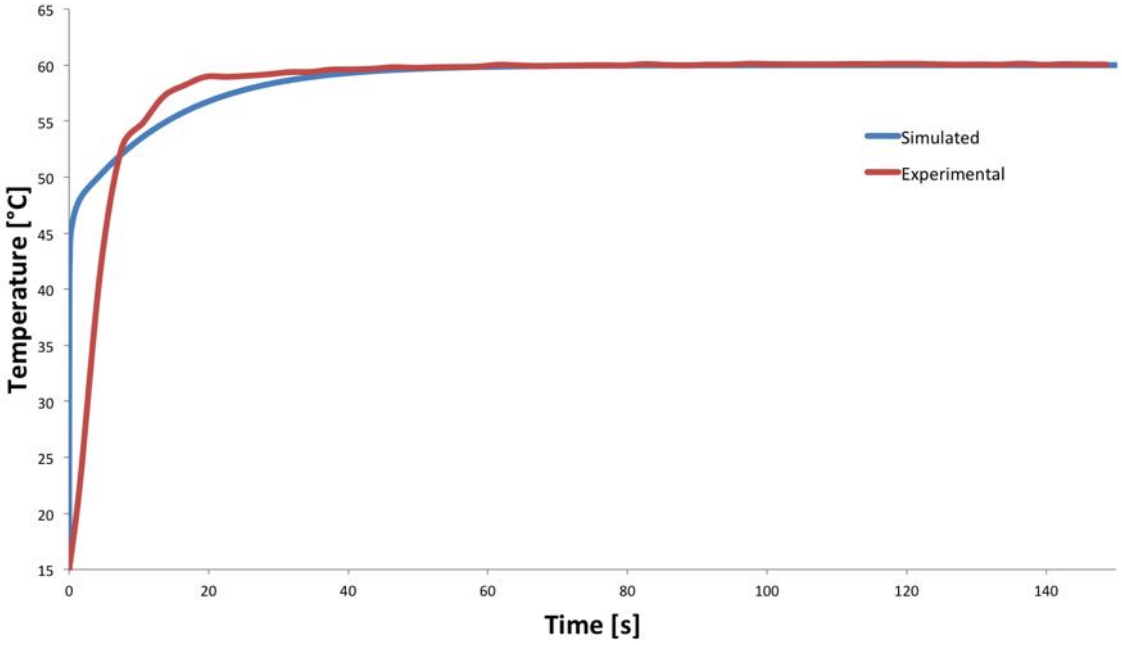

Fig. 3.18 *Experimental and the simulated response of the system for a step input*

3.1.4 Modeling and simulation

To better characterise the examined system a heat transfer analysis was carried out. The study concerns the distribution and evolution of the temperature in the slab. The temperature distribution in the sample is a function $f(x)$, symmetrical with respect of the median plane ($x = 0$) (Bairi et al., 2004). For this 1D transient problem, the second Fourier's equation must be solved:

$$\alpha \bigtriangledown^2 T = \alpha \frac{\partial^2 T}{\partial x^2} = \frac{\partial T}{\partial t} \tag{3.1.26}$$

where $\alpha = \frac{k}{\rho c_p}$ is the thermal diffusivity (W/m^2), k thermal conductivity (W/mK), ρ density (kg/m^3), and c_p the specific heat capacity (J/kgK). Using the outside temperature T_∞ as a reference temperature and inserting the temperature difference defined as:

$$\vartheta(x,t) = T(x,t) - T_\infty \tag{3.1.27}$$

it is possible to re-write the Fourier equation as

$$\alpha \frac{\partial^2 \vartheta}{\partial x^2} = \frac{\partial \vartheta}{\partial t} \tag{3.1.28}$$

The second Fourier equation is a partial differential equation, second order in space and first order in time, then three boundary conditions are necessary (Isachenko et al., 1980).

$$\begin{cases} t = 0 \Rightarrow T(x,0) = T_0 \Rightarrow \vartheta = \vartheta_0 & (3.1.29) \\ x = 0 \Rightarrow \dfrac{\partial \vartheta}{\partial x}|_{x=0} & (3.1.30) \\ x = \delta \Rightarrow -k\dfrac{\partial \vartheta}{\partial x}|_{x=L} = h\vartheta|_{x=L} & (3.1.31) \end{cases}$$

This equation can be solved by means of a separation of the variables. The first one variable time dependent and the second one space dependent, writing

$$\vartheta(x,t) = \phi(t)\psi(x) \tag{3.1.32}$$

Solving for a non-zero solution, the calculation of the successive differentials that appear in 3.1.27 yields

$$\psi(x)\phi'(t) = \psi(x)\frac{d\phi(t)}{dt} = \alpha\frac{d^2\psi(x)}{dx^2}\phi(t) = \phi(t)\psi''(x) \tag{3.1.33}$$

Then the separation of the variables is possible

$$\frac{1}{\alpha}\frac{\phi'(t)}{\phi'(t)} = \frac{\psi''(x)}{\psi(x)} = cost = \lambda^2 \tag{3.1.34}$$

Breaking up the two equations the functions become:

$$\frac{d\phi}{dt} + \lambda^2\alpha\phi = 0 \tag{3.1.35}$$

$$\frac{d^2\psi}{dx^2} + \lambda^2\phi = 0 \tag{3.1.36}$$

whose solutions are respectively

$$\phi = C_1 e^{-\alpha\lambda^2 t} \tag{3.1.37}$$

$$\psi = C_2 sin(\lambda x) + C_3 cos(\lambda x) \tag{3.1.38}$$

from 3.1.32

$$\vartheta(x,t) = C_1 e^{-\alpha\lambda^2 t} C_2 sin(\lambda x) + C_3 cos(\lambda x) \tag{3.1.39}$$

C_1, C_2, C_3 and λ are obtained from boundary conditions. The final solution is

$$\vartheta = \vartheta_0 \sum_{n=1}^{\infty} \frac{2sin(\mu_n)}{\mu_n + sen\mu_n cos\mu_n} cos(\mu_n \frac{x}{L}) e^{-\mu_n^2 \frac{\alpha t}{L^2}} \tag{3.1.40}$$

The parameter $\mu_n|_{n\in N}$ is a function of the Biot number, $Bi = \frac{hL}{k}$, with h convective heat transfer coefficient, L characteristic length of the system and k thermal conductivity.

$$cot\mu_n = \frac{\mu_n}{Bi} \tag{3.1.41}$$

The Biot number is used the characterise the heat transfer resistance "inside" a solid body. The Biot number can be considered as the ratio of internal diffusion resistance, L/k, to external convection resistance, $1/h$. $Bi \to \infty$ means that there is no temperature difference between wall and outside temperature, a distributed parameter system. $Bi \to 0$ the heat flow is much faster inside the body than outside, a lumped parameter system can be adopted. In the case of distributed parameter problem the Fourier number $Fo = \frac{\alpha t}{L^2}$ occurs. This latter represents a dimensionless time predicting of the temperature response of materials undergoing transient conductive heating or cooling In figure 3.19 the internal thermal profile in a slab are represented. By increasing the Fourier number the internal profiles change function of distributed or lumped parameter system (Bird et al., 2006).

To evaluate the temperature variation within the sample a simulation software COMSOL Multiphysics was used. It is a software that performs a Finite Element Analysis (FEA). The FEA is a numerical technique designed to calculate approximate solutions to problems described by partial differential equations, reducing the latter to an algebraic equations system.
The system was considered as three-dimensional and one-dimensional problem. Three-dimensional system to evaluate the overall temperature distribution inside the sample, one-dimensional system to simplify the computational burden by taking advantage from the symmetry of the system.
The modules of COMSOL adopted to carry out the simulation were "heat transfer in fluids" and "phase change". The dimensions of the model match with the dimension of the real system: 1 cm width, 3 cm depth, 3.5 cm height. Figure 3.20 shows the adopted geometry. The thermal history was applied on side 1 and 2. The others side was simulated as external

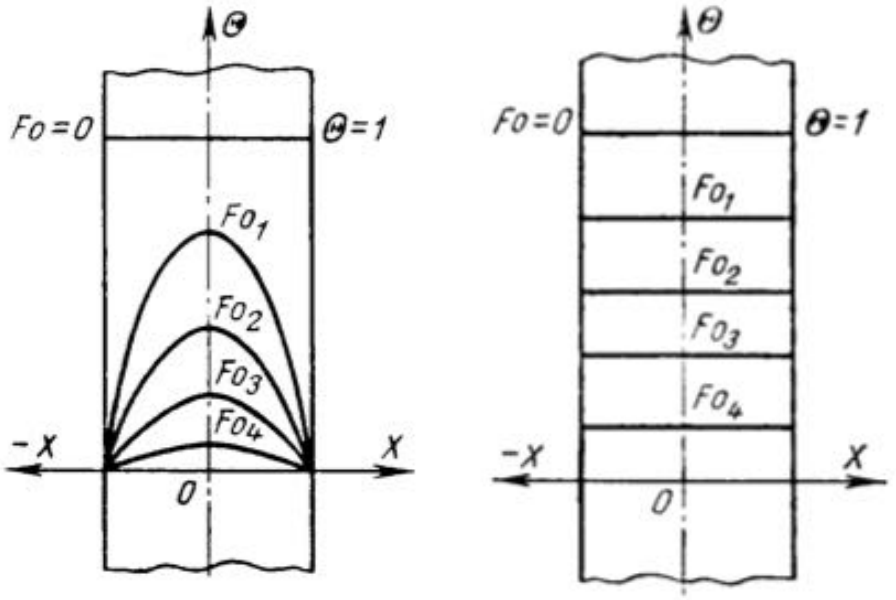

(a) $Bi \to \infty$ (b) $Bi \to 0$

Fig. 3.19 *Internal temperature profile in a slab, by varying the Fourier number*

Propriety	Liquid	Solid
Heat Capacity at constant pressure $[J/kgK]$	2004	2052
Density $[Kg/m^3]$	1002	918
Thermal conductivity $[W/mk]$	0.218	2.31
Latent heat fusion $[J/kg]$	170000	
Melting point $[K]$	274.7	

Table 3.1 *Thermal proprieties of the model*

natural convection to better replicate the physic of the system. Sides 3 and 4 as vertical well, side 5 "horizontal well downside" and side 6 "horizontal well upside". The outside fluid is air at temperature of 20°C. The system simulated was a solution dioxane/water with 87/13 weight ratio, the same mixture adopted for the scaffold production. In table 3.1 the thermal proprieties adopted in the model was summarized. Two thermal history was reported as example of the system behaviour. The first thermal history is a step input from 60°C to 35°C (fig. 3.21), to simulate the internal temperature profiles inside the fluid region. The second one is a step input from 35°C to -20°C (fig. 3.22), to show the temperature profiles when a phase change occurs.

In both cases the temperature profiles on the external surface and in a "virtual" surface on the center of the samples were reported.

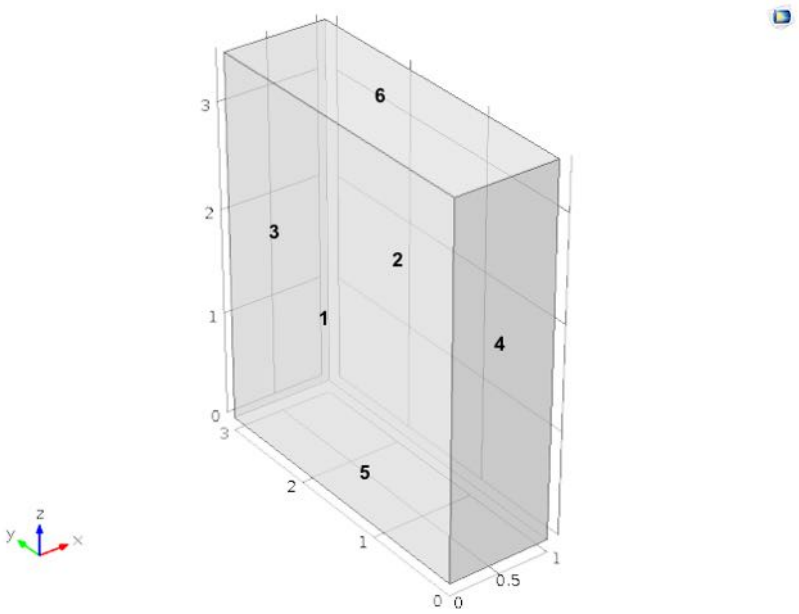

Fig. 3.20 *Geometry in Comsol Multiphysics*

Figure (3.21a), $t = 0s$ all system at 60°C.
Figure (3.21b), $t = 10s$ the temperature span is from 35°C on the side of the slab to 46.2°C on the center part. It is possible to see that almost 500 µm are above 40°C.
Figure (3.21c), $t = 20s$ all system is under 40°C, included the sample center and the parts in contact with the external air.
Figures (3.21d), (3.21e), (3.21f), respectively $t = 30s$, $t = 40s$, $t = 60s$. From $t = 30s$ the temperature range between the set point (temperature on edges 1-2) and the highest temperature in the slab is under the 5%. Consequently the process can be defined concluded at $30 = s$.
The phenomenon is completely different when a change phase occurs. It is necessary more time to reach the desiderated temperature and not all slab attains at -20°Cdue to heat exchange with air outside.
Figure (3.22a), $t = 0s$ all system at 35°C.
Figure (3.22b), $t = 180s$, the edges 1-2 reach very quickly the set point, while the freezing process concerns the major part of the system. After 3 minutes only 2 millimetres are under 2°C.
Figure (3.22c), $t = 360s$, the freezing process proceeds towards the center of the slab. The maximum temperature difference around 2°C, while over half part of piece is solidified.
Figures (3.22d), (3.22e), (3.22f), respectively $t = 540s$, $t = 720s$, $t = 1200s$. From $t = 540s$ all sample is frozen. The system rapidly reach the stationary state until $t = 1200s$ when

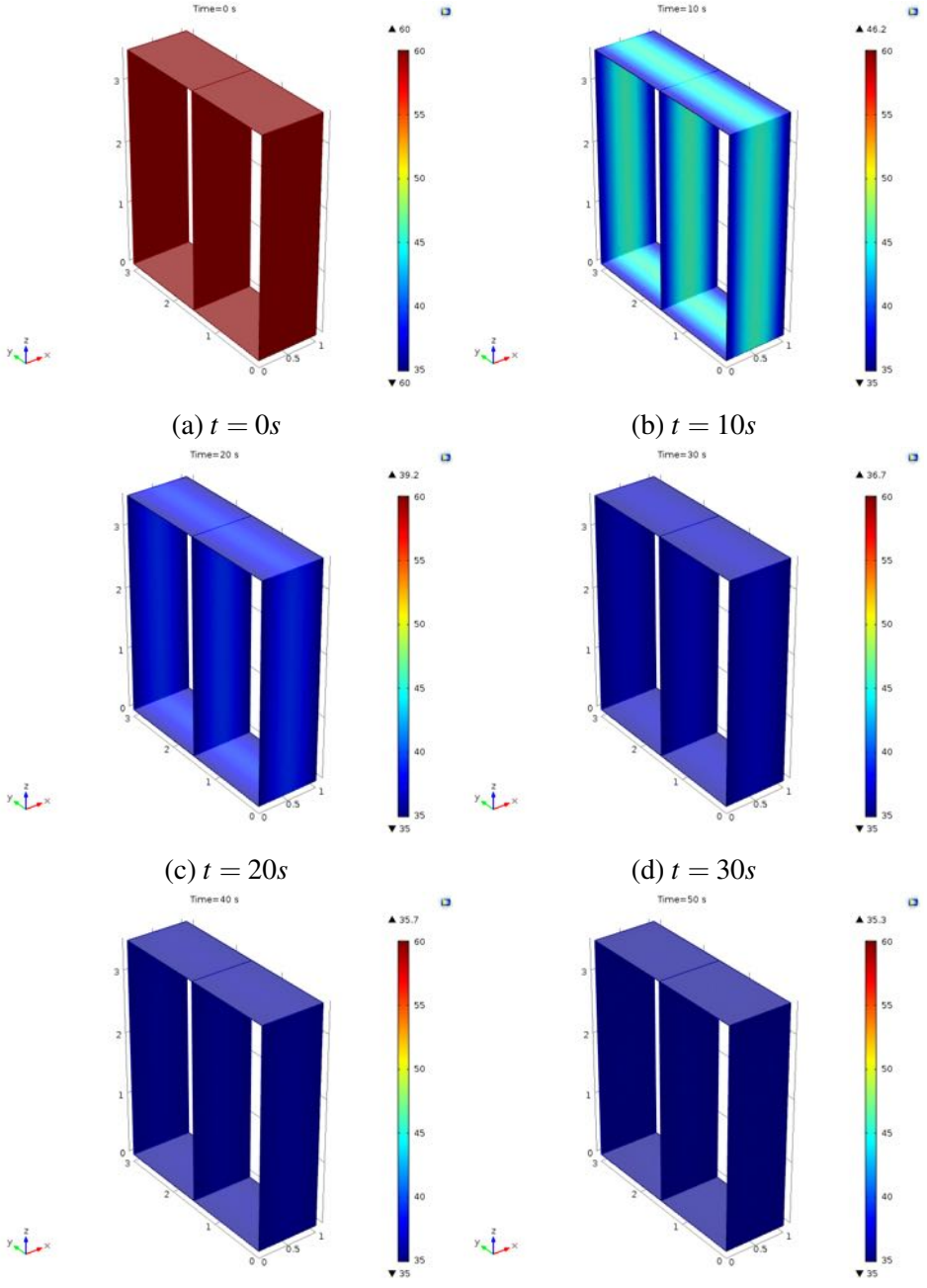

(a) $t = 0s$ (b) $t = 10s$

(c) $t = 20s$ (d) $t = 30s$

(e) $t = 40s$ (f) $t = 60s$

Fig. 3.21 *Internal temperature profiles inside the fluid region*

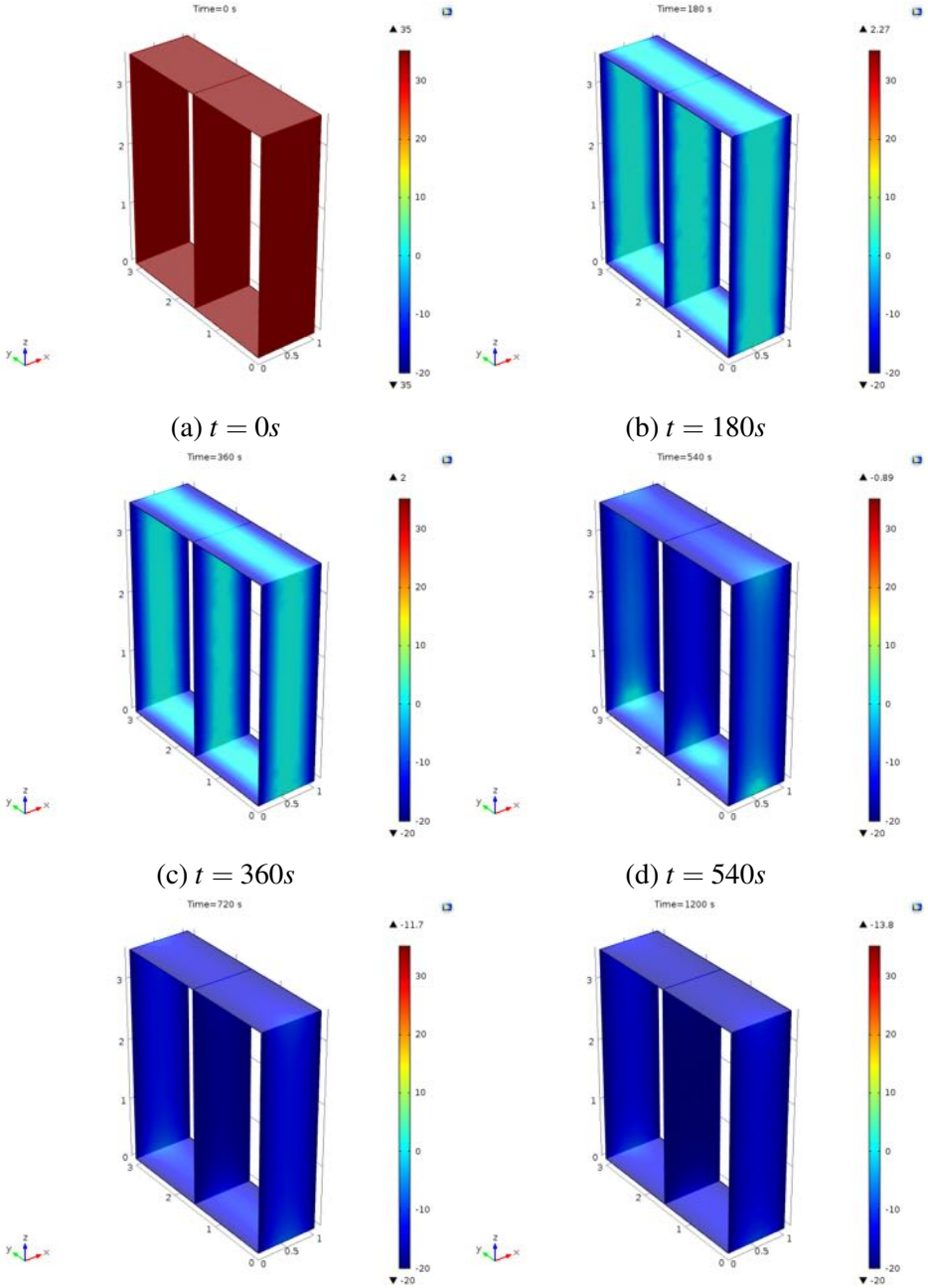

(a) $t = 0s$ (b) $t = 180s$

(c) $t = 360s$ (d) $t = 540s$

(e) $t = 720s$ (f) $t = 1200s$

Fig. 3.22 *Internal temperature profiles for a phase change*

the process is completely finished. The main part is at 253K, except the external contours stabilized at almost -14°C.

3.2 Results

The aforementioned experimental apparatus allows the continuous recording of temperature with thermocouples fixed on the heat sinks and on the Peltier cells. The graph allows to display of the real temperatures, and then the thermal history imposed by the two Peltier on two sides of the sample. In figure 3.23 an example of temperature profiles was reported. The blue curve represents the thermal history of face one, called Slow Cooling Side (SCS). The red curve represents the thermal history of face two, called Fast Cooling Side (FCS).
SCS was taken for 10 minutes at 60°C, to ensure the complete solution homogenization. After that the temperature was decreased at 1°C/min, from 60°C to 35°C in 25 minutes. Then the temperature was maintained at 35°C for 20 minutes and suddenly lowered at -20°C, in order to freeze the formed morphology.
The other side after the maintenance at 60°C, the solution was rapidly brought at 35°C for 45 minutes and thus quenched at -20°C simultaneously to the first side of the sample. It is possible to separate a general thermal path in 3 regions or zones.

- I zone: The solution is above the cloud point, 41°Cfor the examined solution. The mixture is usually brought at 60°C to assure the complete homogenization of the solution.

- II zone: Each side was brought inside the metastable region in independent way. The time inside the region and the rate can change in order to obtain the desiderated final morphology. As "rule of thumb" more time and higher temperature mean larger pore size, less time and lower temperature smaller pore size.

- III zone: The solution is rapidly quenched to freeze the obtained scaffold morphology.

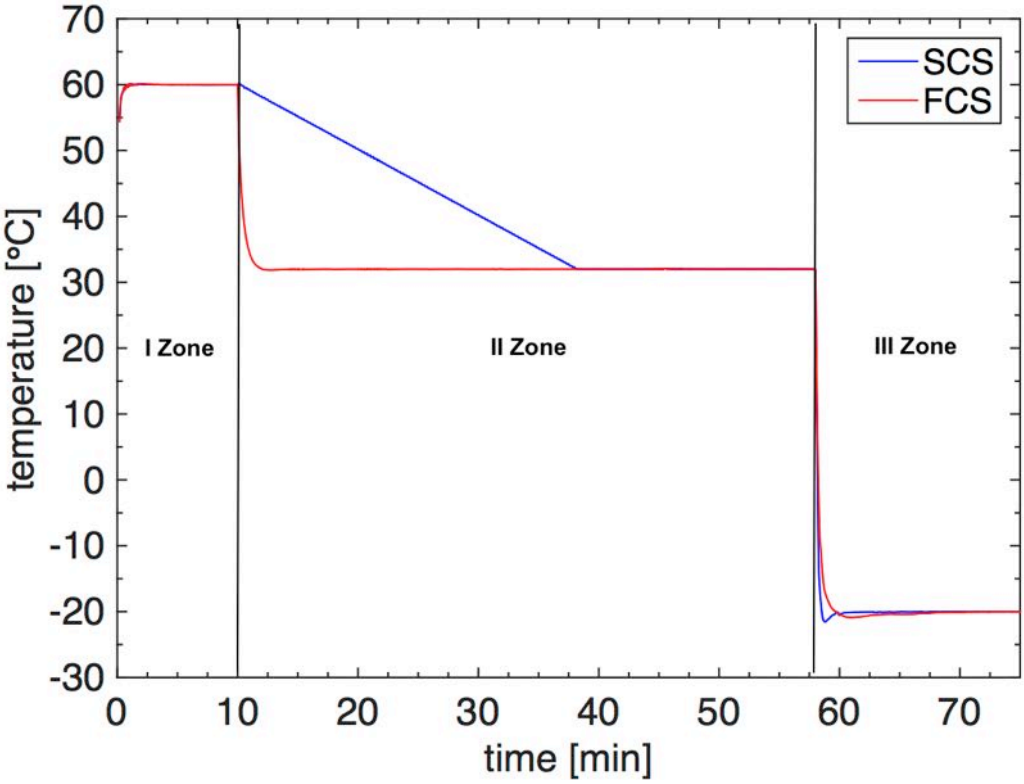

Fig. 3.23 *Example of thermal history. SCS: Slow Cooling Side, FCS: Fast Cooling Side*

Next paragraphs show some examples of different asymmetric scaffolds. For each test the thermal histories applied on two sides of the sample was reported. The foam microstructure was observed via Scanning Electron Microscopy (SEM), by utilising a Philips SEM Quanta 200 F at 10 kV, fractured in liquid nitrogen and gold sputtered. For each SEM micrograph three sections of 1mm length were took into account on FCS (right side), center and SCS (left side). The average pore dimension was determined by counting for at least 50% of pores of each section. In table 3.2 the experimental pattern of gradient pore scaffolds was summarized.

	Thermal History							
	FCS				SCS			
	T_1	dT/dt	T_2	t_2	T_1	dT/dt	T_2	t_2
35-45/35-20	60°C	25°C/min	35°C	45min	60°C	1°C/min	35°C	20min
32-48/32-20	60°C	25°C/min	32°C	48min	60°C	1°C/min	32°C	20min
30-50/30-20	60°C	25°C/min	30°C	50min	60°C	1°C/min	30°C	20min
30-45/30-20	60°C	25°C/min	30°C	45min	60°C	1.2°C/min	30°C	20min
25-45/25-20	60°C	25°C/min	25°C	45min	60°C	1.4°C/min	25°C	20min

Table 3.2 *Experimental pattern of gradient pore scaffolds*

3.2.1 35-45/35-20

Figure 3.24 reports the adopted thermal history for this test. After at the homogenization at 60°C, the FCS was suddenly brought at 35°Cwhile the temperature of SCS was gradually decreased at 1°C/min. The FCS was maintained at 35°C for 45 minutes while the SCS for 20 minutes, then the two sides were rapidly quenched at -20°C.
Figure 3.25 shows the as-obtained scaffold microstructure. The pore dimensions go from 80 µm on SCS, to 130 µm on the center to 260 µm on FCS. 35°C is on the center of the metastable region for this ternary solution, then higher temperature means higher growth rate in the pore formation process.
In the TIPS process inside the metastable region, the temperature plays a more important role than the permanence time, for this reason the scaffold obtained applying the quoted thermal history reaches the highest pore dimension compared to the other scaffolds.

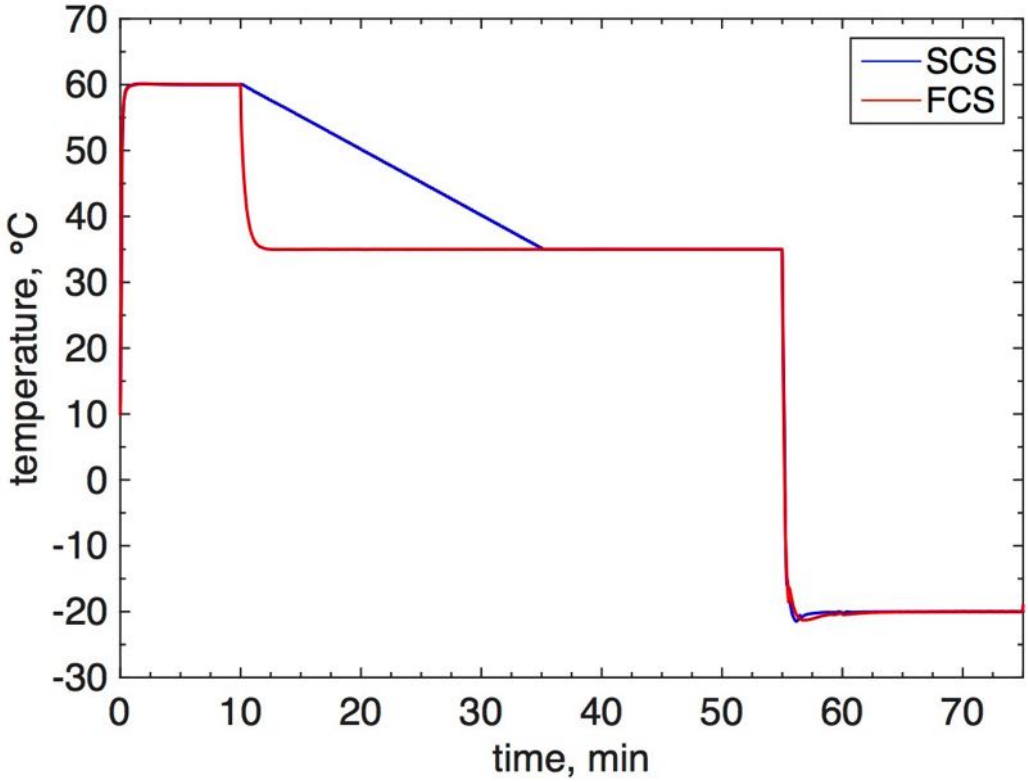

Fig. 3.24 *Thermal history of the test. FCS: from 60°C rapidly to 35°C for 45 minutes and then frozen; SCS: from 60°C to 35°C at 1°C/min, 35°C for 20 minutes and then frozen*

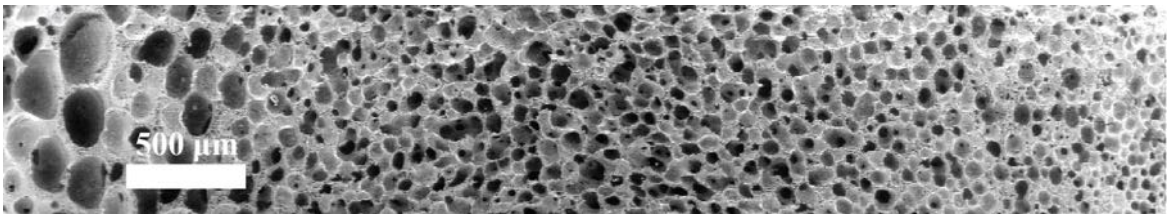

Fig. 3.25 *SEM micrograph of the obtained scaffold. Average pore dimension from 80 µm on SCS, to 130 µm on the center to 260 µm on FCS*

3.2.2 32-48/32-20

Compared to the thermal history of the previous test the same decreasing rate of the temperature was adopted, while the temperature inside the metastable region was set at 32°C. For this reason in order to freeze both side at the same moment the FCS was kept at 32°Cfor 48 minutes (fig. 3.26).

The scaffold morphology showed a linear increasing of pore dimension from 75 µm on SCS,

to 110 µm, 230 µm on the FCS (fig. 3.27). In this case like the following test there are two contrary effects. From one side the increasing of time inside the metastable region (48 minutes) tends to increase the pore dimension, on the other side the diminution of temperature decreases the kinetic of the phenomenon. However, this process is biased towards the kinetics then the pore dimensions on SCS and FCS of the scaffold obtained applying this thermal history are smaller than the pore dimensions with the previous cooling path.

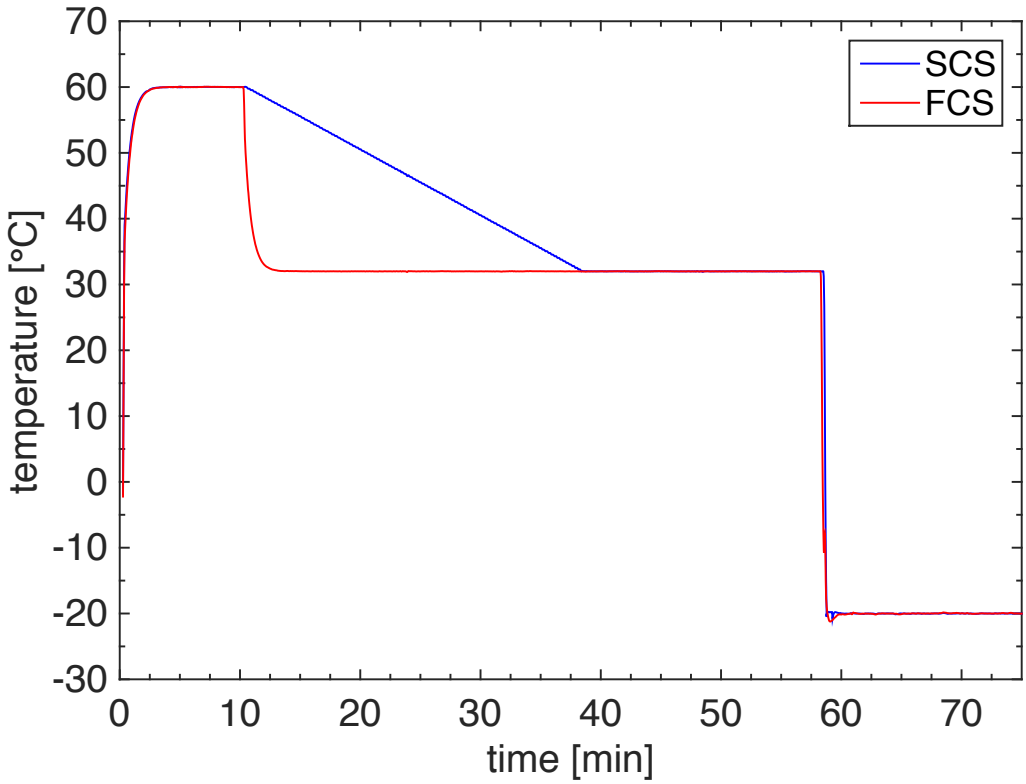

Fig. 3.26 *Thermal history of the test. FCS: from 60°C rapidly to 32°C for 48 minutes and then frozen; SCS: from 60°C to 32°C at 1°C/min, 32°C for 20 minutes and then frozen*

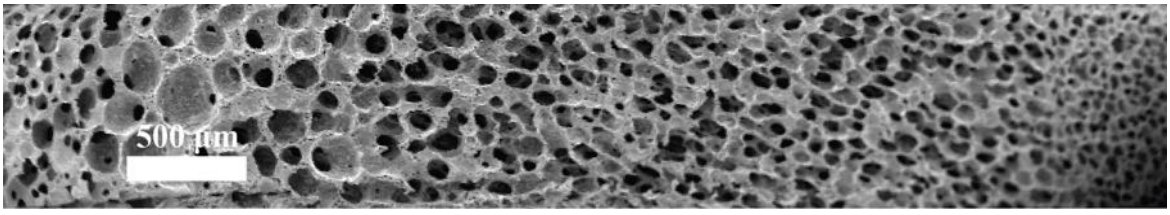

Fig. 3.27 *SEM micrograph of the obtained scaffold. Average pore dimension from 75 µm on SCS, to 110 µm on the center, 230 µm on the FCS*

3.2.3 30-50/30-20

Following the same principle of the previous test, the reference temperature was further decreased up to 30°C. Thus 30°C for 50 minutes on FCS and 20 minutes for SCS (fig. 3.28). Figure 3.29 reports the SEM micrograph of the obtained scaffold. Starting from the right side to the left side the average pore dimensions were: 180 µm, 110 µm, 65 µm, respectively. The same explanation of the previous scaffold can be adopted to describe the so-obtained microstructure. The temperature prevails over the time and a general decreases of pore dimension in all three sectors were found.

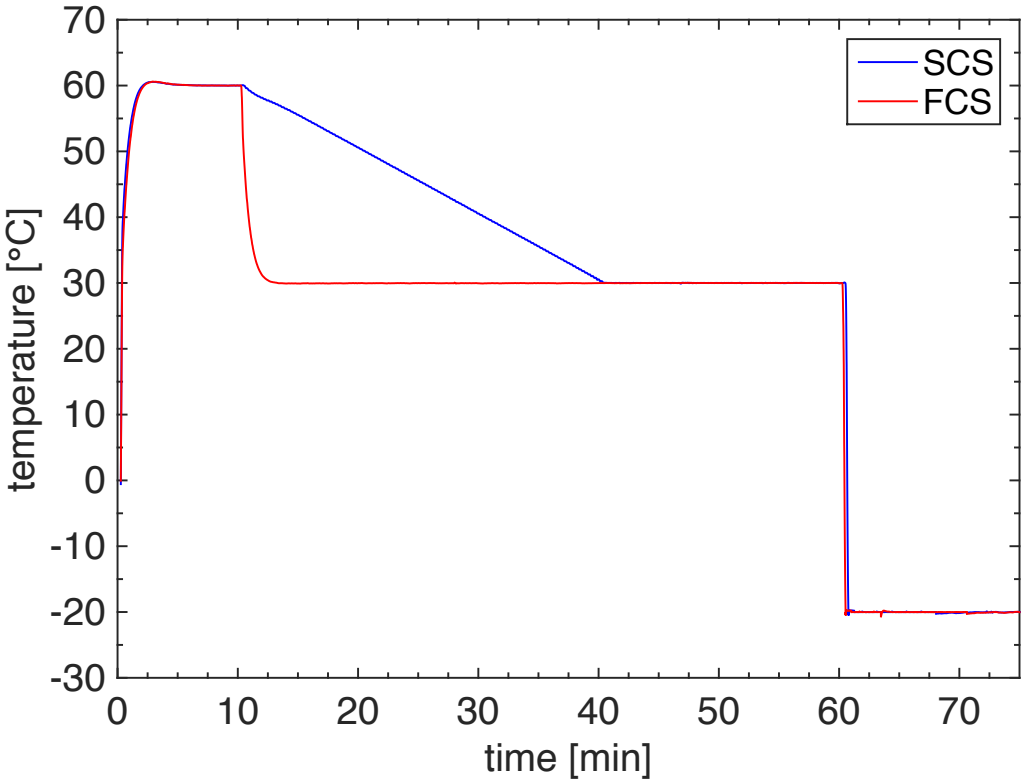

Fig. 3.28 *Thermal history of the test. FCS: from 60°C rapidly to 30°C for 50 minutes and then frozen; SCS: from 60°C to 20°C at 1°C/min, 30°C for 20 minutes and then frozen*

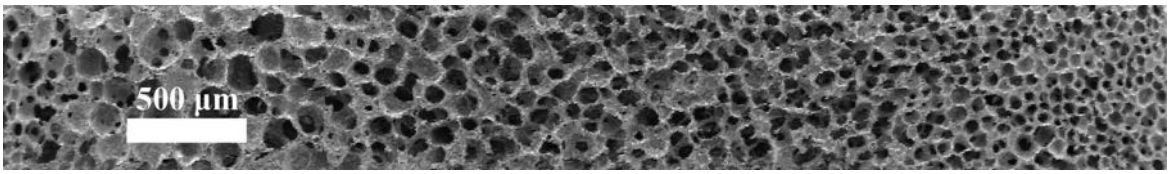

Fig. 3.29 *SEM micrograph of the obtained scaffold. Average pore dimension from 65 µm on SCS, to 110 µm on the center, 180 µm on the FCS*

3.2.4 30-45/30-20

In order to compare the effect of temperature alone keeping constant the permanence time, several tests changing the rate of cooling on SCS were performed. In this case the FSC was maintained at 30°C for 45 minutes, while on SCS the temperature decreased from 60°C to 30°C in 25 minutes. At the end -25°C was imposed to freeze the so-obtained morphology. Figure 3.30 reports the thermal history set at the two face of the sample. As demixing temperature is the same in the whole sample, pore morphology is homogeneous in all foam regions, while changing the pore dimension. SEM micrograph (fig. 3.31) reports a pore dimension of 210 µm on FCS, 115 µm on the center and 60 µm on the SCS.

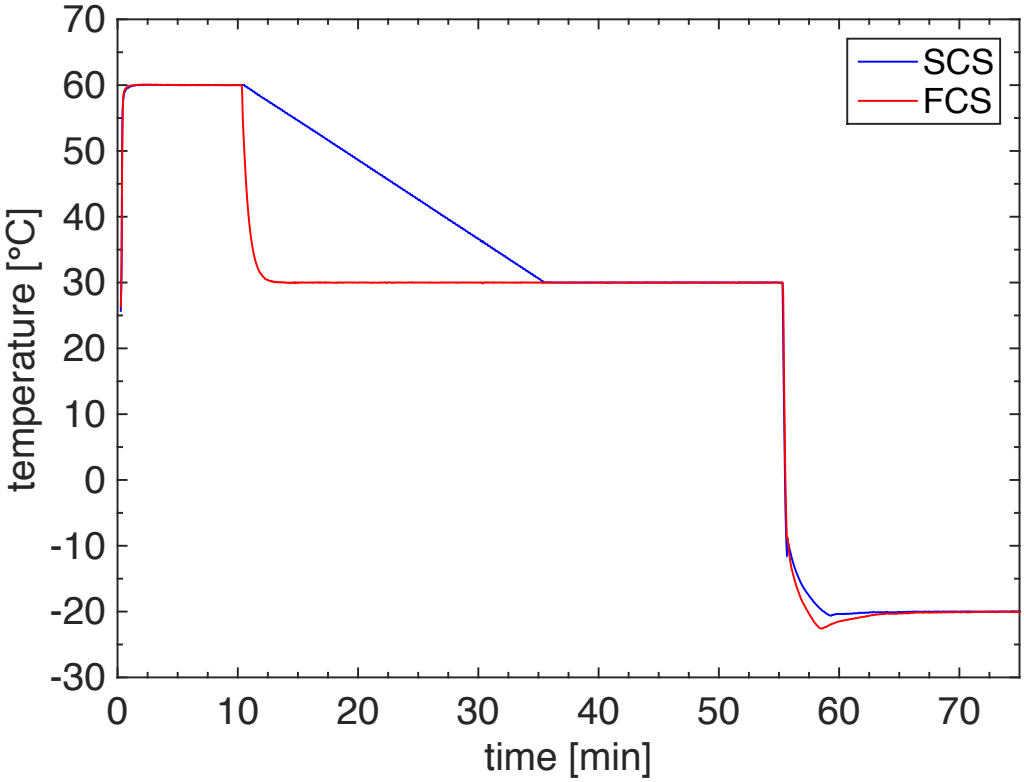

Fig. 3.30 *Thermal history. FCS: from 60°C rapidly to 30°C for 45 minutes and then frozen; SCS: from 60°C to 30°C in 25 minutes, 30°C for 20 minutes and then frozen*

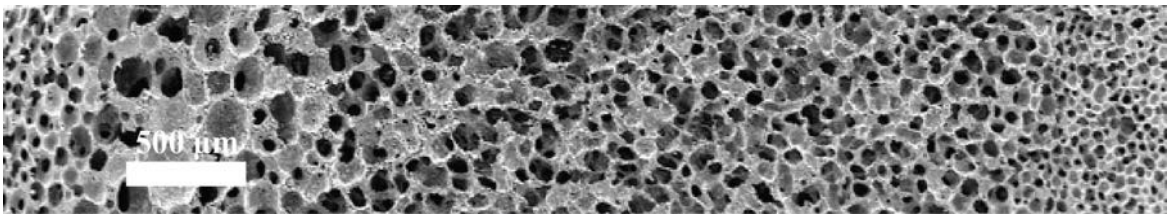

Fig. 3.31 *SEM micrograph of the obtained scaffold. Average pore dimension from 60 µm on SCS, to 115 µm on the center, 210 µm on the FCS*

3.2.5 25-45/25-20

The solution was preliminary homogenised at 60°C, then both FCS and SCS were brought to 25°C, at 25°C/min and 1.4°C/min, respectively (fig. 3.32). Once reached the corner temperature the FCS was maintained for 45 minutes, while the SCS for 20 minutes, then both side were quenched at -25°C/min at the maximum rate of the experimental apparatus. In figure 3.33 the thermal history was shown. The obtained pore size range in this case

was 45-160 µm (fig. 3.33). At 25°C the pore size gradient appears less evident, indeed the temperature is almost on the border between the metastable region and the unstable region where the spinodal decomposition occurs. In the spinodal decomposition mutual diffusion between the two phases (polymer-rich and polymer-less phase) is the dominant mechanism, then the difference of residence time between the two sides of the sample less affect the final morphology.

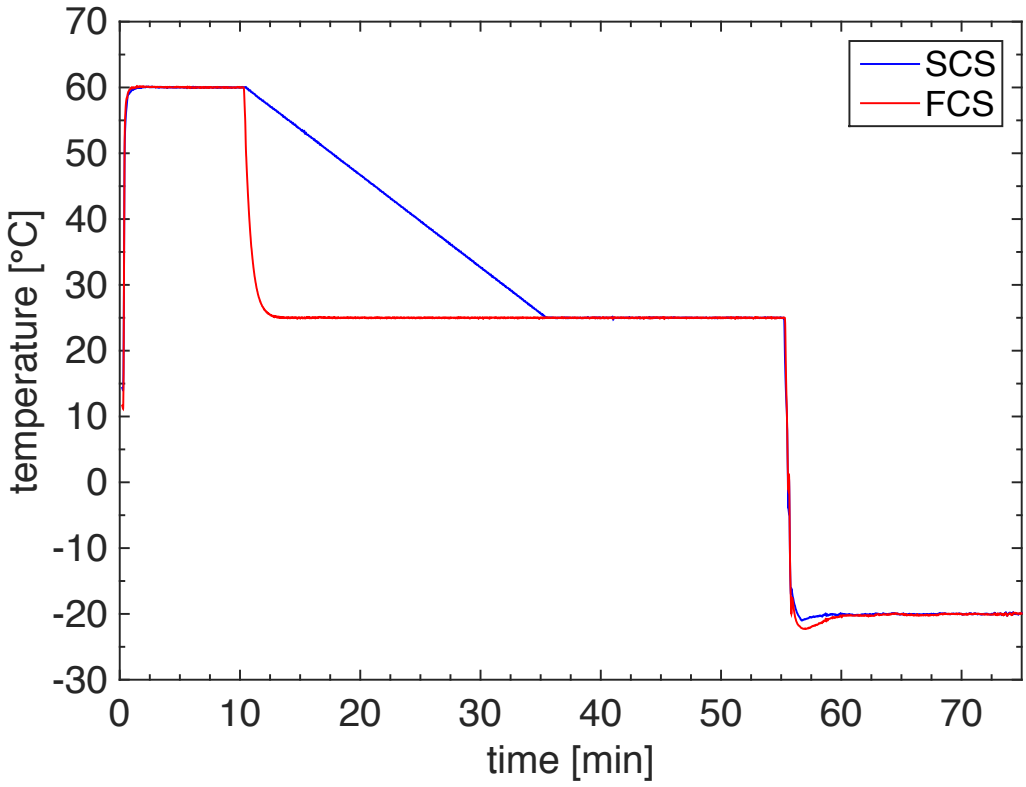

Fig. 3.32 *Thermal history. FCS: from 60°C rapidly to 25°C for 45 minutes and then frozen; SCS: from 60°C to 25°C in 25 minutes, 25°C for 20 minutes and then frozen*

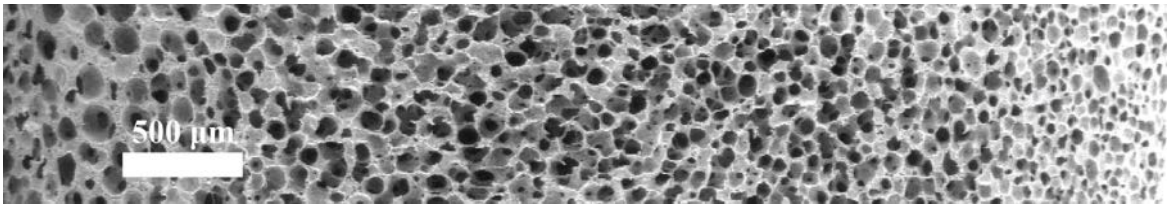

Fig. 3.33 *SEM micrograph of the obtained scaffold. Average pore dimension from 45 µm on SCS, to 90 µm, 160 µm on the FCS*

3.3 Outline

	Thermal History				Pore dimension	
	FCS		SCS		FCS	SCS
	T	t	T	t		
35-45/35-20	35°C	45min	35°C	20min	260µm	80µm
32-48/32-20	32°C	48min	32°C	20min	230µm	75µm
30-50/30-20	30°C	50min	30°C	20min	180µm	65µm
30-45/30-20	30°C	45min	30°C	20min	210µm	60µm
25-45/25-20	25°C	45min	25°C	20min	160µm	45µm

Table 3.3 *Summary of the results of gradient pore scaffolds*

Table 3.3 summarizes the applied thermal histories with the relative results. It is evident that simply manipulating the temperature vs time protocol a wide range of pore dimension was possible to obtain. In general terms an increase in the demixing temperature or time inside the metastable region the corresponding pore dimensions globally globally reflects on to an increase with respect to those obtained at lower temperatures or less time.
Foams were produced via a single step operation without requiring multiple layer or gradient of porogens. As a matter of principle this procedure can be applied to different biomaterial and different thickness could be obtained by varying the distance between the Peltier cells.

References

A. Bairi, N. Laraqi, N. Alilat, and Z. Zouaoui. Fast transient conduction in infinite plate subject to violent thermal effects. *Applied Thermal Engineering*, 24:1–15, 2004.

R. B. Bird, W. E. Stewart, and E. N. Lightfoot. *Transport phenomena*. 2006.

G. Casano and S. Piva. Experimental investigation of the performance of a thermoelectric generator based on Peltier cells. *Experimental Thermal and Fluid Science*, 35(4):660–669, 2011.

A. Chakraborty and N. Kim Choon. Thermodynamic formulation of temperature-entropy diagram for the transient operation of a pulsed thermoelectric cooler. *International Journal of Heat and Mass Transfer*, 49(11-12):1845–1850, 2006.

N. Davidenko, T. Gibb, C. Schuster, S. M. Best, J. J. Campbell, C. J. Watson, and R. E. Cameron. Biomimetic collagen scaffolds with anisotropic pore architecture. *Acta biomaterialia*, 8(2):667–76, 2012.

V. A. Drebushchak. The Peltier effect. *Journal of Thermal Analysis and Calorimetry*, 91(1): 311–315, 2008.

B. a. Harley, A. Z. Hastings, I. V. Yannas, and A. Sannino. Fabricating tubular scaffolds with a radial pore size gradient by a spinning technique. *Biomaterials*, 27(6):866–74, 2006.

C. J. L. Hermes and J. R. Barbosa. Thermodynamic comparison of Peltier , Stirling , and vapor compression portable coolers. *Applied Energy*, 91(1):51–58, 2012.

B. J. Huang and C. L. Duang. System dynamic model and temperature control of a thermoelectric cooler. *Internation Journal of Refrigeration*, 23:197–207, 2000.

B. J. Huang, C. J. Chin, and C. L. Duang. Design method of thermoelectric cooler. *International Journal of Refrigeration*, 23(3):208–218, 2000.

V. P. Isachenko, V. A. Sukomel, and A. S. Osipova. *Heat Transfer*. 1980.

S. J. Kalita, S. Bose, H. L. Hosick, and A. Bandyopadhyay. Development of controlled porosity polymer-ceramic composite scaffolds via fused deposition modeling. *Materials Science and Engineering: C*, 23(5):611–620, 2003.

H. Ma, J. Hu, and P. X. Ma. Polymer scaffolds for small-diameter vascular tissue engineering. *Advanced Functional Materials*, 20(17):2833–2841, 2010.

G. A. Mannella, V. La Carrubba, and V. Brucato. Peltier cells as temperature control elements: Experimental characterization and modeling. *Applied Thermal Engineering*, 63 (1):234–245, 2014.

H. Matsuyama, S. Berghmans, M. T. Batarseh, and D. R. Lloyd. Effects of thermal history on anisotropic and asymmetric membranes formed by thermally induced phase separation. *Journal of Membrane Science*, 142(1):27–42, 1998.

H. Matsuyama, S. Berghmans, and D. R. Lloyd. Formation of anisotropic membranes via thermally induced phase separation. *Polymer*, 40(9):2289–2301, 1999.

D. Mitrani, J. A. Tomé, J. Salazar, A. Turò, M. J. Garcìa, and J. A. Chàvez. Dynamic measurement system of thermoelectric module parameters. In *International Conference on Thermoelectrics, ICT, Proceedings*, volume 2003-Janua, pages 524–527, 2003.

S. H. Oh, I. K. Park, J. M. Kim, and J. H. Lee. In vitro and in vivo characteristics of PCL scaffolds with pore size gradient fabricated by a centrifugation method. *Biomaterials*, 28 (9):1664–71, 2007.

J. L. Pérez-Aparicio, R. Palma, and R. L. Taylor. Finite element analysis and material sensitivity of Peltier thermoelectric cells coolers. *International Journal of Heat and Mass Transfer*, 55(4):1363–1374, 2012.

A. Salerno, S. Iannace, and P. A. Netti. Open-pore biodegradable foams prepared via gas foaming and microparticulate templating. *Macromolecular bioscience*, 8(7):655–64, 2008.

D. E. Seborg, D. A. Mellichamp, T. F. Edgar, and F. J. Doyle. *Process Dynamics and Control*. 2010.

J. K. Sherwood, S. L. Riley, R. Palazzolo, S. C. Brown, D. C. Monkhouse, M. Coates, L. G. Griffith, L. K. Landeen, and A. Ratcliffe. A three-dimensional osteochondral composite scaffold for articular cartilage repair. *Biomaterials*, 23(24):4739–4751, 2002.

J. M. Sobral, S. G. Caridade, R. A. Sousa, J. F. Mano, and R. L. Reis. Three-dimensional plotted scaffolds with controlled pore size gradients: Effect of scaffold geometry on mechanical performance and cell seeding efficiency. *Acta Biomaterialia*, 7(3):1009–1018, 2011.

Y. Tang, K. Zhao, L. Hu, and Z. Wu. Two-step freeze casting fabrication of hydroxyapatite porous scaffolds with bionic bone graded structure. *Ceramics International*, 39(8):9703–9707, 2013.

References

H. Wu, Y. Wan, X. Cao, S. Dalai, S. Wang, and S. Zhang. Fabrication of chitosan-g-polycaprolactone copolymer scaffolds with gradient porous microstructures. *Materials Letters*, 62(17-18):2733–2736, 2008.

H. Y. Zhang, Y. C. Mui, and M. Tarin. Analysis of thermoelectric cooler performance for high power electronic packages. *Applied Thermal Engineering*, 30(6-7):561–568, 2010.

Q. Zhang, H. Lu, N. Kawazoe, and G. Chen. Preparation of collagen porous scaffolds with a gradient pore size structure using ice particulates. *Materials Letters*, 107:280–283, 2013.

Y. Zhu, H. Wu, S. Sun, T. Zhou, J. Wu, and Y. Wan. Designed composites for mimicking compressive mechanical properties of articular cartilage matrix. *Journal of the mechanical behavior of biomedical materials*, 36:32–46, 2014.

Chapter 4

Composite scaffolds: preparation and characterisation

The use of a ceramic filler in a polymeric network is one of the most adopted techniques to mimic the native tissue to replace. In this chapter the possibility to fabricate composite scaffold PLLA/Hydroxyapatite and PLLA/bioglass via thermally induced phase separation was investigated.

4.1 Materials characterisation

4.1.1 Particle size distribution analysis

To evaluate the particle size distribution a laser diffraction analyser was adopted. Laser diffraction measures particle size distributions by evaluating the angular variation in intensity of light scattered as a laser beam passes through a dispersed particulate sample. Large particles scatter light at small angles while small particles scatter light at large angles. When particles are irradiated with a laser beam, light is "diffracted/scattered" in various directions from the particles.
For the intensity of diffracted/scattered light, a fixed spatial pattern is formed in the direction that the light is emitted. This is referred as the "light intensity distribution pattern".
The light intensity distribution pattern is known to change to various shapes according to the particles size. The pattern data is then analyzed to calculate the size of the particles, using the Mie theory of light scattering. The particle size is reported as a volume equivalent sphere diameter.
The main advantages of this method are: wide range of dimensions, from hundred of

nanometers to the millimeter; rapid measurements; repeatability; high sample throughput and standard technique covered by an ISO protocol.

4.1.2 Porosity evaluation

Porosity is defined as the ratio between the void volume, V_v, and the bulk volume, V_b:

$$\phi = \frac{V_v}{V_b} \tag{4.1.1}$$

Different technique can be adopted to evaluate the porosity of a porous structure (Karageorgiou and Kaplan, 2005), in this work two of them were taking into account: liquid displacement method and boyle's pycnometer.
About the liquid displacement method, ethanol was used as a wetting agent for its own facility to penetrate inside the pores. A sample of known mass W_d (dry weight) and volume V_b (bulk volume) is placed in a cylinder containing ethanol. Several vacuum steps are adopted to assure the complete soaking of the sample. Then the sample is removed from the ethanol and, often, eliminating the excess of fluid, accurately weighted, W_w (wet weight). Knowing the density of ethanol, ρ_e it is possible to calculate the porosity of the scaffold as:

$$\phi = \frac{(W_w - W_d)/\rho_e}{V_b} \tag{4.1.2}$$

The gas or boyle's pycnometer is one or the most relevant instruments to evaluate the real volume of a porous solid. The general idea is the calculation of the amount of a gas able to penetrate inside the pores and then, in a indirectly way, the solid volume. The common gas adopted is Helium for three main reasons: it is a very small compound, ables to penetrate in nanometric pores; it is a completely inert gas, there is not possibility to wreck the sample; it follows the ideal gas law: $PV = nRT$.
The pycnometer consists of two chamber: reference and sample chamber at well know volume. During the test, the temperature is kept constant.
The volume of the sample, V_x, can be derived from the following formula:

$$V_x = V_c + V_r \frac{P_e - P_r}{P_e - P_c} \tag{4.1.3}$$

Where V_c and V_r are the chamber and reference volume respectively (accurately measured during the calibration process); P_r is the pressure of the reference chamber, P_c is the pressure of the empty sample chamber, calculated during the calibration and P_e is the equilibrium

pressure between the two chamber during the test.
In fig. 4.1 a schematic representation of the pycnometer is reported.

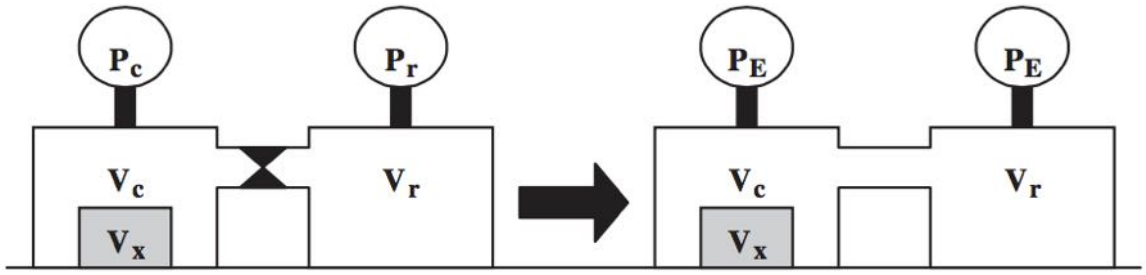

Fig. 4.1 *Illustrative representation of the gas pycnometer functioning, from Ho and Hutmacher (2006)*

4.1.3 TGA analysis

Thermogravimetric analysis (TGA) consists on detecting the weight variation of a sample during a temperature ramp. It allows to evaluate the thermal stability, the speed of reaction, the reaction processes and, in certain cases, the composition of the sample. The sample is subjected to an imposed thermal cycle while recording its weight as a function of temperature. This is an useful technique in the reactions of decomposition, where it is possible to appreciate the variation of the chemical composition in the thermogravimetric graph. The TGA is part of the group of quantitative and qualitative analysis, and classified among the destructive test. It is a method of investigation very useful in the study of hydrated compounds, clay materials, alterations of metallic materials (hot oxidation, etc...).
The thermogravimetric curve is influenced by various factors, the most important are:

- the rate of heating: increasing the rate of heating the decomposition temperatures result higher, then excessive speeds could lead to distortion of the obtained results;

- the mass and size of the sample: it must be not excessive in order to avoid problems of heat transport, but must be present in sufficient quantities to be representative of the sample;

- the flow of the purge gas: must be sufficient to ensure the rapid removal of the volatile products but, on the other hand, it must not be excessive, in order not to cause disturbance in the degradation process;

4.1.4 XRD analysis

An adopted technique to evaluate the material structure was the X-Ray Diffraction analysis (XRD). XRD is one of the most important characterisation tolls used in solid state chemistry and materials science. X-ray diffraction is often used for two main reasons, as a fingerprint of a crystalline materials and for the determination of their structure. Each crystalline solid has a specific X-ray pattern which may be used as a fingerprint

The dominant effect that occurs when an incident beam of X-rays interacts with a target material is scattering of those X-rays from atoms within the target material. In a crystalline materials, the scattered X-rays undergo constructive and destructive interference. The diffraction of X-rays by crystals is described by Bragg's Law:

$$n\lambda = 2dsen\theta \tag{4.1.4}$$

Where n is a positive integer, λ is the wavelength of incident wave, d is the distance between two crystalline plane and θ is the scattering angle.
The directions of possible diffractions depend on the size and shape of the unit cell of the material. The intensities of the diffracted waves depend on the kind and arrangement of atoms in the crystal structure.

4.1.5 FT-IR analysis

FT-IR is the acronym of Fourier Transform InfraRed, the most used method for infrared spectroscopy. During the spectroscopy some infrared radiation is absorbed by the sample and some is transmitted (passed through the sample). This spectroscopic technique gives information on the functional groups present in the molecule. In a IR spectrum two types of signals are present: related to the particular functional groups and related to "finger-print". It is not possible that two different molecules have the same infrared spectrum thanks to finger-print signals. On the other hand, the characteristics peaks of structures fall at the same frequencies regardless the structure where the molecule is present.
In the IR spectrum the interest zone is from 4000 cm^{-1} to 400 cm^{-1}. This range can be ideally divided in two zones: between 4000 cm^{-1} and 1300 cm^{-1} and between 900 cm^{-1} and 400 cm^{-1}. The highest frequency region is the region of the functional groups, while the lowest frequency region is that of the finger-print.
All things considered, the FT-IR analysis can provide several informations: to identify unknown materials, to determine the quality or consistency of a sample and to determine the amount of components in a mixture.

4.2 PLLA/HA scaffolds

Poly-L-lactic-acid, 1,4 dioxane and distilled water were utilized to prepare the starting solution. PLLA was used with a 4% wt/wt concentration and a ratio solvent/non solvent (dioxane/water) 87/13 wt/wt was adopted. Different PLLA/HA ratio were adopted (95/5, 90/10, 70/30, 50/50, 34/66, 25/75). For the first tests hydroxyapatite was kindly given by Professor Licciulli from University of Lecce, later tests for an in situ production of the HA were carried out.

4.2.1 Scaffold preparation

The ternary solution was initially kept at 60°C to allow the complete homogenisation. Thus the powders of HA were added to the solution keeping high temperature to maintain low viscosity and to allow for a complete dispersion. To avoid the formation of clusters, the so-obtained quaternary solution was sonicated for 15 minutes at 35 kHz and maintained at 60°C during the process.
After the complete dispersion of HA, the solution was hot poured in a cylindrical High Density Poly-Ethylene (HDPE) mold (21 mm diameter, 36 mm height) and immersed in a thermal bath at 30°C for 10 minutes (30°C is a temperature within the metastable region for this mixture). At the end of the process, the mold is immersed in an ethanol bath at -25°C for 25 minutes to stop the process and freeze the obtained morphology. The foams, then, were washed in deionised water and dried under vacuum for over than 24h, in order to completely remove any solvent.

4.2.2 Scaffold characterisation

The granulometric analysis (fig. 4.12) carried out on the particles has revealed the size distribution . A bimodal distribution with nanometric particles (100 nm) and micrometric particles (2-100 μm) was analyzed.

The morphology of the composite foams were analysed by SEM-FEI QUANTA 200F, along the cross section fractured in liquid nitrogen and gold sputtered by Scancoat Six, Edwars for 120s under argon atmosphere.

In fig. 4.3 composite scaffolds with different HA concentration are showed. As examples just two concentration are reported, 30/70 w/w, and 50/50 w/w HA/PLLA, respectively. It is evident that the change of the amount of hydroxyapatite does not influence the global morphology of the scaffold. This means the HA, in this case, is basically inert for the

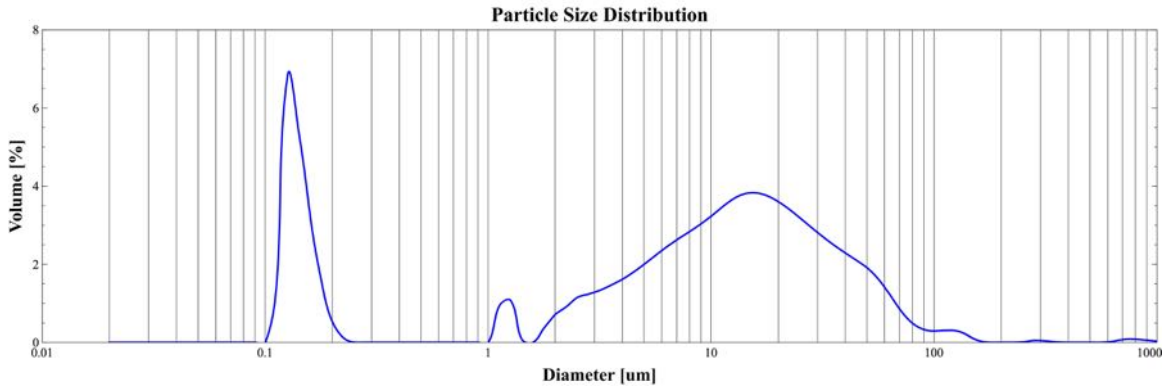

Fig. 4.2 *Particle size distribution of HA*

separation process. Pore dimensions, in both cases, are around 100 µm, very similar to the size attained in the absence of HA (i.e. with neat PLLA). There is a basically regular pore structure with a good pore interconnection. At higher magnification it is possible to appreciate the integration between polymer matrix and particles. HA looks like completely covered and surrounded by the PLLA matrix. As expected, comparing the 50/50 and 30/70, the number of particles in the same section are higher in first case than in the second case and the borders of the pores appears more indented.

In order to evaluate the variation of the structure as a function of the increase of the HA content, XRD analysis were carried out. The Panalytical X Pert Powder Diffractometer was adopted, with 2θ angle ranging from 5° to 70°, step angle and step time of 0.15° and 10 seconds, respectively. The samples were cut in cylindrical shape (14mm diameter and 1mm thickness) and stacked by canada balsam to the sample holder. The balsam has a refractive index similar to crown glass, then very useful for optical application. The results for the different composite scaffold were summarised in a unique graph (fig. 4.4), from pure PLLA (on top) to pure HA (on bottom).

Passing from the neat polymer to the mineral it is possible to recognise a clear trend of the characteristic peaks. The PLLA pattern presents two peaks located at 16.5 and 19 degrees, (zone "a").
Mineral Hydroxyapatite shows a set of typical peaks around 30° (zone "b") and around 50° (zone "c"). At higher concentration HA shows its characteristic peaks are more marked and distinguishable. On the other hand, proceeding from neat PLLA to greater HA content the two peaks of the polymer reduce in intensity. This analysis remarks in an evident way the

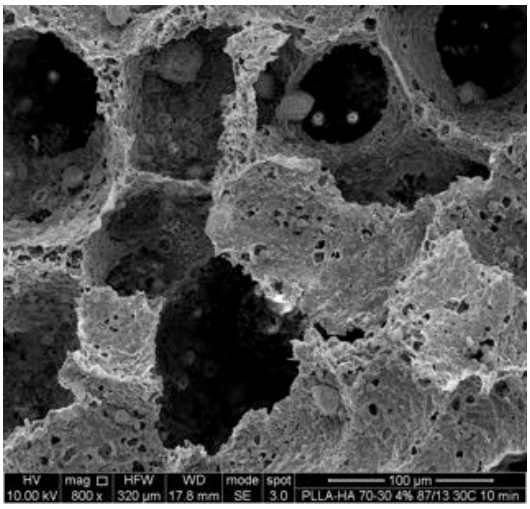

(a) *Composite PLLA/HA 70/30 w/w, [800X]*

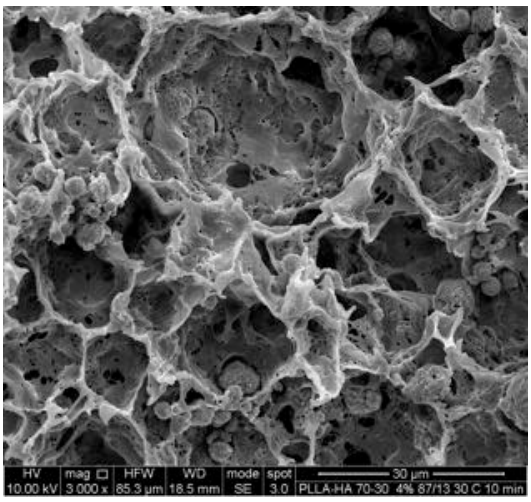

(b) *Composite PLLA/HA 70/30 w/w, [3000X]*

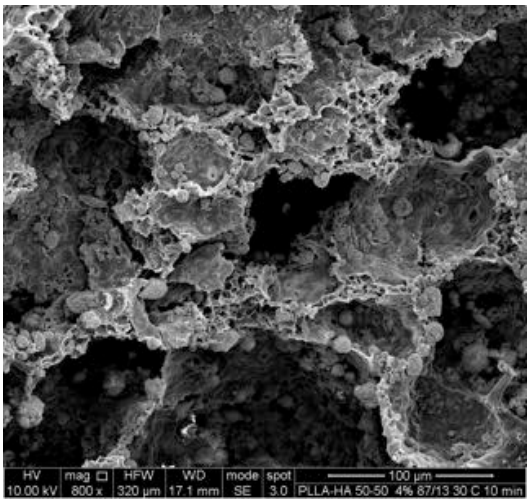

(c) *Composite PLLA/HA 50/50 w/w, [800X]*

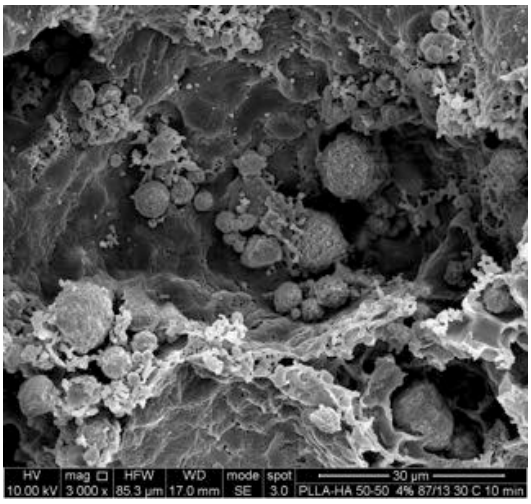

(d) *Composite PLLA/HA 50/50 w/w, [3000X]*

Fig. 4.3 *Different morphologies of composite PLLA/HA scaffolds as a function of the concentration*

HA incorporation within the polymeric support.

About the porosity, the evaluation via boyle's porosimeter and liquid displacement is reported in figure 4.5. It is possible recognize significant agreement among the two techniques.

Increasing HA content, the porosity decreases, since a partial portion of open pore is occupied by HA particles. This slow porosity reduction reaches the ~85% at HA weight percentage of 25%. This means that even in the presence of a large amount of HA, the scaffolds are characterized by a highly porous and interconnected structure, feature necessary

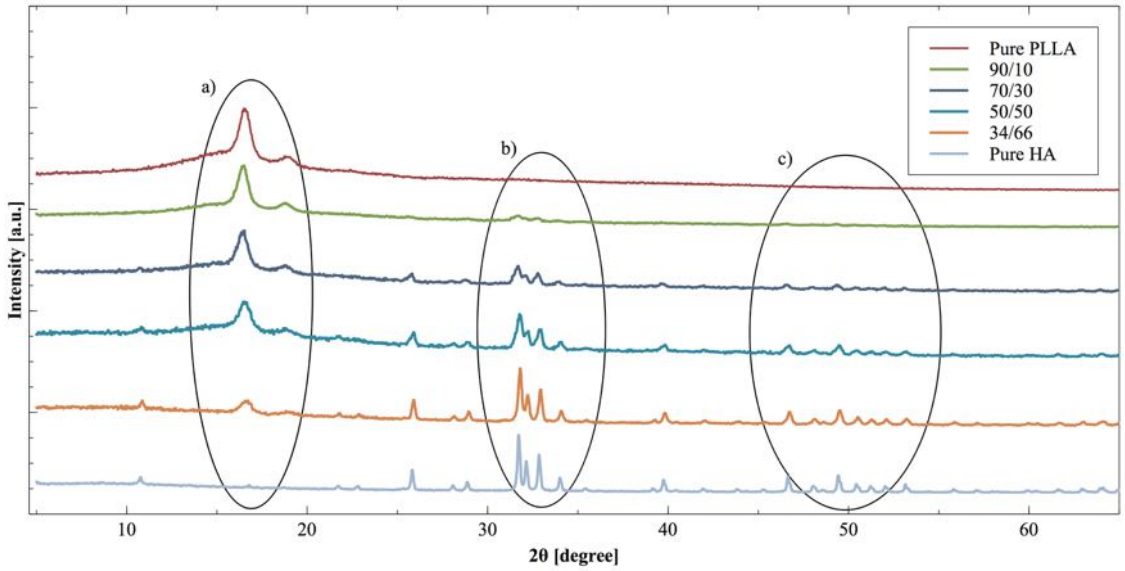

Fig. 4.4 *XRD analysis of composite scaffolds at different concentration in HA*

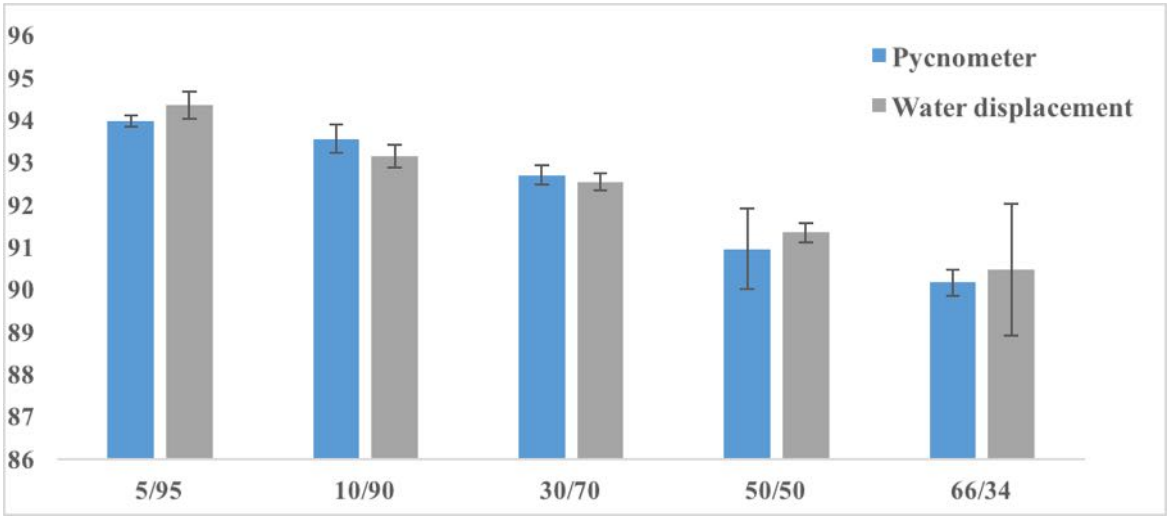

Fig. 4.5 *Porosity evaluation via Boyle's pycnometer and ethanol displacement*

to ensure cell proliferation and tissue regeneration.

PLLA and HA have completely different degradation temperatures, 350°C and 1360°C, respectively. Based on this large difference, it is possibile to carry out measure of TGA, to evaluate the amount of filler present inside the scaffold.
TGA analysis were carried out by Netzsch STA 449 F1 Jupiter. All samples had an average initial weight of 30.5 mg. The imposed thermal history was:

- Initial stabilisation at 30°C

- Increase of temperature from 30°C to 500°C at 10°C/min

- Stabilisation at 500°C for 30 minutes

The non-isothermal TGA measurement of neat polymer, neat filler and their blends are summarised in figure 4.6. In y-axis the percentage of weight loss, in x-asis the temperature from 100°C to 450°C .

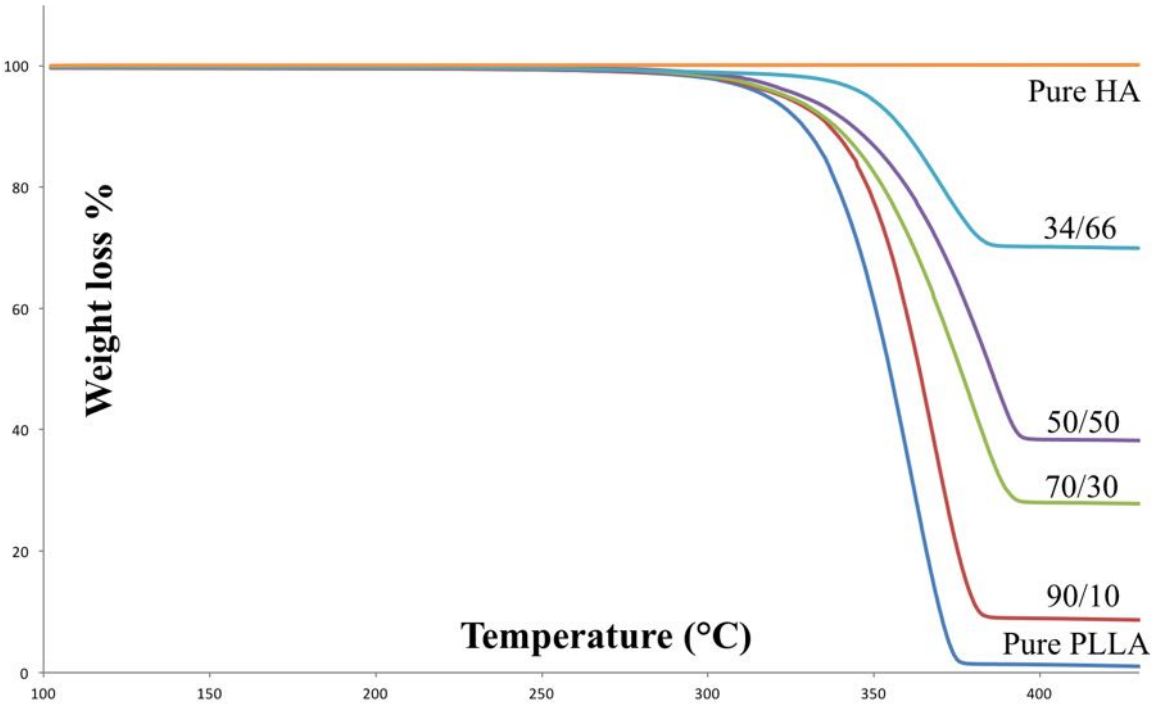

Fig. 4.6 *TGA curves of PLLA/HA foams*

TGA curves show that when the temperature increases up to about 400°C, PLLA scaffold nearly loses the whole weight whereas HA maintains the initial mass. The composite scaffolds rapidly lose their weight starting from 350°C. This indicate that after 350-400°C nearly all the PLLA in the composite was lost and HA remained. The mineral contents in the fabricated composite scaffolds could be assessed from the TGA data. The results show a good according with initial amount of filler inside the solution, the average difference between the nominal and the final concentration is around 10-15% .

4.2.3 HA (in situ) synthesis and characterization

In order to better integrate the filler with the overall preparation technique, several tests for an in situ production of the hydroxyapatite were carried out. The HA can be synthesized in different ways, e.g. wet chemical process (Pang and Bao, 2003; Tian et al., 2008), the hydrothermal method [12], sol-gel procedures [13, 14], the solid-state reaction [15, 16], and emulsion or micro-emulsion routes [17].
In this work the HA was produced via wet chemical process (Wang et al., 2010; Zanotto et al., 2012), using $Ca(NO_3)_2 \cdot 4H_2O$ and $(NH_4)_2 \cdot HPO_4$ purchased from Sigma-Aldrich as Ca and P precursors, respectively.
0.03 M aqueous solution of $(NH_4)_2 \cdot HPO_4$ was added drop wise in a 0.05 M $Ca(NO_3)_2 \cdot 4H_2O$ aqueous solution under stirring condition.
During the process the pH of the reaction solution was adjusted to 11 by adding sodium hydroxide ($NaOH$) and the temperature was maintained at 70 ± 2°C.
After the preliminary tests, in order to improve the HA production, some preparatives with a tenfold concentration were adopted, 0.3 M of $(NH_4)_2 \cdot HPO_4$ and 0.5 M of $Ca(NO_3)_2 \cdot 4H_2O$.
The precipitated HA particles were aged for 24 h at room temperature. The resulting product was centrifuged at the rotation speed of 13000 rpm for 30 min. Then the powder was frozen at -20°C for 1 h and dried in a freeze dryer system at -40°C for 4 days. The as-obtained hydroxyapatite was, in one case, directly characterized and in the other cases, calcinated at 600°C for 1h.

The SEM micrographs (fig. 4.7a, 4.7b, 4.7c, 4.7d) show a small variation of morphologies between the two concentrations, but a large difference in shape between the calcinated and not calcinated hydroxyapatite. This latter HA appears without a specific shape, it is hard to define a line of separation amongst the particles. The morphology of the calcinated hydroxyapatite is quite different. It possesses a regular needle shape, 20nm wide, around 200nm long and the contours of the particles is well defined. The EDX spectrum (fig. 4.8) confirms the presence of calcium (Ca), phosphorus (P) and oxygen (O). Analyzing the area under the curve it is possible to calculate the amount of each element and comparing it with the theoretical atomic percentage of each element of the hydroxyapatite $Ca_{10}(PO_4)_6(OH)_2$. The results, reported in table 4.1, show a satisfactory matching among the theoretical and the experimental values.

XRD analysis of three different HA were carried out and compared. HA produced in prof. Licciulli's laboratory via sol-gel technique, as reference, calcinated HA and not calcinated

		Theoretical	Experimental
	At	% At	% At
Ca	10	23.8	21±1
P	6	14.3	14 ± 1
O	26	61.9	63 ± 1

Table 4.1 *Comparison between theoretical and experimental atomic ratio of HA*

HA to individuate the effects of the thermal process.

The firsts two XRD diffraction patterns (fig. 4.9a and 4.9b) are substantially indistinguishable. Both show the three characteristic peaks around 30°and the other peaks around 50°. The peaks are very sharp and well defined, which means a high level of crystallinity and large crystal.
Different is the case of the not calcinated hydroxyapatite (fig. 4.9c). The pattern displays an increase of the signal at the same angles of the others HA (30°, 50°) but a lower intensity. The amorphous part is larger than the other two cases and the background noise a low angles is more accentuated. In any case, the not calcinated HA presents the same molar ratio and the same configuration of the calcinated HA.

Via laser diffraction analyser the particle size distribution of the so-obtained hydroxyapatite was evaluated. In fig. 4.10 the pattern of the calcinated HA with a tenfold concentration was reported. The other patterns do not present significative variations. The maximum intensity is around 10 µm and there is a relative small range of particles dimension. The size of over than 95% of particles is less than 20 µm.
Small particle dimensions is a mandatory feature for scaffold applications, as the particles must be integrated in the polymer network and they must represent a very small percentage of the volume of the scaffold pores.

4.2.4 Composite PLLA/(in situ)HA scaffolds

The as-produced hydroxyapatite was incorporated in PLLA solution in order to evaluate the feasibility of scaffold production. Preliminary results showed a strong influence of hydroxyapatite in the TIPS process. It was not possible to obtain the scaffold starting from the calcinated HA. Following the same protocol adopted in the previous tests, after the freezing of the scaffold, during the immersion in water the polymeric structure was disgregated. This phenomenon is probably due to the formation of a solvation shell around the HA particles

that makes unstable the polymer network.
In figure 4.11 SEM micrographs of composite scaffold with lyophilised HA were reported. In all cases 10% wt PLLA/filler was adopted. After the preliminary homogenisation at 60°C the solution was poured in a cylindrical HDPE mold in a thermal bath for 30 minutes at different temperatures: 25°C, 27°C, 30°C, 33°C. Then the scaffold was immersed in water to remove the dioxane and dried overnight.
The images report like the temperature has a weak influence on the porous structure, with an average pore dimension much higher compared to the neat polymer scaffold prepared at similar condition. This should suggests an influence of the HA during the nucleation and growth mechanism. Further tests need to be carried out in order to better understand the interaction between the as-synthesized particles and the TIPS process for the scaffold production.

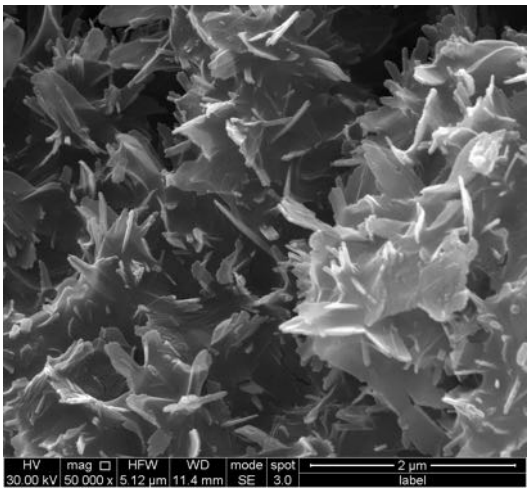

(a) *0.03 M of* $(NH_4)_2 \cdot HPO_4$ *and 0.05 M of* $Ca(NO_3)_2 \cdot 4H_2O$*, not calcinated*

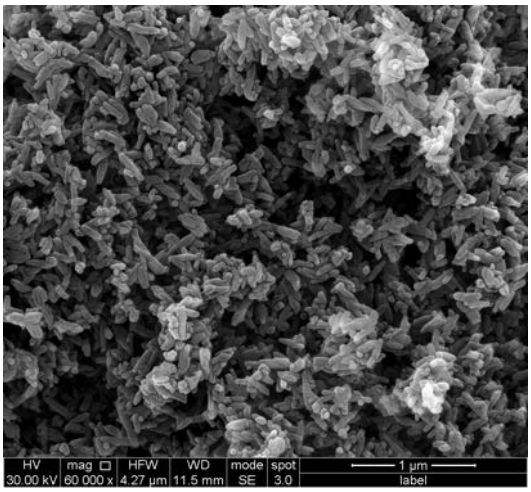

(b) *0.03 M of* $(NH_4)_2 \cdot HPO_4$ *and 0.05 M of* $Ca(NO_3)_2 \cdot 4H_2O$*, calcinated*

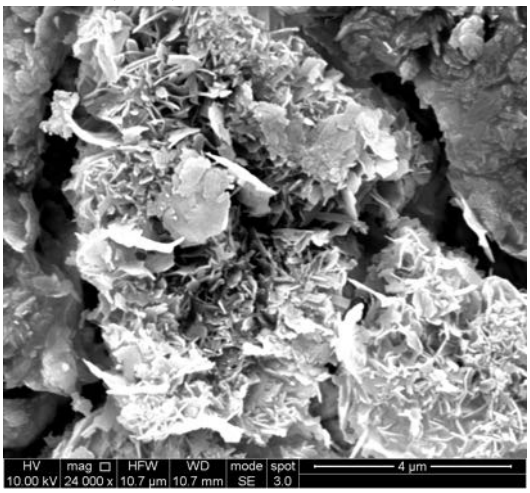

(c) *0.3 M of* $(NH_4)_2 \cdot HPO_4$ *and 0.5 M of* $Ca(NO_3)_2 \cdot 4H_2O$*, not calcinated*

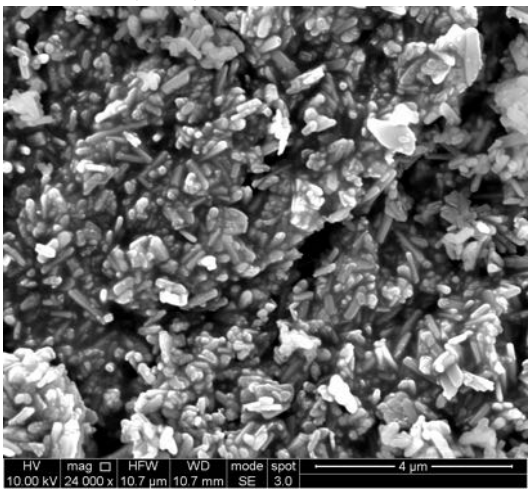

(d) *0.3 M of* $(NH_4)_2 \cdot HPO_4$ *and 0.5 M of* $Ca(NO_3)_2 \cdot 4H_2O$*, calcinated*

Fig. 4.7 *Different morphologies as a function of the thermal process and concentration*

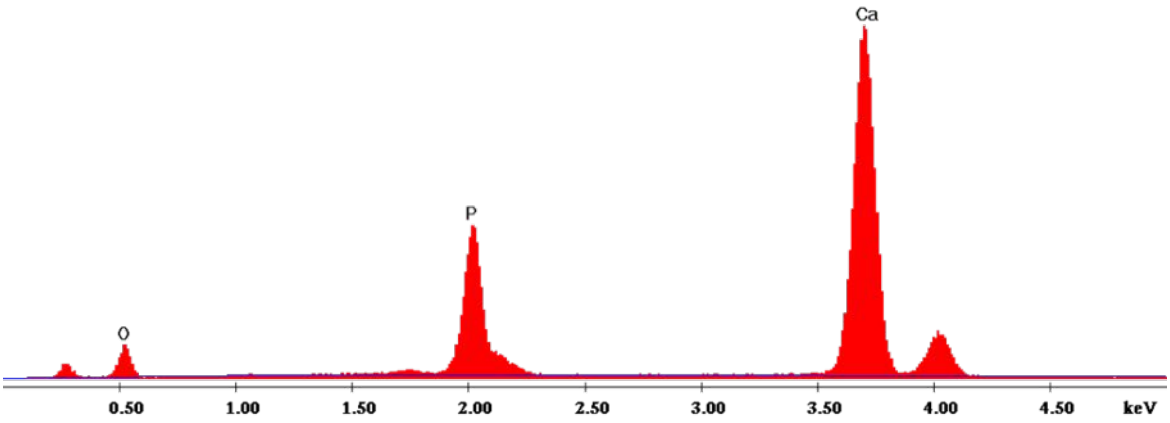

Fig. 4.8 *EDX spectrum of HA synthesised via wet chemical method*

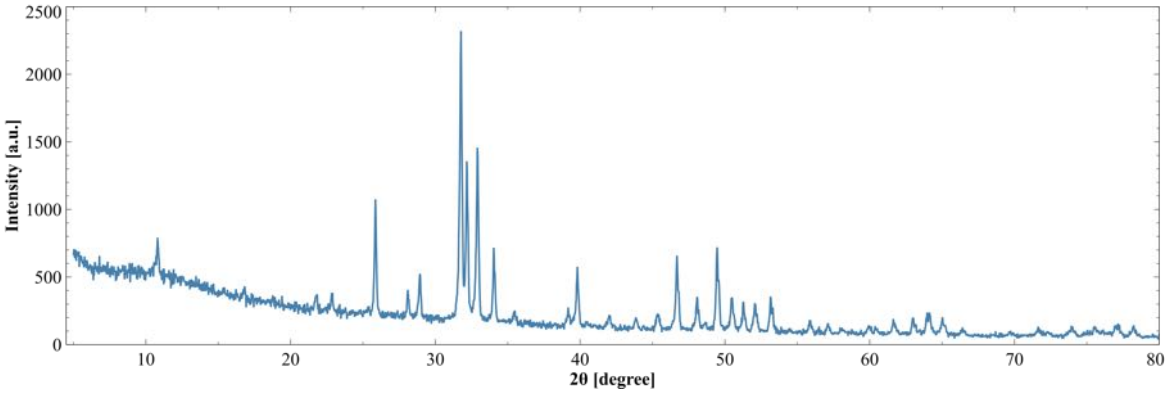

(a) *HA, via sol-gel method*

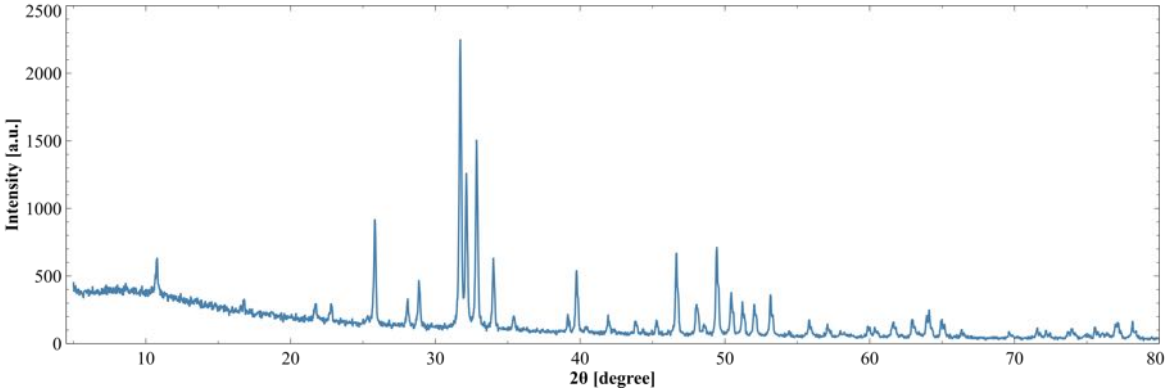

(b) *HA calcinated, via wet chemical method*

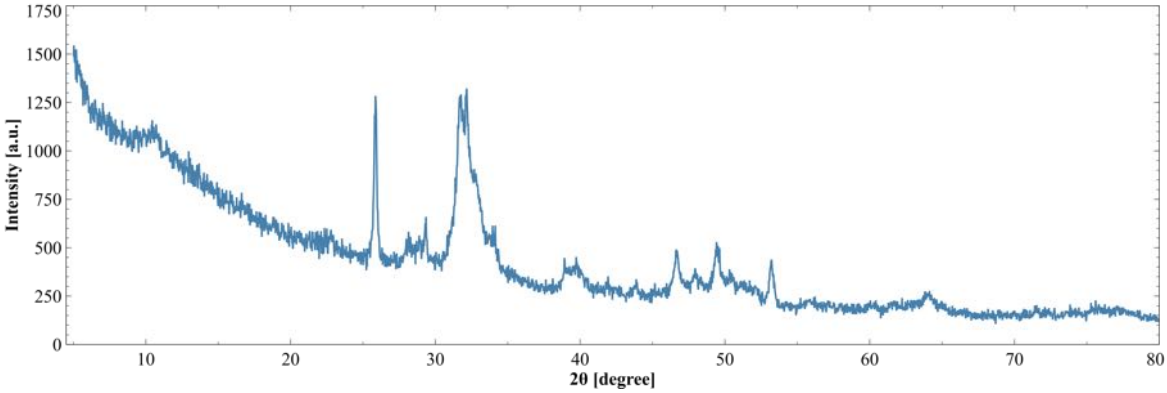

(c) *HA not calcinated, via wer chemical method*

Fig. 4.9 *XRD patterns of different HA*

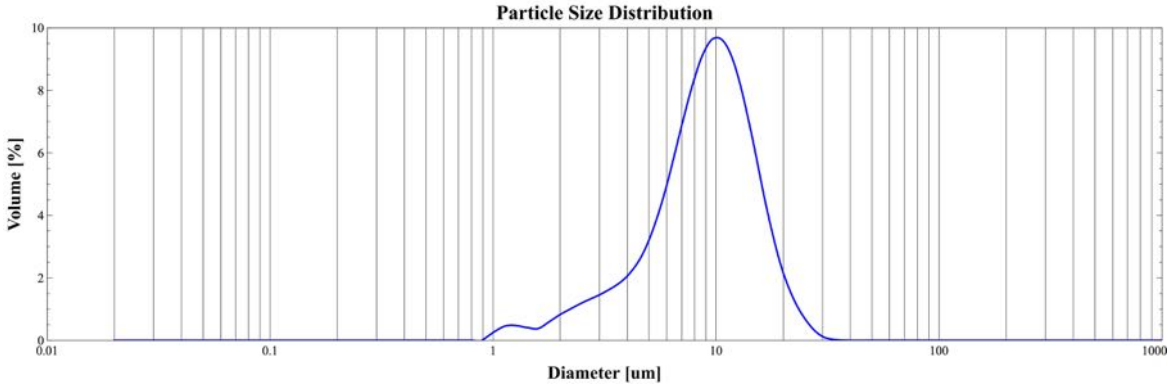

Fig. 4.10 *Particle size distribution of synthesised HA*

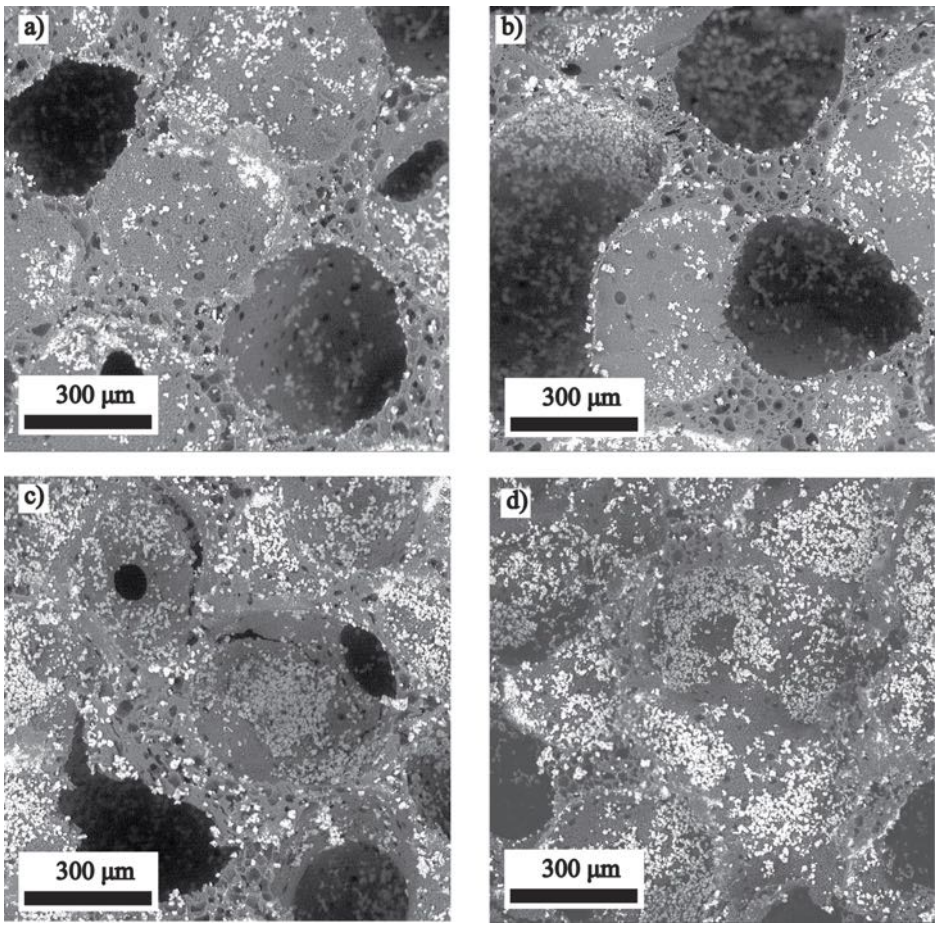

Fig. 4.11 *SEM micrographs of composite PLLA/(in loco)HA at 10% wt of filler. a) 25°C 30 minutes, b) 27°C 30 minutes, 30°C 30 minutes, 33°C 30 minutes*

4.3 PLLA/Bioglass scaffolds

Several studies showed the possibility to include bioglass in a polymer matrix via TIPS starting from a solution of a binary polymer/solvent mixture (Boccaccini and Maquet, 2003; Maquet et al., 2003, 2004). The scaffold prepared along this route results in a final ladder-like, anisotropic structure. In this set of experiments a ternary solution polymer/solvent/non-solvent (PLLA/dioxane/water) was adopted, leading to a wide range of scaffold structures by varying the thermal history and assuring high interconnectivity, good reproducibility and homogeneity (Akbarzadeh and Yousefi, 2014; Mannella et al., 2014). The idea is to assess an experimental protocol to produce composite PLLA/bioglass scaffold via TIPS, starting from a ternary polymeric solution. PLLA/45S5 and PLLA/1393 scaffold prepared at different bioglass concentration were compared in order to individuate which type of bioglass best match this scaffold production technique. Biodegradation study and bioactivity test in prof. Boccaccini's laboratory at the University of Erlangen-Nuremberg were carried out.

4.3.1 Scaffold preparation

The scaffolds were fabricated via a TIPS technique, applied to a ternary polymer/solvent/non-solvent system. The weight concentrations of PLLA was 6% and a ratio solvent/non solvent (dioxane/water) 87/13 w/w. Starting from this ternary solution the two different types of bioglass were added at different concentrations: 1%, 2.5%, 5% w bioglass/w polymer for 45S5 (namely PLLA/45S5 BG_1, PLLA/45S5BG_2.5, PLLA/45S5BG_5, respectively), 1%, 2.5%, 5% for 1393 (PLLA/1393BG_1, PLLA/1393BG_2.5, PLLA/1393BG_5, respectively). Considering the density of PLLA (1270 kg/m^3, (Gong et al., 2006)) and density of both bioglasses (2825 kg/m^3, (Blaker et al., 2011)), the corresponding volume concentration were: 0.45%, 1.13% and 2.3%, respectively. Both kinds of bioglass were fabricated via a melt derived route (Hoppe et al., 2013, 2014). Neat (unfilled) polymeric foams were also prepared and characterized and used as control. Neat polymer scaffolds were prepared along the same route and evaluated as control.

The protocol to incorporate the bioglass particles in the polymer solution was very similar to the PLLA/HA scaffold. Initially, the solution was kept at 60°C to allow the complete homogenization of the mixture, then the powders of bioglass, at different concentration, were added. Thus the solution was sonicated for 15 minutes at 35 kHz to avoid the formation of clusters. During this process, the solution was maintained above 60°C to reduce the viscosity and facilitate the complete dispersion of the powders. After this step, the mixture was first hot-poured into an aluminium disc-shaped mould (4 cm diameter, 2 mm height) and, subsequently, pool immersed in a thermostatic bath at 30°C, for 10 minutes. Finally the

mould was immersed in an ethanol bath for 20 minutes at -20°C to block any kind of process. At the end of the preparation, the foams were rinsed in distillate water and dried under vacuum for at least 24 h, to completely remove the solvents. For the various characterizations, several parallelepiped samples 6 mm to 8 mm large were cut from the disk. Neat PLLA scaffold was add as control.

4.3.2 Particle size and SEM analysis

Mastersizer 2000 (Malvern Instruments Ltd) was adopted to evaluate the particle size distribution of the two types of BG powders. 0.1g of BG were dispersed in 0.8l of distilled water and the average of 10 measures was considered.
To analyze the morphology of the scaffolds, these latters were cut along the cross section by cutting with a scalpel to avoid compression damages. Thus, the samples were mounted in an aluminium stab and observed under SEM Phenom Pro-X (Phenom-World, Netherlands). SEM images were used to evaluate the homogeneity of the microstructure and the average pore size for each type of scaffold.

4.3.3 Biodegradation study

For the biodegradation study composite and neat scaffold were cut and grouped in separate vials. The specimens were soaked in phosphate buffered saline (PBS) solution (Amresco LLC, USA) at 37°C and placed in an orbital shaker (KS 4000i control, IKA-Werke GmbH KG, Germany) at 90 rpm. The weight of each specimen before aging was recorded. The medium was changed once a week to maintain constant the pH value. At days 3, 7, 14, 21, 28 three specimens at each time points were removed from the buffer and analysed. Water uptake and weight loss were evaluated as follows. Water uptake (WA): after pulling out of the PBS solution, the sample was accurately rinsed in water and, after removing the excess of water, weighted. Then, the water uptake was calculated according to the following formula:

$$WA(\%) = \frac{W_w - W_b}{W_b} * 100 \tag{4.3.1}$$

where W_w is the weight of the wet scaffold and W_b is weight before aging.
Weight loss: After the calculation of the water uptake the scaffolds were dried under vacuum to remove any presence of liquid and weighted again. The weight loss (WL) was evaluated

as follow:

$$WL(\%) = \frac{W_b - W_d}{W_b} * 100 \tag{4.3.2}$$

in which W_d represents the weight of the biodegraded dry scaffolds.

4.3.4 Bioactivity test

Bioactivity tests were carried out using the standard in vitro procedure described by Kokubo and Takadama (2006). According to the protocol, the cut samples were soaked in simulated body fluid (SBF) in conic flasks and placed in an orbital shaker set at 37°Cand 90 RPM. The pH of the solution was controlled at 7.25. The SBF was replaced every three days for the cation concentration decreasing during the course of the experiments (Blaker et al., 2011). Three samples at 3, 7, 14, 21, 28 days were extracted, abundantly rinsed in distilled water and then in acetone to prevent any further reaction (Mi et al., 2014). Finally, the scaffolds were dried for 48h at room temperature.
To evaluate the presence and the morphology of the formed HCA several tests were carried out:

- SEM analysis at different magnifications by Auriga 0750 Zeiss.
- XRD measurements by Panalytical X-Pert Powder Diffractometer with a Cu K_a radiation source. The spectra were recorded in the range of 2θ 10-60 ° with a 0.15 step size and a step time of 10s. High voltage and tube current were 40kV and 30 mA, respectively.
- FTIR spectroscopy by Nicolet 6700 (Thermo Scientific, Germany) using attenuated total reflectance (ATR) technique. Each sample was scanned 32 times at a resolution of 4 cm^{-1} over the frequency range of 4000-550 cm^{-1}. A window of CsI was employed.

4.3.5 Results

Particle size distribution

In order to compare the two types of BGs a preliminary analysis about the particle size distribution was carried out. The median of the distributions, D50=8.86m and D50=11.26m for 1393 and 45S5 BGs, respectively, were calculated. From figure 4.12 it was possible to observe a very similar particle size distribution. This homology in terms of particle mean

sizes allows a more reliable comparison between the two types of scaffolds, since BG particle dimensions could influence the interaction between PLLA and BG.

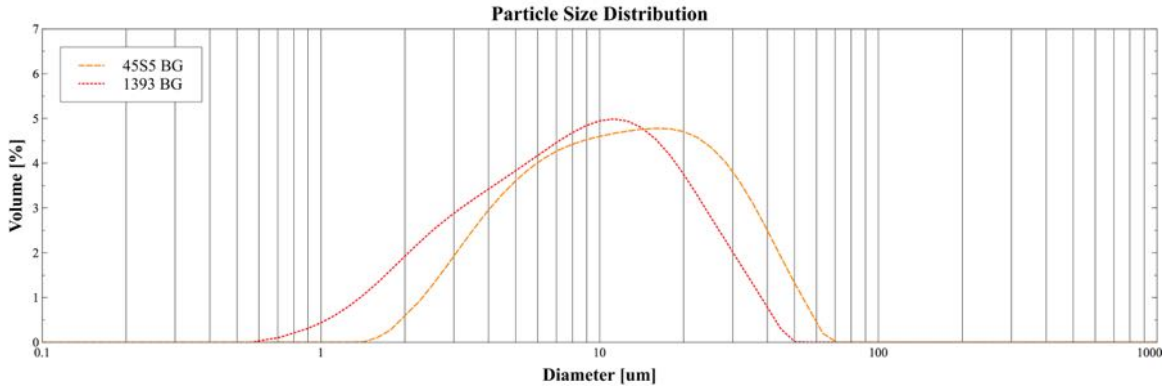

Fig. 4.12 *Particle size distribution of 1393 BG and 45S5 BG*

Scaffold morphology

In figure 4.13 the morphology of the obtained scaffolds were reported. A different behaviour for the two types of BGs was observed. As a matter of fact, for PLLA/1393 BG samples the presence of the particles does not seem to influence the phase separation and then the final morphology of the scaffold. Moreover, when increasing the BG concentration to 5%, the structure of the scaffold results unmodified. The average pore dimension was 80 µm for the different 1393 BG content.
A different behaviour was detected for the 45S5 BG, low percentages of BG (1-2.5%) do not seem to alter the process of formation of pores. Conversely, a significant presence of micropores in the structure was observed when a percentage of 5% 45S5 BG was used. t is reasonable to infer that the presence of BG altered the nucleation rate during the nucleation and growth process occurring in this ternary solution at 30°C (Mannella et al., 2014). Furthermore, it has been reported that the 45S5 BG exhibits a higher reactivity than 1393 BG, i.e. a faster capacity of ions release (Hoppe et al., 2014). Consequently, during the process of pore formation, the BG particles surrounded by their released ions may act as nucleating agents and, due to the difference in reactivity, this effect is clearly distinguishable for the 45S5 BG, whereas is not detectable for the 1393 BG. The nucleating effect increases with BG concentration, then this effect is evident on 5% of BG on the contrary of the 2.5%.

Weight loss and water uptake

Weight loss and water uptake as a function of immersion time in PBS are reported in figure 4.14 and figure 4.15, respectively. The mass of composite scaffold monotonously decreased

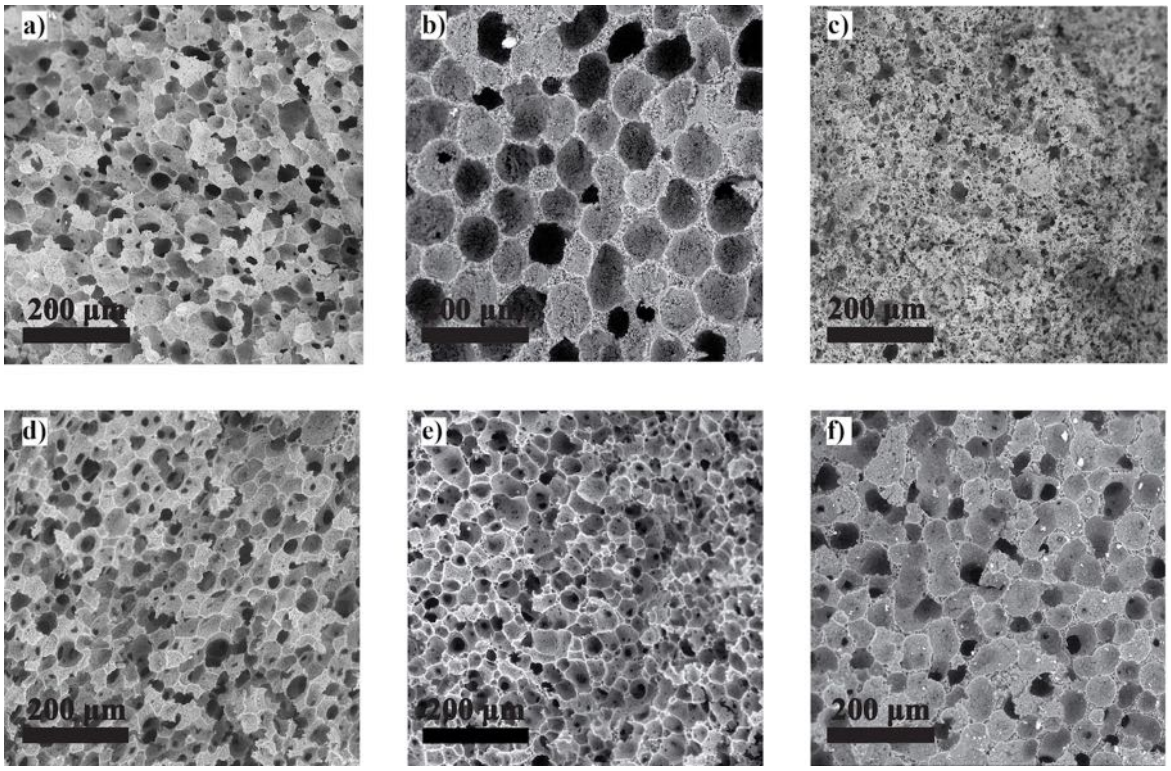

Fig. 4.13 *SEM micrographs of composite PLLA/BG scaffold. a) PLLA/45S5 BG_1, b) PLLA/45S5BG_2.5, c) PLLA/45S5BG_5, d) PLLA/1393BG_1, e) PLLA/1393BG_2.5, f) PLLA/1393BG_5*

with the BG concentration accordingly, on the contrary of neat PLLA that remained almost constant until the last time point, with a range of 0-2%. Comparing the same BG type, a significant difference can be confirmed among samples with different concentrations. Particularly relevant is that just the presence of 1% of BG induces a significant difference with respect to the unfilled PLLA. As expected, the highest weight loss was for 5% 45S5 BG sample with $26 \pm 4\%$ versus the $20 \pm 4\%$ for 5% of 1393 BG. BG particles dissolution, particle loss and erosion of the scaffold (Lim and Park, 2012) induce a more rapid weight loss on composite scaffolds than the neat PLLA. The presence of the BG particles, even in small amounts, reduces the integrity of the matrix and then the stability of the foams. In addition, the difference of reactivity between the two types of BG compositions caused a trend on weight loss profile, the biodegradation of PLLA/45S5 BG scaffold was always grater than PLLA/1393 BG keeping constant the concentration.

In figure 4.15 the water uptake results were reported. It is evident there is not large difference between composite scaffolds at different concentrations. Considering the standard deviation turing the 28 days, the water uptake can be considered almost constant, in agreement

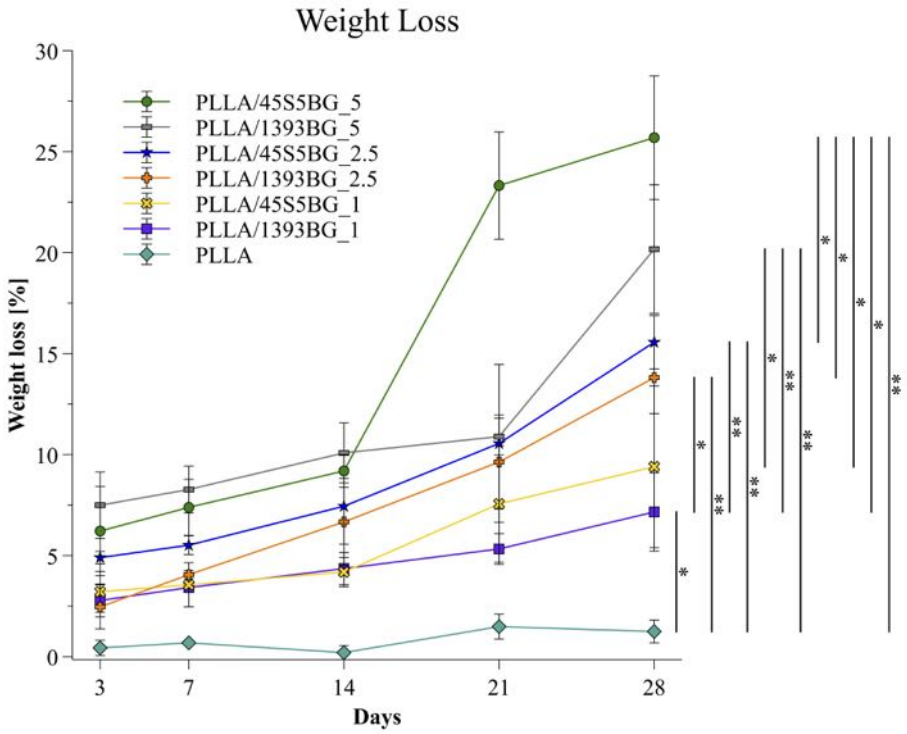

Fig. 4.14 *Weight loss of composite PLLA/BG scaffolds at different time points*

with previous works. The high water uptake value (>600%) just after 3 days denotes the high porosity and the good interconnectivity of the scaffold. Thus the addition of BG does not influence in a relevant way the water uptake capacity due to the low amount of filler. After 28 days, the maximum weight loss was around 25% (in the case of BG at its maximum concentration, 5%) that implies a change of total porosity from ca. 95% to ca. 96%, with a negligible influence on the water uptake, in any case below the measurement protocol sensitivity.

Bioactivity test

Three samples for each time point (3, 7, 14, 21, 28 days) were extracted from SBF, washed and analysed via SEM, XRD and FTIR. For the sake of brevity only results concerning 5% at 28 days are here discussed, being representative of all samples. To evaluate the differences in HA formation of the two BG types, SEM analysis after 28 days of immersion in SBF were carried out. In figure 4.16 micrographs of composite scaffolds at different magnifications were reported. In both cases the typical cauliflowers-like shape of HCA was individuated (Mi et al., 2014). SEM micrographs were taken along the cross section, then the significant con-

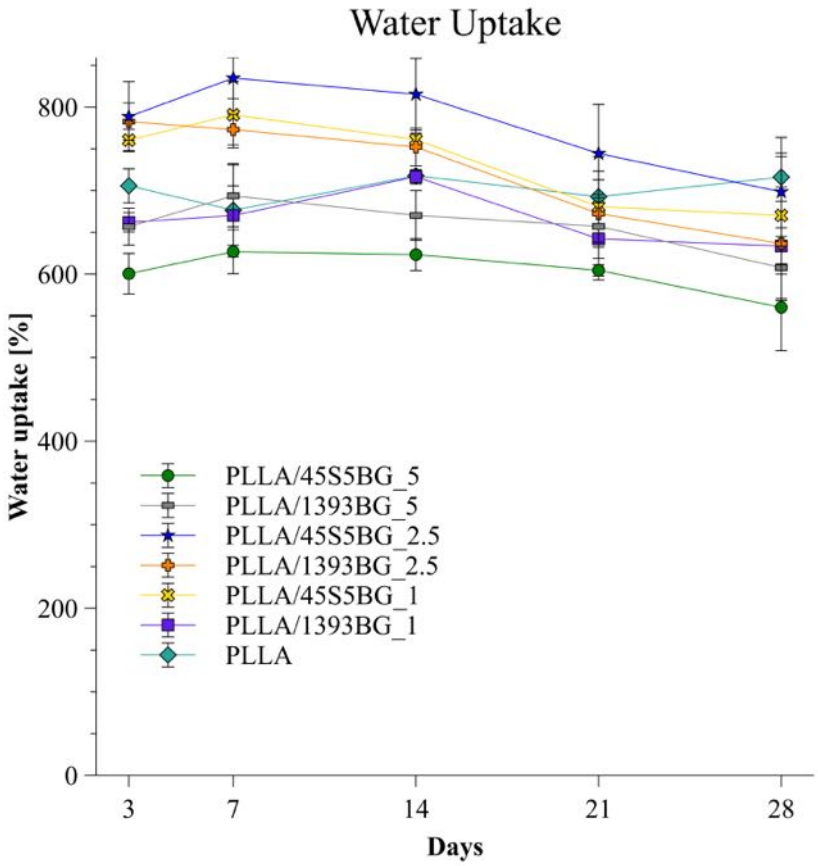

Fig. 4.15 *Water uptake of composite PLLA/BG scaffolds at different time points*

tent of HCA within the structure denotes the good ability of the SBF to penetrate inside the pore, in particular composite PLLA/45S5 BG exhibits a homogenous HCA-layer. Interesting is the presence of the inorganic compound not only around the BG particles, but almost on the whole surface. Although the presence of HCA-layer inside the PLLA/1393 BG scaffold appears less evident, also in this case the distribution of HCA appeared homogeneous along the internal surface of the scaffold. Moreover, in the 1393 BG composite scaffold the original pore structure remains still evident.

The effect of immersion in SBF after 28 days in terms of chemical structure (fig. 4.17), was significantly different for neat PLLA and composite scaffolds. The crystallinity of PLLA was weakly influenced from the presence of BG and there is no presence of peaks of other molecular structures. In the composite scaffold the peaks corresponding to the polymer were still present but, at the same time, some of the usual diffraction peaks of HA appeared. Indeed, the peaks centered at 2θ=29°, 32° and 46°, highlighted by the vertical bar, underline

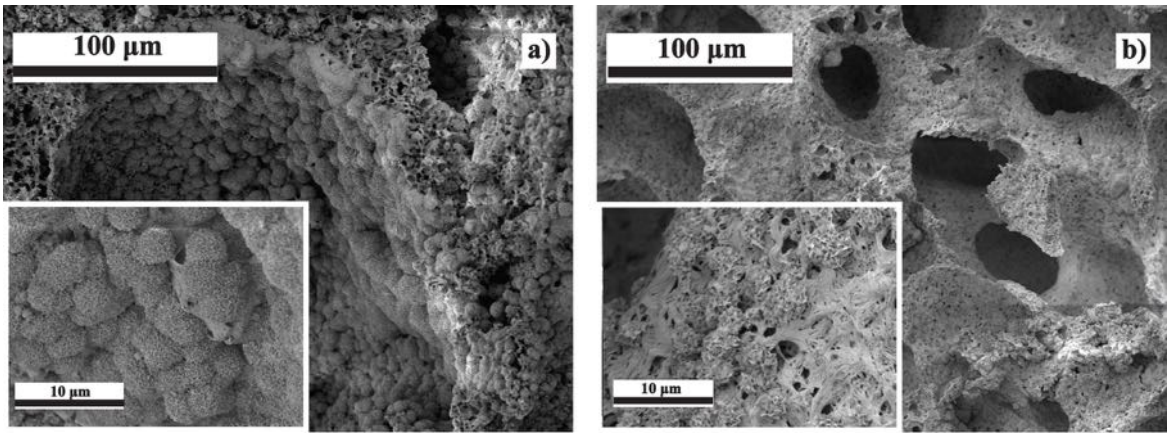

Fig. 4.16 *SEM micrographs of PLLA/BG scaffolds after 28 days of immersion in SBF. a) PLLA/45S5BG_5, b) PLLA/1393BG_5*

the formation of a HCA-like layer, confirming the SEM observation.

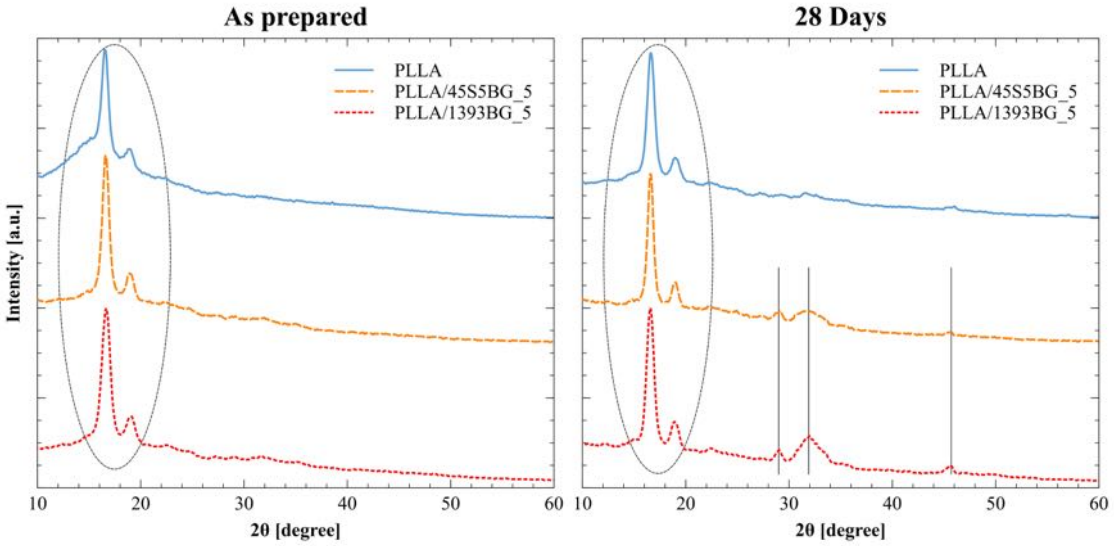

Fig. 4.17 *XRD pattern of neat and composite scaffolds, as prepared and after 28 days of immersion in SBF*

Figure 4.18 shows the FT-IR spectra of PLLA composites as prepared and at 28 days. As it is possible to see in figure 4.18a, the three patterns of the specimens before immersion (as prepared) are basically identical. The peaks of PLLA largely overcome the peaks of BG, for the low percentage of this latter. Characteristic absorption bands for PLLA of *CH* at 2920 cm^{-1}, COO^{-} at 1759 cm^{-1}, CH_3 at 1457 and 1383 cm^{-1}, C-O-C at 1183 and 1088 cm^{-1} are easily discernible. The spectra of the PLLA and PLLA/BG composite scaffolds after 28 days

in SBF are presented in figure 4.18b The blue curve shows the already mentioned absorption bands arising from PLLA; on the other hand, the composite specimens presented numerous new peaks. Bands at 3635 cm^{-1} have been assigned to OH anti symmetric stretching and 3550 cm^{-1} to symmetric OH- stretching (Ryszkowska et al., 2010). The bands of PO_4^{3-} at 564 and 605 cm^{-1} with the absorption bands of CO_3^{2-} at 1448 cm^{-1} are characteristic of the FTIR spectrum of HCA layer (Ji et al., 2015). The peaks at 1460 and 1420 cm^{-1} indicated that B-type HCA was formed because CO_3^{2-} replaced sectional PO_4^{3-}. A displacement of the carbonyl signal from 1746 cm^{-1} to 1755 cm^{-1} was also observed, which is attributed to the interaction of the hydrogen bond of the carbonyl group of the PLLA and the surface P-OH groups of HA (Zhou et al., 2007). All these evidences corroborate the hypothesis of the formation of a HCA-like layer in both types of BGs upon immersion in SBF.

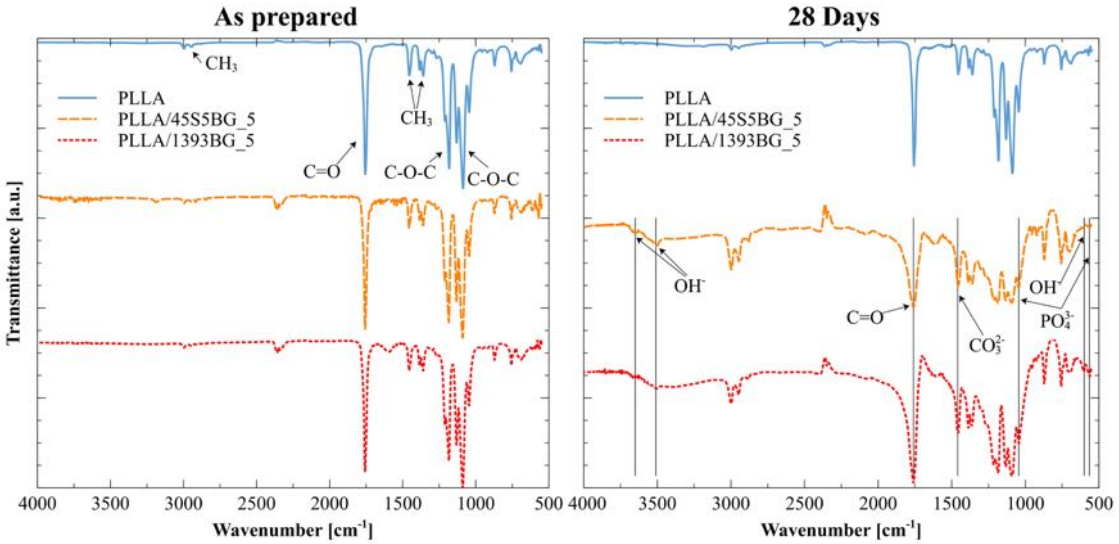

Fig. 4.18 *FT-IR spectra of neat and composite scaffolds, as prepared and after 28 days of immersion in SBF*

4.4 Outline

In this chapter composite PLLA/HA and PLLA/BG scaffolds were presented. Neat PLLA does not possess the appropriate biointegration capability and mechanical proprieties, then to overcome this limit composite polymer/ceramic filler were produced. About the scaffold with HA, based on the results, SEM images revealed that the presence of the HA did not influence the global scaffold morphology. As a matter of fact, a porous and interconnected structure was observed in the bulk of the scaffolds. By increasing the HA content the porosity reaches

the ~90%, this means that even with a large amount of HA, scaffolds are characterized by a high porous structure. Test of XRD and TGA confirmed the presence of HA inside the polymer network.
In order to individuate which BG composition best matches the scaffold production technique, two compositions were tested: 1393 and 45S5. SEM micrographs showed that the 45S5 BG interacted with the phase separation mechanism during the formation of the scaffold, on the contrary of the 1393 which did not affect the morphology of the scaffold. The different behavior could be due to the higher reactivity of 45S5 respect to 1393. The presence of BG did not modify the water uptake capability, contrarily on the case of weight loss where, also at low percentage of filler, a significant difference with the unfilled polymer was found. Bioactivity tests showed positive results for both composite PLLA/BG scaffolds; SEM images reveled typical cauliflowers-like shape of HCA after 4 weeks of soaking in SBF and XRD and FTIR analysis confirmed the formation of HCA layer. These results confirmed the possibility to successfully include BG and HA particles in PLLA scaffolds via a modified ternary TIPS and to tune the structure of the scaffold.

References

R. Akbarzadeh and A.-M. Yousefi. Effects of processing parameters in thermally induced phase separation technique on porous architecture of scaffolds for bone tissue engineering. *Journal of biomedical materials research. Part B, Applied biomaterials*, pages 1–12, 2014.

J. J. Blaker, S. N. Nazhat, V. Maquet, and A. R. Boccaccini. Long-term in vitro degradation of PDLLA/bioglass bone scaffolds in acellular simulated body fluid. *Acta biomaterialia*, 7 (2):829–40, 2011.

A. R. Boccaccini and V. Maquet. Bioresorbable and bioactive polymer/Bioglass® composites with tailored pore structure for tissue engineering applications. *Composites Science and Technology*, 63(16):2417–2429, 2003.

Y. Gong, Z. Ma, C. Gao, W. Wang, and J. Shen. Specially elaborated thermally induced phase separation to fabricate poly(L-lactic acid) scaffolds with ultra large pores and good interconnectivity. *Journal of Applied Polymer Science*, 101(5):3336–3342, 2006.

S. T. Ho and D. W. Hutmacher. A comparison of micro CT with other techniques used in the characterization of scaffolds. *Biomaterials*, 27(8):1362–76, 2006.

A. Hoppe, R. Meszaros, C. Stähli, S. Romeis, J. Schmidt, W. Peukert, B. Marelli, S. N. Nazhat, L. Wondraczek, J. Lao, E. Jallot, and A. R. Boccaccini. In vitro reactivity of Cu doped 45S5 Bioglass® derived scaffolds for bone tissue engineering. *Journal of Materials Chemistry B*, 1(41):5659, 2013.

A. Hoppe, B. Jokic, D. Janackovic, T. Fey, P. Greil, S. Romeis, J. Schmidt, W. Peukert, J. Lao, E. Jallot, and A. R. Boccaccini. Cobalt-Releasing 1393 Bioactive Glass-Derived Sca ff olds for Bone Tissue Engineering Applications. *ACS Applied Materials and Interfaces*, 6 (4):2865–2877, 2014.

L. Ji, W. Wang, D. Jin, S. Zhou, and X. Song. In vitro bioactivity and mechanical properties of bioactive glass nanoparticles/polycaprolactone composites. *Materials Science and Engineering C*, 46:1–9, 2015.

V. Karageorgiou and D. Kaplan. Porosity of 3D biomaterial scaffolds and osteogenesis, 2005.

T. Kokubo and H. Takadama. How useful is SBF in predicting in vivo bone bioactivity. *Biomaterials*, 27(15):2907–2915, 2006.

References

J. I. Lim and H. K. Park. Fabrication of macroporous chitosan/poly(L-lactide) hybrid scaffolds by sodium acetate particulate-leaching method. *Journal of Porous Materials*, 19 (3):383–387, 2012.

G. A. Mannella, F. Carfì Pavia, G. Conoscenti, V. La Carrubba, and V. Brucato. Evidence of mechanisms occurring in thermally induced phase separation of polymeric systems. *Journal of Polymer Science, Part B: Polymer Physics*, 52(14):979–983, 2014.

V. Maquet, A. R. Boccaccini, L. Pravata, I. Notingher, and R. Jérôme. Preparation, characterization, and in vitro degradation of bioresorbable and bioactive composites based on Bioglass(R)-filled polylactide foams. *Biomed Mater Res A*, 66A:335–346, 2003.

V. Maquet, A. R. Boccaccini, L. Pravata, I. Notingher, and R. Jérôme. Porous poly(alpha-hydroxyacid)/Bioglass composite scaffolds for bone tissue engineering. I: Preparation and in vitro characterisation. *Biomaterials*, 25(18):4185–94, 2004.

H. Y. Mi, X. Jing, M. R. Salick, T. M. Cordie, X. F. Peng, and L. S. Turng. Morphology, mechanical properties, and mineralization of rigid thermoplastic polyurethane/hydroxyapatite scaffolds for bone tissue applications: Effects of fabrication approaches and hydroxyapatite size. *Journal of Materials Science*, 49(5):2324–2337, 2014.

Y. Pang and X. Bao. Influence of temperature, ripening time and calcination on the morphology and crystallinity of hydroxyapatite nanoparticles. *Journal of the European Ceramic Society*, 23(10):1697–1704, 2003.

J. L. Ryszkowska, M. Auguścik, A. Sheikh, and A. R. Boccaccini. Biodegradable polyurethane composite scaffolds containing Bioglass® for bone tissue engineering. *Composites Science and Technology*, 70(13):1894–1908, 2010.

T. Tian, D. Jiang, J. Zhang, and Q. Lin. Fabrication of bioactive composite by developing PLLA onto the framework of sintered HA scaffold. *Materials Science and Engineering: C*, 28(1):51–56, 2008.

X. Wang, G. Song, and T. Lou. Fabrication and characterization of nano composite scaffold of poly(L-lactic acid)/hydroxyapatite. *Journal of materials science. Materials in medicine*, 21(1):183–8, 2010.

A. Zanotto, M. L. Saladino, D. C. Martino, and E. Caponetti. Influence of Temperature on Calcium Hydroxyapatite Nanopowders. *Advanced in Nanoparticles*, (1):21–28, 2012.

S. Zhou, X. Zheng, X. Yu, J. Wang, J. Weng, X. Li, B. Feng, and M. Yin. Hydrogen Bonding Interaction of Poly(d,l-Lactide)/hydroxyapatite Nanocomposites. *Chemistry of Materials*, 19(2):247–253, 2007.

Chapter 5

Static cell cultures

Cell culturing in the scaffold is one of the crucial point to consider a particular biomaterial suitable for tissue engineering. In the thesis work cell culture experiments were performed by using mesenchymal stem cells, chondrocytes and osteoblasts in various PLLA-based scaffold.
In-vitro tests of chondrocytes seeded on PLLA scaffold and PLL/BG scaffold in the prof. Gundula Schulze-Tanzil's laboratory at the Paracelsus Medizinische Privatuniversitat were carried out. Biological evaluation of gradient pore scaffolds with mesenchymal stem cells in the prof. Rocky Tuan's laboratory at the University of Pittsburgh were realized.

5.1 Chondrocytes in PLLA scaffolds

Cell functions as well as new tissue regeneration is strictly dependent on the size of the pores. It is possible to find in literature many works documenting the influence of the pore size in a porous scaffold for tissue engineering, but with different opinions. Some papers report that a larger pore size promotes the production of cartilaginous matrix (Zhang et al., 2014), whereas other papers assert that smaller pore sizes enhance the chondrocyte phonotype and proliferation (Oh et al., 2010).
The different results are due to a complex combination of factors in the 3D culture, such as nutrient diffusion, but also exchange and removal of metabolic waste during cell culture. In any case PLLA scaffolds, were produced via TIPS with two different pore dimensions, 100 µm and 200 µm, respectively to evaluate the influence of the microtopography.

5.1.1 Scaffold production and analysis techniques

Starting from the same ternary solution, the two types of scaffolds were obtained following two slightly different thermal histories. Initially the solution was kept above 60°C to ensure the homogeneity, then poured in a cylindrical high density polyethylene (HDPE) mould and placed in a thermal bath.
For PLLA with 100 micron sized pores (PLLA-100), the mould was maintained at 25°C for 45 minutes, for PLLA with 200 micron sized pores (PLLA-200), at 32°C for 75 minutes.
Thereafter, the solution was immersed in an ethanol bath at -20°C for more than 20 minutes to allow the complete freezing of the obtained morphology. Finally, the foams were washed in distilled water and esiccated under vacuum for 24 hours to ensure the whole removal of any solvent trace.
Scaffold pore size and topography were analyzed via SEM (Phenom ProX, Phenom-World, Netherlands) at 5 kV along the cross section. The samples were cut by means of a razor blade to avoid the collapse of the structure and mounted in an aluminum stub. The porosity was measured via gas pycnometer and evaluated as the average of three replica (section 4.2.2).

5.1.2 Chondrocyte isolation and cell seeding

Donors of human articular chondrocytes were males (n=2) and females (n=4) with an average age of 71.6 years (range 64-74) who underwent knee joint or hip joint replacement surgeries. Donors of human hyaline nasoseptal cartilage (n=11) with an average age of 36.55$\pm$14.01 years (range 18-63). This sampling was approved by the Charite-Universitatsmedizin ethical committee/review board for experiments with human derived tissues. The harvested cartilage chips were digested by pronase E derived from Streptomyces griseus at 20 mg/mL (6 U/mg, Serva Electrophoresis GmbH, Heidelberg, Germany) in Ham's F-12/Dulbecco's modified Eagle's medium (DMEM) (50/50, Merck KGaA, Darmstadt, Germany) for 30 minutes at 37°C. Then, the samples were incubated with collagenase NB5 derived from Clostridium histolyticum (1 mg/mL, Sigma Aldrich) in chondrocyte growth medium overnight. Isolated chondrocytes were resuspended in growth medium (96% (v/v) DMEM/Ham's F-12 (1:1) with stable L-glutamin, 1% (v/v) amphotericin B, 1% (v/v) MEM-amino acids, 1% (v/v) penicillin/streptomycin, 1% (v/v) ascorbic acid supplemented with 10% fetal calf serum (FCS).
Before seeding, the chondrocytes were expanded in T175 flasks.
Scaffolds (cylindrical shape, 4 mm diameter and 3.5 mm) were seeded by using at a cell density of 25000 chondrocyte/mm^3 in 80 µl. The scaffolds were sterilised adopting 70% ethanol overnight and preconditioned by abundantly rinsing in PBS and finally in FCS for 24

hours.To guarantee a uniform distribution of cells in the sample, the seeding was mede in two steps: 40 µL of cell suspension on the top of the scaffold and then after 20 minutes this latter was turned upside down and seeded with the remaining 40 µL.
Seeded scaffolds were cultured in 6 well plates coated with cell culture suitable agarose (1%, Sigma-Aldrich) with 5 mL of growth medium for each well. Medium was changed every 3 days. Cells were cultured on the scaffolds for 1 day, 7 days or 14 days.

5.1.3 Live/dead assay

Cell vitality of colonized scaffolds was determined after 7 and 14 days. Live-death staining was performed using fluorescein diacetate (FDA, Sigma-Aldrich) combined with ethidium bromide (EtBr, Carl Roth GmbH) or propidium iodide (PI, Sigma-Aldrich) staining. Seeded scaffolds were incubated in the FDA/EtBr or FDA/PI staining solution and examined under DMi8 confocal laser scanning microscope (Leica, Wetzlar, Germany).

5.1.4 Histological staining and immunolabeling

In order to carry out histological staining and immunolabeling the scaffolds were fixed for 1 day with a 4% paraformaldehyde (PFA) and stored at 4°C. They were dehydrated in ascending alcohol series before embedded in paraffin and cut in section of 5 µ.
For HE staining sections were incubated for 6 minutes in Harry‘s hematoxylin (Sigma-Aldrich), before rinsed in water and counterstained for 4 minutes in eosin (Carl Roth GmbH, Karlsruhe, Germany).
To perform AB staining the sections were incubated for 3 minutes in 1% acetic acid and then incubated for 30 minutes in 1% AB (Carl Roth GmbH). Subsequently, after rinsing in 3% acetic acid and 2 minutes washing in distillate water, cell nuclei were counterstained in nuclear fast red aluminium sulphate solution (Carl Roth GmbH) for 5 minutes.
Two immunolabeling protocols were carried out. For the first one, the sections or small segments of the scaffolds (2 mm) were washed with Tris buffered saline (TBS: 0.05 M Tris, 0.015 M NaCl), overlaid with protease-free donkey serum (5% diluted in TBS) for 20 minutes at room temperature, permeabilized by 0.1% Triton X-100 for 6 minutes, rinsed and incubated with primary antibodies type I collagen and type II collagen for 1h at room temperature. Controls without primary or secondary antibody were also included. For the second immunolabeling donkey-anti-goat-Alexa-488 (Invitrogen, Ca, USA) or donkey-anti-rabbit-Alexa-cy3 (Invitrogen) coupled secondary antibodies were adopted. Cell nuclei were counterstained using 4’,6’-diamidino-2-phenylindol (DAPI, Roche, Mannheim, Germany) and phalloidin-633 (1:100, Santa Cruz Biotechnologies,) to depict cytoskeletal actin architec-

ture.
In both cases the sections were examined unger DMi8 confocal microscope.

5.1.5 Gene expression analysis

At 7 and 14 days the seeded scaffold were snap frozen and then crushed using mortar and pistil in liquid nitrogen. The frozen scaffold powder was suspended in 1 ml Qiazol and homogenized using an ULTRA-Turrax rotor stator. Then, 0.2 mL 1-bromo-3-chloro-propane was added and samples were centrifuged at 12.000 g for 15 minutes. The upper phase was combined with a similar volume of 70% ethanol. Samples were further processed as recommended for the RNeasy Mini Kit (Qiagen) without on-column DNase digestion step. Quality and quantity of the RNA of all samples were determined with the Nanodrop ND-1000 spectrophotometer.
The cDNA was reverse transcribed using the QuantiTect Reverse Transcription Kit (Qiagen) according to the manual. 6 ng cDNA were used for each quantitative real-time PCR (qRT-PCR) reaction using TaqMan Gene Expression Assays (Life Technologies) with primer pairs for type II collagen (COL2A1), aggrecan (ACAN) and SOX9. qRT-PCR was performed using the real time PCR detector StepOnePlus (Applied Bioscience [ABI], Foster city, USA) thermocycler. The primers was supplied by Applied Biosystems with the following NCBI Gene Reference: $COL2A1 - Hs00264051\_m1$, $ACAN - Hs00202971\_m1$, $SOX9 - Hs00165814\_m1$. The relative gene expression was normalized to the 18S expression and calculated for each sample using the $\Delta\Delta$ CT method described by Livak and Schmittgen (Livak and Schmittgen (2001). A scaffold seeded in the same condition and evaluated at the first day was adopted as a reference for qRT-PCR.

5.1.6 Results

Scaffold morphology

The dimensions of the round or ovoid pores were evaluated using SEM (fig. 5.10).

PLLA-100 presents average pore sizes of 100 µm, while PLLA-200 average pore sizes of 200 µm. Both topographies showed the presence of micropores, from 10m to 40m, in the wall of the large pore size. This aspect enhances the interconnection of the scaffold ensuring nutrients and metabolites exchange.
PLLA-100 was fabricated at 25°C. As reported in a previous work (Mannella et al., 2014) this temperature is on the boundary between the binodal and the spinodal region, when the

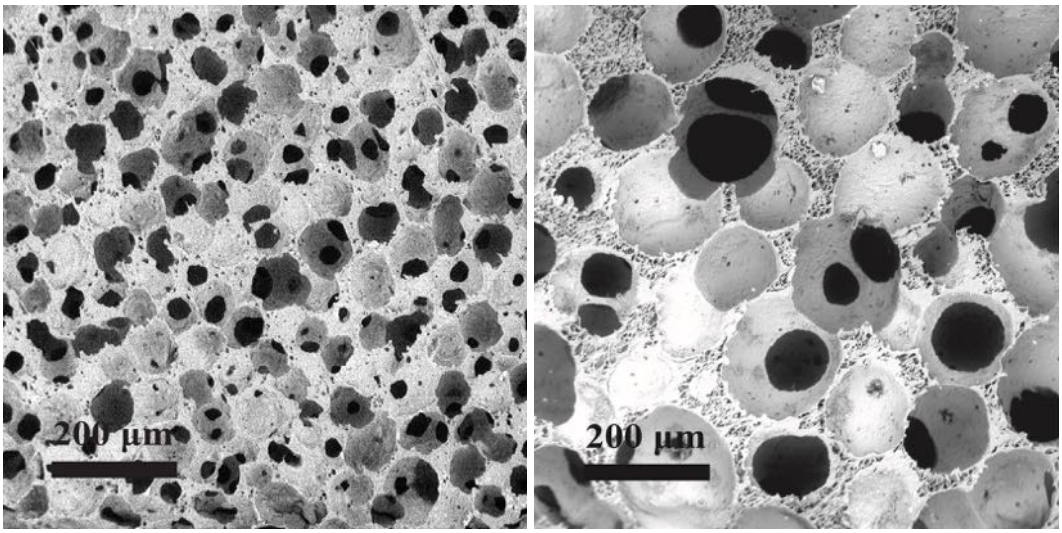

(a) (b)

Fig. 5.1 *SEM micrographs of the adopted PLLA scaffold topography. a)PLLA scaffold average pore dimension 100µm, b) PLLA scaffold average pore dimension 200 µm*

nucleation-growth and spinodal decomposition, respectively, occur. In the mechanism of nucleation-growth the dimension of pore size is strictly related on time. In the second case, spinodal region, there is no formation of cluster and then, a mechanism of coalescence, but the decomposition is determined solely by diffusion. The tuning of these factors allows the formation of a scaffold with a high degree of interconnection (the major part of large pores present interconnecting channels of larger than 10 µm) and a good control of pore size. For the production of PLLA-200 temperature of 32°C and 75 minutes were chosen to obtain pore dimensions almost double compared to PLLA-100. Under this condition the solution is within the metastable zone and the higher demixing time allows the widening of the pores. In both scaffolds, the porosity evaluated via gas pycnometer was $93\pm0.2\%$. The phase separation, indeed, basically does not influence the porosity of the material, this latter depends on the initial solution concentration.

Cell viability

Live/dead staining was used to prove cell survival within the two different foams. The green marker, FDA, labels the viable cells, whereas the red markers, EtBr or PI, indicate the dead cells or the scaffold. Fluorescence micrographs via confocal microscope were taken after 1 and 2 weeks of culture. The vitality assay showed that the majority of the chondrocytes were still alive within all foams during the two weeks of observation time (figs. 5.2, 5.3). It could also be noticed that chondrocytes rapidly attached and spread over the surface of the scaffolds.

At day 7 (fig. 5.2a,b) there was already a large amount of cells on the scaffolds with mostly live cells (green cytoplasmic fluorescence) and few dead cells (red nuclear fluorescence). The confocal images highlight the topography of the scaffold, the cells, indeed, spread around the pore and in most cases it is possible to individuate a flattened or elongated shape of the cells with many attachment points to the scaffold, which indicates a very good cytocompatibility. At day 14 (fig. 5.2c,d), an even larger amount of the surface was covered with viable cells in the two scaffold types. In particular, the surface of the scaffold PLLA-100 is essentially completely covered by viable cells. On PLLA-200, despite the surface is not so plentifully bestrew, caused also from the larger pore, the amount of viable cells after 14 days is much higher compared to 7 days. In this case, the autofluorescence of the scaffold is more evident.

Similar behaviour to that observed with articular chondrocytes is recognisable in the scaffolds seeded with nasoseptal chondrocytes. After 7 or 14 days the scaffold were cut along the frontal plane with a razor blade, stained with FDA/PI and cell viability was evaluated on the cross section. The figure 5.3 shows the cell distribution and viability inside the scaffold for both types of scaffolds and both time points. After 7 days the cells adhered and spread inside the scaffolds. Qualitative analysis of numbers of cells attached and spreading on each scaffold type revealed that after 14 days the number is higher compared to the previous time point and the PLLA-100 better supports cell proliferation.

Histological and ECM expression

After the chondrocyte/scaffold constructs were cultured for 2 weeks, they were retrieved and histologically examined via alcian blue (fig. 5.4). The positive staining indicated the presence of cartilage-specific sulfated glycosaminoglycan in the constructs. On PLLA-100 the chondrocyte spread from the surface of the scaffold towards the inner part, creating a dense layer. On PLLA-200 the cells penetrated more deeply compared to PLLA-100 but presented a less evident AB staining.

For both scaffold topographies, typical chondrocyte morphology could be clearly seen via HE staining, in fig. 5.5 A greater number of round morphological chondrocytes were observed in the PLLA-100 than in the PLLA-200. As obvious the chondrocytes were attached to the polymer skeleton of the scaffold and cell-cell interactions were evident.

In order to evaluate the ECM protein expression, two different immunohistochemical analysis were carried out. The confocal micrographs were taken after the articular chondrocytes have been cultured for 1 weeks on the scaffolds. In figure 5.6 type I (green) and type II

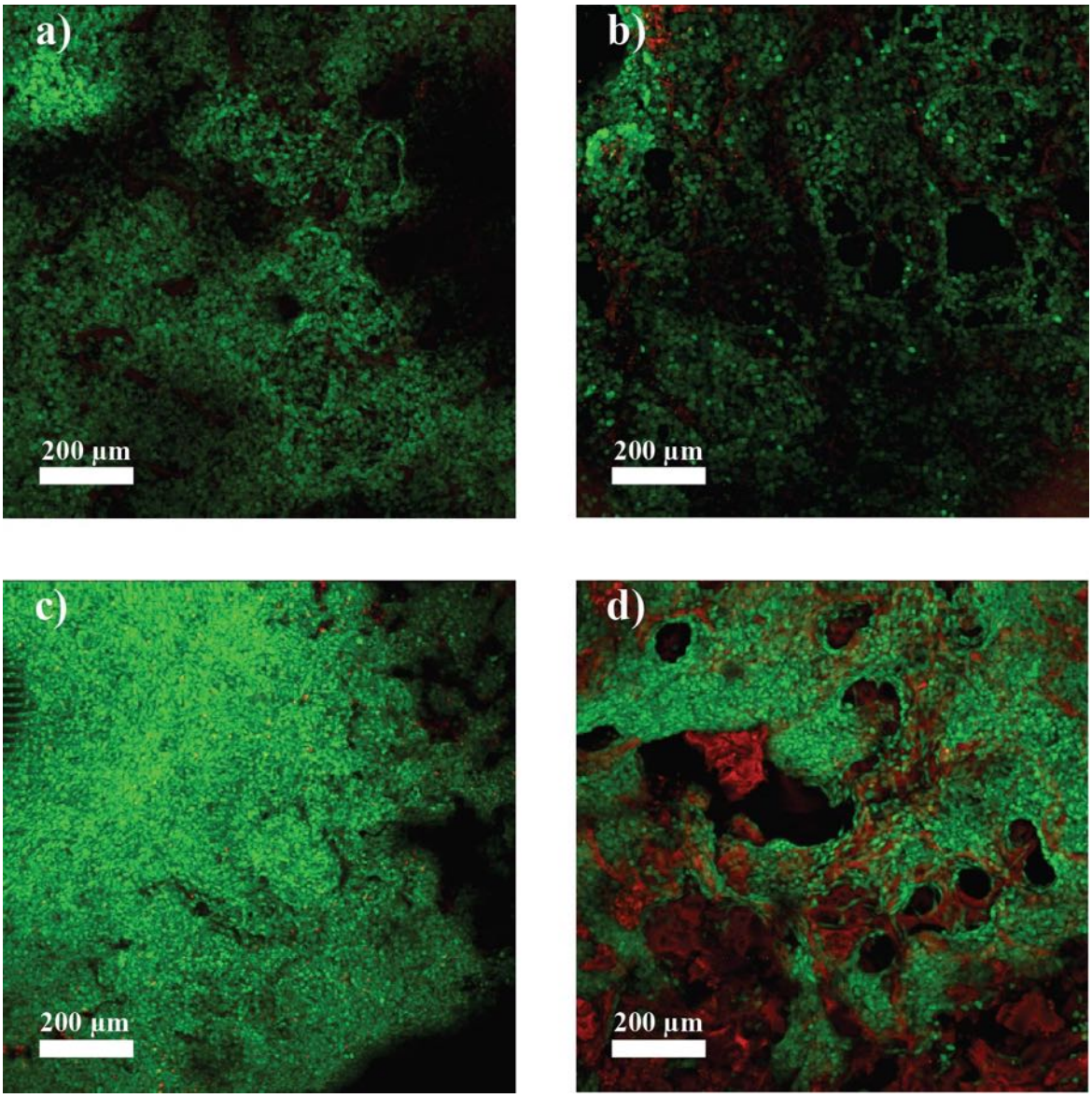

Fig. 5.2 *Cell viability of articular chondrocytes on different scaffolds and time points. a) PLLA-100, 7 days cell culture, b) PLLA-200, 7 days cell culture; c) PLLA-100, 14 days cell culture, d) PLLA-200, 14 days cell culture*

(red) collagen staining is reported. The nuclei were stained in blue with DAPI. Assessment of collagen types I and II was qualitative and was based on evaluation of the abundance of collagen types I and II present around and between the cells within the two foams. The large amount of type II collagen spread within and on the surface of the scaffold indicates the high synthetic activity of the chondrocytes. In particular, type II collagen allows the formation of the fibrils that provide the adequate tensile strength to the tissue. As previous result, the

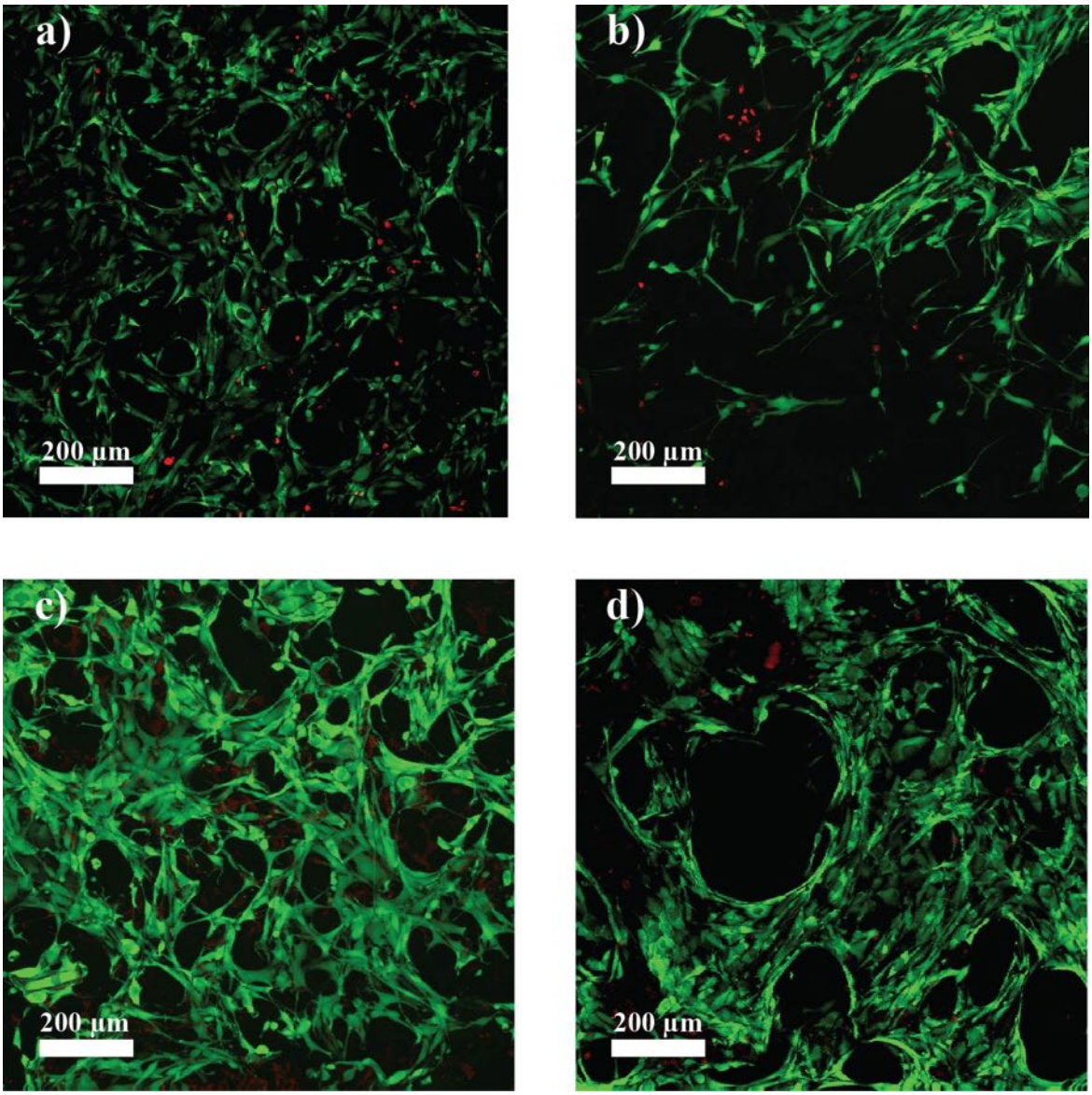

Fig. 5.3 *Cell viability of nasoseptal chondrocytes on different scaffolds and time points. a) PLLA-100, 7 days cell culture, b) PLLA-200, 7 days cell culture; c) PLLA-100, 14 days cell culture, d) PLLA-200, 14 days cell culture*

PLLA-100 scaffold shows a higher cell density probably due to a more compact topography.

The second staining is reported in figure 5.7, SOX9 was labeled in red, in green the proteoglycan expression was depicted. DAPI counterstained the cell nuclei in blue. The presence of sulfated glycosaminoglycans is a generally accepted indicator of the differentiated phenotype of chondrocytes. The presence of the immunolabeled markers could be clearly shown, DAPI and SOX9 inside the cell and proteoglycans within the ECM. On PLLA-100

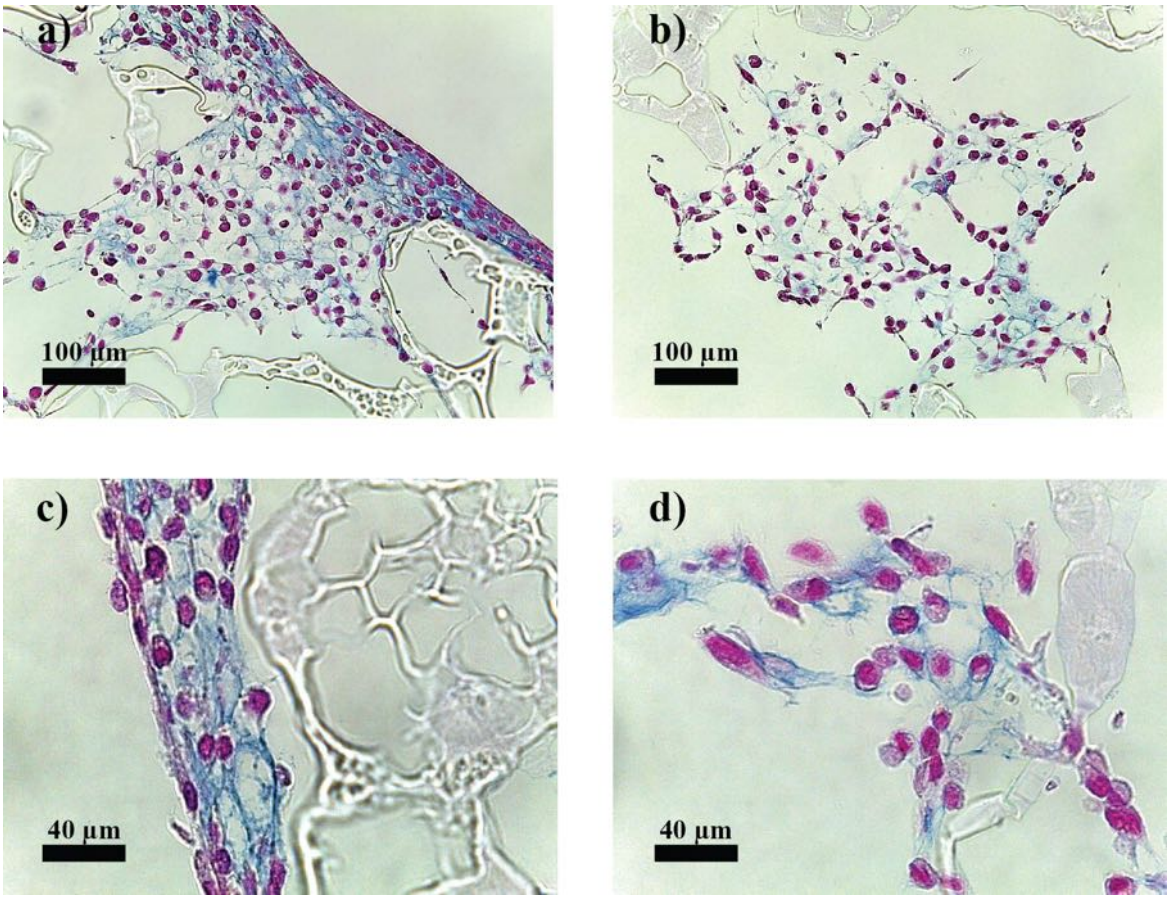

Fig. 5.4 *Alcian blue staining at 14 days. In reddish pink nuclei, in blue sGAG. a), c) PLLA-100; b), d) PLLA-200*

the presence of SOX9 is less apparent inside the scaffold owing to the strong blue staining of DAPI.

Gene expression

To further investigate the chondrocyte differentiation in the foams, real-time PCR analysis was carried out. Three positive markers for chondrogenic differentiation were adopted: type II collagen (important marker of cartilage), aggrecan (major proteoglycan in the articular cartilage) and SOX9 (principal transcription factor for chondrogenic genes). The results of PCR analysis after 7 days and 14 days were reported in figure 5.8. For each time point, 7 or 14 days, the gene expression of PLLA-100 were higher than the corresponding PLLA-200 and in particular the results was significant for ACAN and SOX9 at both investigated time points. Furthermore at 14 days the gene expression was always more expressed of the analogous at 7 days. This difference was significant for SOX9 for both time points and PLLA-100 for

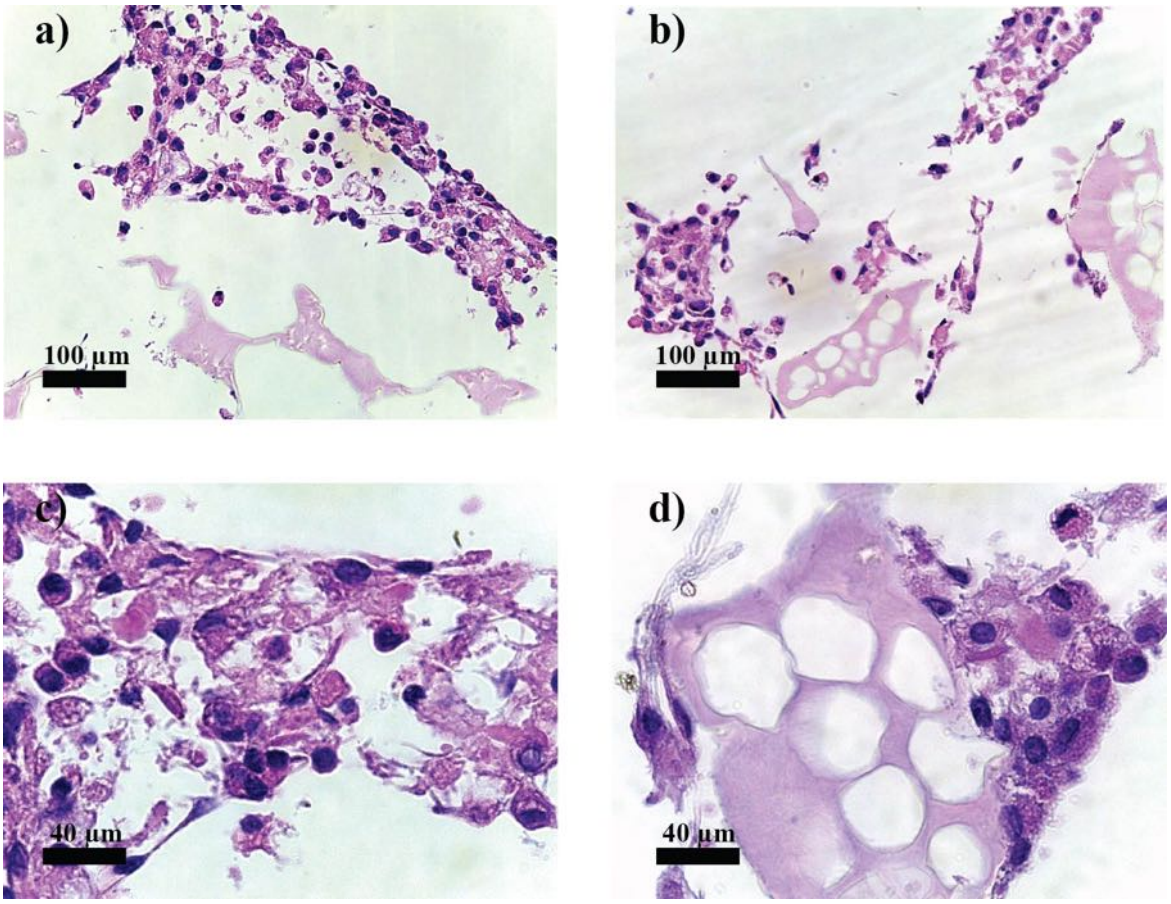

Fig. 5.5 *HE histological staining at 14 days. a), c) PLLA-100; b), d) PLLA-200*

ACAN. Particularly relevant is the increasing of SOX9, passing from 1 week to 2 weeks the upregulation is almost fivefold. The PCR results showed that the PLLA scaffold allowed the expression of cartilaginous genes in both variants as time passes. The gene expressions of type II collagen, aggrecan and SOX9 significantly decreased with the increasing of the scaffold pore size to 200 µm.

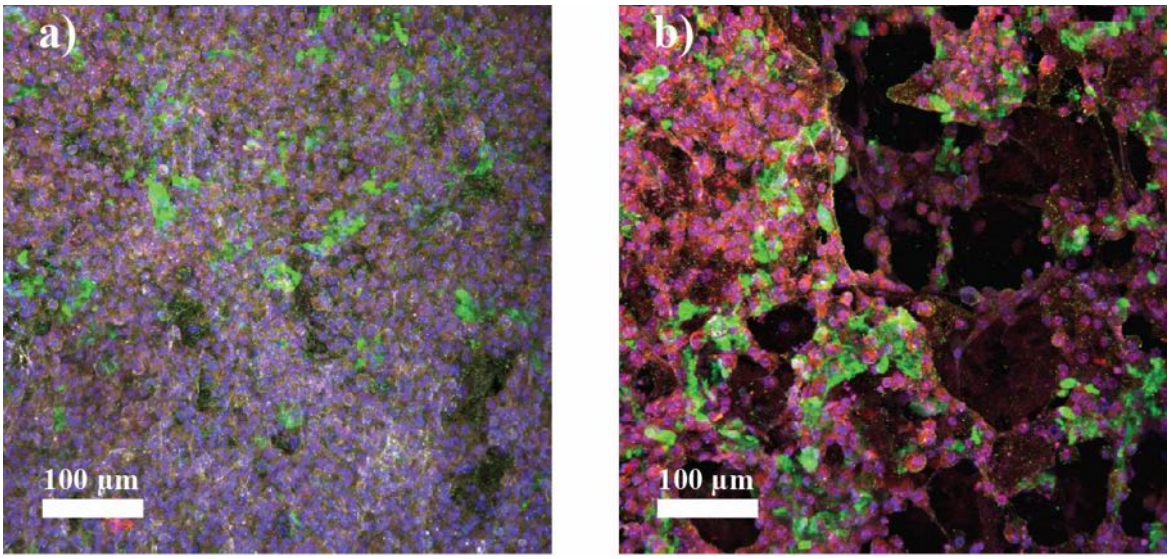

Fig. 5.6 *Immunohistochemical analyses of ECM synthesis after 7 days from the seeding. Red -Type II collagen, Green- Type I collagen, Blue-Nuclei. a) PLLA-100, b) PLLA-200*

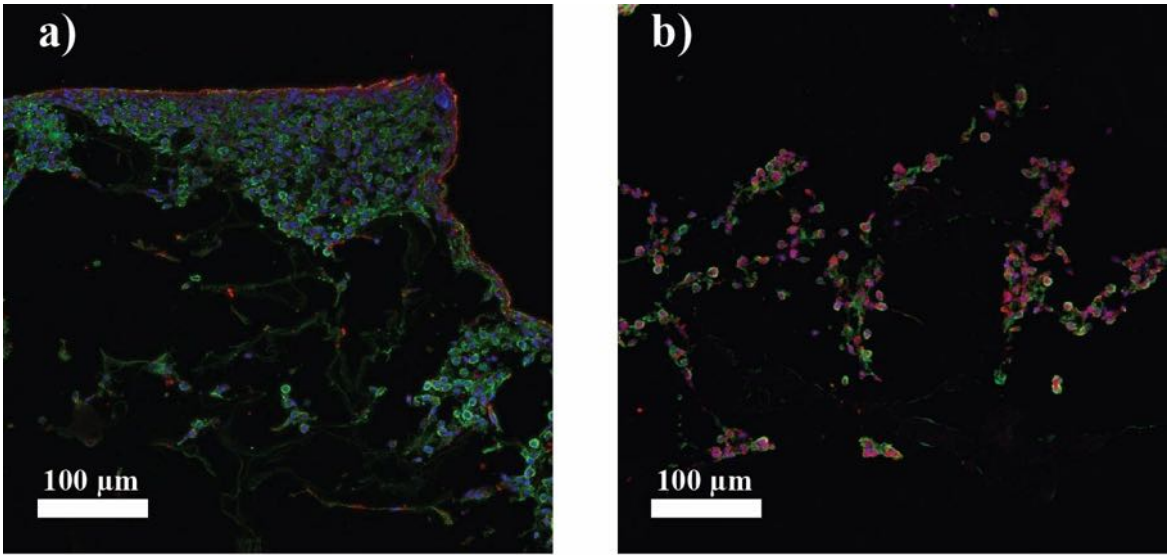

Fig. 5.7 *Chondrogenic gene expression at 7 days of cell culture: SOX9 (Red), PG (Green), Nuclei (Blue). a) PLLA-100, b) PLLA-200*

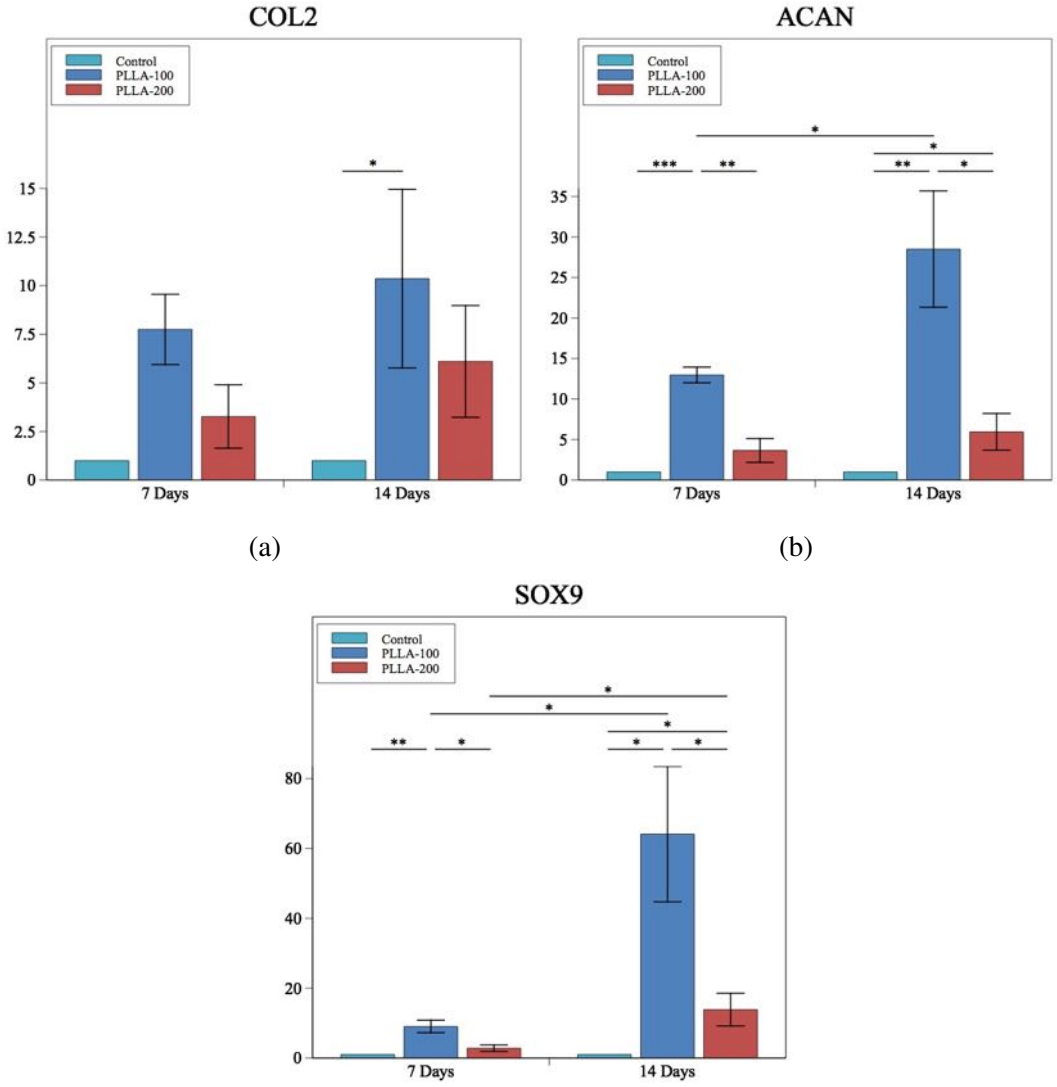

Fig. 5.8 *Gene expression of type II collagen (a), aggrecan (b) and SOX9 (c) in the two different type of scaffolds, PLLA-100 and PLLA-200 after 7 and 14 days. Significant difference: *p<0.05; **p<0.01; ***p<0.001*

5.2 Mesenchimal Stem Cell in gradient pore scaffolds

5.2.1 Mesenchimal Stem Cell (MSCs)

Mesenchymal stem cells were described for the first time, by Friedenstein and Petrakov in 1966, as progenitors derived from the stromal fraction of rat bone marrow (Jackson et al., 2007). Meanwhile the definitive evidence for the presence in adult bone marrow able to grow in the form of fibroblasts and to differentiate into various mesenchymal elements arrived by Friedenstein et al. (1976) in the mid-70. Numerous studies have subsequently confirmed the multipotentiality of these cells. In the presence of appropriate stimuli, they differentiate into adipocytes (with cytoplasmic vacuoles containing lipids), osteoblasts (with the deposition of hydroxyapatite crystals), chondrocytes (with synthesis of the cartilage matrix), and muscle cells (rich in myotubes) (Jiang et al., 2002). MSCs are relatively rare cells in the bone marrow ($1/10^5$ nucleated cells), preserving the stem properties (Javazon et al., 2004). They are able to express the genes of embryonic origin, to synthesise cell-cell contact molecules and components of the extracellular matrix such as collagen and fibronectin, to secrete cytokines such as interleukin IL-7, IL-8, IL-11, stem cell factor (SCF) and stromal-derived-factor-1 (SDF-1), that regulate the mobilisation of hematopoietic stem cells from the marrow. For this reason, MSCs play the essential role of homeostatic compartment of bone marrow stromal cells, constantly renewing the microenvironment required for hematopoiesis. Moreover, given their derivation from intra-embryonic mesoderm, the MSCs are able to differentiate in several lineages in addition to those lines of the osteogenic (Arpornmaeklong et al., 2009; Birmingham et al., 2012), adipogenic (Jackson et al., 2007; Rodríguez et al., 2008), chondrogenic (Bhardwaj and Kundu, 2012; Huang et al., 2015) and muscle (Meligy et al., 2012), such as endodermal cells (hepatocytes, pneumocytes) and ectodermal (cells nerve, glial cells) (Jamnig and Lepperdinger, 2012; Tseng and hui Hsu, 2014; Wang et al., 2016). This pluripotency, however, is progressively lost as a result of the process of senescence (Cheng et al., 2011). Tests were carried out in a murine model of osteogenesis imperfecta, a congenital disease of mesenchymal tissue, characterised by ossification defect. In this case MSCs from bone marrow were injected in the bone, obtaining functionally bone and cartilaginous tissue (Kadiyala et al., 1997). Positive results of injection of MSCs were found also in clinical test: MSCs were infused in children with ostogenesis imperfecta; three months later the cells rooted without side effect, with an increase of osteoblastic component and formation of new lamellar bone (Horwitz et al., 1999).

For example in order to develop an osteoblastic phenotype, MSCs are cultured in medium supplemented with ascorbic acid (AA), β-glycerophosphate (βGP), and dexamethasone (DEX) (Haynesworth et al., 2016). Three phases can be distinguished in differentiation of

osteblastic phenotype. During the proliferation phase (first or growth phase) cells tend to express mRNA for related growth proteins including c-fos, histone, c-myc, transforming growth factor-β (TGF-β), procollagen I, and fibronectin (Siggelkow et al., 1999). During the matrix maturation (second phase) phase cells differentiate into osteoblasts and secrete alkaline phosphatase (ALP) and produce type I collagen (Togel and Westenfelder, 2011). Finally, mineralisation is marked by the secretion of collagenous proteins including osteopontin (OPN), osteocalcin (OC), bone sialoprotein (BSP), and deposition of calcium/phosphate minerals (Stein and Lian, 1993).

5.2.2 Scaffold preparation

PLLA (MW=114000 kg/mol), 1,4-dioxane (Sigma-Aldrich) and distilled water were used to produce the PLLA scaffold. The ternary solution employed has a PLLA concentration of 4 % wt, in 87/13 wt/wt dioxane/water (solvent/non-solvent). Different thermal histories were imposed on sample sides by an experimental apparatus made in-house using software controlled Peltier cells (chapter 3). Starting from a solution kept at 60°C for 10 minutes (well above the cloud point), one side (Slow Cooling Side - SCS) was cooled at 1°C/min to 30°C and maintained for 20 minutes, whereas the other surface (Fast Cooling Side - FCS) was suddenly cooled to 30°C, and held for 50 minutes. At the end, the solution was rapidly quenched to -20°C to freeze the so-obtained microstructure. Thus, to completely remove the solvents, the foams were washed in deionised water and drying under vacuum. A schematisation of the thermal history imposed on two side of the sample is depicted in figure 5.9.

5.2.3 Cell seeding

Utilizing a protocol approved by the Thomas Jefferson University Institutional Review Board, human MSCs extract from bone marrow (hbMSCs) were isolated from healthy donors with the patients consent (Hu et al., 2009).
An aliquot of bone marrow was harvested from the iliac crest, filtered through a 40 µm strainer and the flow-through was centrifugated at 300g for 5 min to sediment the red blood cells. The pellets were suspended using growth medium DMEM containing: 10% FBS (Invitrogen), 2% antibiotics-antimycotic, 1% Sodium Pyruvate, 4.5 g/L D-Glucose, 4 mM L-Glutamine and 25 mM HEPES and then plated into 150 cm^2 tissue culture flasks at a density of 10^6 cells/flask.
The medium was changed every 3 to 4 days. Once 70% to 80% confluence was reached, cells were passaged. The colony formation and trilineage mesenchymal differentiation capacity

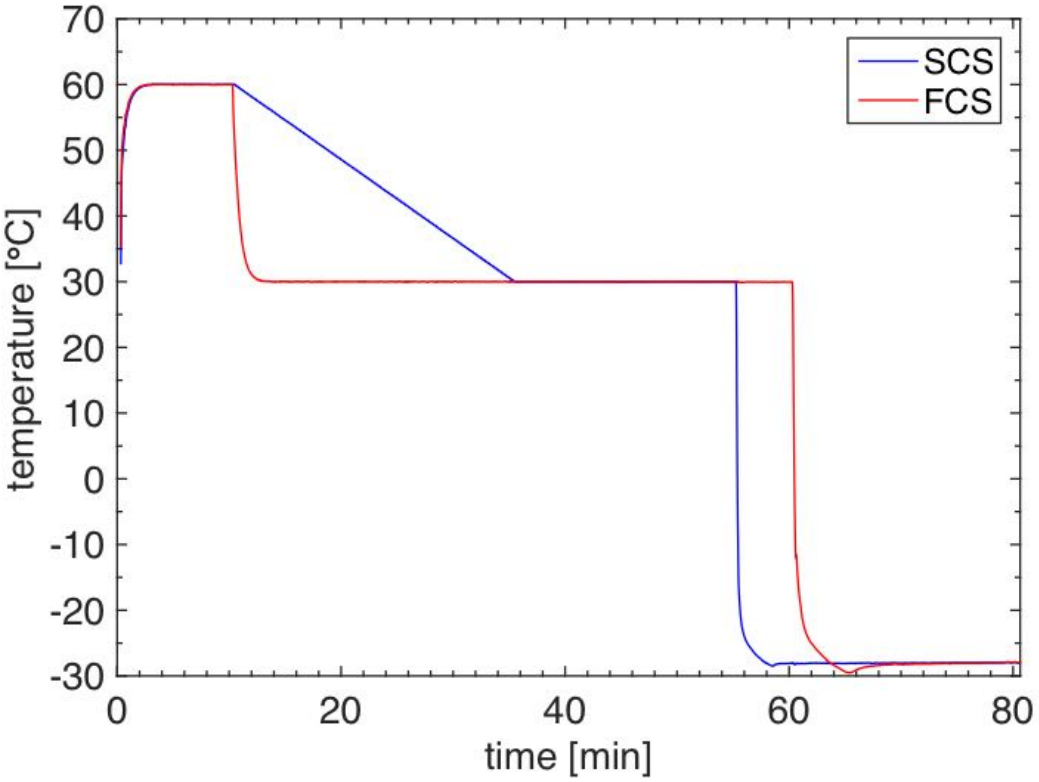

Fig. 5.9 *Thermal history. SCS: Slow Cooling Side, FCS: Fast Cooling Side*

of hBMSCs was validated before use. For the preliminary tests different hMSCs were used, from a female patient 45 years old and two male patients 45 and 59 years old.
$8 * 10^5$ mesenchymal stem cells were seeded per PLLA scaffold. The scaffolds were preconditioned by soaking in DMEM cell culture medium overnight, after an overnight in ethanol 70% to allow the sterylization. The cells were seeded in static conditions by injecting them with a pipette.

5.2.4 Live/dead and MTS assay

Scaffolds were harvested at days 1, 3 and 7 of culture, rinsed in PBS and stained with ethidium homodimer-1 and calcein to perform a live/dead stain (abcam, ab115347). The images were taken under a SZX16 Olympus Stereomicroscope. Stereomicroscopy is a fast and simple method that allows the characterisation of cells in their medium. If performed quickly, it can be used to illustrate the cells that are dead and alive. It does not offer however, information on 3D distribution. Live cells are identified on the basis of intracellular esterase

activity (generating green fluorescence) and exclusion of the red dye. Dead cells are identified by the lack of esterase activity and non-intact plasma membrane which allows red dye staining.
Furthermore to evaluate from a quantitative point of view the cell proliferation rate the MTS assay (abcam, ab197010) was adopted. MTS (3 - (4,5 - dimethylthiazol - 2 - yl) - 5 - (3carocymethoxyphenyl - 2 - 4 - (sulfophenyl) - 2H - tetrazolium) assay is a colorimetric method to determine the number of viable cells in culture. The yellow MTS tetrazolium compound is reduced to a brown formazan product that is soluble in culture medium. This conversion is achieved by NADPH which is produced by dehydrogenase enzymes in metabolically active cells. After incubating for 3-4 hours at 37°C, three 100 µl samples were pipetted out from the scaffolds and absorbance was read at 490 nm.

5.2.5 Results

Scaffold morphology

In figure 5.10 the SEM micrograph of the adopted scaffold is reported.

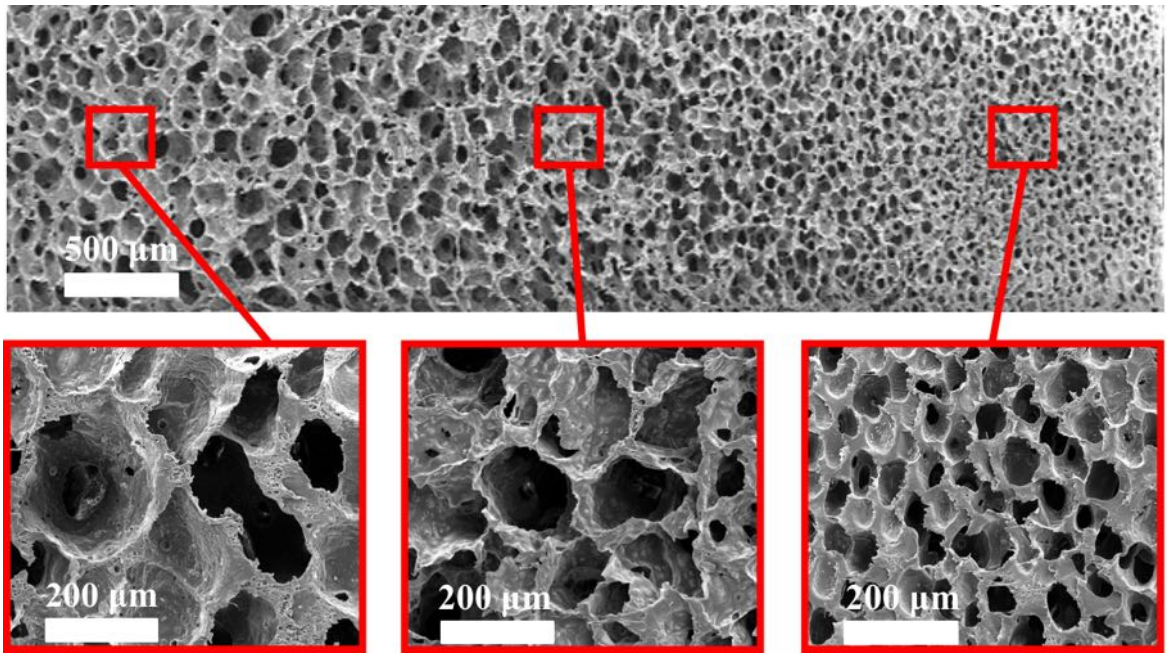

Fig. 5.10 *SEM micrograph of the PLLA gradient scaffold adopted. a) FCS - 200 µm; b) 140 µm; c) SCS - 70 µm*

The scaffold presents an average pore dimension of 200 µm on the fast cooling side (left side) and gradually decrease, 140 µm in center, up to 70 µm on the slow cooling side (right side). It can be ideally divided in three sections, equally distributed.

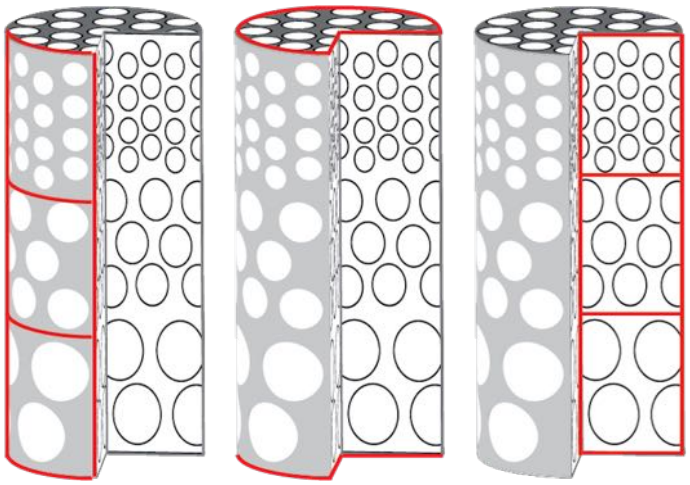

(a) (b) (c)

Fig. 5.11 *Schematic representation of different parts of the scaffolds analysed via Live/Dead cell viability assay in PLLA scaffold*

Cell viability

Samples via Live/Dead were analysed on side of the scaffold (fig. 6.18a), top/bottom (fig. 6.18b) and cross section (fig. 6.18c).

As an example the live/dead assay after 7 days of cell culture was reported. Fig. 5.12 reports the assay at 7 days on side and the cross section of the scaffold, fig. 5.13 reports the upper and lower surface.

Comparing the images between side of the scaffold and cross section the difference of cell viability is evident. On the side there are much more live cells than of the cross section. The static cell culture do not facilitate the penetration of the medium and than the proliferation and growth of the cells. As expected, large pore sizes imply a larger presence of live cell but, in any case, the few amount of dead cells in the small pore size portion of the scaffold is a good results. Analogous behavior was recognized on the top and the bottom of the scaffold, the amount of live cells largely overcome dead cells.

MTS assay

To evaluate the cell proliferation following the supplied protocol a preliminary calibration curve was calculated. $10^4 - 5*10^4 - 10^5 - 4*10^5 - 8*10^5$ cells were counted and seeded in different wells in triplicate. After 24 hours of incubation 20 µL/well MTS reagent into each well were added and incubated for 4 hours at 37°C. Figure 5.14 shows the calibration curve with an $R^2 = 0.99499$.

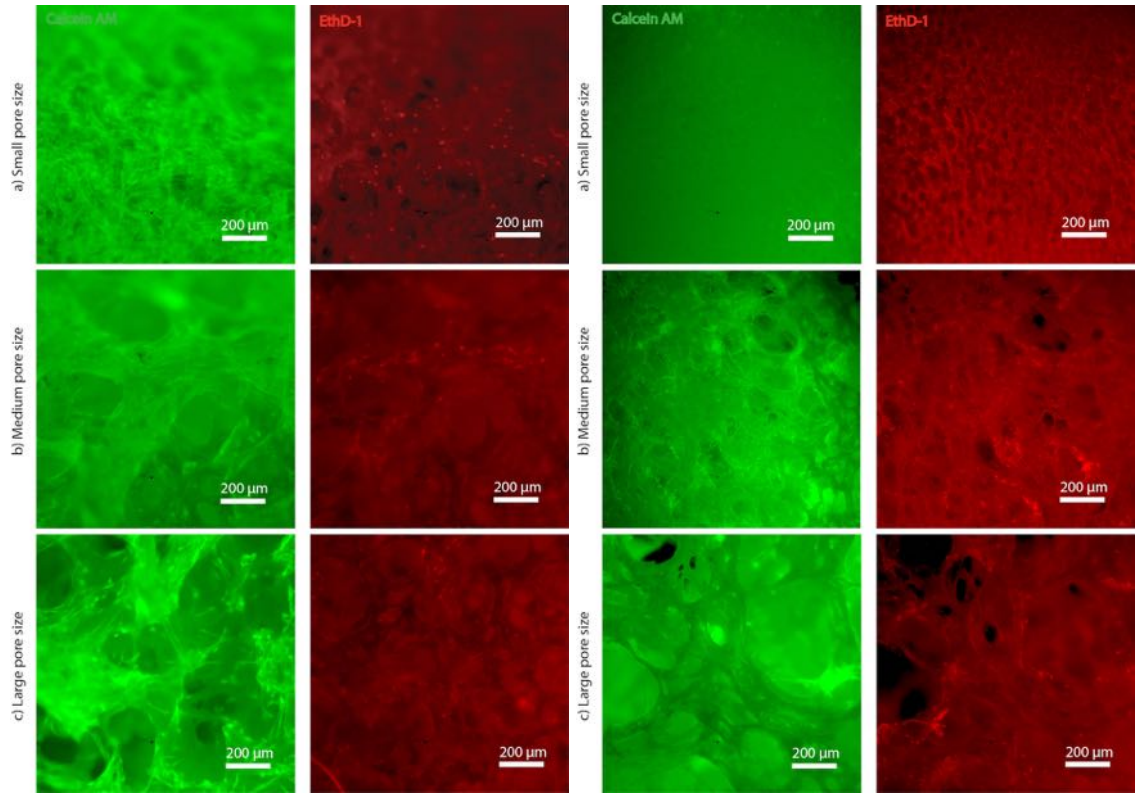

(a) (b)

Fig. 5.12 *Live/Dead Cell Viability Assays of the scaffold in static conditions. a) External surface. b) Cross section*

Adopting the calibration curve as a reference the cell number in the scaffold after 1, 3 and 7 days of culturing was evaluated. Dividing the cell number after 1 day of incubation by the cell number seeded on the scaffold the cell seeding efficiency was calculate. In this case considering a cell density of seeding of 800000 cell/scaffold and number of cell after 1 day of 183000 ± 11100, the cell seeding efficiency is $22.8\% \pm 1.3\%$. As reported in figure 5.15 the cell number in the scaffold after 7 days is more than duplicated compared to the initial one.

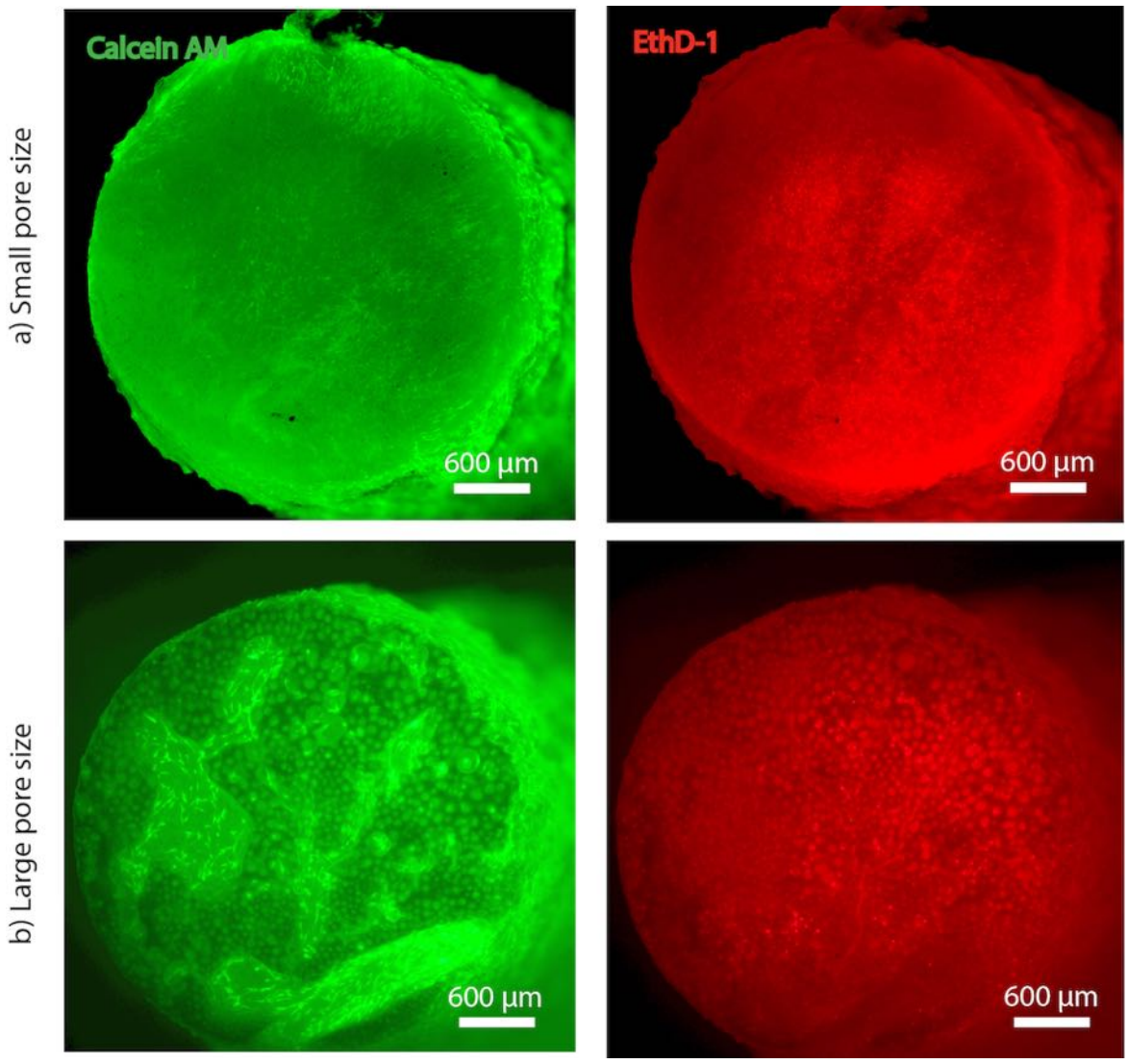

Fig. 5.13 *Live/Dead Cell Viability Assays on top and bottom of the scaffold in static conditions*

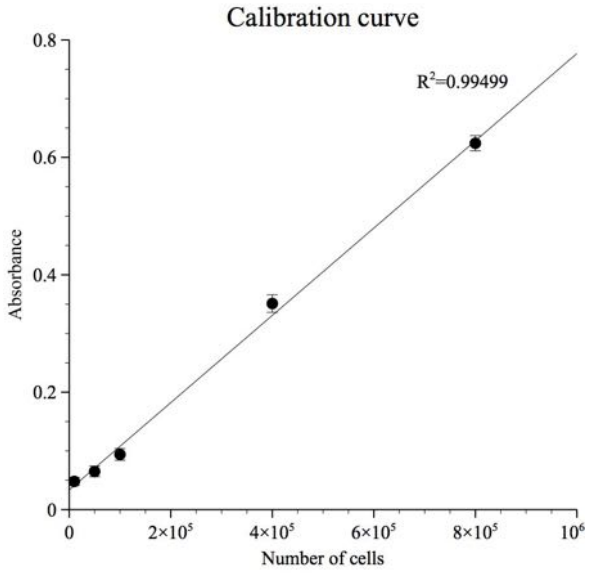

Fig. 5.14 *Calibration curve for MTS assay from* 10^4 *to* $8 * 10^5$ *cells/well*

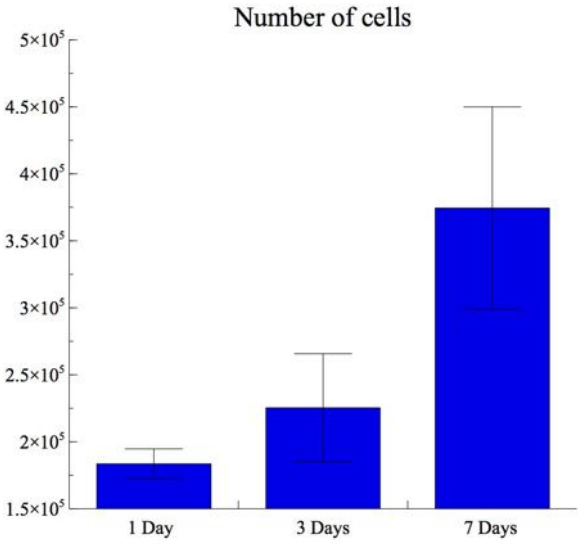

Fig. 5.15 *MTS assay on porous PLLA gradient scaffold at 1, 3, 7 days*

5.3 Chondrocytes in composite PLLA/Bioglass scaffolds

To evaluate the influence of bioglass on chondrocyte proliferation, growth and differentiation, composite PLLA/Bioglass scaffolds at different concentration were produced via TIPS. Several studies showed that the addition of bioglass in the polymer network increases the hydrophilicity (Dziadek et al., 2016; Maji et al., 2016; Puppi et al., 2010) of the scaffold as well as mechanical proprieties (Fabbri et al., 2010) and bioactivity (Miguez-Pacheco et al., 2015). As previously reported (chap. 2) the bioactivity propriety is the ability to bond with the living tissue. Bioglass with bioactivity index more than 8 is able to bond with soft and hard tissue. Hench and Greenspan (2013) showed the HCA crystallites formed on the bioactive glass surface nucleate and bond to the interfacial metabolites of the cartilage, first of all type I collagen. Furthermore, the addition of bioglass creates an antimicrobial effect. In literature the use of composite polymer/bioglass scaffold for cartilage tissue engineering was reported (Boccaccini et al., 2010; Tellisi and Ashammakhi, 2012; Wu et al., 2013; Zhou and Yu, 2014), but there are not studies of PLLA/bioglass scaffold. As reported in the section 4.3, 1393 composition better matches with the this production technique, for this reason the 1393 BG was chosen for the cell culture experiment. Two different concentrations (1% and 2.5%) were chosen to evaluate the influence of the amount of bioglass in the cell culture.

5.3.1 Scaffold preparation

Scaffolds were fabricated via ternary TIPS technique, polymer/solvent/non-solvent. The weight concentrations of PLLA was 6% and a ratio solvent/nonsolvent (Dioxane/water) 87/13. Starting from this ternary solution the bioglass was added at 1% and 2.5% of the polymer. Initially the solution was kept at 65°C to allow the complete homogenization of the mixture, then the powders of bioglass, in different concentration, were added. To avoid the formation of cluster, the as-obtained quaternary solution was sonicated for 15 minutes at 35 kHz. During this process, the solution was maintained above 60°C to reduce the viscosity and facilitate the complete dispersion of the powders. Thus the solution was poured in a HDPE mould and immersed in a thermal bath at 30°C for 75 minutes. At the end, the mould was immersed in an ethanol bath at -20°C for 20 minutes to stop any TIPS process. Finally washed in distilled water and dried under vacuum for more the 24h to complete remove the solvents.
For the cell culture experiments the scaffolds were cut in cylindrical shape of 4mm diameter and 3mm height.

5.3.2 Chondrocyte isolation and seeding

Donors of human articular chondrocytes were isolated following the same protocol previously described (section 5.1.2). Briefly, sampling were extracting from male (n=2) and females (n=4) with an average age of 71.6 years from knee joint or hip joint replacement surgeries. The cartilage chips where digested by pronase E and incubated with collagenase NB5 in growth medium. The as-isolated chondrocyte were expanded in T175 flasks before seeding. The scaffolds were preconditioned adopting 70% ethanol overnight, abundantly rinsed in PBS to remove any trace of alcohol and finally in FCS overnight. A cell density of 25000 chondrocytes per mm^3 of scaffold was used. Seeded scaffolds were cultured in 6 well plates coated with cell culture suitable agarose (1%, Sigma-Aldrich) with 5 mL of growth medium for each well. Medium was changed every 3 days. Cells were cultured on the scaffolds for 1 day, 7 days or 14 days.

5.3.3 Live/dead assay and PCR analysis

Cell vitality inside the scaffolds was determined after 7 and 14 days of cell culture. Live/dead staining was performed using FDA (green label) and PI (red label). Seeded scaffolds were incubated in the FDA/PI solution and examined under DMi8 confocal microscope.
To evaluate the gene expression of chondrocytes in the scaffold PCR analysis was performed adopting the same procedure previously reported (section 5.1.6) after 7 and 14 days. The primers was supplied by Applied Biosystems with the following NCBI Gene Reference: $COL2A1 - Hs00264051\_m1$, $ACAN - Hs00202971\_m1$, $SOX9 - Hs00165814\_m1$. The relative gene expression was normalized to the 18S expression and calculated for each sample using the $\Delta\Delta$ CT method described by Livak and Schmittgen (2001). Scaffold seeded in the same condition and evaluated at the first day was adopted as reference for qRT-PCR.

5.3.4 Results

Scaffold morphology

Figure 5.16 shows the scaffold morphologies of the scaffolds adopted for cell seeding. The first figure reports the scaffold containing 1% of BG, while the second one 2.5%. With respect to the previous tests, to compare the influence of BG on the chondrocyte growth the same thermal history for the two compositions was adopted. An average pore dimension of 150 μm was calculated. In both cases a temperature of 30°C was chosen to allow the process of nucleation and growth but similarly ensuring a good degree of interconnectivity. The presence of the BG is evident in both micrographs.

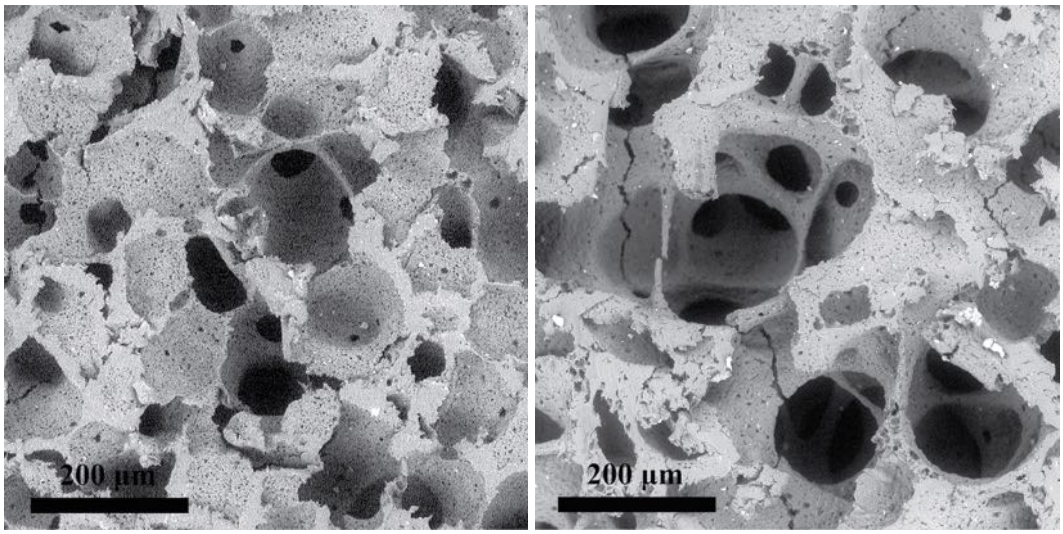

(a) (b)

Fig. 5.16 *SEM micrographs of the PLLA/BG scaffold micrography. a)PLLA/BG 1%, b) PLLA/BG 2.5%*

Cell viability and gene expression

Cell viability after 7 and 14 days were verified in both scaffold concentration. Staining FDA/PI were adopted to label in green the viable cells and in red the died cells, respectively. The images (fig. 5.17) show a good vitality of chondrocytes in both time points and foams. In particular already from 7 days the largest part of scaffold surface is covered by green cells with a slight majority in the scaffold with 2.5% of BG. The confocal microscopies highlight the very few amount of dead cells after 14 days too. Like at 7 days of culture the composite scaffold with the larger amount of BG appears with a bigger amount of cells than the other one. The typical elongated shape of chondrocytes, in most case recognisable, denotes the very good cytocompatibility of the PLLA/BG foam.

As concerns the gene expression, three gene markers were investigated: type II collagen, aggrecan and SOX9. Figure 5.18 reports the gene expression for all conditions. The difference was considered statistic significantly if a p-value was less than 0.05 (*) or 0.01 (**). The results show that there is not a homogenous trend between 1% and 2.5% of BG. The upregulation for collagen is higher in the case of 1% than 2.5%, for ACAN at 7 days the two foams are almost equal while there is an increase of 2.5% at 14 days, for SOX9 in both time points the scaffolds 2.5% of BG are more expressed than the relative 1%. In any case the general trend is an upregulation in every conditions respect to the control with a significant difference for ACAN at 14 days and collagen at 7 days. Further tests need to be performed to better understand the different trends recorded as a function of the BG content.

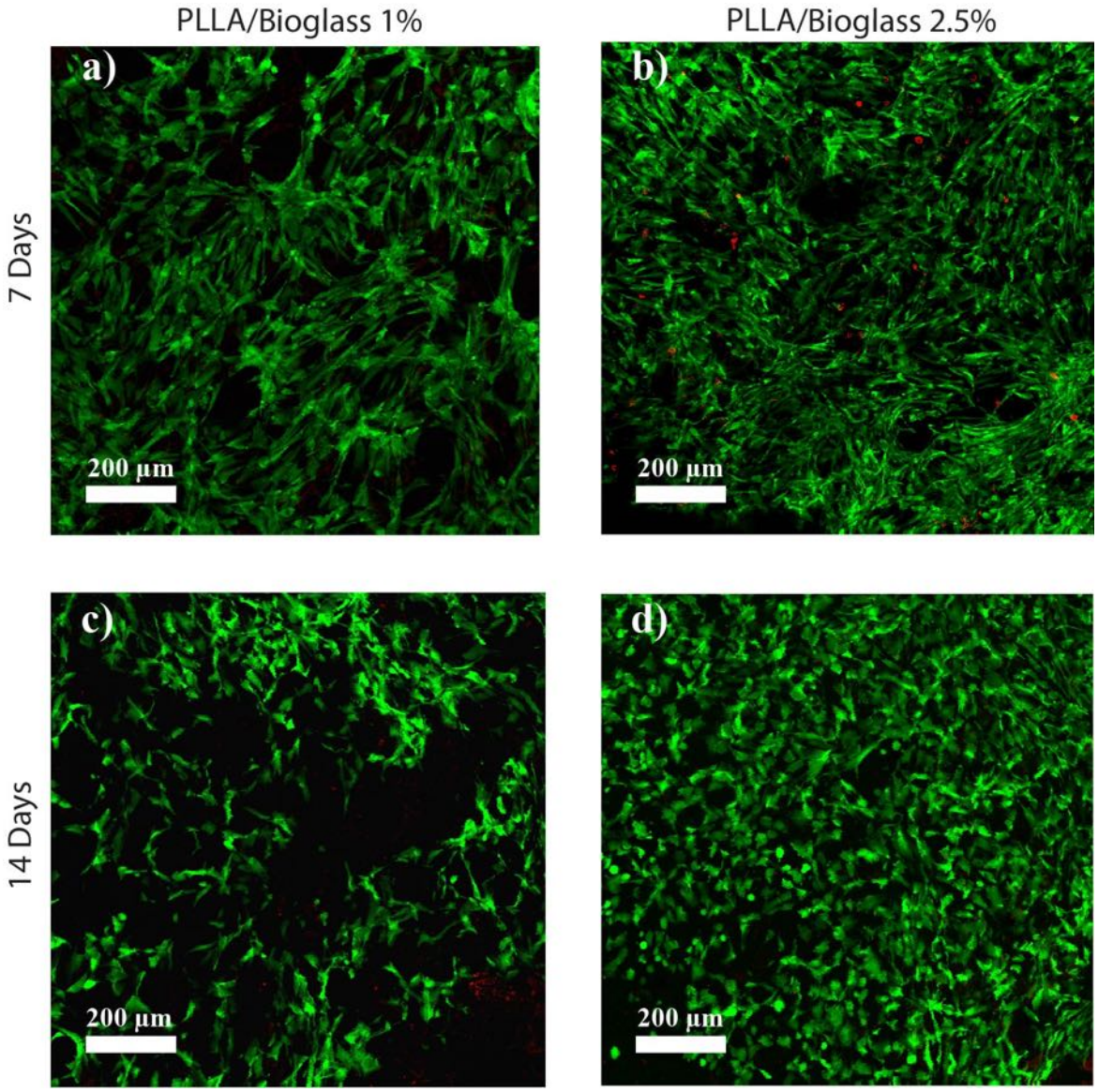

Fig. 5.17 *Cell viability of nasoseptal chondrocytes on composite PLLA/BG scaffolds. a) PLLA/BG 1%, 7 days, b) PLLA/BG 2.5%, 7 days; c) PLLA/BG 1%, 14 days, d) PLLA/BG 2.5%, 14 days*

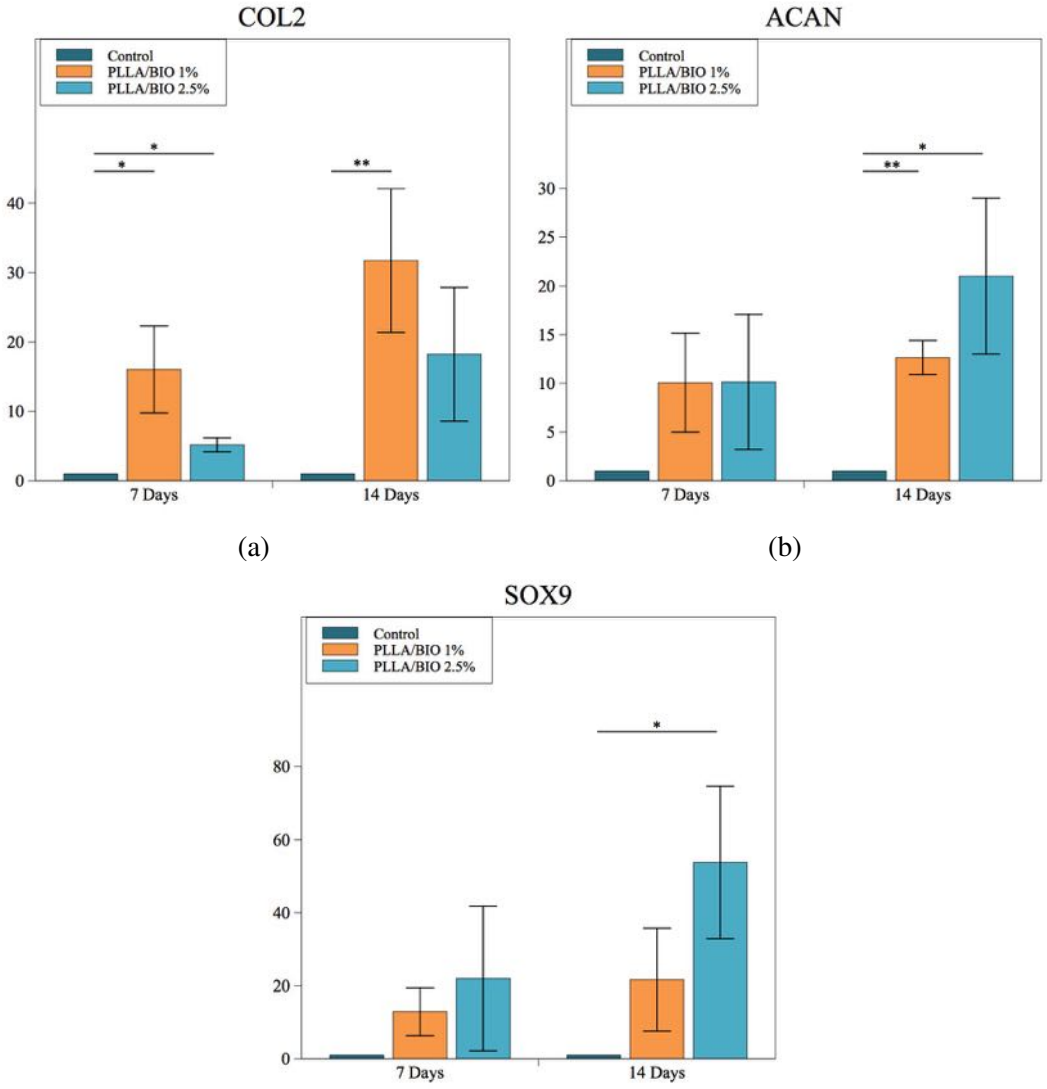

Fig. 5.18 *Gene expression of type II collagen (a), aggrecan (b) and SOX9 (c) in the two different types of scaffolds, PLLA/BG 1% and PLLA/BG 2.5% after 7 and 14 days. Significant difference: *p<0.05; **p<0.01*

5.4 Osteoblasts in composite PLLA/HA scaffolds

Many researchers have carried out biological in vitro studies on scaffolds containing HA using osteoprogenitor cells, like MC3T3-E1, analysing the biocompatibility and osteoinductivity through proliferation and differentation assays. In particular, alkaline phosphatase activity (ALP) and the presence of calcium deposits are the investigated markers that evidence the osteoblastic differentiation.

5.4.1 Scaffold preparation

PLLA (Resomer L 209 S), 1,4 dioxane (Sigma) and distilled water were utilised to prepare the ternary solution. HA was kindly provided by Professor Licciulli from University of Lecce. Initially, a homogeneous solution composed by PLLA, dioxane and water was prepared, then HA particles in a PLLA/HA ratio of 93/7 were added. The solution was initially sonicated at 35kHz for 15 minutes and then kept in a thermal bath at 60°C. Thus the temperature was suddenly lowered to 30°C for 10 minutes. Later, a quench by direct pool immersion in an ethanol bath at a temperature of -25°Cwas performed. Finally the foams were washed and dried under vacuum. Neat PLLA scaffolds, produced following the same protocol, were added as control.

5.4.2 Cell seeding

Pre-osteoblastic MC3T3-E1 cells (Sigma Aldrich) were cultured in DMEM (Sigma Aldrich) supplemented with 10% of fetal bovine serum (FBS), 1% of glutamine and 1% of streptomycin/penicillin (growth medium) in $75cm^2$ cell culture flasks incubating at 37°C with 5% CO_2. Scaffolds were cut in circular-shaped slices: 5mm diameter and 1.5mm of thickness. The samples were preliminarily sterilised under vacuum in a 70% ethanol solution, then abundantly rinsed in PBS with calcium and magnesium (Euroclone) for 2 hours and treated with a 100µg/ml type I collagen solution in 0.02N acetic acid to increase the cell attachment. Finally, the scaffolds were washed in growth medium to activate the collagen mesh formation thanks to pH shift. A cell density of $2.5 * 10^5$ cell/scaffold in 25 µl were used. The samples were placed in a multiwell plate replacing the medium every three days up to 27 days.

5.4.3 Proliferation assay

Cell proliferation in PLLA and PLLA/HA scaffolds was evaluated through viability assays employing Cell Counting Kit 8 (CCK8, Sigma Aldrich); a sensitive colorimetric kit containing WST-8. This latter is a salt reduced by mitochondrial dehydrogenases to orange

formazan, evaluated in absorbance at 450 nm. Given that the number of living cells is directly proportional to the value of absorbance, a standard curve was created to convert the absorbance value in terms of cell number. Each sample was incubated at 37°C and 5% CO_2 for 3 hours with 500 µl of 1:10 diluted reagent in fresh medium. Finally, the medium was collected and analysed with a spectrophotometer at absorbance of 450 nm. The essays were carried out at 0, 7, 14, 21 and 27 days of culture in triplicate for each time. Furthermore, not seeded scaffolds were used as negative controls in each measurement.

5.4.4 ALP assay

The osteoblastic differentiation process was investigated with SensoLyte pNPP Alkaline Phosphatase Assay kit (Anaspec, AS-72146) measuring the alkaline phosphatase activity, a marker expressed during the osteoblastic maturation. Incubating the protein extracts with the enzymatic substrate, p-nitrophenyl phosphate (pNPP), a dephosphorylation process occured causing the formation of a yellow product, p-nitrophenol. The spectrophotometric measure through absorbance at 405 nm reveals the ALP activity. According to the protocol kit, the seeded scaffolds were washed in PBS and incubated with washing buffer. Successively, samples were grinded and 100µl of 0.2% Triton X-100 lisys buffer was added to each scaffold and vortex. After the centrifugation at 2500 g at 4°C for 10 minutes, 50 µl of supernatant was harvested and mixed with 50 µl of substrate for 1 hour into wells of a 96 well plate. The measurement were performed at 0, 7, 14, 21 and 27 days in triplicate. The data are expressed in ng/cell using a standard curve to convert absorbance values in ng of alkaline phosphatase.

5.4.5 Results

Cell viability

Cell number variation as a function of days of culture on both kinds of sample in figure 5.19 is reported. From 0 to 21 days, on both substrates, viable cell number has regularly increased from a starting point of almost 10^5 to $4.5 * 10^5$ cells, reaching the maximum peak. The small decrease to $3.5 * 10^5$ cells in the last week can be due to the reach of confluence with a weak detachment of the cell due the the lack of available surface. Neat and composite scaffolds show a very similar trend, demonstrating a comparable biocompatibility degree.

ALP activity

The histogram in figure 5.20 shows the ALP activity as nanograms of ALP normalized with number of cells. From 7 to 14 days, obtained data revealed an increase in ALP activity,

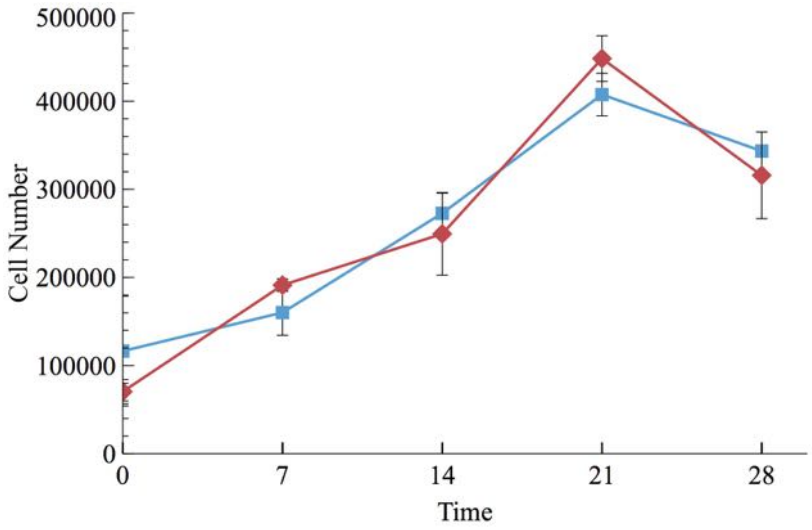

Fig. 5.19 *Cell viability of MC3T3-E1 cells in PLLA and PLLA/HA scaffolds up to 27 days*

despite there is not significant difference between neat and composite scaffold. At 21 and 27 days PLLA/HA showed a regular growth, while pure PLLA remained quite constant. This aspect implies a statistically significant difference at these time points between the two types of scaffolds. Considering simultaneously the proliferation and ALP assays, it seems evident that the substrates similarly promote cell growth but the presence of HA increased the osteoblastic maturation through a significant raise in ALP activity after 21 days when cell confluence is reached.

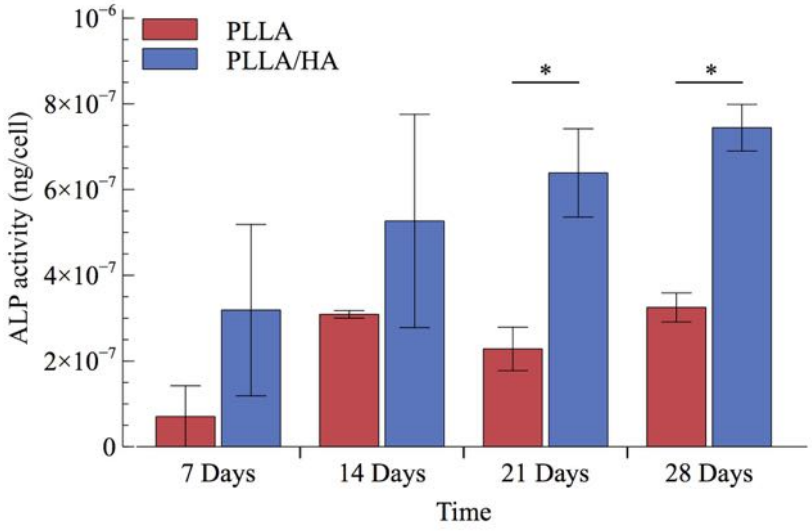

Fig. 5.20 *ALP activity at 7, 14, 21 and 27 days. Data are normalized using not seeded-scaffold as negative control and represented by means of average ± SD; *p<0.05*

References

P. Arpornmaeklong, S. E. Brown, Z. Wang, and P. H. Krebsbach. Phenotypic Characterization, Osteoblastic Differentiation, and Bone Regeneration Capacity of Human Embryonic Stem Cell–Derived Mesenchymal Stem Cells. *Stem Cells and Development*, 18(7):955–968, 2009.

N. Bhardwaj and S. C. Kundu. Chondrogenic differentiation of rat MSCs on porous scaffolds of silk fibroin/chitosan blends. *Biomaterials*, 33(10):2848–2857, 2012.

E. Birmingham, G. L. Niebur, P. E. Mchugh, G. Shaw, F. P. Barry, and L. M. McNamara. Osteogenic differentiation of mesenchymal stem cells is regulated by osteocyte and osteoblast cells in a simplified bone niche. *European Cells and Materials*, 23(353):13–27, 2012.

A. R. Boccaccini, M. Erol, W. J. Stark, D. Mohn, Z. Hong, and J. F. Mano. Polymer/bioactive glass nanocomposites for biomedical applications: A review. *Composites Science and Technology*, 70(13):1764–1776, 2010.

H. Cheng, L. Qiu, J. Ma, H. Zhang, M. Cheng, W. Li, X. Zhao, and K. Liu. Replicative senescence of human bone marrow and umbilical cord derived mesenchymal stem cells and their differentiation to adipocytes and osteoblasts. *Molecular Biology Reports*, 38(8): 5161–5168, 2011.

M. Dziadek, B. Zagrajczuk, M. Ziabka, K. Dziadek, and K. Cholewa-Kowalska. The role of solvent type, size and chemical composition of bioactive glass particles in modulating material properties of poly(ε-caprolactone) based composites. *Composites Part A: Applied Science and Manufacturing*, 90:90–99, 2016.

P. Fabbri, V. Cannillo, A. Sola, A. Dorigato, and F. Chiellini. Highly porous polycaprolactone-45S5 Bioglass scaffolds for bone tissue engineering. *Composites Science and Technology*, 70(13):1869–1878, 2010.

A. J. Friedenstein, J. F. Gorskaja, and N. N. Kulagina. Fibroblast precursors in normal and irradiated mouse hematopoietic organs. *Experimental hematology*, 4(5):267–74, 1976.

S. E. Haynesworth, J. Goshima, V. M. Goldberg, and A. I. Caplan. Characterization of cells with osteogenic potential from human marrow. *Bone*, 13(1):81–88, 2016.

L. L. Hench and D. Greenspan. Interactions between bioactive glass and collagen: A review and new perspectives, 2013.

E. M. Horwitz, D. J. Prockop, L. a. Fitzpatrick, W. W. Koo, P. L. Gordon, M. Neel, M. Sussman, P. Orchard, J. C. Marx, R. E. Pyeritz, and M. K. Brenner. Transplantability and therapeutic effects of bone marrow-derived mesenchymal cells in children with osteogenesis imperfecta. *Nature medicine*, 5(3):309–313, 1999.

J. Hu, K. Feng, X. Liu, and P. X. Ma. Chondrogenic and osteogenic differentiations of human bone marrow-derived mesenchymal stem cells on a nanofibrous scaffold with designed pore network. *Biomaterials*, 30(28):5061–7, 2009.

Z. Huang, P. Nooeaid, B. Kohl, J. A. Roether, D. W. Schubert, C. Meier, A. R. Boccaccini, O. Godkin, W. Ertel, S. Arens, and G. Schulze-Tanzil. Chondrogenesis of human bone marrow mesenchymal stromal cells in highly porous alginate-foams supplemented with chondroitin sulfate. *Materials Science and Engineering C*, 50:160–172, 2015.

L. Jackson, D. R. Jones, P. Scotting, and V. Sottile. Adult mesenchymal stem cells: differentiation potential and therapeutic applications. *Journal of postgraduate medicine*, 53(2): 121–7, 2007.

A. Jamnig and G. Lepperdinger. From tendon to nerve: an MSC for all seasons. *Canadian Journal of Physiology and Pharmacology*, 90(3):295–306, 2012.

E. H. Javazon, K. J. Beggs, and A. W. Flake. Mesenchymal stem cells: Paradoxes of passaging. *Experimental Hematology*, 32(5):414–425, 2004.

Y. Jiang, B. N. Jahagirdar, R. L. Reinhardt, R. E. Schwartz, C. D. Keene, X. R. Ortiz-Gonzalez, M. Reyes, T. Lenvik, T. Lund, M. Blackstad, J. Du, S. Aldrich, A. Lisberg, W. C. Low, D. A. Largaespada, and C. M. Verfaillie. Pluripotency of mesenchymal stem cells derived from adult marrow. *Nature*, 418(6893):41–9, 2002.

S. Kadiyala, R. G. Young, M. A. Thiede, and S. P. Bruder. Culture expanded canine mesenchymal stem cells possess osteochondrogenic potential in vivo and in vitro. *Cell Transplantation*, 6(2):125–134, 1997.

K. J. Livak and T. D. Schmittgen. Analysis of relative gene expression data using real-time quantitative PCR and. *Methods*, 25:402–408, 2001.

K. Maji, S. Dasgupta, K. Pramanik, and A. Bissoyi. Preparation and Evaluation of Gelatin-Chitosan-Nanobioglass 3D Porous Scaffold for Bone Tissue Engineering. *International Journal of Biomaterials*, 2016(4):1–14, 2016.

G. A. Mannella, F. Carfì Pavia, G. Conoscenti, V. La Carrubba, and V. Brucato. Evidence of mechanisms occurring in thermally induced phase separation of polymeric systems. *Journal of Polymer Science, Part B: Polymer Physics*, 52(14):979–983, 2014.

F. Y. Meligy, K. Shigemura, H. M. Behnsawy, M. Fujisawa, M. Kawabata, and T. Shirakawa. The efficiency of in vitro isolation and myogenic differentiation of MSCs derived from adipose connective tissue, bone marrow, and skeletal muscle tissue. *In Vitro Cellular and Developmental Biology - Animal*, 48(4):203–215, 2012.

V. Miguez-Pacheco, L. L. Hench, and A. R. Boccaccini. Bioactive glasses beyond bone and teeth: Emerging applications in contact with soft tissues. *Acta Biomaterialia*, 13:1–15, 2015.

S. H. Oh, T. H. Kim, G. I. Im, and J. H. Lee. Investigation of pore size effect on chondrogenic differentiation of adipose stem cells using a pore size gradient scaffold. *Biomacromolecules*, 11(8):1948–55, 2010.

D. Puppi, F. Chiellini, A. M. Piras, and E. Chiellini. Polymeric materials for bone and cartilage repair. *Topical Issue on Biomaterials*, 35(4):403–440, 2010.

J. P. Rodríguez, P. Astudillo, S. Ríos, and A. M. Pino. Involvement of adipogenic potential of human bone marrow mesenchymal stem cells (MSCs) in osteoporosis., 2008.

H. Siggelkow, K. Rebenstorff, W. Kurre, C. Niedhart, I. Engel, H. Schulz, M. J. Atkinson, and M. Hüfner. Development of the osteoblast phenotype in primary human osteoblasts in culture: Comparison with rat calvarial cells in osteoblast differentiation. *Journal of Cellular Biochemistry*, 75(1):22–35, 1999.

G. S. Stein and J. B. Lian. Molecular Mechanisms Mediating Proliferation/Differentiation Interrelationships During Progressive Development of the Osteoblast Phenotype. *Endocrine Reviews*, 14(4):424–442, 1993.

N. Tellisi and N. Ashammakhi. Comparison of meshes, gels and ceramic for cartilage tissue engineering in vitro. *European Journal of Plastic Surgery*, 35(2):159–170, 2012.

F. Togel and C. Westenfelder. The role of multipotent marrow stromal cells (MSCs) in tissue regeneration. *Organogenesis*, 7(2):96–100, 2011.

T. C. Tseng and S. hui Hsu. Substrate-mediated nanoparticle/gene delivery to MSC spheroids and their applications in peripheral nerve regeneration. *Biomaterials*, 35(9):2630–2641, 2014.

References

Y. Wang, H. Liu, and H. Ma. Intrathecally Transplanting Mesenchymal Stem Cells (MSCs) Activates ERK1/2 in Spinal Cords of Ischemia-Reperfusion Injury Rats and Improves Nerve Function. *Medical science monitor : international medical journal of experimental and clinical research*, 22:1472–1479, 2016.

J. Wu, K. Xue, H. Li, J. Sun, and K. Liu. Improvement of PHBV scaffolds with bioglass for cartilage tissue engineering. *PloS one*, 8(8):e71563, 2013.

Q. Zhang, H. Lu, N. Kawazoe, and G. Chen. Pore size effect of collagen scaffolds on cartilage regeneration. *Acta Biomaterialia*, 10(5):2005–2013, 2014.

M. Zhou and D. Yu. Cartilage tissue engineering using PHBV and PHBV/Bioglass scaffolds. *Molecular Medicine Reports*, 10(1):508–514, 2014.

Chapter 6

Bioreactors in tissue engineering

Bioreactor devices allow to carry out cell cultures in dynamic regimes. In a general perspective, a bioreactor allows to control the growth environment replicating as closely as possible the conditions of the native tissue, considering several aspects: pH , temperature, pressure, concentration of metabolites and catabolites, but also mechanical and chemical stimuli. Bioreactors play a key role in the processes of biological tissue engineering and implementation of dynamic cell culture in three-dimensional environments. More specifically, these latter relate to cell seeding, optimization of the mass transport in 3D constructs and use of these devices for in vitro models. The main purpose of the bioreactors can be summarised in the following points:

1. to allow a homogeneous cell distribution;
2. to maintain vitality of cells seeded on/in porous 3D scaffolds during cultivation;
3. to increase the mass transport (both diffusion and convection mechanism);
4. to achieve specific physical stimulation of the TE construct.

In literature it is possible to find various types of bioreactors depending on the application. As an example bioreactor for ligament/tendon and for bone are reported.
Bioreactors for ligament and tendon are focused on the replication of the mechanical conditions of the native tissue. Tendons and ligaments transfer the force from muscle to bone and bone to bone, respectively. They consist of collagens, cells, proteoglycans, elastin, glycolipids, and water. Water is about 65%-70% of the total weight with a highly organized structure. Collagen type I is the main structural/functional component and comprises around 70%-80% of the dry weight. Type III collagen is mainly present in the endotenon and epitenon, but is also in the early phase of tendon repair.

In fig. 6.1 an example of bioreactor system for ligamen/tendon is reported. The main component is the actuating system, which provides the different mechanical regimes. The most common actuators for this type of bioreactor are: pneumatic actuators (Nirmalanandhan et al., 2008), linear motors (Doroski et al., 2010) and step motor-ball screws (SMBSs) (Webb et al., 2006). The pneumatic actuators present the following advantages: cleanliness, low cost, and high power-to-weight ratio, but it is not possible to use them adopting air as a medium. Linear motors are electric devices, that implies they are more expensive compared to pneumatic motors but with a superior accuracy. Moreover, by eliminating the mechanical transmission, the linear motor can reach higher velocity. The SMBS actuators incorporate ball screw drives and provide low friction. They offer a combination of high-speed and high-load capacity, therefore they are ideally suited for applications that require high-speed precision motion control. Unlike trapezoidal leadscrews, ball screws have rolling surfaces that wear less than sliding interfaces. The choice between the different types of actuators depends of the specific test to carry out.

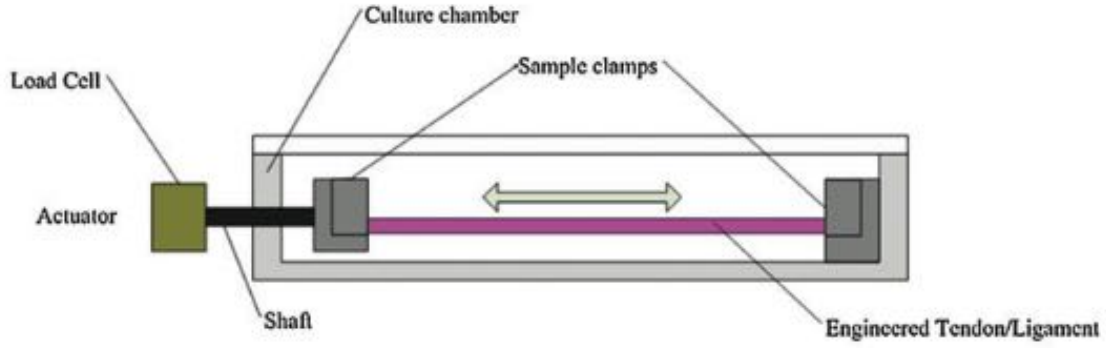

Fig. 6.1 *Example of bioreactor system for ligamen/tendon tissue engineering, from Wang et al. (2013)*

Bone tissue engineering needs different bioreactor specifications. Supplying the correct amount of nutrient to allow the cells proliferation is one of the main tasks in the case of bone tissue. Cells, indeed, product an extracellular matrix that restricts the amount of oxygen and growth factor concentration. The bioreactor for osteogenesis have to force the medium inside the pore of the scaffold, promoting the fresh medium exchange. In figure 6.2 a schematic representation of different available bioreactors is reported.

Rotating wall vessel bioreactors (fig. 6.2a) consist in a cylindrical growth chamber with a gas exchange membrane. The solid-body rotation is accomplished by a vessel rotating horizontally around its axis, randomising the gravitational forces acting on the cell surface. The

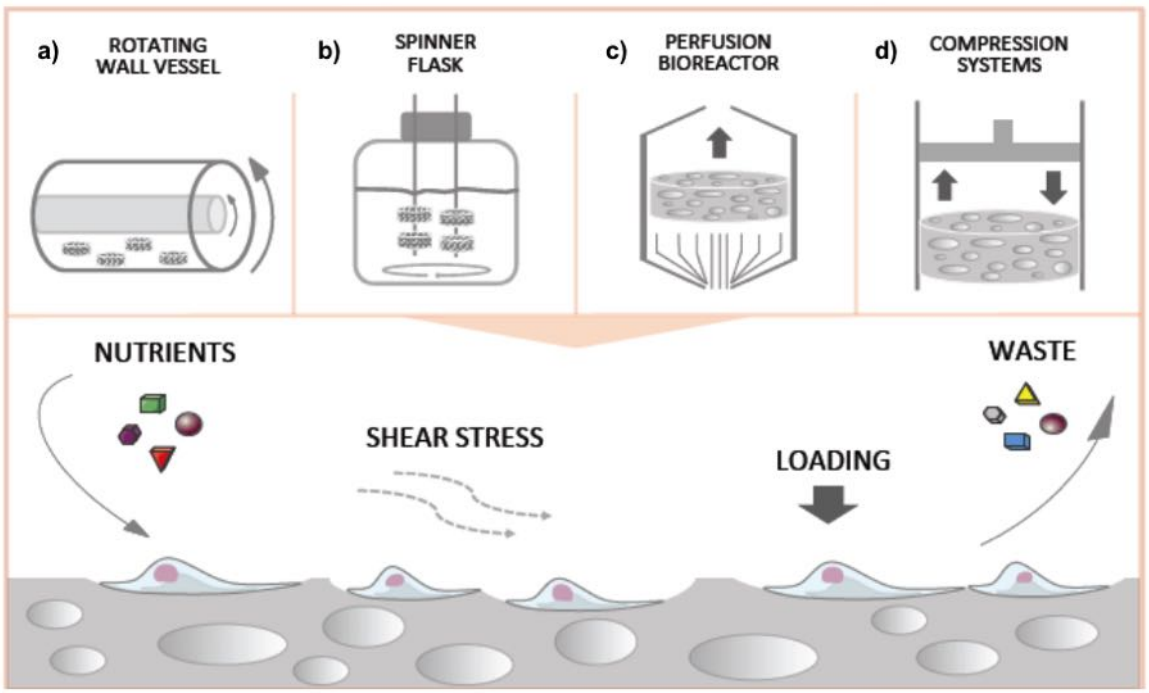

Fig. 6.2 *Example of bioreactor system for bone tissue engineering, adapted from Sladkova and de Peppo (2014)*

culture chamber is completely filled with culture medium (zero headspace) and oxygenated through a silicone rubber membrane by an air pump that draws incubated air through a filter. As the vessel rotates, the liquid inside accelerates, until the entire fluid mass is rotating at the same angular rate as the wall (under no-slip hypothesis). When the velocity of the rotating fluid reaches the same of sedimentation rate of the cell/scaffold constructs, these latter are maintained in a "free-fall" state and subjected to dynamic laminar flow (Granet et al., 1998). Spinner flasks are simple bioreactor systems (fig. 6.2b) composed of a glass or plastic vessel in which cell/scaffold constructs are suspended inside the medium. The top of the vessel is usually used for gas exchange and medium oxygenation. A stir bar at the bottom of the vessel maintains the mixing of the medium. The convective forces generated during stirring mitigate the nutrient concentration gradients at the surface of the cell/scaffold constructs and produce turbulences to enhance the mass transport toward the centre of the samples. This effect is thought to result from the convective transport of nutrients to the surface of the scaffold in spinner flask culture in contrast to the purely diffusional transport in static culture. This aspect will increase concentrations of oxygen throughout the scaffold, compared to the static culture, when a nutrient concentration gradient can form where cells in the centre of the scaffold receive an insufficient supply of nutrients (Kim et al., 2007; Wang et al., 2009; Yeatts and Fisher, 2011).

About the perfusion bioreactor (fig. 6.2c), different systems have been developed, but all concepts share the similar basic design consisting of a medium reservoir, a pump, a tubing circuit and a perfusion cartridge. The perfusion cartridge holds the scaffold that is sealed to avoid the medium flow around it, thus perfusing medium directly through the pores of the scaffold (Braccini et al., 2005). Many perfusion bioreactor systems have been developed and tested for bone tissue engineering purposes (Bjerre et al., 2008; Carmona-Moran and Wick, 2015; Hossain et al., 2014; Schmelzer et al., 2015; Yeatts and Fisher, 2011).
The last type is the compression bioreactor (fig. 6.2d). The idea is to mimic the bone physiological environment in vitro, characterized by repeated mechanical stimulation required for functional bone regeneration. These culture systems consist in a motor, a system providing linear motion and a compression chamber in which some pistons apply static or dynamic compressive loads directly to the scaffold constructs. Furthermore, the continuous movement of piston force the fluid inside the construct, which makes it also similar to the perfusion bioreactor (Damaraju et al., 2014; Puetzer et al., 2012; Tran et al., 2011; Wartella and Wayne, 2009) for some aspects.
All things considered, all bioreactors try to reproduce in vitro the complex set of stresses to which the tissues are subjected during the development in vivo.

6.1 Microphysiological Tissue System (MTS) Bioreactor

A microphysiological tissue system (MPS) bioreactor has been developed to replicate in vitro the in vivo OC physiological conditions (Lozito et al., 2013). The MPS allows a separate control of the chondral and osseous environment while permitting communication between chondrocytes and osteoblasts across the OC junction (Alexander et al., 2014), similar to the conditions of OC tissue in vivo. The structure of the bioreactor, reported in figure 6.3, was modeled using Solidworks 2014 (Dassault, Systemes). Well, insert, base and lid were fabricated using via 3D Systems Viper (Rock Hill, South Carolina) using WaterShed XC 11122 resin (DSM Somos, Heerlen, Netherlands). The bioreactor was developed and tested in the Rocky Tuan's laboratory at the University of PIttsburgh.

One of the main problem about the reproduction of the osteochondral unit it is the difficulty to supply culture medium conditions in the same complex. The divergent environments in which cartilage and bone develop are a particularly relevant issue. Features such as growth factors and supplements, oxygen, pH, and mechanical stimulation are known to be both important for histogenesis and tissue-specific for bone or cartilage. Should benefit from the

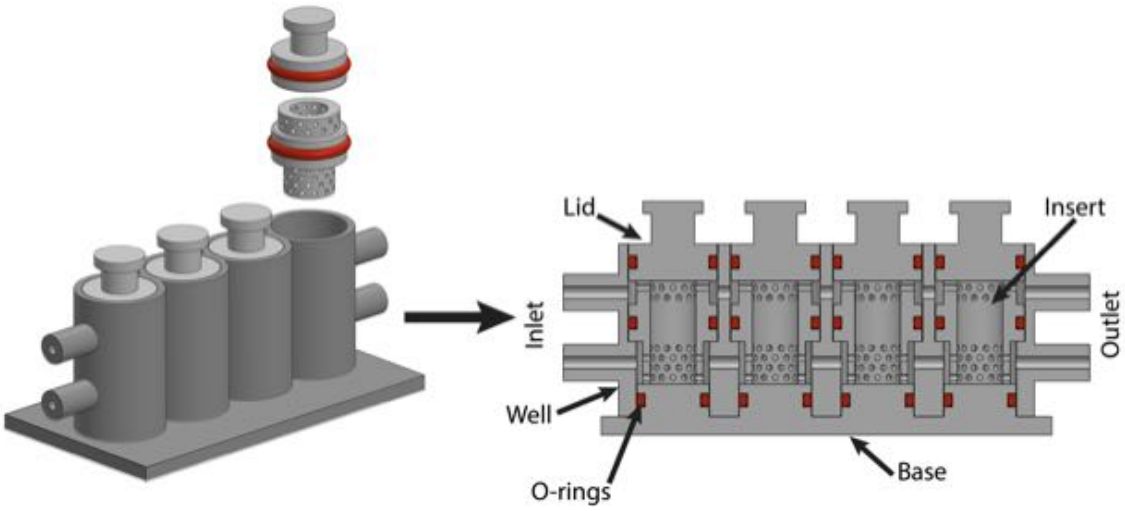

Fig. 6.3 *Schematic representation of the bioreactor. External view and cross section*

application of these external conditions, while maintaining an intimate contact between the two tissues for a well designed bioreactors.
The illustrated bioreactor is composed by four compartments (cells). Each cell is composed by perforated removable inserts, where the scaffold is allocated. A detachable base facilitates the removal of the insert at the end of the test. An o-ring, located outside the insert at 5.05 mm from the bottom, ideally divides the chamber in two parts: the lower part for bone tissue and the upper part for cartilage tissue. Two channels, below and above the o-ring, allow the necessary nutrient provision. The channels are connected to syringes and bags, the first ones to supply the medium, the latter to collect the eluted medium. Lids, o-ring provided, seal the whole bioreactor to prevent from the outside contamination.
The bioreactor can be also used for drug screening. It is a modular device and the number of cells can be easily modified, from 1 (fig. 6.4a) to 4 (fig. 6.4b) to 96 (fig. 6.4c).

6.1.1 Computational model

A methodology to characterize flow and transport into a MTS bioreactor has been developed. The rationale is to meet the following questions via fluid dynamics computational model:

- Can the growth medium reach the whole bioreactor?
- Is the concentration of growth factor sufficient for all constructs inside the bioreactor?
- What is the intensity of fluid mixing between the upper and the lower chamber?

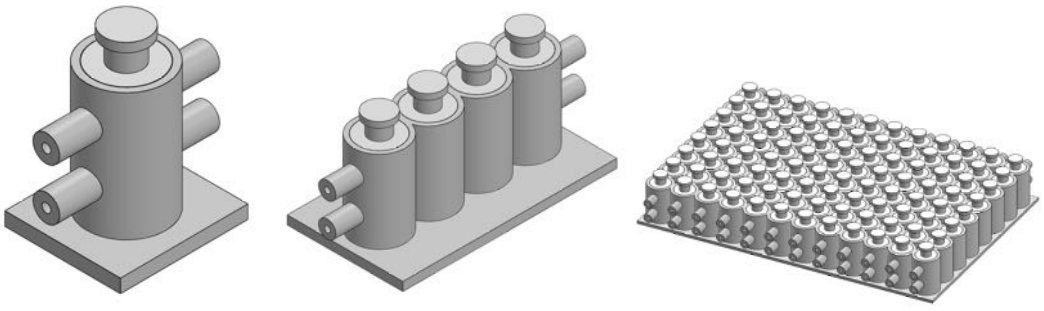

(a) (b) (c)

Fig. 6.4 *Different configurations of the bioreactor: a) 1 cell, b) 4 unit cells array, c) 96 unit cells plate*

By combining distributed and lumped parameter models it is possible to fulfill all these requirements. In particular, the degree of perfusion and mixing of nutrients in each region of the device will be estimated, quantified and compared with data derived from specific experiments.

Since the bioreactor is a combination of free flow for the inlets and outlets with porous medium flow for the culture chamber, a fluid-porous interaction model was used. In each region, the flow was considered incompressible. For momentum balance a general equation that encompasses the nature of both types of flows was selected. In this way, it is easy to switch from one to the other by suitably tuning the parameters in each region. This equation has the structure of Brinkman equation for flow in porous medium, because it combines viscous terms, such as in Stokes, with friction terms, such as in Darcy. To model free flow, a convective term (which play a significant role in case of high Reynolds regimes) was added. In figure 6.5a the computational domain is reported with the relative mesh in ANSYS adopted (fig. 6.5b).

The momentum balance equation reads as follows:

$$\bigtriangledown(\rho\gamma\overline{U}\times\overline{U})-\bigtriangledown(\mu\gamma(\bigtriangledown\overline{U}+(\bigtriangledown\overline{U})^{T}))=-\gamma\frac{\mu}{K_{perm}}\overline{U}\bigtriangledown P$$
$$\forall x\in\Omega_{c\_up}\cup\Omega_{c\_down}\cup\Omega_{scaff} \quad (6.1.1)$$

Where $\overline{U}$ is the velocity vector field, ρ and μ are fluid viscosity and density respectively, γ is the porosity of the medium ($\gamma=1$ for the free fluid), K_{perm} is hydraulic conductivity of the porous medium ($k_{perm}=0$ for the free fluid) and $\bigtriangledown P$ the hydrostatic pressure.

The culture medium that perfuses the bioreactor was assumed comparable to water ($\rho=999.97\frac{kg}{m^3}$ and $\mu=0.001Pa*s$) because the dissolved nutrients and other chemical species

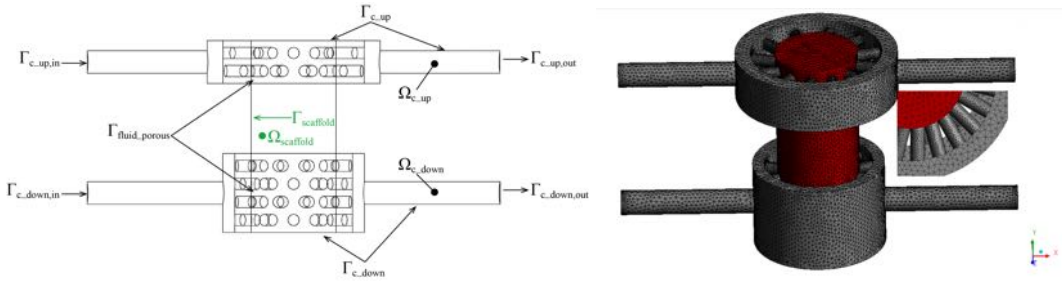

(a) (b)

Fig. 6.5 *Bioreactor arrangement in the computational model. a) Bioreactor domain.* Γ *and* Ω *denote surface and volume respectively.* $\Gamma_{c\_up,in}$*: inlet, upper chamber,* $\Gamma_{c\_down,in}$*: inlet, lower chamber,* $\Gamma_{c\_up,out}$*: outlet, upper chamber,* $\Gamma_{c\_down,out}$*: outlet, lower chamber,* $\Gamma_{scaffold}$*: scaffold/wall interface,* Γ_{c_up}*: upper chamber,* Γ_{c_down}*: lower chamber,* $\Gamma_{fluid-porous}$*: fluid/porous interface,* Ω_{c_up}*: upper chamber,* Ω_{c_down}*: lower chamber,* $\Omega_{scaffold}$*: scaffold. b) Bioreactor mesh. In grey the free fluid region, in red the porous region*

are diluted. The applied boundary conditions were: at the bioreactor inlet ($\Gamma_{c\_up,in}$, $\Gamma_{c\_down,in}$) a given flow rate; at the surfaces that separate the free fluid and the porous medium from the bioreactor walls (Γ_{c_up},Γ_{c_down},$\Gamma_{c\_scaffold}$) the no-slip condition and at the outlet ($\Gamma_{c\_up,out}$, $\Gamma_{c\_down,out}$) the street-free condition ($P = 0$). An important part of this study consists in modeling the transport of bio-molecules dissolved in the culture medium that perfuse the bioreactor. The different nutrients have been modeled as variables passively transported by the culture medium. Their governing equations have been formulated in terms of volumetric concentrations.

Under these conditions the equations for the transport of biomolecules are:

$$\bigtriangledown(D_s\gamma_s \bigtriangledown C_s + \rho_s\gamma_s\overline{U}C_s) = 0 \qquad \forall x \in \Omega_{scaff} \tag{6.1.2}$$

$$\bigtriangledown(D_f \bigtriangledown C_f + \overline{U}C_f) = 0 \qquad \forall x \in \ \Omega_{c\_up} \cup \Omega_{c\_down} \tag{6.1.3}$$

D is the diffusion coefficient for the different biomolecules, C is the solute concentration and f and s indicate the fluid and scaffold respectively. The specific boundary conditions for the biomolecules transport were: at the inlet boundaries ($\Gamma_{c\_up,in}$, $\Gamma_{c\_down,in}$) a known concentration has been imposed, using independent values on each inlet section. Homogeneous Neumann condition has been adopted on the bioreactor wall and outlets ($\Gamma_{c\_up,out}$, $\Gamma_{c\_down,out}$, Γ_{c_up}, Γ_{c_down}). The wall is considered impermeable to nourishments and biomolecules' flux in the direction normal to the outlets is assumed equal to zero. Moreover, conservation of

concentrations and of biomolecules flux have been applied at the interface between fluid and porous medium ($\Gamma_{fluid-porous}$).

The computational model was implemented using ANSYS ICEM CFD v.15.0 (AnsysInc., Canonsburg, PA). The geometry of the device was created using ICEM tool and the domain has been discretized with tetrahedral elements by means of the octree mesh method, which ensures a refinement of the computational grid where necessary in order to reduce the computational costs.

6.1.2 PLLA gradient scaffold and GelMA scaffold: fabrication and modelling

PLLA (MW=114000 kg/mol), 1,4-dioxane (Sigma-Aldrich) and distilled water were used to produce the PLLA scaffold. The ternary solution employed has a PLLA concentration of 4 % wt, in 87/13 wt/wt dioxane/water (solvent/non-solvent). The adopted scaffold was the same as the preliminary tests in static conditions (section 5.2). Briefly the scaffold presents an average pore dimension of 200 µm on the fast cooling side (left side) that gradually decreases going to 140 µm in center, up to 70 µm on the slow cooling side (right side). It can be ideally divided in three sections, equally distributed.

The gelatine metacrylate (GelMA) scaffold was synthesized according to a modified method of Van Den Bulcke et al. (2000). Powdered, type A gelatin from porcine skin was obtained from Sigma-Aldrich (St. Louis, MO). One gram of gelatin was added to 33mL of deionized water and heated at 37°C while stirring for approximately 180 min, or until all gelatin was dissolved. One milliliter of 94% methacrylic anhydride (Sigma-Aldrich), was added to the stirring mixture at a constant rate of 150 rpm, and the reaction was allowed to proceed for 16h at 37°C. The reaction products were dialyzed with 12-14 kDa molecular weight cutoff dialysis tubing to remove the methacrylic acid and other impurities. Then the solution was frozen with liquid nitrogen and lyophilized for 1 week. The dry gelMA powder was resuspended in PBS 1X, mixed with LAP, the final concentration was 10% GelMA and 0.15% LAP. For the final shape, the solution was poured into the insert and cured using an UV light with wavelength of 390-395 nm.
Concerning the modelling of the two porous medium, in ANSYS environment the porous component is composed of a fluid phase and a solid phase. The scaffolds constituent the solid phase were schematized as repetition of one base unit. The pore has a spherical shape and it is inscribed in a cube with the side equal to a pore diameter. The combination between sphere and cube represents the base unit (fig. 6.6).

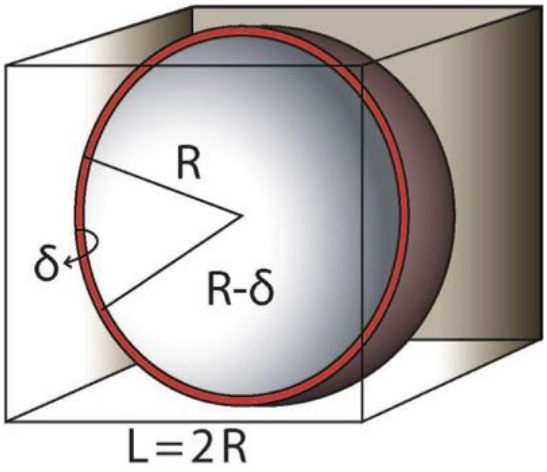

Fig. 6.6 *Base unit of the porous medium. R: External pore radius, δ: Pore thickness, L: Cube side, $R-\delta$: Internal pore radius*

An important parameter to full specify the interaction between the solid and the liquid phase is the IAD. The interface area density was estimated as a function of the unit base that describes the porous structure. IAD was calculated as follow:

$$IAD = \frac{S_{e_s} + S_{i_s}}{V_c} \tag{6.1.4}$$

Where $S_{e_s} = 4\pi R^2$ is the external surface; $S_{i_s} = 4\pi(R-\delta)^2$ is the internal surface and V_c is the total volume of the unit base cell. In table 6.1 the value for different scaffolds and sections are reported.

	IAD [1/m]		
Gelma	10 µm		
	$2.9094 * 10^5$		
PLLA	70 µm	140 µm	200 µm
	$3.8924 * 10^4$	$1.5675 * 10^4$	$1.09156 * 10^4$

Table 6.1 *IAD values for GelMA and PLLA scaffold*

In table 6.2 and 6.3 the physical and chemical characteristics of fluid and solid phase are reported, respectively.

The porosity is defined as the ratio between the void volume, V_v, and the total volume, V_t:

$$\phi = \frac{V_v}{V_t} \tag{6.1.5}$$

	Fluid phase (Water)
Molar Mass [$\frac{Kg}{Kmol}$]	18.2
Density [$\frac{Kg}{m^3}$]	997.0
Specific heat capacity [$\frac{J}{KgK}$]	4181.7
Reference temperature [°C]	37.5
Reference pressure [atm]	1
Reference enthalpy [$\frac{J}{Kg}$]	0
Reference entropy [$\frac{J}{KgK}$]	0
Dynamic viscosity [$\frac{Kg}{ms}$]	$8.899*10^{-4}$
Thermal conductivity [$\frac{W}{mK}$]	0.6069
Thermal expansion [$\frac{1}{K}$]	$2.57*10^{-4}$

Table 6.2 *Physical characteristics of fluid phase assumed as water*

	GelMA scaffold	PLLA scaffold
Molar Mass [$\frac{Kg}{Kmol}$]	1.0012	114000
Density [$\frac{Kg}{m^3}$]	1190	1220
Thermal conductivity [$\frac{W}{mK}$]	0	0
Porosity (ϕ)	0.8	0.93
Permeability (K_{perm}) [m^2]	10^{-16}	$3.234*10^{-9}$

Table 6.3 *Proprieties of solid phase*

but also

$$\phi = 1 - \frac{V_s}{V_t} \tag{6.1.6}$$

where V_s is the volume of the solid part.
In this case, solid volume is defined as:

$$V_s = \frac{V_{ring}}{V_{cube}} = \frac{4\pi R^2 \delta}{L^3} \tag{6.1.7}$$

Usually K_{perm} in an anisotropic structure, is a tensor quantity. Here, since the scaffolds under consideration are isotropic, it becomes a scalar parameter. The porosity and the permeability of the PLLA scaffold have been measured via Boyle's pycnometer and SEM analysis. Data for GelMa are scarce in literature. Since it is a surrogate material for cartilage and it remodels into it after a sufficient incubation time into the bioreactor, we have initialised the model for the former bioreactor configuration using data that have been previously measured for native tissue (Taffetani et al., 2014).

6.1.3 Experimental validation

In order to validate the fluid dynamics model, tests about mixing (neat fluid and bovine serum albumin) and glucose consumption were carried out. The bioreactor is connected to syringes that allow the fluid perfusion. The pump is a Kyiatec model 200 series, volume, flow rate and syringes depending on the speed test carried out. The syringes are connected to bioreactor by assembled tubing in platinum-cured silicone and polypropylene fittings. At the end of the process a gas exchange medium reservoirs collect the medium passed through the bioreactor. In fig. 6.7 a schematic representation of the system is shown.

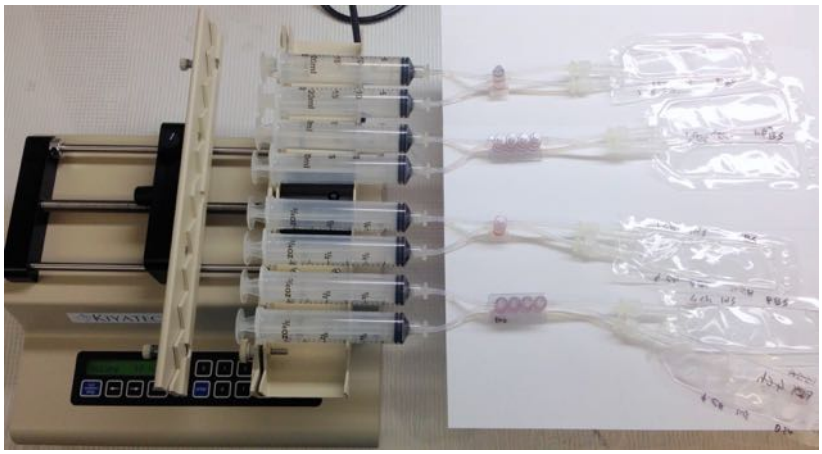

Fig. 6.7 *Schematic representation of adopted system*

Two different bioreactor configurations were tested, 1 unit cell and 4 unit cells array. Furthermore, to validate the fluid dynamics model in different conditions, each configuration was tested with the empty insert, insert with GelMA scaffold and insert with PLLA scaffold (fig. 6.10) and three different fluid dynamic regimes. In figure 6.9 a sketch of the simulation

pattern adopted is reported.

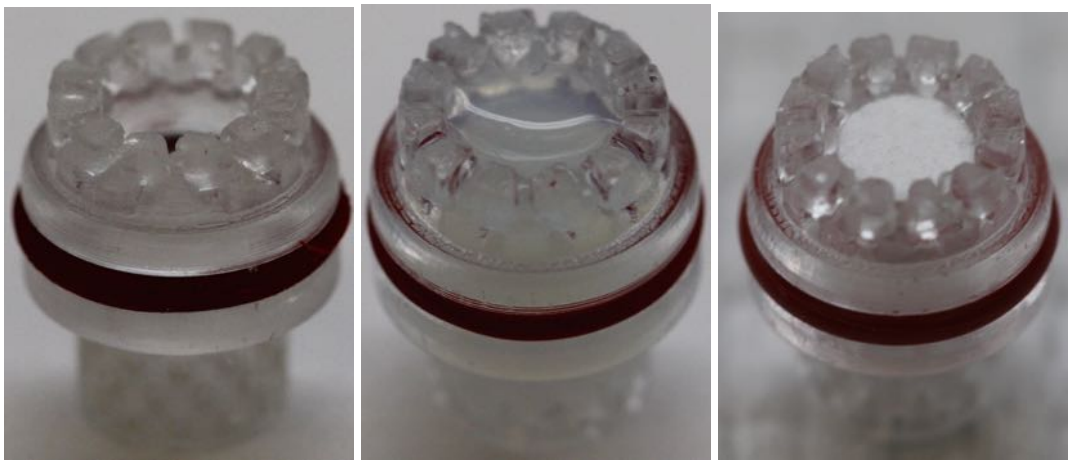

(a) (b) (c)

Fig. 6.8 *Different insert conditions: a) Empty insert, b) Insert with gelMA scaffold, c) Insert with PLLA scaffold*

6.1.4 Mixing tests

For the flow model, the characteristics Reynolds number of the flow in the bioreactor was calculated as follow:

$$Re = \frac{\rho v D}{\mu} = \frac{\rho v \pi D^2}{4\mu}\frac{4}{\pi D} = \frac{\rho \dot{Q}}{\mu}\frac{4}{\pi D} \tag{6.1.8}$$

where $D = 1mm$ is the inlet diameter, $\rho = 999.97Kg/m^3$ and $\mu = 0.001Pa*s$ density and dynamic viscosity of water, $\dot{Q}$ is the flow rate in each chamber, equal to 1 ml/day, 2 ml/day and 10 ml/day. $Re \ll 0.01$ was found for each condition, thus the hypothesis of laminar flow can be applied.
In table 6.4 and in table 6.5 the simulation results are reported.

To evaluate the difference of flow rate in the upper channel and in the lower channel after the passage through the bioreactor, two different colours were adopted (fig. 6.10), green in the upper part (diluted safrainin o fast green) and red in the lower part (diluted alizarin red). It is not possible, indeed, to control the amount of flow rate in a direct way, the different flow rate between the two fluids being too little for an experimental validation. In this way it was

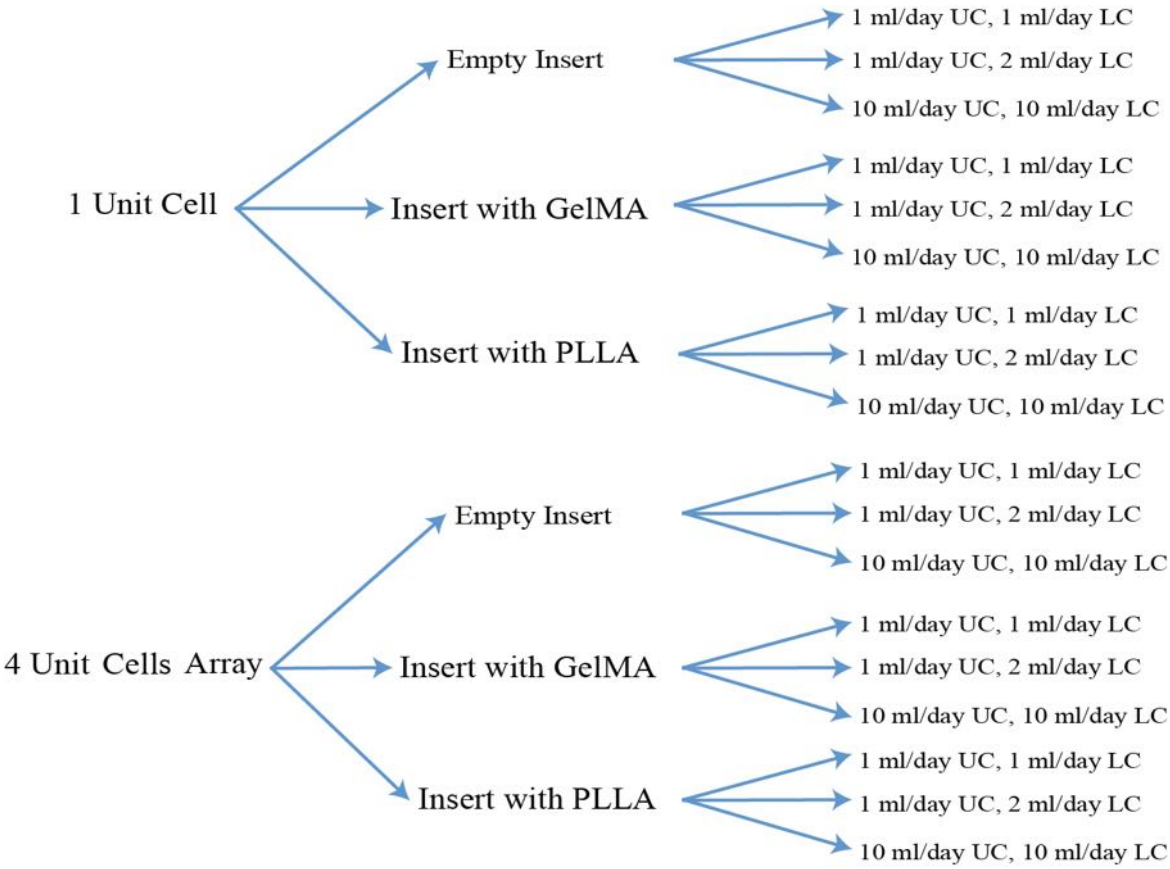

Fig. 6.9 *Simulation pattern: two configurations (1 unit cell and 4 unit cells array), three conditions (empty insert, insert with GelMA scaffold, insert with PLLA gradient scaffold) and three different fluid dynamic regimes (LC=Lower Channel; UC=Upper Channel)*

possibile to provide, at least, a qualitative trend.

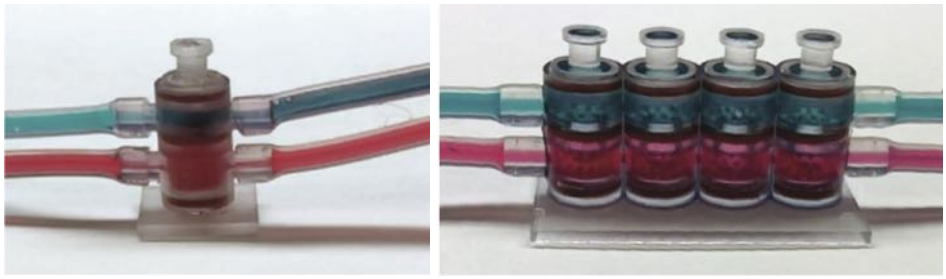

(a) *1 Unit Cell* (b) *4 Unit Cells Array*

Fig. 6.10 *Arrangement of the tests for mixing of the colours*

The different fluids were collected after one day of perfusion. The analysis was carried out via spectrophotometer. A spectrophotometer consists of two instruments, a spectrometer

	1 Unit Cell [ml/day]			
	Inflow		Outflow	
	UC	LC	UC	LC
Empty Insert	1	1	1.033	0.965
	1	2	1.530	1.469
	10	10	10.333	9.659
Insert with GelMA scaffold	1	1	1	1
	1	2	1	2
	10	10	10	10
Insert with PLLA scaffold	1	1	1.032	0.968
	1	2	1.427	1.572
	10	10	10.032	9.676

Table 6.4 *Simulated results of fluid flow rate for 1 Unit Cell*

	4 Unit Cells Array [ml/day]			
	Inflow		Outflow	
	UC	LC	UC	LC
Empty Insert	1	1	1.035	0.964
	1	2	1.553	1.446
	10	10	10.353	9.643
Insert with GelMA scaffold	1	1	1	1
	1	2	1	2
	10	10	10	10
Insert with PLLA scaffold	1	1	0.898	0.827
	1	2	1.495	1.374
	10	10	8.985	8.268

Table 6.5 *Simulated results of fluid flow rate for 4 Unit Cells Array*

for producing light at a specific wavelength, and a photometer for measuring the intensity of light. A cuvette containing a liquid is placed between the spectrometer beam and the photometer. The amount of light passing through the tube is measured by the photometer, which records a voltage signal depending on the amount of light absorbed by the liquid. First of all the intensity of light (I_0) passing through a blank is measured. The intensity is the number of photons per second. Then, the intensity of light (I) passing through the sample solution is measured. The transmittance (T) is ratio between the intensity of light passing through the sample solution and the reference 6.1.9, meanwhile the absorbance (A) is the decimal logarithm of the reciprocal of the transmittance 6.1.10.

$$T = \frac{I}{I_0} \tag{6.1.9}$$

$$A = -log_{10}T \tag{6.1.10}$$

The data were registered in terms of absorbance in a range from 400 nm to 700 nm with an interval of 10 nm. In y-axis the percentage peak intensity was reported (fig. 6.11, 6.12, 6.13).

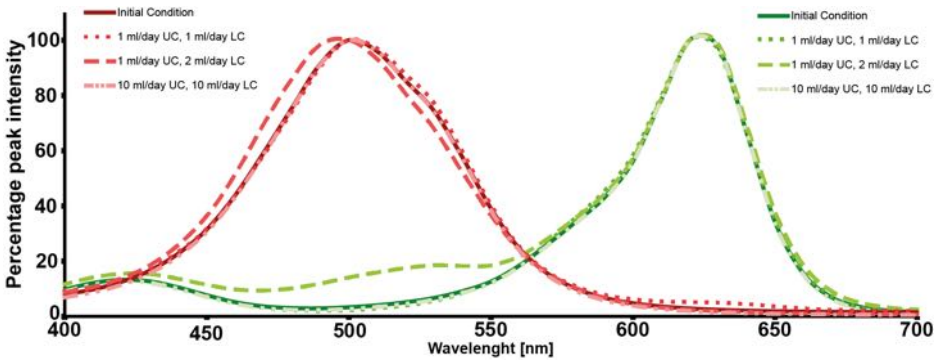

(a) *1 unit cell empty insert*

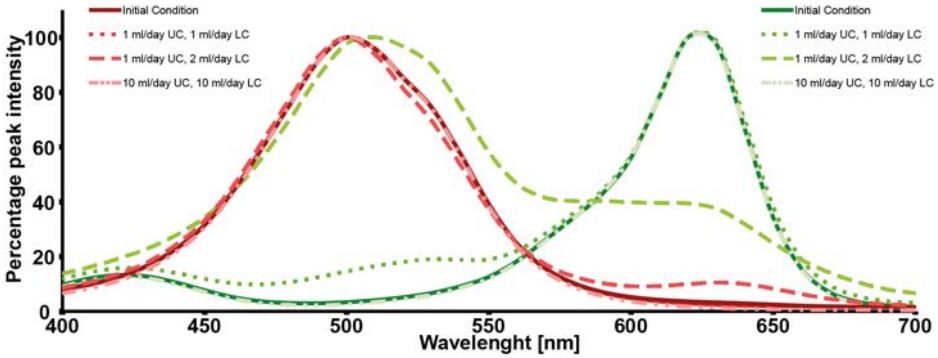

(b) *4 unit cell empty insert*

Fig. 6.11 *Mixing colours tests: empty insert*

In all graphs (fig. 6.11, 6.12, 6.13) are the same symbols are used. In solid line the background, which is the spectrum of colours inside the syringes. Fluid flow rate 1 ml/day in the upper channel and 1 ml/day in the lower channel in dotted line. In dashed line with 1 ml/day in the upper channel and 2 ml/day in the lower channel. A long dash-dot-dot line for 10 ml/day upper channel and 10 ml/day lower channel.
A qualitative comparison of trends with numerical simulation to verify the outcome of numerical predictions was possible.
As a matter of facts the experimental trends agree well with the numerical simulations. In all configurations and flow rates, fluid mixing follows the pressure gradient between lower and upper chamber. The small difference in inner diameter between the two chambers

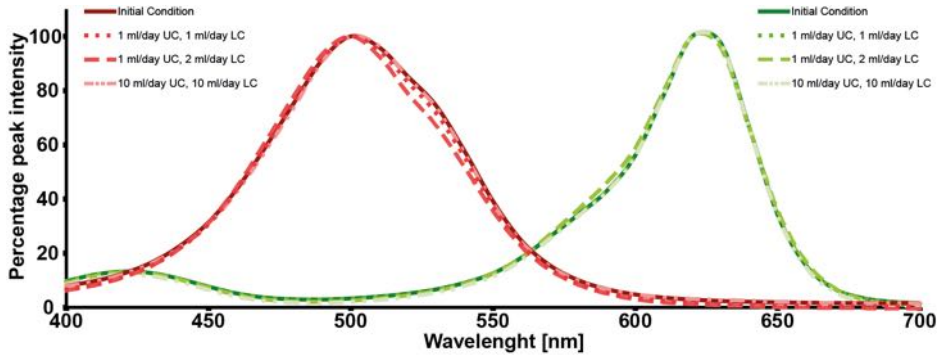

(a) *1 unit cell with GelMA scaffold*

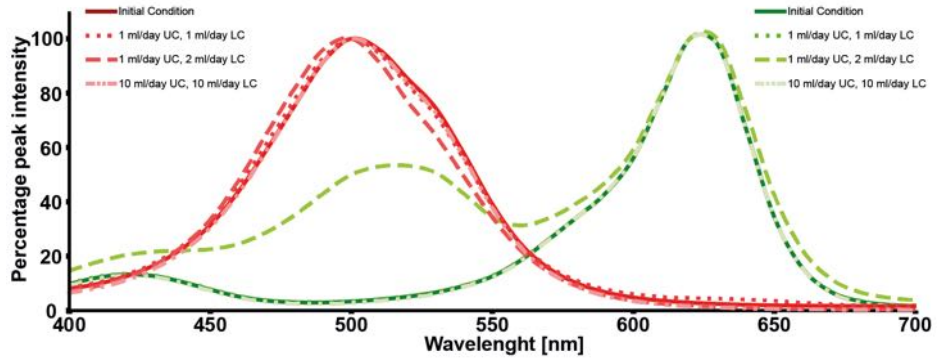

(b) *4 unit cell array with GelMA scaffold*

Fig. 6.12 *Mixing colours tests: GelMA scaffold*

implies that the upper outlet has a higher flow rate, and a red-in-green color mixing with the associated change of green absorption spectrum. In the case of empty insert in 1 unit cell, the model predict an inlet-outlet difference of 3.3% for the same flow rate configuration, 1-1 and 10-10, (1.033 ml/day or 10.333 ml/day upper outflow for 1 and 10 ml/day in inflow, respectively) and a 53% upper inflow-outflow difference for the different upper and lower flow rate configuration (1.530 ml/day outflow compared to 1 ml/day inflow). This prediction is reflected onto the respective color spectra (fig. 6.11a). At equal flow rates the color spectra perfectly overlap, at different flow rates the green color presented an increase in the peak in correspondence of the maximum of the red peak. The combination of color is more accentuated in the case of 4 unit cells case, figure 6.11b, as also confirmed by numerical data. 3.5% for equal flow rate, 1-1 and 10-10, 55% for different flow rate 1-2. As expected the most relevant mixing occurs for the unequal flow rate configuration, with a complete change in outflow maximum peak intensity (green dashed line). By visual inspection, this corresponds to a violet tint and the main peak at 510 nm (coincident with the red color inflow peak) and a minor peak at 620 nm (coincident with the green color inflow peak). Focusing

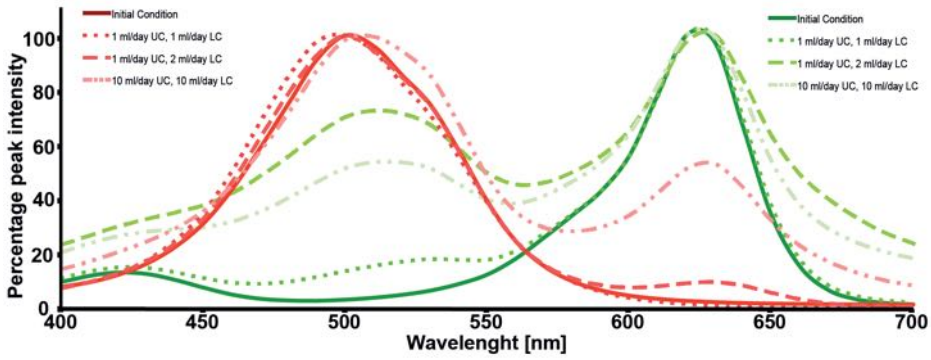

(a) *1 unit cell with PLLA scaffold*

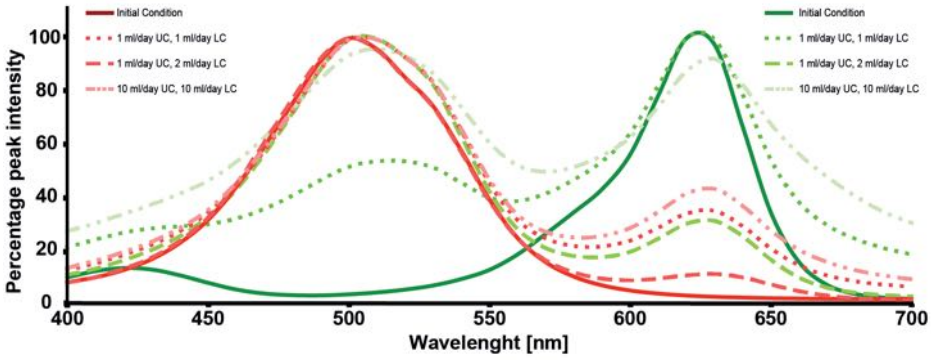

(b) *4 unit cell array with PLLA scaffold*

Fig. 6.13 *Mixing colours tests: PLLA scaffold*

on a 1 unit cell with the GelMA scaffold in the insert figure 6.12a, the simulation predicts no fluid mixing, and effectively the experimental inflow and outflow spectra superimpose perfectly. Different is the case of the 4 unit cells array (6.12b). The numerical modelling suggests no mixing, essentially the same outcome as for the 1 unit cell. However, in the experimental flow results there is an additional peak in the upper chamber outflow spectrum at 510 nm. This suggests that the GelMA scaffold, indeed, allows some degree of diffusion, and that the cumulative effect of 4 chambers in series makes this more apparent.
Finally, for the PLLA scaffold, both for the 1 cell and the 4 cells bioreactor (fig. 6.13), the spectra show a more pronounced commingling between the two chambers than would be expected from the numerical modeling. This is hardly unexpected since the porous PLLA scaffold is far from being as regular as modeled in the numerical simulations, and the mechanism governing transport is a combination of diffusion and perfusion inside the pores. As in the other cases, the most significant commixing occurs for the different fluid flow rates in upper and lower chambers.

6.1.5 BSA transport

Tests to experimental validate the fluid dynamics model about the diffusion of a specific molecule were performed.
In this study, Alexa Fluor 555-conjugated albumin from bovine serum (BSA) (BSA555, 65kDa, Molecular Probes) was adopted.
The BSA is a serum albumin protein isolated from cows. Bovine serum albumin (often from a fetal bovine source) is also used as a nutrient in cell and microbial culture. In molecular biology, BSA is used to stabilize some restriction enzymes during digestion of DNA and to prevent adhesion of the enzyme to reaction tubes, pipet tips, and other vessels. BSA is considered to be a universal blocking reagent in many applications. This is because BSA does not affect the functions of other proteins (enzymes) that do not need it for stabilization. BSA is also commonly used to determine the quantity of other proteins, by comparing an unknown quantity of protein to known amounts of BSA in, for instance, the Bradford Protein Assay. BSA is used because of its stability to increase signal in assays, its lack of effect in many biochemical reactions, and its low cost, since large quantities of it can be readily purified from bovine blood, a byproduct of the cattle industry.
From literature (Lin et al., 2014) a BSA concentration of 10 µg/ml was used. In all different flow rate regimes the BSA was perfused in the lower channel. To full specify the BSA transport in ANSYS model two parameters are necessary: $D_{s,s}$ the diffusion coefficient inside the porous media; τ the mass transfer coefficient between solid and liquid phase.
The diffusion coefficient is zero considering the PLLA impermeable to the solute, while $4.5x10^{-10}[m^2/s]$ for GelMA. Evaluating a diffusion regime inside the pores, the Sherwood number is around the unit, then τ becomes the ratio between the diffusion coefficient and the pore diameter.

$$Sh = \frac{\tau d}{D_{s,s}} = 1 \Rightarrow \tau = \frac{D_{s,s}}{d} \tag{6.1.11}$$

In table 6.6 the transport coefficients for BSA and glucose are summarized. Concerning the experimental test, after 1 day the medium was collected and analysed by Biotek synergy HT spectrofluorometer in fluorescence detection method, 530/25 filter excitation and 590/35 filter emission.
First of all a standard curve was realised (fig. 6.14). To construct the standard curve 6 different concentrations were adopted: 1, 2.5, 5, 10, 20, 30 $\mu g/ml$, for each concentration a different intensity signal, expressed in Relative Fluorescence Units (RFU), was registered. The RFU is used in analysis employing fluorescence detection. Fluorescence is identified using a charged coupled device (CCD), when the labeled fragments, are energized by laser

	BSA		Glucose	
	GelMA	PLLA	GelMA	PLLA
$D_f = D_{s,f}[m^2/s]$	$7.1 * 10^{-10}$	$7.1 * 10^{-10}$	$6.7 * 10^{-10}$	$6.7 * 10^{-10}$
$D_{s,s}[m^2/s]$	$3.918 * 10^{-18}$	0	$3.958 * 10^{-10}$	0
$\tau[m/s]$	$2.025 * 10^{-5}$	0	$1.56 * 10^{-9}$	0

Table 6.6 *Transport coefficients for BSA and glucose in PLLA and GelMA environment. The values were acquired from (Anandan et al., 2007)*

light and travel across the detection window. A software measures the results, determining the quantity or size of the fragments, at each data point, from the level of fluorescence intensity. Via standard curve, slope of the interpolating straight line, it was possible to calculate the concentration of BSA on the different samples.

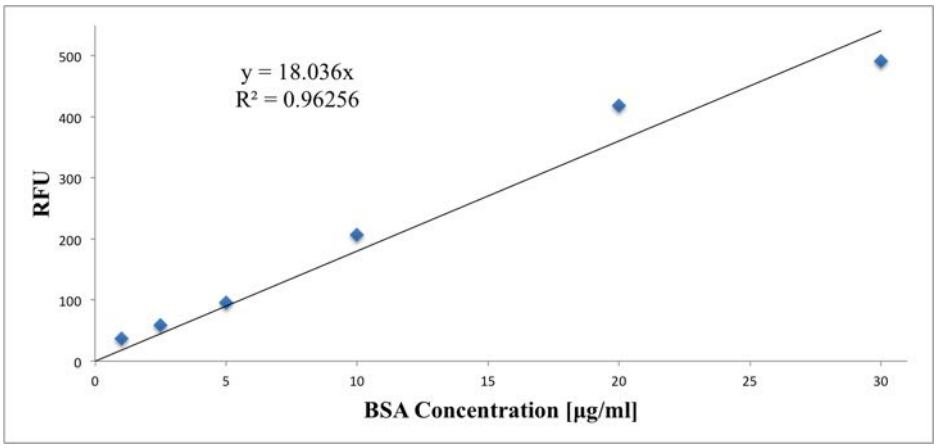

Fig. 6.14 *Standard curve of BSA concentration from 0 µg/ml to 30 µg/ml*

In figure 6.15 the comparison between experimental and simulated data is reported. The graph shows the in y-axis the BSA concentration in µg/ml and x-axis the three conditions (without, gelMA and PLLA scaffold) in different regimes. In bar graph the experimental results each one with a specific error bar, in star symbol the modeled data.

Except for the case of different flow rates between lower and upper channel empty insert and with PLLA scaffold, the BSA concentration basically remains unchanged after crossing of bioreactor. The main deviation compared to the initial concentration is in 4 unit cells. The final concentration in the lower channel is almost $5g/ml$, whereas $4g/ml$ in upper channel. In each case a good accord amongst the simulated and the experimental check can be noticed.

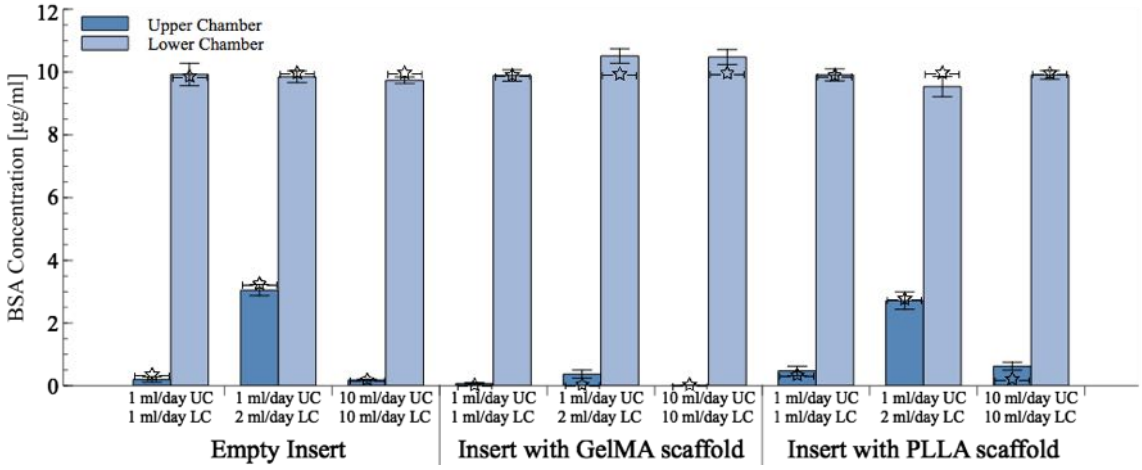

(a) *1 Unit Cell*

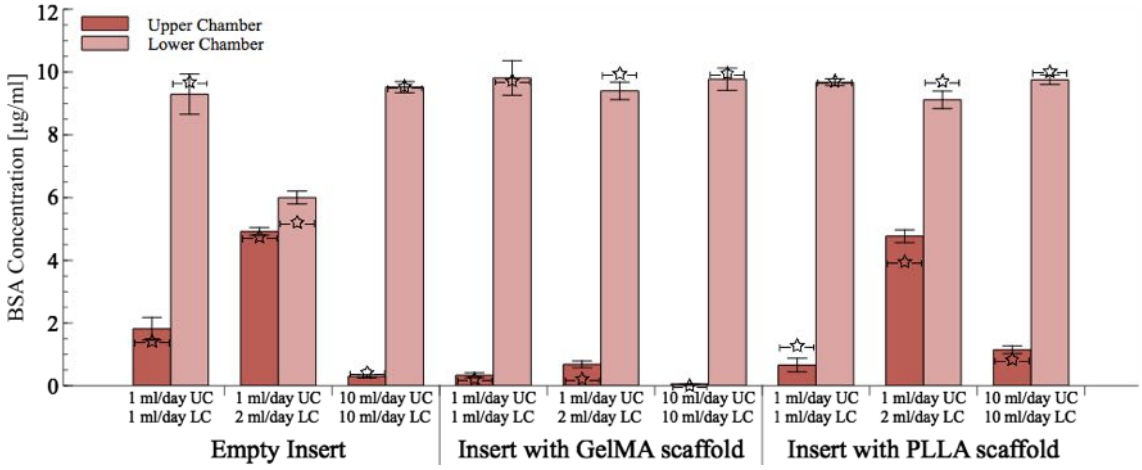

(b) *4 Unit Cells Array*

Fig. 6.15 *BSA concentration in µg/ml in different conditions and regimes. In bar graph the experimental results each one with a specific error bar, in star symbol the simulated data*

6.1.6 Glucose consumption

Animal cells, heterotrophs, derive their energy from coupled oxidation-reduction reactions. Glucose ($C_6H_{12}O_6; MW : 180.16 g/mol$) is a primary fuel for heterotrophs. Energy derived from glucose is stored in the form of high-energy phosphate bonds in ATP, or other nucleotide triphosphates, and as energy-rich hydrogen atoms associated with the co-enzymes NADP and NAD.

Efficient energy metabolism and maintenance of a reduced cellular environment depend upon the fine balance of the pathways in response to environmental factors.

Glucose is unable to diffuse across the cell membrane without the assistance of transporter proteins. Some hexose transporters allow glucose to flow passively from high to low concen-

tration without requiring the expenditure of cell energy. Those that move glucose against its concentration gradient consume energy, generally in the form of ATP. In vitro, the external glucose concentration exceeds the intracellular concentration. Once inside the cell, glucose is phosphorylated to glucose-6-phosphate (G6P) primarily by hexokinase. G6P can be converted to glucose-1-phosphate (G1P), or enter the glycolytic or pentose phosphate pathway. Glucose provides the reducing power needed to neutralize oxidative species (oxidative stress) that form in vivo and in vitro.
When glucose levels are sufficient, its metabolites move through the PPP and glycolytic pathways to form glyceraldehyde-3-phosphate (G3P). Energy from glycolysis that is ultimately stored as ATP is derived from reactions that occur at the level of glyceraldehyde-3-phosphate and below. Pyruvate and the vitamin NAD have distinct roles in the transfer of reducing equivalents into the mitochondrial systems. NAD delivers reducing equivalents to the electron transport system by shuttles that bypass the TCA cycle and pyruvate delivers reducing equivalents through the TCA cycle.
Cell lactic acid dehydrogenase (LDH) can re-oxidize cytoplasmic NADH by converting pyruvate to lactic acid. This is a wasteful process that leads to a metabolic dead-end. NADH that has not been oxidized by the aspartate:malate or gylcerol:phosphate shuttle is metabolized by LDH. A buildup of lactic acid in cell culture systems is evidence that the shuttles are unable to re-oxidize all of the NAD required to support G3P catabolism. At high levels, lactic acid becomes toxic to cells.
The glucose consumption was modelled by Michaelis-Menten term. In this way the relationship between nutritious consumption and nutritious concentration is not linear and it can be described as:

$$v = \frac{V_{max}C}{K_m + C}\varepsilon_s C \tag{6.1.12}$$

where v is the reaction rate , V_{max} is the maximum consumption rate depending on the species and cell type, C is the concentration of the species, K_m is the Michaelis-Menten constant, equal to concentration of species when the reaction rate is half of V_{max} and ε_s is the solid fraction of the porous medium.
The aforementioned values were imposed to $V_{max} = 9.925 * 10^{-17} mol/cells$ and $K_m = 0.5026464 kg/m^3$ (Pattappa et al., 2011). In this way, the non-linear model of Michaelis-Menten allows to consider the variation of consumption rate as a response to the concentration of the metabolite. This one involves a better approximation of the metabolic behaviour of the cells.
GelMA and PLLA gradient scaffold with a MSCs suspension respectively of 10^6 cells/ml and

$2.5 * 10^5$ cells/scaffold (taking into account the cell seeding efficiency) in a 4 unit cell array were adopted. After 1 day the medium was collected and analysed by Biotek synergy HT spectrofluorometer, in this case via colorimetric detection. The Glucose Assay Kit (abcam ab65333) adopted in this study, specifically oxidizes glucose to generate a product which reacts with a dye to generate color with a peak intensity of $\lambda = 570nm$.
To measure the glucose concentration a calibration curve was built. Following the protocol provided from the kit, standard curve dilution were prepared, 0, 2, 4, 6, 8, 10 nnmol/well (fig. 6.16).
A time point of 1 day was chosen as representative time to compare the two result sources.

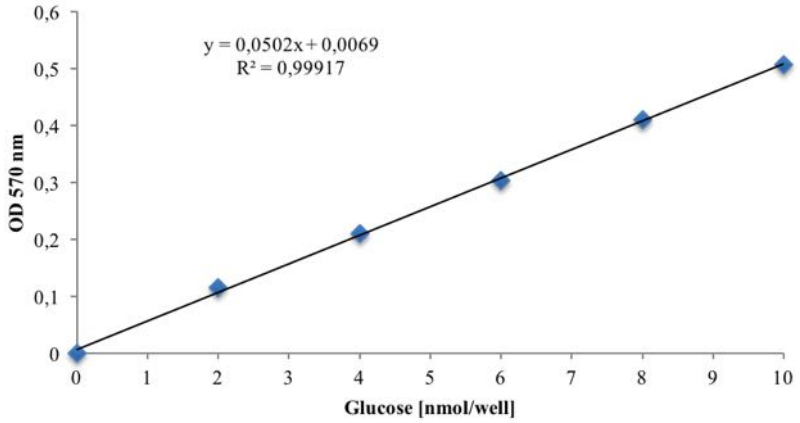

Fig. 6.16 *Standard curve of Glucose Assay Kit*

Indeed one day is a enough to emphasize eventual relevant differences from the initial concentration of glucose, but, in the same time, the cell density is basically the same as the beginning.
Table 6.7 and figure 6.17 report a comparison between the obtained data from the model and the empirical results.
As shown, there is a very good matching in both cases. About GelMA scaffold the difference between the average and the simulated value is less then 7% in the upper channel case and less then 4% in the lower channel case. On the other hand, for PLLA scaffold, considering the standard deviation, the data matching are substantially the same between the two different conditions.

	Initial Condition	GelMA scaffold % Consumption		PLLA Scaffold % Consumption	
		Simulated	Experimental	Simulated	Experimental
UC	1.0053	4.90	5.23 ± 1.11	6.54	5.38 ± 1.2
LC	1.0053	8.14	7.95 ± 1.08	10.81	8.65 ± 2.05

Table 6.7 *Glucose consumption in GelMA and PLLA scaffold after 1 day of proliferation inside the bioreactor, all values are expressed in mg/ml*

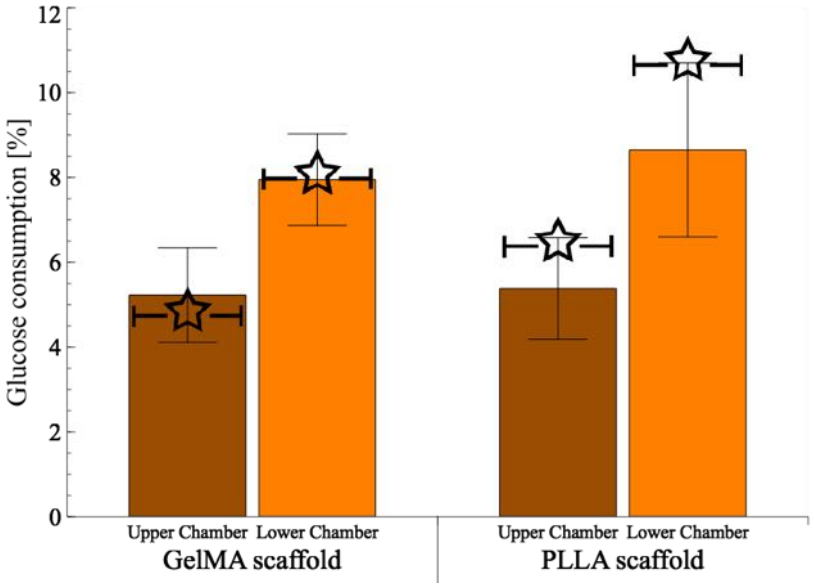

Fig. 6.17 *Graphic representation of glucose consumption in GelMA and PLLA scaffold. In bar graph the experimental results, in star symbol the simulated data*

6.2 Cell culture inside the bioreactor system

Preliminary tests to examine the cell viability inside the bioreactor were carried out. Gradient pore scaffold in PLLA and GelMA scaffold were adopted.
The cell seeding protocol reported in chapter 5 was adopted. Brefly 800,000 mesenchymal stem cells were seeded per PLLA scaffold. The scaffolds were preconditioned by soaking in DMEM cell culture medium overnight, after an overnight in ethanol 70% to ensure the sterylization. The cells were seeded in static conditions by injecting them through a pipette. In the GelMA scaffold a suspension of $10 * 10^6$ cells/ml was injected.
Scaffolds were harvested at days 3 and 7 of culture and evaluated via live/dead stain and MTS assay.

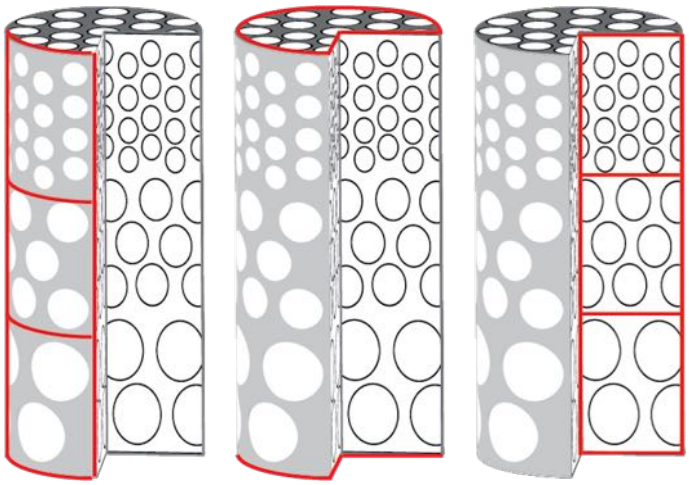

(a) (b) (c)

Fig. 6.18 *Schematic representation of different parts of the scaffolds analysed via Live/Dead cell viability assay in PLLA scaffold*

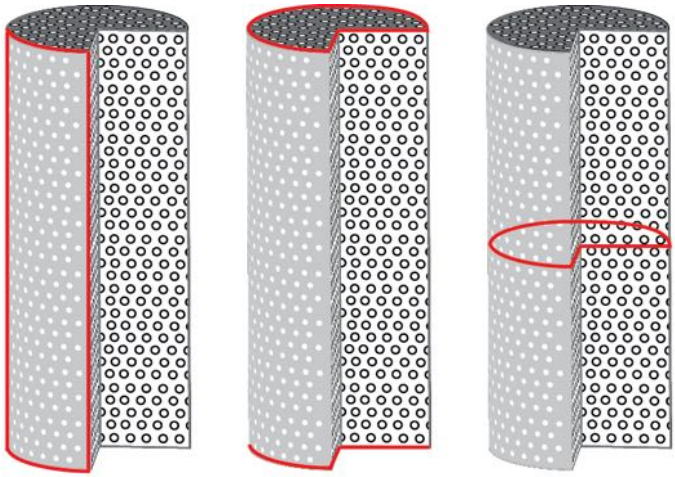

(a) (b) (c)

Fig. 6.19 *Schematic representation of different parts of the scaffolds analysed via Live/Dead cell viability assay in GelMA scaffold*

6.2.1 Live/Dead

Samples via Live/Dead were analyzed on the side of the scaffold (see fig. 6.18a and fig. 6.19a), top/bottom (fig. 6.18b and fig. 6.19b) and cross sections (fig. 6.18c and fig. 6.19c).

For each configuration, the cell colonization corresponding to different pore dimension was analysed.

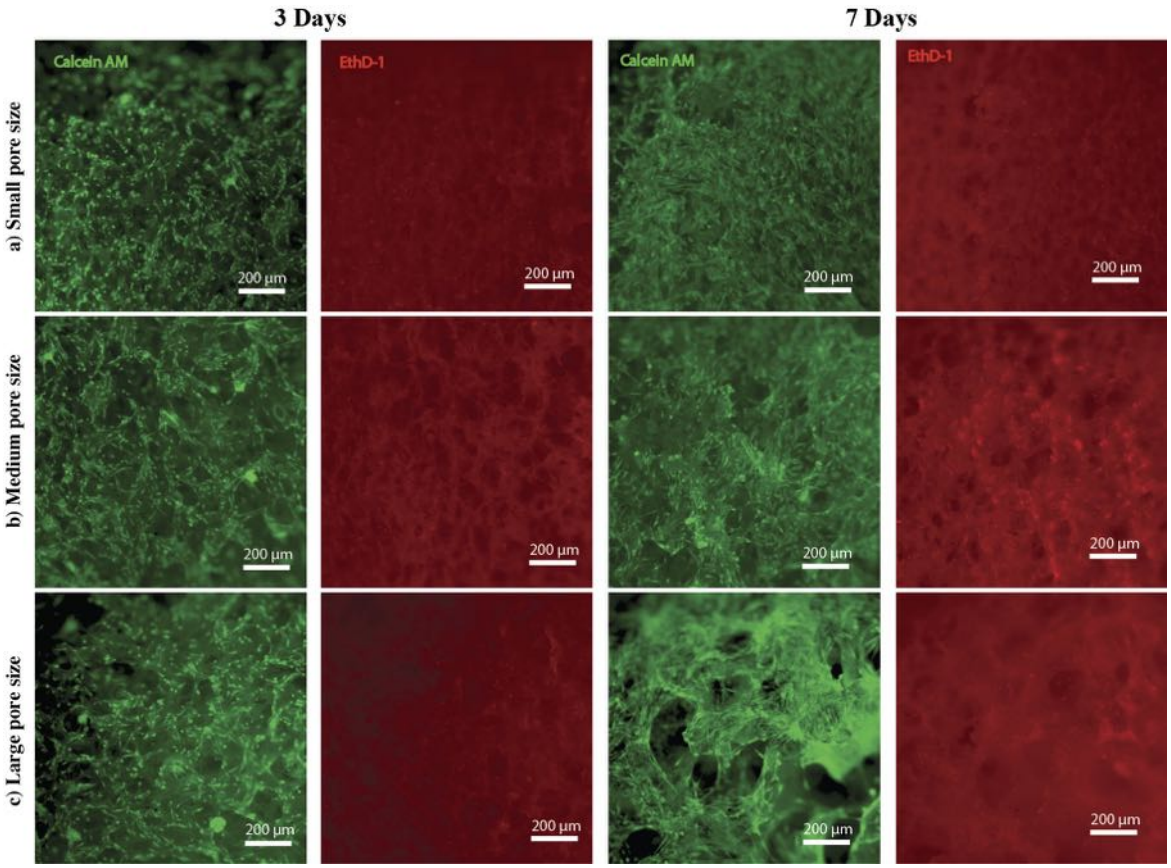

Fig. 6.20 *Live/Dead Cell Viability Assays on the side of scaffold in different pore dimensions regions*

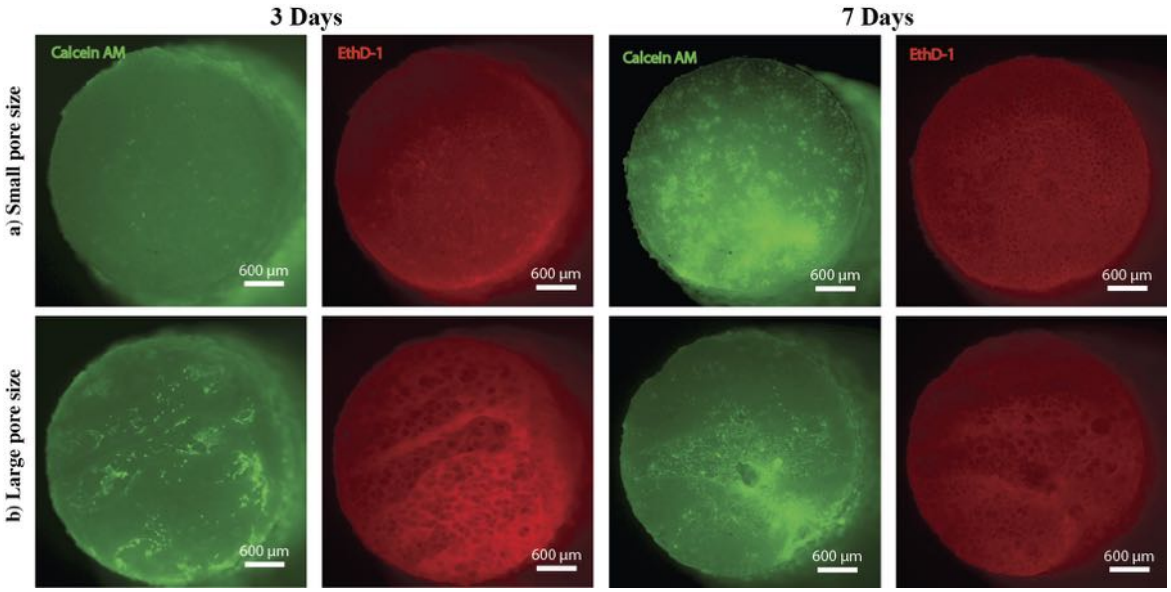

Fig. 6.21 *Live/Dead Cell Viability Assays on top and bottom of the scaffold*

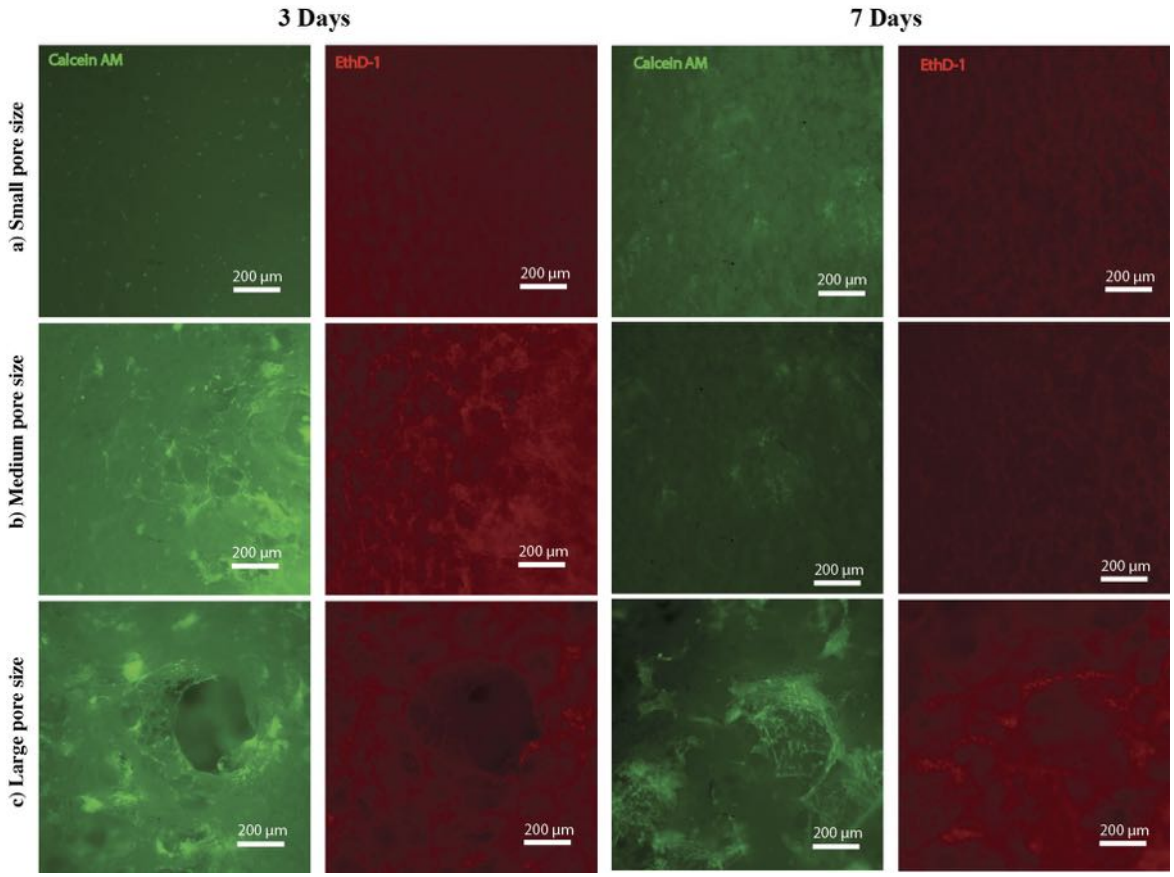

Fig. 6.22 *Live/Dead Cell Viability Assays on the cross section of scaffold in different pore dimensions regions*

Figure 6.20 report the live and dead at 3 days and 7 days on the side of the scaffold, figure 6.21 upper surface and lower surface, figure 6.22 on the cross section, in different pore dimensions regions.

After 3 days it is possibile to see as there is a good cellular adhesion in all sides of scaffold but also on the upper part and in the lower part. Notwithstanding there is not a direct channel inside the bioreactor to feed the cell to the center, the presence of a good amount of live cells shows that the perfusion regime allows a complete diffusion of nutrient.

The cross sections underline a good penetration though non perfectly homogeneous. As expected large pore sizes show a better penetration but the few amount of dead cells also in a small pore size portion of the scaffold is a good results.

After 7 days, the total amount of cells is higher compared to 3 days, especially on the side of the scaffold and everywhere one observe a good cell vitality.

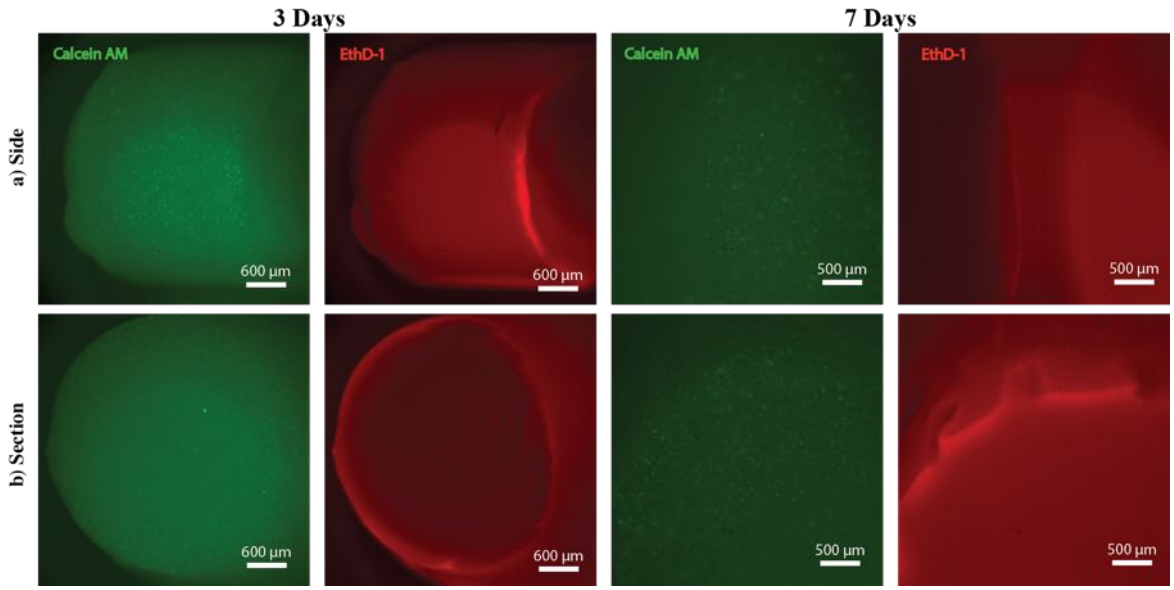

Fig. 6.23 *Live/Dead Cell Viability Assays on GelMA scaffold*

As concerning the gelatine methacrylate (fig. 6.23) both in the side and in center the number of live cells far exceed the dead cells. This demonstrates the good quality of the gelatine for cell vitality and proliferation.

6.2.2 MTS

The ability of the fabricated scaffolds and GelMA to allow adhesion and proliferation of hMSCs was evaluated by MTS assay after three and seven days. The cell seeding efficiency inside the PLLA scaffold was preliminary evaluated around 25%. One can notice (fig. 6.24a) after seven days of proliferation a neat increase of mesenchymal cells, $4.5 * 10^5$ compared to $2.7 * 10^5$ after three days. This result proofs the ability of the materials to support and promote cell proliferation.
The same test was carried out for gelMA scaffold (fig. 6.24b). This technique allows to see the amount of viable cells by chemical conversion of MTS, this process involves two steps: diffusion of MTS from medium to cell and diffusion of formazan from cell to medium. Both steps are slow processes, then probably three-four hours are not a sufficient time to estimate the correct amount of cells. In any case from a relative point of view, the number of cells is almost duplicated. This aspect coupled with the Live/Dead vitality test show the good quality of the gelatine for cell culture.

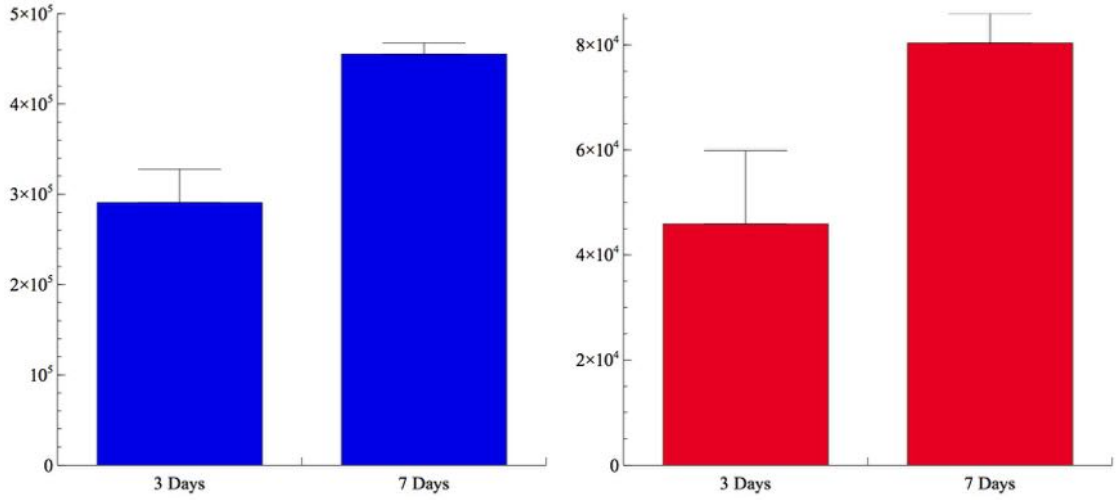

(a) *MTS assay in PLLA scaffold* (b) *MTS assay in GelMA scaffold*

Fig. 6.24 *MTS assay at 3 and 7 days in PLLA and GelMA scaffold inside the bioreactor*

6.3 Osteochondral regeneration

6.3.1 Chondro-Osteo differentiation

PLLA gradient scaffolds and GelMA scaffolds were seeded to induce the differentiation in osseous-like tissue and cartilage-like tissue of human Mesenchymal Stem Cells. In order to obtain a very strong experimental evidence of the capacity of the system to allow the cells differentiation, hBMSCs from different patients were used.
The three replica of the experiments were performed pooling hBMSCs at passage 3 (P3) from diverse patients: 1st replica (1 female patient 44 years old and 2 male patients 45 and 59 years old), 2nd (1 female patient 70 years old and 2 male patients 60 and 66 years old), 3rd (1 female patient 62 years old and 2 male patients 39 and 55 years old). Cylindrical PLLA scaffolds (same dimension of the insert) and GelMA scaffold were uniformly seeded with 800,000 bone marrow hBMSCs derived from total joint arthroplasty patients.
The scaffolds were preconditioned by soaking in DMEM cell culture medium, after an overnight immersion in ethanol 70% to allow the sterylization. Then the scaffolds were placed in the bioreactor or in multi-well plate. The gradient scaffolds in the bioreactor were placed with the small pore side (~70 μm) in the upper chamber (UC) and the large pore side (~200 μm) in the lower chamber (LC). In the bioreactor for 7 days a growth medium (DMEM, 10% fetal bovine serum (FBS), penicillin/streptomycin/fungizone) was perfused at 2 ml/day, meanwhile in the multi-well plate the same growth medium was changed every 2-3

days. After 7 days different media were adopted. Three sets of experiments were carried out.

- 1^{st} Set. Influence of culture media. To obtain a distinct differentiation between the two parts of the scaffold, different media were adopted. Chondrogenic medium (DMEM, 10 ng/ml TGF-β3 (PeproTech), 1% insulin-transferrin-selenium, 50 µM L-ascorbic acid 2-phosphate (AsA2-P), 40 µg/ml L-proline) was supplied to the UC, and osteogenic medium (DMEM, 10% FBS 0.1 µM dexamethasone, 50 µg/ml AsA2-P, 10 mM β-glycerophosphate) to the LC, both at a flow rate of 2 ml/day. In this case PLLA scaffold and GelMA were adopted.

- 2^{nd} Set. Influence of pore size. To identify the influence of pore dimension in the differentiation of hMSCs, the same medium in upper chamber and in the lower chamber was adopted. In one case only osteogenic medium in the other case only chondrogenic medium, with the same aforementioned compositions and at the same flow rate 2 ml/day. For both test the PLLA gradient scaffold was used.

- 3^{rd} Set. Influence of bioreactor. As a control two gradient scaffolds and two homogeneous scaffolds were seeded and placed in 6-well plate. About the homogeneous scaffolds two different pore size were adopted, ~70 µm and ~200 µm, Gradient scaffolds and 200 µm scaffolds in osteogenic medium were cultured on the one side, whereas gradient scaffolds and the 70 µm scaffolds in chondrogenic medium on the other side.
  In fig. 6.25 a schematic representation of the experimental pattern is reported.

After 30 days of differentiation the scaffolds in bioreactor and in plate were analyzed. One scaffold for each type was fixed for histology staining. The other three scaffolds were cut in two parts on the traverse plane for real-time PCR analysis.

6.3.2 Histology staining

The scaffolds removed from bioreactor and multi-well plate were fixed in 4% paraformaldehyde overnight and then followed the deparaffinization process. After a double immersion in xylene, the samples were dipped in paraffin and maintained at 4°C. At the end of the process the scaffolds were cut in 10 µm section and stained with alcian blue and alizarin

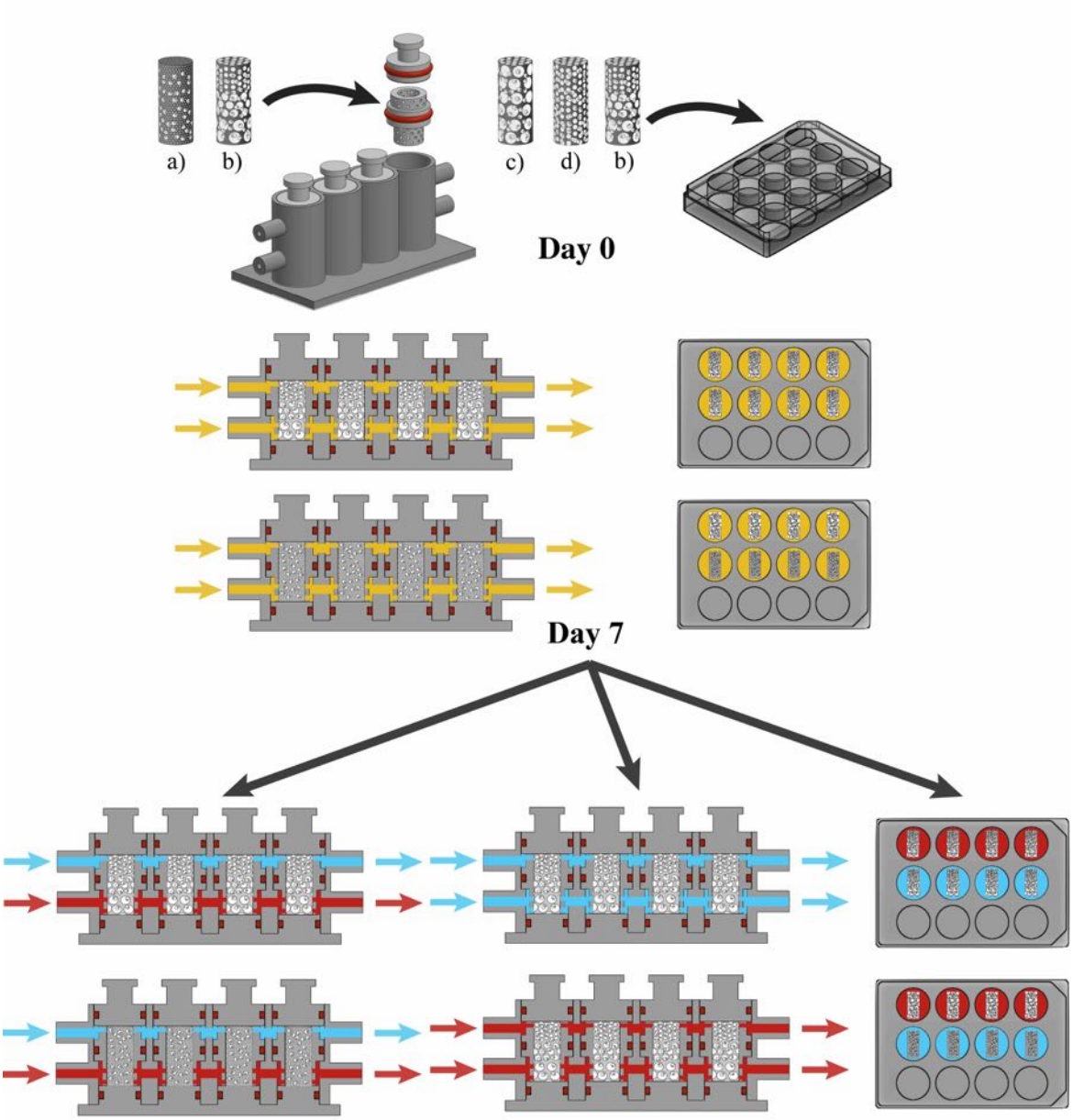

Fig. 6.25 *Graphic representation of the adopted experimental pattern. a) GelMA scaffold, b) PLLA gradient scaffold, c) 200 µm, d) 70 µm scaffold,. In yellow colour the growth medium, in blue colour the chondrogenic medium and in red colour the osteogenic medium*

red. Alcian blue is one of the most widely used cationic (it has many positive charges on the molecule) dyes for the highlights of glycosaminoglycans. It is thought to work by forming reversible electrostatic bonds between the cationic dye and the negative (anionic) sites on the polysaccharide. These electrostatic bonds can be readily broken, revealing what appears to be a variation in bonding among different types of glycosominoglycans. When the concentration of electrolyte required to break the bond is increased progressively, then neutral, sulphated

and phosphated mucopolysaccharides may be identified in tissue sections. Alizarin Red S, an anthraquinone derivative, may be used to identify calcium in tissue sections. The reaction is not strictly specific for calcium, since magnesium, manganese, barium, strontium, and iron may interfere, but these elements usually do not occur in sufficient concentration to interfere with the staining. Calcium forms an Alizarin Red S-calcium complex in a chelation process, and the end product is birefringent.

- 1^{st} Set. Influence of culture media. At 4 weeks of differentiation, cell morphology and extracellular matrices (ECMs) were examined by histological analysis. In both cases, PLLA the constructs exhibited strong alcian blue staining on the side residing in the upper chamber perfused with chondrogenic medium and alizarin red staining in the part residing in the lower chamber (exposed to osteogenic medium) (6.31).
  Less evident but equally visible is the case of GelMA. In this case the cell spots clearly different from gel matrix were possible to distinguish (fig. 6.33).

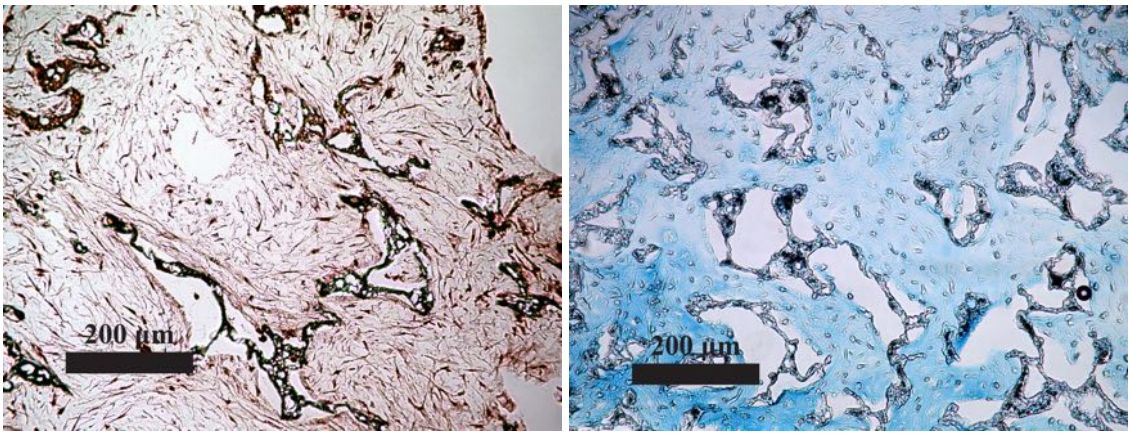

(a) *Alizarin red staining in PLLA scaffold* (b) *Alcian Blue staining in PLLA scaffold*

Fig. 6.26 *Histology staining. a) Small pore size in the upper chamber exposed to chondrogenic media; b) Large pore size in the lower chamber exposed to osteogenic media*

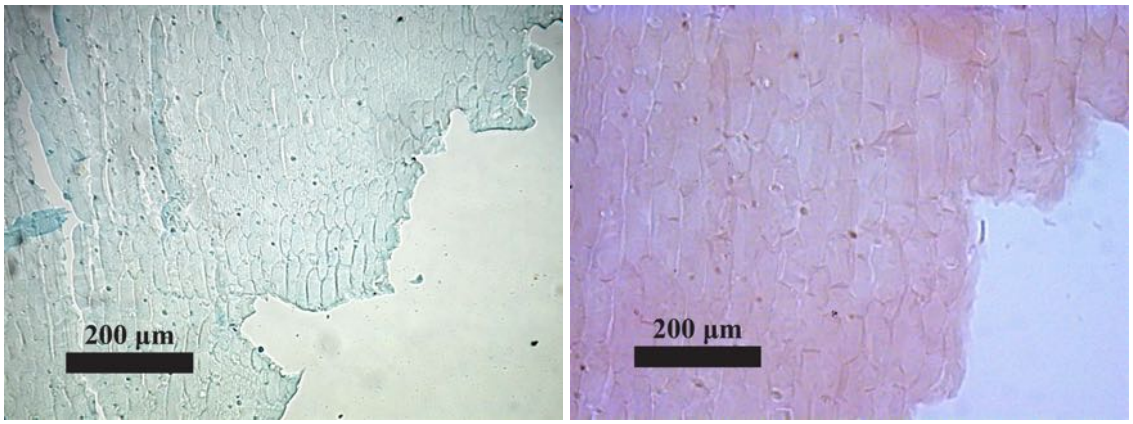

(a) *Alcian Blue staining in GelMA scaffold* (b) *Alizarin red staining in GelMA scaffold*

Fig. 6.27 *Histology staining. a) Upper chamber exposed to chondrogenic media; b) Lower chamber exposed to osteogenic media*

- 2^{nd} Set. Influence of pore size. In figures 6.28a and 6.28b the whole scaffold section is reported. In both cases it is evident a gradient of differentiation along the pore dimension gradient. In the first case, fig. 6.28a, the hMSC differentiation affects the entire scaffold but there is a higher production of GAGs in the upper part, corresponding to small pore size. This is probably due to the fact that the small pore dimension can recreate the hypoxic environment to promote the cartilage formation (see section 5.1). In the second case (fig. 6.28b) a higher alizarin red staining is evident in the large pore dimension, the bottom of the scaffold. The possible causes can be the larger dimension of osteoblasts compared to chondrocyte and an easier nutrient perfusion.

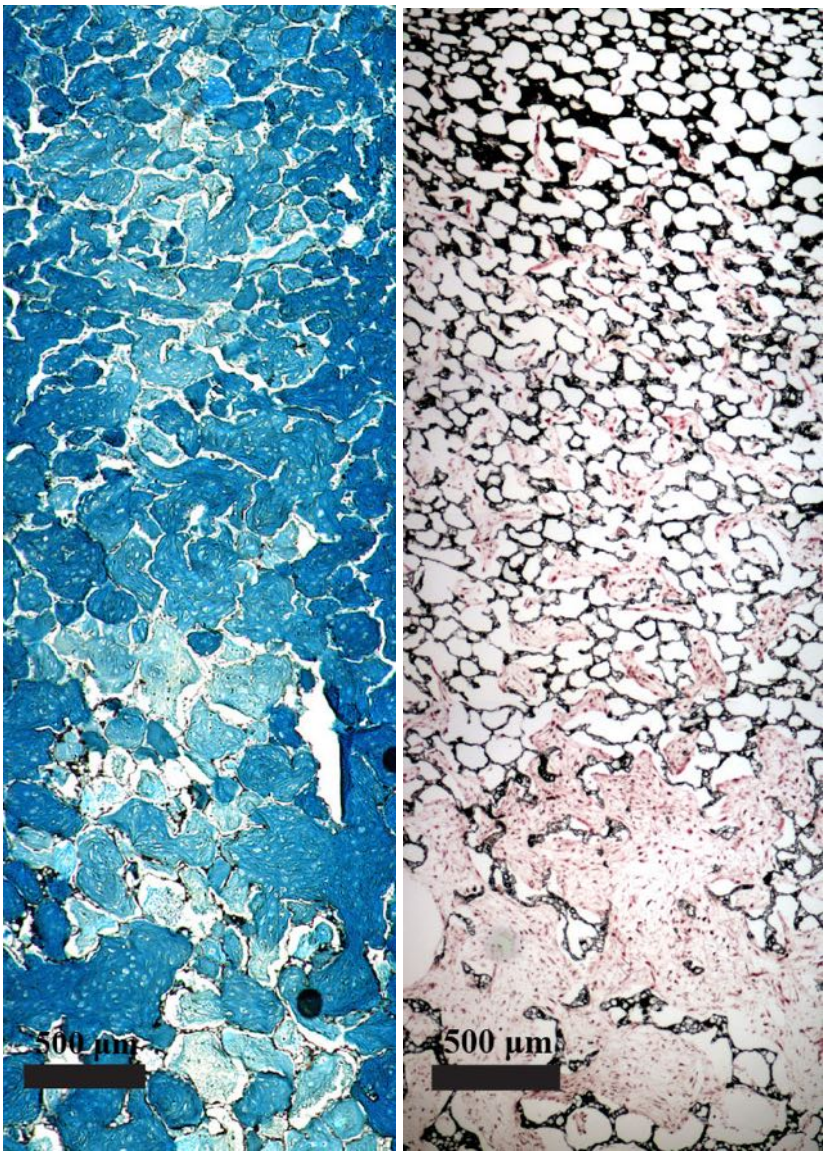

(a) *Alcian blue staining. Gradient scaffold in bioreactor*

(b) *Alizarin red staining. Gradient scaffold in bioreactor*

Fig. 6.28 *Histology staining of gradient pore PLLA scaffold exposed to the same medium in upper and lower chamber. a) Gradient scaffold cultured in the bioreactor, exposed to osteogenic medium, b) Gradient scaffold cultured in the bioreactor, exposed to chondrogenic medium*

- 3^{rd} Set. Influence of bioreactor. To evaluate the influence of the bioreactor different tests in multi-well plate were carried out. For the first group, gradient and 200 µm scaffold in osteogenic medium (fig. 6.29), it is possible to individuate in both cases the production of calcium from osteoblasts, though less than in the bioreactor. The perfusion of the nutrient inside the construct in this case is less accentuate.
  Dissimilar the behaviour is for the second group, gradient and 70 µm scaffold. The

homogenous scaffold has an uniform and elevate production of GAGs in the entire scaffold that means a good cartilage-like tissue. The gradient scaffold presents an comparable expression of the bioreactor.

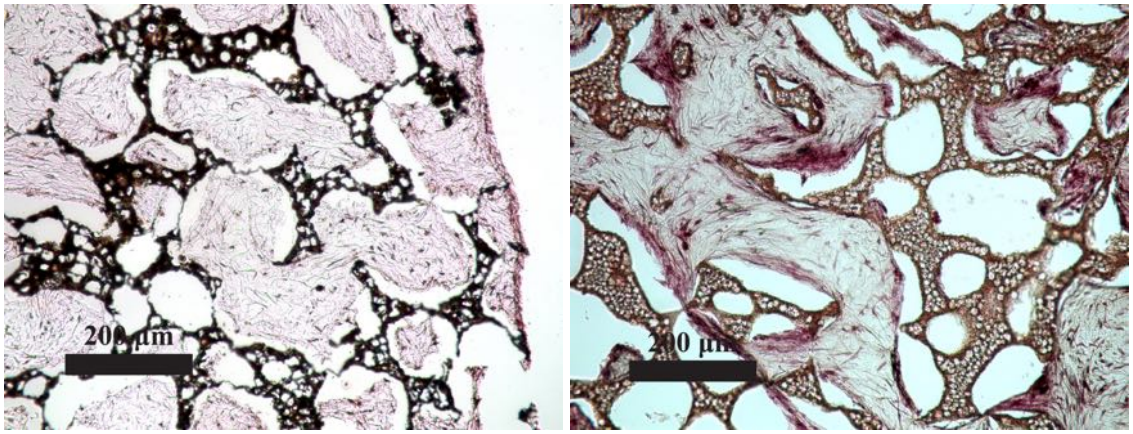

(a) *Alizarin red staining* (b) *Alizarin red staining*

Fig. 6.29 *PLLA scaffold with gradient and homogenous pore size, cultured in multi well plate, exposed to osteogenic medium. a) Gradient scaffold; b) 200 µm scaffold*

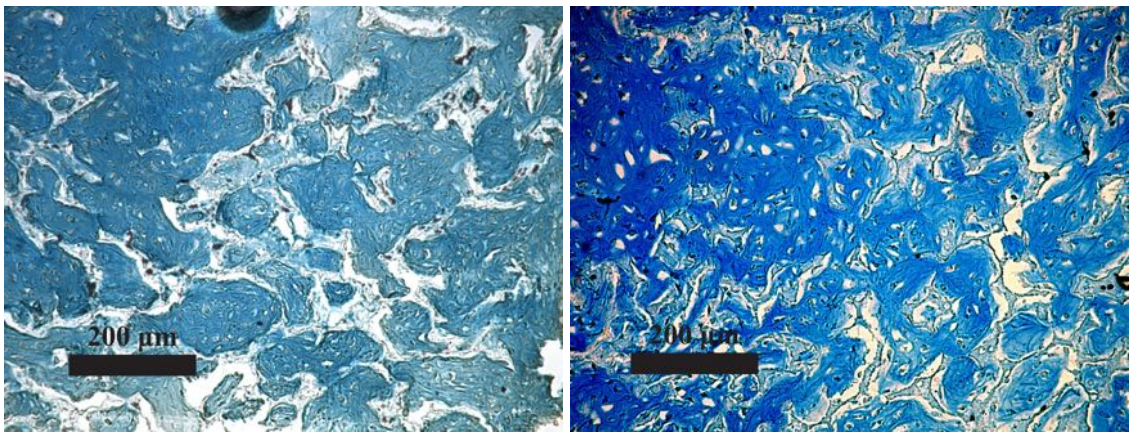

(a) *Alcian blue staining* (b) *Alcian blue staining*

Fig. 6.30 *PLLA scaffold with gradient and homogenous pore size, cultured in multi well plate, exposed to chondrogenic medium. a) Gradient scaffold; b) 70 µm scaffold*

6.3.3 Real-Time quantitative PCR

Simultaneous to the histological analysis, Real-Time quantitative PCR was carried out. The scaffolds were collected separately. Each construct was cut and analysed the top and the

bottom of the scaffold. RNA was extracted using Trizol (Invitrogen) following the standard protocol after the smashing of the sample in liquid nitrogen environment. SuperScript III kit (Invitrogen) was utilised with random hexamer primers to complete the reverse transcription. Real-time RT-PCR was performed using the StepOnePlus thermocycler (Applied Biosystems, Foster City, CA) and SYBR Green Reaction Mix (Applied Biosystems). The expression levels of 18S were used as endogenous controls and the various gene expression levels were calculated using the comparative Ct method. SOX 9, Aggrecan (ACAN), collagen type II (COL2) were used as indicative genes for cartilage, Runt-related transcription factor 2 (RUNX2), Bone sialoprotein 2 (BSP II) and osteopontin (OPN) for bone. The gene expressions were analysed.

- 1^{st} Set. Influence of culture media. In both cases, chondrogenic and osteogenic media, the regulation of tissue specific genes is very well defined. hBMSCs cultured in 3D scaffold were used as control, all values were reported as relative gene expression related to hBMSCs not differentiated. The scaffolds were cut in parts corresponding to upper chamber and lower chamber, and each part was analyzed via Real-Time PCR. In figures 6.31, 6.32, 6.33, 6.34 the different gene expressions were reported. Focusing on chondrogenic genes (COL 2, ACAN and SOX 9) their upregulation is up to several hundred thousands times (COL 2) more expressed in the case of UC compared to LC. In the case of bone-like tissue the difference of gene expression between the two parts is less marked than the chondro-like tissue but in any case a clear trend is distinguishable.

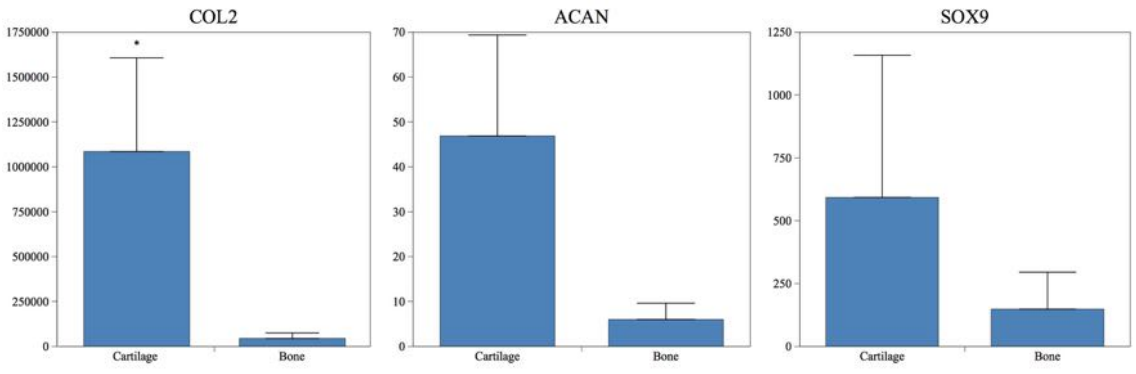

(a) (b) (c)

Fig. 6.31 *Relative gene expression of cartilage markers in PLLA gradient scaffold cultured in the bioreactor with diverse differentiation media in upper and lower chamber*

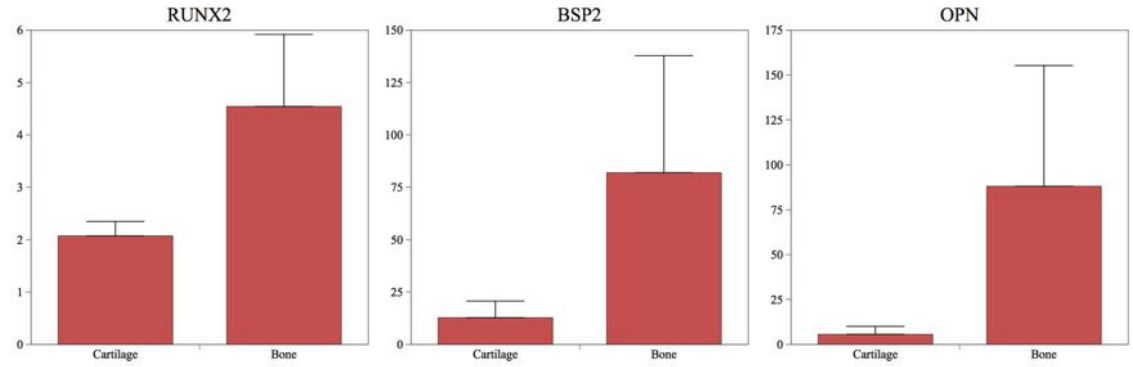

Fig. 6.32 *Relative gene expression of bone markers in PLLA gradient scaffold cultured in the bioreactor with diverse differentiation media in upper and lower chamber*

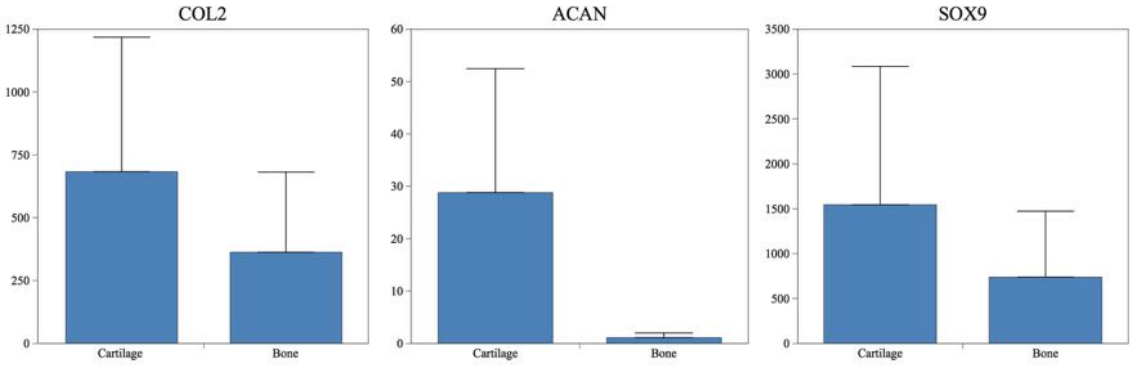

Fig. 6.33 *Relative gene expression of cartilage markers in GelMA scaffold cultured in the bioreactor with diverse differentiation media in upper and lower chamber*

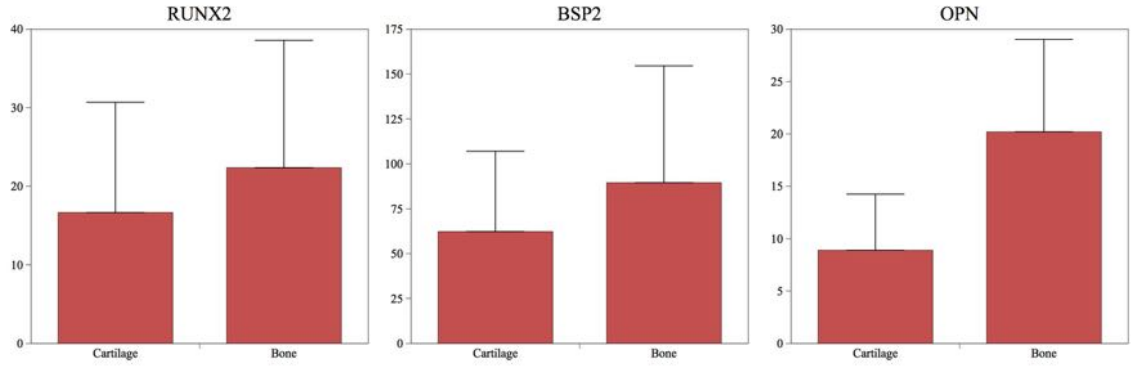

Fig. 6.34 *Relative gene expression of bone markers in GelMA scaffold cultured in the bioreactor with diverse differentiation media in upper and lower chamber*

- 2^{nd} Set. Influence of pore size. For the second set of experiments after one week of cells proliferation the same differentiation media for upper chamber and lower chamber were adopted. In one case chondrogenic medium, in the other case osteogenic medium. This set of experiment was carried out to verify if the only difference in morphology, without other factors, could influence the gene expression. Adopting the same protocol of previous test, the scaffold was cut in parts to enlighten the diverse contribution. Both in chondrogenic and in osteogenic media the trend is well defined. For cartilage-like tissue the small pore size higher enhances the chondro-differentiation (fig. 6.35), while the bone-like is enhanced from the large pore size (fig. 6.36).
  In the case of cartilage tissue this behavior can be due to more intense contact between cells. The larger pores required more cells to fill the entire free space, while the smaller pores can be more easily filled with cells. Filling the pores can increase the cell-cell interactions and provide a good three-dimensional microenvironment to promote chondrogenic differentiation and cartilage tissue formation.

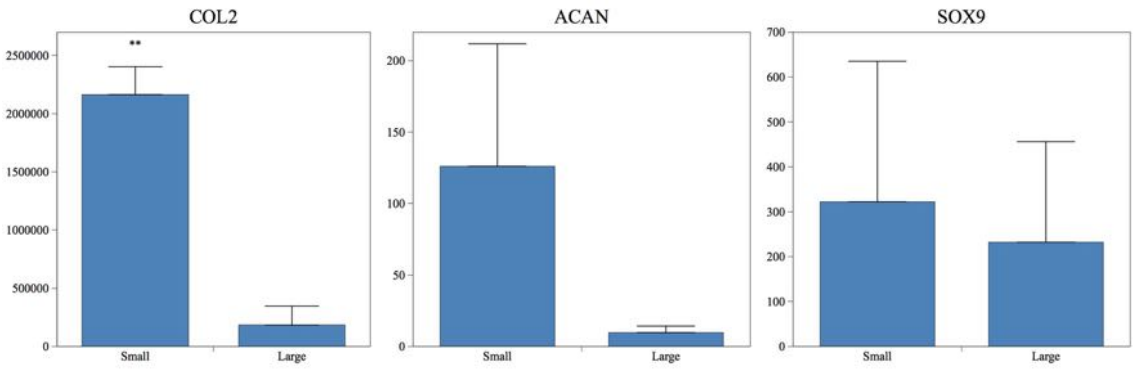

(a) (b) (c)

Fig. 6.35 *Relative gene expression of cartilage markers in PLLA gradient scaffold cultured in the bioreactor with the same differentiation media in upper and lower chamber*

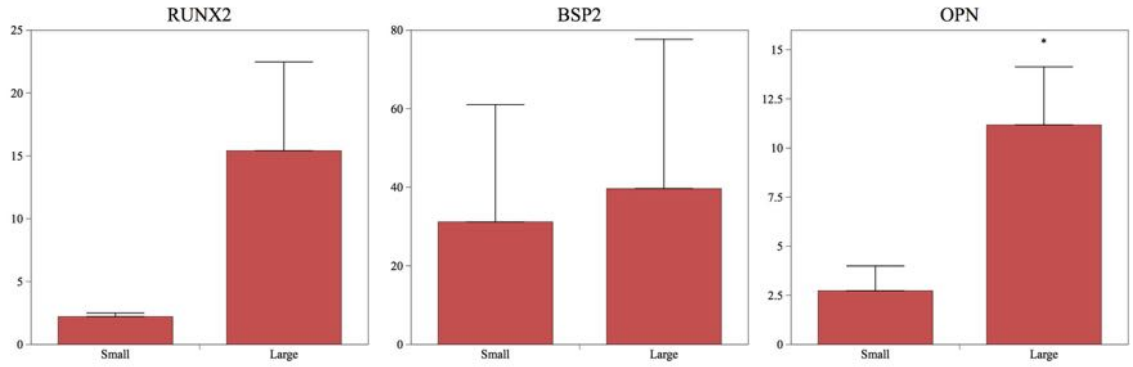

(a) (b) (c)

Fig. 6.36 *Relative gene expression of bone markers in PLLA gradient scaffold cultured in the bioreactor with the same differentiation media in upper and lower chamber*

- 3^{rd} Set. Influence of bioreactor. The third set of experiment was realised in multi-well plate to show the influence of the bioreactor in the cell culture. Furthermore, tests in homogeneous scaffold in term of pore dimension were effectuated as endogenous control. Taking into account the chondrogenic tests (fig. 6.37) it is possible to see a trend in the case of gradient scaffold, the small pore size are always more expressed that the large pore size. In the case of 70 µm scaffold (fig. 6.38) the main upregulation of the gene it is not persistent on the same part of the scaffold (COL2 and ACAN bottom, SOX9 top). The PCR results show very high values in absolute terms for all chondro genes, this aspect proves the good capacity of the scaffold to allow the cell proliferation and differentiation also in the simplest cell culture conditions.
  Similar results were found in the osteogenic test reported in figure 6.39. In both cases the span of the values between large and small pore is less remarkable than in the chondro differentiation, in any case, while in the gradient scaffold this tendency is constant, the 200 µm (fig. 6.40) does not exhibit a constant higher upregulation of the gene in a specific section of the scaffold.

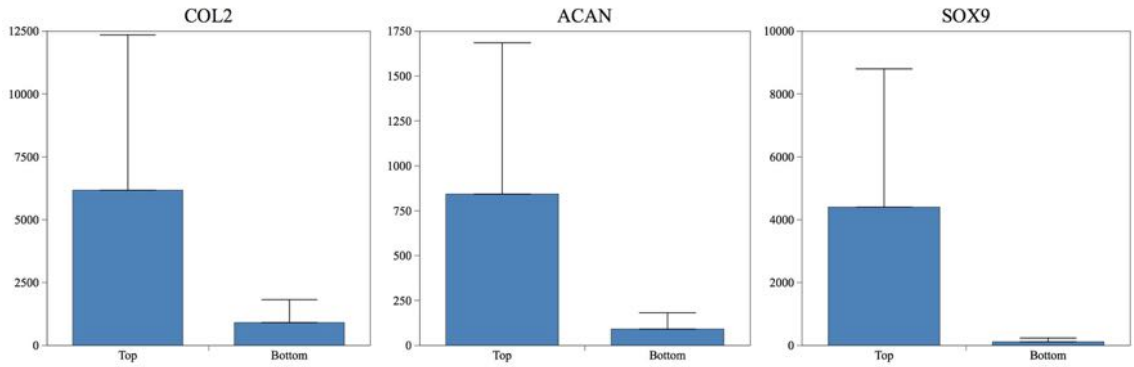

(a) (b) (c)

Fig. 6.37 *Relative gene expression of cartilage markers in PLLA gradient scaffold cultured in multi well plate*

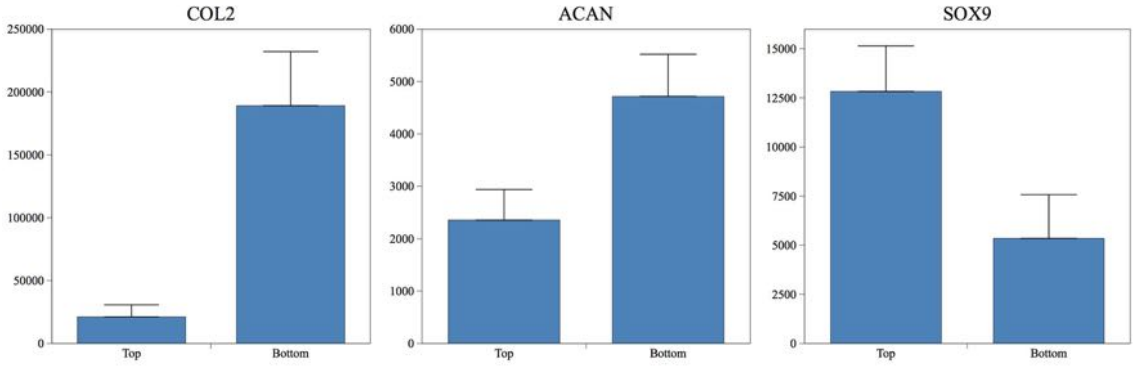

(a) (b) (c)

Fig. 6.38 *Relative gene expression of cartilage markers in PLLA 70μm scaffold cultured in multi well plate*

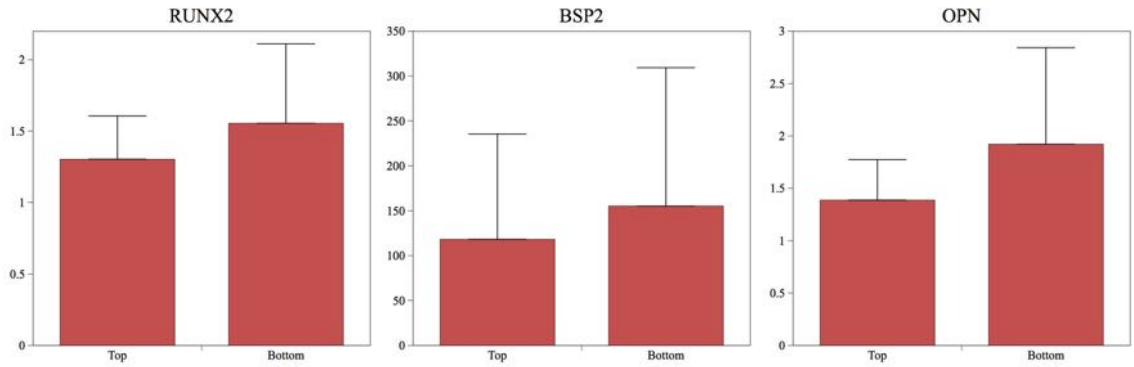

(a) (b) (c)

Fig. 6.39 *Relative gene expression of cartilage markers in PLLA gradient scaffold cultured in multi well plate*

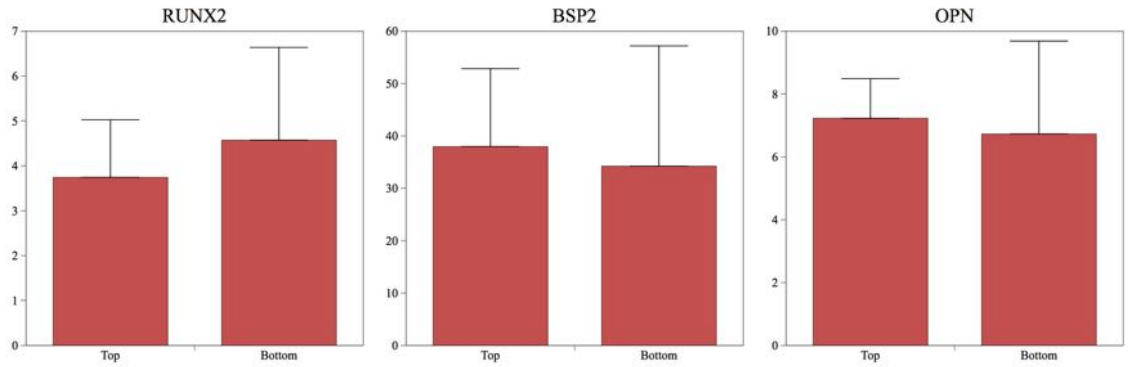

(a) (b) (c)

Fig. 6.40 *Relative gene expression of bone markers in PLLA 70µm scaffold cultured in multi well plate*

References

P. G. Alexander, R. Gottardi, H. Lin, T. P. Lozito, and R. S. Tuan. Three-dimensional osteogenic and chondrogenic systems to model osteochondral physiology and degenerative joint diseases. *Experimental biology and medicine (Maywood, N.J.)*, pages 1080–1095, 2014.

V. Anandan, X. Yang, E. Kim, Y. L. Rao, and G. Zhang. Role of reaction kinetics and mass transport in glucose sensing with nanopillar array electrodes. *Journal of biological engineering*, 1:5, 2007.

L. Bjerre, C. E. Bünger, M. Kassem, and T. Mygind. Flow perfusion culture of human mesenchymal stem cells on silicate-substituted tricalcium phosphate scaffolds. *Biomaterials*, 29(17):2616–2627, 2008.

A. Braccini, D. Wendt, C. Jaquiery, M. Jakob, M. Heberer, L. Kenins, A. Wodnar-Filipowicz, R. Quarto, and I. Martin. Three-Dimensional Perfusion Culture of Human Bone Marrow Cells and Generation of Osteoinductive Grafts. *Stem Cells*, 23(8):1066–1072, 2005.

C. a. Carmona-Moran and T. M. Wick. Transient Growth Factor Stimulation Improves Chondrogenesis in Static Culture and Under Dynamic Conditions in a Novel Shear and Perfusion Bioreactor. *Cellular and Molecular Bioengineering*, 8(2):267–277, 2015.

S. Damaraju, J. R. Matyas, D. E. Rancourt, and N. a. Duncan. The Effect of Mechanical Stimulation on Mineralization in Differentiating Osteoblasts in Collagen-I Scaffolds. *Tissue engineering: Part A*, 00(00):1–12, 2014.

D. M. Doroski, M. E. Levenston, and J. S. Temenoff. Cyclic tensile culture promotes fibroblastic differentiation of marrow stromal cells encapsulated in poly(ethylene glycol)-based hydrogels. *Tissue engineering. Part A*, 16(11):3457–3466, 2010.

C. Granet, N. Laroche, L. Vico, C. Alexandre, and M. H. Lafage-Proust. Rotating-wall vessels, promising bioreactors for osteoblastic cell culture: Comparison with other 3D conditions. *Medical and Biological Engineering and Computing*, 36:513–519, 1998.

M. S. Hossain, D. J. Bergstrom, and X. B. Chen. Prediction of cell growth rate over scaffold strands inside a perfusion bioreactor. *Biomechanics and Modeling in Mechanobiology*, 14 (2):333–344, 2014.

H. J. Kim, U.-J. Kim, G. G. Leisk, C. Bayan, I. Georgakoudi, and D. L. Kaplan. Bone regeneration on macroporous aqueous-derived silk 3-D scaffolds. *Macromolecular bioscience*, 7(5):643–55, 2007.

H. Lin, T. P. Lozito, P. G. Alexander, R. Gottardi, and R. S. Tuan. Stem Cell-Based Microphysiological Osteochondral System to Model Tissue Response to Interleukin-1 β. *Molecular Pharmaceutics*, 11:2203–2212, 2014.

T. P. Lozito, P. G. Alexander, H. Lin, R. Gottardi, A. W.-M. Cheng, and R. S. Tuan. Three-dimensional osteochondral microtissue to model pathogenesis of osteoarthritis. *Stem cell research & therapy*, 4 Suppl 1(Suppl 1):S6, 2013.

V. S. Nirmalanandhan, J. T. Shearn, N. Juncosa-Melvin, M. Rao, C. Gooch, A. Jain, G. Bradica, and D. L. Butler. Improving Linear Stiffness of the Cell-Seeded Collagen Sponge Constructs by Varying the Components of the Mechanical Stimulus. *Tissue Engineering Part A*, 14(11):1883–1891, 2008.

G. Pattappa, H. K. Heywood, J. D. de Bruijn, and D. A. Lee. The metabolism of human mesenchymal stem cells during proliferation and differentiation. *Journal of Cellular Physiology*, 226(10):2562–2570, 2011.

J. L. Puetzer, J. J. Ballyns, and L. J. Bonassar. The Effect of the Duration of Mechanical Stimulation and Post-Stimulation Culture on the Structure and Properties of Dynamically Compressed Tissue-Engineered Menisci. *Tissue Engineering Part A*, 18(13-14):1365–1375, 2012.

E. Schmelzer, A. Finoli, I. Nettleship, and J. C. Gerlach. Long-term three-dimensional perfusion culture of human adult bone marrow mononuclear cells in bioreactors. *Biotechnology and Bioengineering*, 112(4):801–810, 2015.

M. Sladkova and G. de Peppo. Bioreactor Systems for Human Bone Tissue Engineering. *Processes*, 2(2):494–525, 2014.

M. Taffetani, R. Gottardi, D. Gastaldi, R. Raiteri, and P. Vena. Poroelastic response of articular cartilage by nanoindentation creep tests at different characteristic lengths. *Medical engineering & physics*, 36(7):850–8, 2014.

S. C. Tran, A. J. Cooley, and S. H. Elder. Effect of a mechanical stimulation bioreactor on tissue engineered, scaffold-free cartilage. *Biotechnology and Bioengineering*, 108(6): 1421–1429, 2011.

a. I. Van Den Bulcke, B. Bogdanov, N. De Rooze, E. H. Schacht, M. Cornelissen, and H. Berghmans. Structural and rheological properties of methacrylamide modified gelatin hydrogels. *Biomacromolecules*, 1(1):31–38, 2000.

T. Wang, B. S. Gardiner, Z. Lin, J. Rubenson, T. B. Kirk, A. Wang, J. Xu, D. W. Smith, D. G. Lloyd, and M. H. Zheng. Bioreactor Design for Tendon/Ligament Engineering. *Tissue Engineering Part B: Reviews*, 19(2):133–146, 2013.

T.-W. Wang, H.-C. Wu, H.-Y. Wang, F.-H. Lin, and J.-S. Sun. Regulation of adult human mesenchymal stem cells into osteogenic and chondrogenic lineages by different bioreactor systems. *Journal of Biomedical Materials Research Part A*, 88A(4):935–946, 2009.

K. a. Wartella and J. S. Wayne. Bioreactor for biaxial mechanical stimulation to tissue engineered constructs. *Journal of biomechanical engineering*, 131(4):044501, 2009.

K. Webb, R. W. Hitchcock, R. M. Smeal, W. Li, S. D. Gray, and P. a. Tresco. Cyclic strain increases fibroblast proliferation, matrix accumulation, and elastic modulus of fibroblast-seeded polyurethane constructs. *Journal of Biomechanics*, 39(6):1136–1144, 2006.

A. B. Yeatts and J. P. Fisher. Bone tissue engineering bioreactors: Dynamic culture and the influence of shear stress. *Bone*, 48(2):171–181, 2011.

Chapter 7

Conclusions

Different strategies to produce PLLA-based scaffolds for osteochondral regeneration purposes were investigated in this thesis. PLLA has been widely used as material for three-dimensional polymer scaffolds suitable for cell transplantation, owing to its biodegradability and biocompatibility. The scaffolds were produced via TIPS technique starting from a ternary solution, which presents the main advantage to control pore size simply by varying the T vs. time protocol.

By taking advantage of this aspect, an experimental apparatus able to produce porous foams with a monotonous uni-dimensional pore size gradient via TIPS was developed and presented. Generally, one of the most adopted techniques to produce foams with a gradient pore dimension consists in the bonding together of several layers with different controlled pore distribution. Although these techniques are versatile, the main disadvantage is represented by the number of steps necessary to obtain the overall morphology and the resulting discontinuity between layers. According to the technique proposed in this thesis work, the foams were produced via a single step operation, without requiring the junction of multiple layers or the use of graded porogens.

A monotonous unidimensional variation of pore dimensions along the foam thickness was obtained by imposing different thermal histories on the two surfaces of sample (via programmed Peltier cells). Manipulating the temperature and/or the time during the nucleation and growth process, a relatively large pore size range can be obtained. By increasing demixing temperature pore size globally increases (i.e. 80-260 μm at 35°C); on the other hand, when decreasing the temperature, pore size globally decrease (i.e. 40-160 μm at 25°C).

In principle, this procedure can be adopted to produce foams with various overall thicknesses or different materials, by varying the distance between the Peltier elements or the ternary solution.

To mimic as closely as possible the tissue to regenerate, a neat polymer is often not adequate.

PLLA, indeed, does not posses the appropriate bioactivity and, in the case of bone tissue, osteoconductivity. To overcome these limits, composite PLLA/HA scaffolds were produced. Some papers described the possibility to include HA in a polymer network via TIPS, starting from a binary mixture polymer-solvent. However, in those cases, the so-obtained scaffolds show an irregular and anisotropic structure with very few parameters to tune as a function of the specific tissue applications. The exploitation of the liquid-liquid separation can overcome these limits.

Based on the results of the thesis work, it is possible to state that the presence of the HA did not influence the phase separation process in terms of demixing temperature. As a matter of fact, a porous and interconnected structure was observed in the bulk of the scaffolds. SEM analysis revealed the presence of HA particles, confirmed by XRD analysis. As for porosity, when increasing HA content, the overall porosity decreases since a partial portion of open pore is occupied by HA particles. In spite of this slow reduction, porosity reaches about ~90% at HA weight percentage of 66%. This result confirms that even in the presence of a large amounts of HA, the scaffolds are characterized by a highly porous structure. TGA analysis showed a good agreement with the amount of filler within the initial solution, with an average discrepancy of 10-15%.

Besides hydroxyapatite different varieties of another very interesting filler was tested: the bioglass. In particular, two different BGs compositions (1393 and 45S5) were compared in terms of topography, biodegradation and bioactivity. About the scaffold morphology, SEM micrographs showed that the addition of 1393 BG did not affect the final morphology of the scaffolds; on the contrary, the presence of 45S5 BG, at higher percentages, interacted with the phase separation process, probably due to the higher reactivity of the 45S5 compared to the 1393. The composite scaffolds showed a significant increase in weight loss when compared to the pure PLLA. The bioactivity tests showed positive results for both composite PLLA/BG scaffolds; via SEM images the typical cauliflowers-like shape of HA morphology was observed after 4 weeks of soaking in SBF; XRD and FTIR analysis confirmed the formation of HCA layer. These results strengthen the possibility to successfully include BG or HA particles in PLLA scaffolds via a modified ternary TIPS in a reliable 'one-shot' protocol for the synthesis of foamed composites where the compositional variable (filler content) can be tuned up separately. This fact allows one to compare the effectiveness of different types of fillers and contemporary accurately tune the structure of the scaffold.

In addition to the material characterization, several biological tests for cell culturing of different cell lineages on different substrates were also carried out.

TIPS technique was adopted to produce pure PLLA scaffold with two different average pore dimensions ~100 μm and ~200 μm. The results showed that the scaffolds maintained

the differentiated phenotype of articular and nasoseptal chondrocytes and supported the proliferation of MSCs. The important influence of the pore size in a porous scaffold for cartilage tissue engineering was previously reported with divergent results as a function of the scaffold material and cell type. This is the first work investigating the influence of pore sizes of PLLA scaffolds on human chondrocyte differentiated phenotype. The study reveals that a relative small difference in scaffold pore size determined recognizable effects on cartilage markers, in particular small pore dimensions (100 μm) best promote chondrogenesis in PLLA scaffolds.

Live/dead and MTS assay in PLLA gradient scaffolds seeded with MSCs showed the remarkable ability of the scaffold to support the proliferation, specifically via MTS assay a cell number more than duplicated compared to the initial one after 7 days of culture was observed.

Preliminary viability tests of articular chondrocytes in composite PLLA/BG showed a very satisfactory cytocompatibility of the scaffold to support the cell culture.

Biological studies on PLLA/HA demonstrated that filler did not influence the cell viability on scaffold during in vitro cell cultures with mouse preosteoblastic MC3T3-E1 cells. Furthermore, the osteoblastic phenotype was supported by the presence of HA particles evidencing the ability of the filler to increase the ALP activity respect to pure PLLA.

The last part of the thesis was dedicated to the study of a bioreactor capable to reproduce the physiological conditions of the osteochondral junction. The bioreactor was preliminary characterized and modeled, then tested with the gradient pore scaffold. The microphysiological tissue system (MTS) bioreactor has been developed to replicate in vitro the in vivo the osteochondral physiological conditions, allowing a separate control of the condral and osseous environments. At the end of the period of culturing (7 days of cell expansion and 28 days of differentiation) a spatially defined biphasic differentiation of hMSCs within the scaffold was observed. The different cells type (chondrocytes and osteoblasts) were obtained from a unique cell variety. Furthermore, the effect of the culture media, pore size and bioreactor were separately investigated. Finally, single unit biodegradable scaffold produced with local gradient pore structure was tailored for chondro- and osteoinduction and successfully used in-vitro for studying and improving osteochondral tissue repair, providing mechanical stability and local cues for cell differentiation.

In conclusion, different approaches were adopted in order to fathom which strategies best work on chondral and osteochondral regeneration based on PLLA scaffold produced via TIPS technique.

Chapter 8

Future work

The results showed in this thesis seem to open new perspective for future developments. First of all, a better comprehension of the phase separation mechanism could increase the possibility to obtain wider pore dimension range. Phase separation is a complex combination of thermodynamics and kinetic mechanisms that depends on the specific adopted system. A deeper knowledge of the system, by simulating a complete phase diagram of the solution, should allow a better control of the final morphology of the scaffold.
As for the gradient pore scaffold, we focused on the gradient of pore size generated by the different time periods spent by each sample layer inside the metastable region at a given temperature. Further tests can be carried out by setting different temperatures at each side of the scaffold, to investigate the effect of two mechanisms (nucleation-and-growth and spinodal decomposition) inside the same construct. The methodology to produce the gradient pore scaffold here developed is potentially easily scalable and applicable to multiple systems. Moreover, different polymer solutions and thickness of the foam can be tested. The composite scaffolds, preliminary investigated, need further investigations. A combination of the gradient pore dimension with HA particles should perfect mimic the difference of morphology between the compact bone and the spongy bone. At the same time, by taking advantage of the TIPS technique, a gradient of filler along the axis of the foam or a combination of compositional and pore dimension gradient can be designed and attained. In principle, local average pore dimension and spatial dispersion of filler can be easily manipulated by a single-step production process.
Furthermore, concerning bioglass particles, once assessed that the 1393 better matched with the scaffold production technique, different ions can be added to the standard composition, such as Cu, Li, etc. in order to increase the interaction scaffold-living tissue.
Preliminary in-vitro tests with different cell lineage showed the good biomimetic capacity of the scaffold but to really verify if the scaffold can be used for clinical applications, in-

vivo tests should be designed and carried out. Tests in animal models can provide crucial informations to optimize the scaffold's design and performance.
Finally, the seeded scaffold inside the bioreactor system can be used for in-vitro screening of new drugs for chondral and bone repair as a model for analysing the response of cell response due to an inflammatory signal (e.g. IL-β1) in a customizable 3D system.